UNIVERSIDAD DE BUENOS AIRES

Facultad de Ciencias Exactas y Naturales

Departamento de Física

Radiative models for jets in X-ray binaries

A thesis submitted for the degree of
Doctor of Philosophy in Physics

Gabriela Soledad Vila

Supervisor: Dr. Gustavo E. Romero

Counsellor: Dr. Pablo D. Mininni

Workplace: Instituto Argentino de Radioastronomía

Buenos Aires, 2012

UNIVERSIDAD DE BUENOS AIRES

Facultad de Ciencias Exactas y Naturales

Departamento de Física

Modelos radiativos para jets en binarias de rayos X

Tesis presentada para optar al título de
Doctor de la Universidad de Buenos Aires en el área Ciencias Físicas

Gabriela Soledad Vila

Director de Tesis: Dr. Gustavo E. Romero

Consejero de Estudios: Dr. Pablo D. Mininni

Lugar de Trabajo: Instituto Argentino de Radioastronomía

Buenos Aires, 2012

This work has been awarded the *Carlos M. Varsavsky Prize* to the Best PhD Thesis on Astronomy and Astrophysics in Argentina 2010-2012, granted by the Astronomical Society of Argentina.

Este trabajo ha sido galardonado con el *Premio Carlos M. Varsavsky* a la Mejor Tesis Doctoral en Astronomía y Astrofísica de la Argentina 2010-2012, otorgado por la Asociación Argentina de Astronomía.

ABSTRACT

Radiative models for jets in X-ray binaries

An outstanding feature of astrophysical accreting sources at all scales in the Universe is the production of jets - collimated, bipolar, extended flows of matter and electromagnetic field ejected from the surroundings of a rotating object. Microquasars are X-ray binaries that produce relativistic jets. Jets in microquasars emit along the whole electromagnetic spectrum. The radiation is non-thermal; this reveals that jets accelerate particles up to relativistic energies. Understanding the origin of the emission is, then, one way to probe the interior of jets.

In this thesis we develop a lepto-hadronic model for the electromagnetic radiation from jets in microquasars with low-mass companion stars. We consider the interaction of relativistic particles with matter, radiation, and magnetic field, and obtain broadband spectral energy distributions. We investigate how the shape of the spectrum changes as the parameters that model the conditions in the jet are varied within the constraints imposed by theory and observations. We present general results, as well as applications to some specific systems. Motivated by the growing volume and quality of the data now becoming available at high and very high energies, we carefully analyse the predictions of the model in the gamma-ray band. The results will be directly tested in the near future with the present and forthcoming space-borne and terrestrial gamma-ray telescopes.

Keywords: *microquasars; jets; non-thermal radiation; gamma rays; X-ray binaries: individual: GX 339-4; X-ray binaries: individual: XTE J1118+480.*

RESUMEN

Modelos radiativos para *jets* en binarias de rayos X

Una propiedad notable de los sistemas astrofísicos acretantes a toda escala en el Universo es la producción de *jets* - flujos colimados, bipolares y extendidos de materia y campo electromagnético eyectados desde las cercanías de un objeto en rotación. Los *microcuasares* son binarias de rayos X con *jets*. Los *jets* en microcuasares emiten a lo largo de todo el espectro electromagnético. La radiación es no térmica, lo que indica que los *jets* aceleraran partículas hasta energías relativistas. Comprender el origen de la emisión electromagnética es, entonces, una de las maneras de explorar el interior de los *jets*.

En esta tesis se desarrolla un modelo lepto-hadrónico para la radiación electromagnética de *jets* en microcuasares con estrellas compañeras de baja masa. Se considera la interacción entre las partículas relativistas con materia, radiación y campo magnético para obtener espectros de banda ancha. Se investiga cómo se modifica la forma de los espectros al variar los valores de los parámetros que modelan las condiciones físicas en los *jets*, dentro de las cotas impuestas por teoría y observaciones. Se presentan resultados generales y aplicaciones a sistemas específicos. En vista de la creciente calidad y cantidad de los datos que es actualmente posible obtener a altas y muy altas energías, se analizan en detalle las predicciones del modelo en la banda de rayos gamma. Los resultados podrán ser directamente contrastados en el futuro cercano con las observaciones de telescopios de rayos gamma espaciales y terrestres de presente y futura generación.

Palabras clave: *microcuasares; jets; radiación no térmica; rayos gamma; binarias de rayos X: GX 339-4; binarias de rayos X: XTE J1118+480.*

ACKNOWLEDGEMENTS

The vocabulary of pages that follow is made up of formulas, graphics, and specialised jargon. Writing down the results of the work of five years using those tools has been, however, easier than putting down in everyday words my gratitude to whom accompanied me in the process. These paragraphs are my unsatisfactory attempt.

To Gustavo Romero, my supervisor and my friend. For all the opportunities you have given me, that are so many! For trusting that I'd be able to cope with every challenge (and for accepting it when I refused to take some of them). For always caring about my career (and that of all your students) in spite of your tiredness and your other obligations; your unlimited commitment is for me a great example. For caring also for my development as a person. For the many pieces of advice you gave me, and for creating the necessary trust for me to ask for them. Thank you, Gustavo.

To the members of the GARRA group. Very special thanks to Paula, for her friendship and her help during my first years in La Plata. Also to Matías, for the discussions and for sharing his knowledge with me, and to Leonardo, for his great human qualities. And mostly to the girls, Florencia, María Victoria, and Daniela, for their company and the joy they bring to the office hours.

To the Instituto Argentino de Radioastronomía and the Facultad de Ciencias Exactas y Naturales of the Universidad de Buenos Aires. To all my teachers and professors. I am proud of being the product of Argentinian public education.

To the members of the examining committee, Drs. Rafael Ferraro, Josep M. Paredes, and Leonardo J. Pellizza. My special acknowledgement to Dr. Paredes for travelling from Barcelona to attend the defense of this thesis.

To Valentí Bosch-Ramon, for his friendship and his invaluable advice on scientific matters.

To Prof. Dr. Felix Aharonian, for the opportunity of working in his group at the Max-Planck-Institut für Kernphysik, in Heidelberg.

To my friends and colleagues Alejandra and Cecilia, for their friendship, their support, and the mutual understanding. To Ale very specially, as well, for the three years of shared household chores.

To my friends from childhood and teenage years, for still being my friends despite my months (even years) of absence. Thinking of you immediately puts my whole life in perspective; it helps me become conscious of the long road I've walked since the first day at "the 23" (with Lili) till today, passing by the classrooms of the Excelsior (with Claudia, Mariana, and Paola), and with a stop now and then on Saturday afternoons to buy magazines and cassettes (with Samanta). Thank you, friends.

More than anyone, to my parents Alicia and Ernesto, *the eternal rocks beneath*. For letting me choose my future freely, and for teaching me that the only way to achieve what I wish is through work and effort. All I've reached is for you. To my grandparents, because their love and the memories of my childhood have definitely shaped my nature. Those of them who cannot see me today, I guess would be proud of me.

And to Nicolás, for his company, his patience, his help, his support, his encouragement, his trust, and for teaching me almost everything else I still had to learn. *Tu n'es encore pour moi qu'un petit garçon tout semblable à cent mille petits garçons. Et je n'ai pas besoin de toi. Et tu n'as pas besoin de moi non plus. Je ne suis pour toi qu'un renard semblable à cent mille renards. Mais, si tu m'apprivoises, nous aurons besoin l'un de l'autre. Tu seras pour moi unique au monde. Je serai pour toi unique au monde...*

Gabriela

AGRADECIMIENTOS

El vocabulario de las páginas que siguen se compone de fórmulas, gráficos y términos especializados. Redactar los resultados del trabajo de cinco años usando esas herramientas ha resultado, sin embargo, más fácil que poner en palabras sencillas mi agradecimiento a aquellos que me acompañaron en el proceso. Estos párrafos son mi insatisfactorio intento en ese sentido.

A Gustavo Romero, mi director y mi amigo. Por todas las oportunidades que me has dado, ¡que son tantas! Por confiar en que iba a poder con cada desafío (y por aceptarlo cuando no quise afrontar alguno). Por ocuparte siempre de mi carrera (y la de todos tus estudiantes) a pesar del cansancio y tus demás obligaciones; tu compromiso y dedicación sin límites es para mi un gran ejemplo. Por preocuparte por mi crecimiento como persona, a la par de mi crecimiento como científica. Por los muchos consejos que me diste, y por que exista la confianza necesaria para pedírtelos. Gracias Gustavo.

A los integrantes del grupo GARRA. Gracias muy especiales a Paula, por su amistad y su ayuda en mis primeros años en La Plata. También a Matías, por las discusiones y por compartir conmigo sus conocimientos, y a Leonardo por su gran calidad humana. Y sobre todo a las chicas, Florencia, María Victoria y Daniela, por su compañía y por la alegría que aportan a las horas de oficina.

Al Instituto Argentino de Radioastronomía y a la Facultad de Ciencias Exactas y Naturales de la Universidad de Buenos Aires. A todos mis maestros y profesores. Estoy orgullosa de ser producto de la educación pública argentina.

A los miembros de jurado examinador, Dres. Rafael Ferraro, Josep M. Paredes y Leonardo J. Pellizza. Mi especial agradecimiento al Dr. Paredes por haber viajado desde Barcelona para asistir a la defensa de esta tesis.

A Valentí Bosch-Ramon, por su amistad y su invaluable consejo en cuestiones científicas.

Al Profesor Dr. Felix Aharonian, por la oportunidad de trabajar junto a su grupo en el Max-Planck-Institut für Kernphysik, en Heidelberg.

A mis amigas y colegas Alejandra y Cecilia, por su amistad, su ayuda y la mutua comprensión. A Ale muy especialmente, también, por los tres años de quehaceres domésticos compartidos.

A mis amigas de la infancia y la adolescencia, por seguir siendo mis amigas a pesar de mis meses (y hasta años) de ausencia. Pensar en ustedes pone inmediatamente mi vida entera en perspectiva; me ayuda a tomar conciencia del largo camino que he recorrido desde el primer día en la 23 (con Lili) hasta hoy, pasando por las aulas del Excelsior (con Claudia, Mariana y Paola), y con alguna parada intermedia un sábado a la tarde para comprar revistas y cassettes (con Samanta). Gracias amigas.

Más que a nadie, a mis padres Alicia y Ernesto, *the eternal rocks beneath*. Por dejarme elegir con libertad mi futuro y por enseñarme que la única forma de lograr lo que uno desea es con esfuerzo y trabajo. Todo lo que lo he logrado es para ustedes. A mis abuelos, porque su cariño y los recuerdos de mi infancia han moldeado definitivamente mi carácter. Los que hoy no pueden verme, creo que se sentirían orgullosos de mi.

Y a Nicolás, por su compañía, su paciencia, su ayuda, su apoyo, su confianza, y por enseñarme casi todo lo que me faltaba aprender. *Tu n'es encore pour moi qu'un petit garçon tout semblable à cent mille petits garçons. Et je n'ai pas besoin de toi. Et tu n'as pas besoin de moi non plus. Je ne suis pour toi qu'un renard semblable à cent mille renards. Mais, si tu m'apprivoises, nous aurons besoin l'un de l'autre. Tu seras pour moi unique au monde. Je serai pour toi unique au monde...*

Gabriela

A mis padres y mis abuelos

To my parents and my grandparents

The most beautiful thing we can experience is the mysterious. It is the source of all true art and all science. He to whom this emotion is a stranger, who can no longer pause to wonder and stand rapt in awe, is as good as dead: his eyes are closed.

Albert Einstein

When I have a terrible need of - shall I say the word - religion, then I go out and paint the stars.

Vincent van Gogh

CONTENTS

LIST OF FIGURES

LIST OF TABLES

1

INTRODUCTION: ACCRETION AND JETS

Nothing can ever pass outwards through the Schwarzschild sphere of radius $r = 2GM/c^2$, which we shall call the Schwarzschild throat. We would be wrong to conclude that such massive objects in space-time should be unobservable, however. It is my thesis that we have been observing them indirectly for many years.

D. Lynden-Bell
Nature, 223, 690-694 (1969)

Some of the most energetic phenomena in the Universe take place in accreting sources that host black holes. The gravitational energy lost by the infalling matter may be efficiently released as radiation reaching the highest energies of the electromagnetic spectrum. Investigating the effects of accretion is one of the few ways to probe astrophysical black holes.

Active galactic nuclei (AGN) were the first astrophysical sources recognized to be powered by accretion (Salpeter 1964, Zel'Dovich 1964, Lynden-Bell 1969). Other types of accreting sources are known, among them young stellar objects, cataclysmic variables, X-ray binaries (XRBs), and gamma-ray bursts (GRBs). These objects display a very varied phenomenology brought about by the nature of the accretor, the source of the accreted matter, and the surrounding environment. The basics of the process of accretion are, nonetheless, the same: matter spirals around a rotating body forming an *accretion disc*, losing angular momentum, and radiating away part of its gravitational energy. All the sources mentioned above have yet another common characteristic: they can

produce *jets*.

Astrophysical jets are collimated bipolar outflows ejected from the vicinities of a central object. Jets are found in the Universe at all scales (Romero et al. 2010); they can be launched from accreting supermassive and stellar-mass black holes, neutron stars, white dwarfs, and protostars. The typical length, bulk velocity, lifetime, and power of astrophysical jets range over several orders of magnitude. Jets launched from black holes and neutron stars may have velocities close to the speed of light; these are *relativistic* jets.

X-ray binaries with jets are called *microquasars* (Mirabel et al. 1992). The name directly suggests that they are small-scale versions of quasars, but the analogy goes beyond morphology. The radiative properties of active galactic nuclei and microquasars point to an unified description of accretion inflows/outflows in supermassive and stellar-mass black holes (Mirabel & Rodríguez 1998). The fundamental variables in this description are the accretion rate and the mass (and possibly the spin) of the black hole (e.g. Sams et al. 1996, Heinz & Sunyaev 2003).

The development of self-consistent models of accretion inflows/outflows coupled with their radiative properties has proved to be a difficult task. There are still some blanks, but much is understood about the launching, collimation, acceleration, and stability of jets. Significant progress has been done in recent years as supercomputers became commonly available and huge numerical simulations feasible. Most of these simulations, however, do not deal with the microphysical processes that give rise to the observed electromagnetic spectrum of jets (see, nonetheless, Bordas et al. 2009, Bosch-Ramon et al. 2011, Huarte-Espinosa et al. 2011).

Current models for the radiation of relativistic jets are based on a series of assumptions about the physical conditions in the outflows, founded in observations, theory, and simulations. The output of radiative jet models are theoretical electromagnetic (or neutrino) emission spectra. It is expected that the comparison of these spectra with observations helps to constrain the values of the physical parameters that characterise the source.

Radiative models not only provide possible explanations for observations, but may also predict detectable radiation (or not) in energy bands not yet observed. It is nowadays particularly interesting to obtain predictions for the

gamma-ray emission of relativistic jets. This is largely motivated by the detection in recent years of thousands of galactic and extragalactic gamma-ray sources, including a few X-ray binaries. Two of the galactic binaries with gamma-ray emission (Cygnus X-1 and Cygnus X-3) are confirmed microquasars.

Continuum gamma-ray emission is non-thermal. High-energy photons are created by the interaction of *relativistic particles* with matter, photons, and magnetic field. The synchrotron spectrum at radio wavelengths of relativistic jets reveals the presence of relativistic electrons. Jets appear then as probable sites of gamma-ray production.

This thesis deals with the development of a lepto-hadronic model for the radiation of relativistic jets in microquasars. It is intended to contribute to the understanding of the physical conditions in the jets through the study of their broadband electromagnetic spectrum. As a particular goal, we aim to assess the efficiency of different processes of gamma-ray emission in microquasars with a low-mass donor star.

The thesis is organized as follows. Chapter 2 is an introduction to microquasars. A one-zone jet model is developed in detail in Chapter 3. We characterize the jet and the injection and distribution of primary and secondary particles. We also discuss the mechanisms of interaction of the relativistic particles with matter, radiation, and magnetic field. Chapter 4 presents two applications of the one-zone model. On the one hand, we study the possible association with microquasars of a group of unidentified galactic gamma-ray sources detected by the satellite *AGILE*. On the other hand, we apply the model to fit the observed spectrum of the microquasar GX 339-4, and make predictions for its high-energy emission. In Chapter 5 we develop an inhomogeneous jet model. We present some general results and an application to the microquasar XTE J1118+480. The general results of the thesis and the perspectives for future works are discussed in Chapter 6. Three appendices complete this work: one on radiative processes, another on non-thermal radiation from microquasar coronae, and the last with the list of publications related to the thesis.

2

MICROQUASARS

The first relativistic galactic jet was discovered by Spencer (1979) in the X-ray binary SS 433. More than a decade later, Mirabel et al. (1992) obtained a clear radio image of a two-sided jet in 1E 1740.7-2942, see Figure 2.1. These authors used for the first time the word *microquasar* to name X-ray binaries with jets.

Jets in microquasars appear as steady outflows or discrete ejections. Steady jets are mildly relativistic, with bulk Lorentz factors $\sim 1.5 - 2$. Discrete ejections (*blobs*) may be much faster. Bulk velocities close to the speed of light are inferred from the apparent superluminal motion of some ejections. A famous first example of this effect was observed by Mirabel & Rodríguez (1994) in the microquasar GRS 1915+105 (see Figure 2.1). The apparent speed of the blobs was $\sim 1.25c$, corresponding to a real bulk velocity $\sim 0.98c$.

Over the last two decades there has been an extensive multiwavelength monitoring of X-ray binaries. The latests catalogues (Liu et al. 2006, 2007) list 299 of these sources. Among them 65 are microquasar candidates since they show non-thermal radio emission (Paredes & Zabalza 2010). The number of confirmed or strong microquasar candidates in the Milky Way is ~ 20,[1] and there is one confirmed microquasar in the spiral galaxy NGC 7793 (Pakull et al. 2010, Soria et al. 2010).

The observational and theoretical study of microquasars has sound motivations. Many of the processes at work in accreting supermassive black holes can be investigated as well in microquasars: launching, acceleration, and col-

[1] Chaty (2010), http://www.aim.univ-paris7.fr/CHATY/Microquasars/microquasars.html.

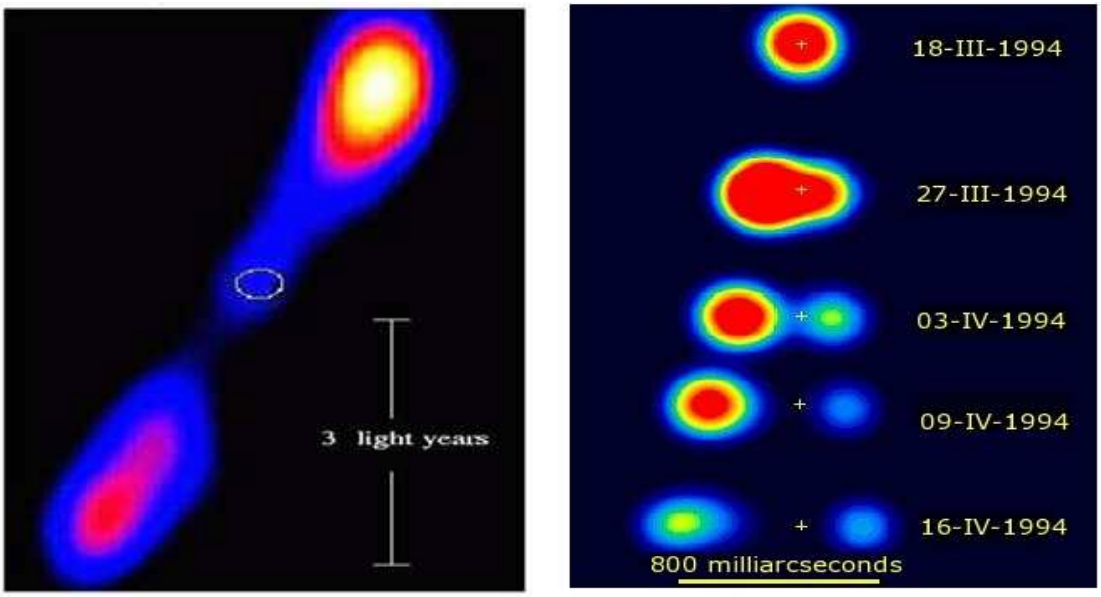

Figure 2.1: Left: radio contours at 6 cm of the source 1E 1740.7-2942 obtained with the Very Large Array (VLA). The circle is the error box of the position of central core determined with the X-ray satellite *ROSAT*. From Mirabel et al. (1992). Right: radio contours at 3.5 cm of the X-ray source GRS 1915+105, obtained with the Very Large Array (VLA) at the epochs indicated. Two discrete ejections are launched from the core (marked with a cross); the one on the left moves at an apparent velocity of 1.25c. From Mirabel & Rodríguez (1994).

limation of jets, physics of black holes, relativistic shock waves in magnetized plasmas, particle acceleration, and high-energy radiation processes. Furthermore, microquasars present two "advantages" over active galactic nuclei. First, they are nearby objects. And second, the typical timescales of the accretion processes in microquasars (from months to years) are much shorter than in AGN. This allows to observe the transition between different accretion regimes on human lifetimes.

The following sections present a short introduction to microquasars. The physical components and the observational characteristics of microquasars are described. A brief discussion on the theoretical modeling of their radiative spectrum follows. The chapter closes stating the scope of this thesis in the context of our present knowledge of the field. For additional details the reader is referred to the reviews by Mirabel & Rodríguez (1999), Mirabel (2007), Bosch-Ramon & Khangulyan (2009), Paredes & Zabalza (2010), and Paredes (2011).

2.1 PHYSICAL COMPONENTS OF A MICROQUASAR

Microquasars are formed by a non-collapsed star and a stellar-mass compact object, that may be a neutron star or a black hole. The compact object (also called primary star) accretes matter lost by the donor (also called secondary or companion) star. A fraction of this matter is ejected from the system as two collimated jets. The presence of jets distinguishes microquasars from the rest of X-ray binaries. Figure 2.2 shows a simplified sketch of a microquasar. It shows the components of the accretion flow: the accretion disc, the corona, and the jets.

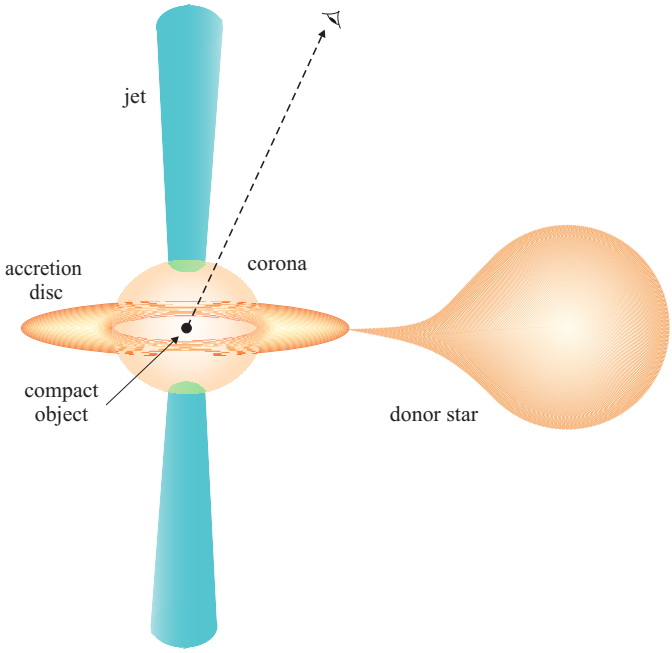

Figure 2.2: Sketch of a microquasar.

2.1.1 *The companion star*

According to the mass of the donor star, microquasars (and all XRBs) are classified into low-mass and high-mass systems. In high-mass microquasars (HMMQs) the donor star is an O, B, or Wolf Rayet star of mass $M_2 \approx 8 - 20 M_\odot$. These stars lose mass mainly through strong winds. Donor stars in low-mass microquasars (LMMQs) have $M_2 \lesssim 2 M_\odot$. They are old stars of spectral type B

or later, that transfer mass to the compact object through the overflow of their Roche lobe.

Out of the 299 sources catalogued by Liu et al. (2006, 2007), 185 are low-mass and 114 are high-mass XRBs. The spatial distribution of high-mass XRBs in our galaxy traces the star forming regions in the spiral arms (Bodaghee et al. 2012, Coleiro & Chaty 2011). This is expected, since the companion star is relatively young ($\lesssim 10^7$ yr) and should not have departed significantly from its birthplace. Low-mass X-ray binaries are concentrated towards the center of the galaxy, especially in the bulge. These systems are old ($\sim 10^9$ yr), and some have migrated from the galactic plane towards higher latitudes (e.g. Mirabel et al. 2001). The position of the known galactic microquasars is shown in Figure 2.3. With some exceptions - most notably that of XTE J1118+480 - they are all located near the plane of the galaxy.

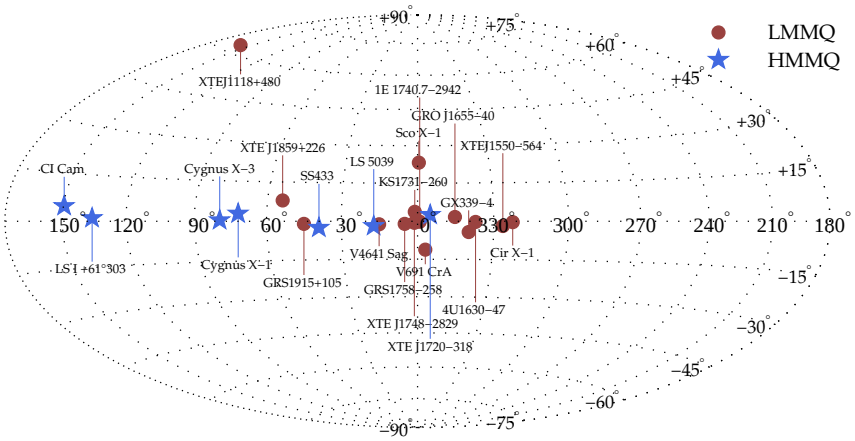

Figure 2.3: Spatial distribution in galactic coordinates of microquasars in the Milky Way. Data taken from Chaty (2010), available online at http://www.aim.univ-paris7.fr/CHATY/Microquasars/microquasars.html. The nature of some of the systems (e.g. LS 5039 and LS I $+61°$ 303) is still disputed, but they have been included in the figure for historical reasons.

The noteworthy absence of microquasars detected at galactic longitudes $150° \lesssim l \lesssim 330°$ is most probably due to an observational bias, introduced by the capabilities of the presently available X-ray observatories and radiotelescopes. On the one hand, as noticed by Grimm (2003), the sensitivity level of the X-ray satellites allows the detection and identification of those XRBs

nearer than $\sim$ 10 kpc from Earth. This is clearly seen when the position of the known microquasars is plotted on a face-on view of the Galaxy, see Figure 2.4. On the other hand, almost all the known microquasars are radio sources visible from the Northern Hemisphere allowing their detection with the Very Large Array, that has a better resolution compared to the arrays in the Southern Hemisphere.

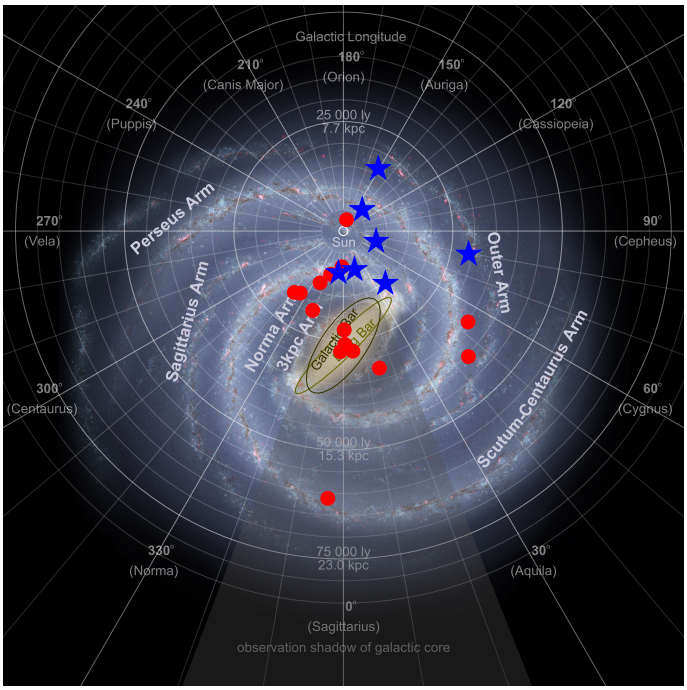

Figure 2.4: Spatial distribution of microquasars in the Milky Way, face-on view of the Galaxy. The sources were located taking into account their distance to Earth. The position of the Sun is indicated. Sketch of the Galaxy from Churchwell et al. (2009).

2.1.2 *The accretion disc*

Accretion onto a compact object in binary systems is not spherical. In general, the angular momentum of the infalling matter is large enough to form an accretion disc. The discussion on accretion disc theory presented below follows mainly that in Frank et al. (2002) and King (2006).

Let J be the specific angular momentum of an element of plasma when it gets trapped in the gravitational field of the compact object. Assuming that the plasma loses energy faster than angular momentum, matter will drift to the

orbit with the lowest energy compatible with the value of J. This is a circular Keplerian orbit of radius

$$R_{\rm circ} = \frac{J^2}{GM_1}, \tag{2.1}$$

where G is the gravitational constant and M_1 the mass of the compact object; $R_{\rm circ}$ is called the *circularization radius*. An accretion disc can form if $R_{\rm circ}$ is larger than the effective size of the compact object, i.e., the radius of the innermost stable circular orbit (ISCO) in a black hole, or the radius of the magnetosphere in a neutron star.

Dissipative processes heat the accretion flow at the expense of its rotational and gravitational energy. The plasma also transfers angular momentum outwards due to internal torques. If the typical timescale of energy dissipation is much shorter than the timescale of angular momentum redistribution, matter will slowly spiral towards the compact object in a series of approximately circular orbits, forming an accretion disc. The characteristics of the disc strongly depend on the efficiency of the dissipation of energy and angular momentum. Collectively, the dissipation mechanisms are loosely termed "viscosity".

Let us assume that the disc is axisymmetric and lies close to the plane $z = 0$, and let R and ϕ be the radial and angular cylindrical coordinates, respectively. The velocity of an element of plasma in the disc has a tangential component v_ϕ and a small radial component v_R. The disc is in differential rotation with angular velocity $\Omega(R)$, not necessarily equal to the Keplerian value

$$\Omega_{\rm K}\left(R\right) = \left(\frac{GM_1}{R^3}\right)^{1/2}. \tag{2.2}$$

The structure of the disc is found solving the hydrodynamical equations for mass, energy, and momentum conservation. To simplify the problem it is usually assumed that the disc is thin: $H \ll R$, where H is the half-thickness of the disc. In this approximation the dependence on z of all variables except the mass density is neglected. The equation for the conservation of mass is integrated in the z-direction to write it in terms of the surface density $\Sigma\left(R, t\right)$,

$$\frac{\partial \Sigma}{\partial t} + \frac{1}{R}\frac{\partial}{\partial R}\left(R\Sigma v_R\right) = 0. \tag{2.3}$$

The same procedure applied to the ϕ-component of the momentum equation yields

$$\frac{\partial}{\partial t}\left(\Sigma R^2 \Omega\right) + \frac{1}{R}\frac{\partial}{\partial R}\left(\Sigma R^3 \Omega v_R\right) = \frac{1}{R}\frac{\partial}{\partial R}\left(R^2 T_{R\phi}\right). \tag{2.4}$$

The left-hand side represents the variation of the angular momentum per unit mass and the right-hand side the internal torques; $T_{R\phi}$ is a component of the stress tensor integrated over z.

The form of the stress tensor depends on the mechanism of angular momentum dissipation. If the torques are generated only by shear viscosity

$$T_{R\phi} = \nu \Sigma R \frac{\partial \Omega}{\partial R}, \tag{2.5}$$

where ν is the coefficient of kinematic viscosity. This is not expected to be a realistic approximation, since accretion discs are prone to develop instabilities and become turbulent. One particular type of magnetohydrodynamical instability, the magneto-rotational instability (Balbus & Hawley 1991), might be a very efficient mechanism of angular momentum transport.

Shakura & Sunyaev (1973) proposed a general expression for the stress tensor based on dimensional arguments. The z-integrated component of the stress tensor has dimensions of pressure times length. The simplest expression for $T_{R\phi}$ is then

$$T_{R\phi} \approx \alpha \Sigma c_{\mathrm{s}}^2, \tag{2.6}$$

where α is a constant, c_{s} is the speed of sound, and Σc_{s} is the z-integrated isothermal pressure. Equation (2.6) is the so called "α-prescription".

It is possible to relate α to an effective viscosity. In the thin disc approximation the half-thickness of the disc is

$$H \approx c_{\mathrm{s}} \left(\frac{R}{GM_1}\right)^{1/2} R. \tag{2.7}$$

Using this expression for H, assuming that the angular velocity is Keplerian, and equating Eqs. (2.5) and (2.6), yields

$$\nu \approx \alpha c_s H. \tag{2.8}$$

Equation (2.8) is useful to put a loose constraint on the value of α. In a turbulent flow the kinematic viscosity is approximately given by

$$\nu \approx v_{\text{turb}}\, l_{\text{turb}}, \tag{2.9}$$

where v_{turb} is the velocity of the turbulent cells relative to the mean velocity of the plasma and l_{turb} the maximum size of the turbulent cells. In an accretion disc l_{turb} cannot exceed the height scale H, and the speed v_{turb} is expected to be subsonic - otherwise turbulence would be likely dissipated through shocks. This implies that $\alpha \lesssim 1$.

An expression for the kinematic viscosity, the α-prescription for example, must be provided to calculate the detailed structure of the disc. Interestingly, in steady-state some important parameters are independent of the viscosity.

If the rotation of the disc is assumed to be Keplerian and the stress tensor given by Eq. (2.5), combining Eqs. (2.3) and (2.4) gives an expression for the rate of energy dissipation per unit area

$$D(R) = \frac{9}{8}\nu\Sigma\frac{GM_1}{R^3} = \frac{3GM_1\dot{M}}{8\pi R^3}\left[1-\beta\left(\frac{R_{\text{in}}}{R}\right)^{1/2}\right]. \tag{2.10}$$

Here $\dot{M}$ is the mass accretion rate and β is an adimensional parameter that depends on the boundary condition imposed at the inner radius R_{in} of the disc. Integrating $D(R)$ over the two faces of the disc from R_{in} to infinity gives the total radiated power,

$$L_{\text{d}} = \left(\frac{3}{2}-\beta\right)\frac{GM_1\dot{M}}{R_{\text{in}}}. \tag{2.11}$$

This is an important result: only a fraction (independent of the value of the viscosity) of the gravitational energy of the accretion flow is radiated. The rest is dissipated at $R < R_{\text{in}}$, or advected onto the compact object if this is a black

hole.

The radial dependence of the temperature of the disc can be directly obtained from Eq. (2.10) under the hypothesis that it radiates as a black body

$$T(R) = \left[\frac{D(R)}{\sigma_{\rm SB}}\right]^{1/4} = \left(\frac{3GM_1\dot{M}}{8\pi\sigma_{\rm SB}R^3}\right)^{1/4}\left[1-\beta\left(\frac{R_{\rm in}}{R}\right)^{1/2}\right]^{1/4}, \tag{2.12}$$

where $\sigma_{\rm SB}$ is the Stefan-Boltzmann constant. For $R \gg R_{\rm in}$, the temperature has the characteristic profile

$$T(R) \approx T_{\rm d}\left(\frac{R}{R_{\rm in}}\right)^{-3/4}, \tag{2.13}$$

with

$$T_{\rm d} = \left(\frac{3GM_1\dot{M}}{8\pi\sigma_{\rm SB}R_{\rm in}^3}\right)^{1/4}. \tag{2.14}$$

The emission spectrum of the disc is found integrating the emissivity function of a black body over radius. The flux emitted at frequency ν (in units of erg s^{-1} cm^{-2} Hz^{-1} sr^{-1}) is

$$F_\nu = \frac{\cos\theta_{\rm d}}{d^2}\int_{R_{\rm in}}^{R_{\rm out}} 2\pi\, R\, B_\nu(R)\, dR, \tag{2.15}$$

where d is the distance to the source, $\theta_{\rm d}$ is the angle between the plane of the disc and the line of sight, and

$$B_\nu(R) = \frac{2h\nu^3}{c^2\left(\exp\left[h\nu/kT(R)\right]-1\right)}. \tag{2.16}$$

Here h is the Planck constant and k the Boltzmann constant.

The shape of the spectral energy distribution (SED) is shown in Fig. 2.5. It is a superposition of black body spectra of temperature $T(R)$. The flux grows as $F_\nu \propto \nu^2$ for photon energies $h\nu \ll kT\,(R_{\rm out})$, and decreases exponentially for $h\nu \gg kT\,(R_{\rm in})$. For intermediate energies the spectrum has the characteristic

dependence $F_\nu \propto \nu^{1/3}$. As $T(R_{\rm out})$ approaches $T(R_{\rm in})$ this part of the SED narrows, and the spectrum becomes similar to that of a simple black body.

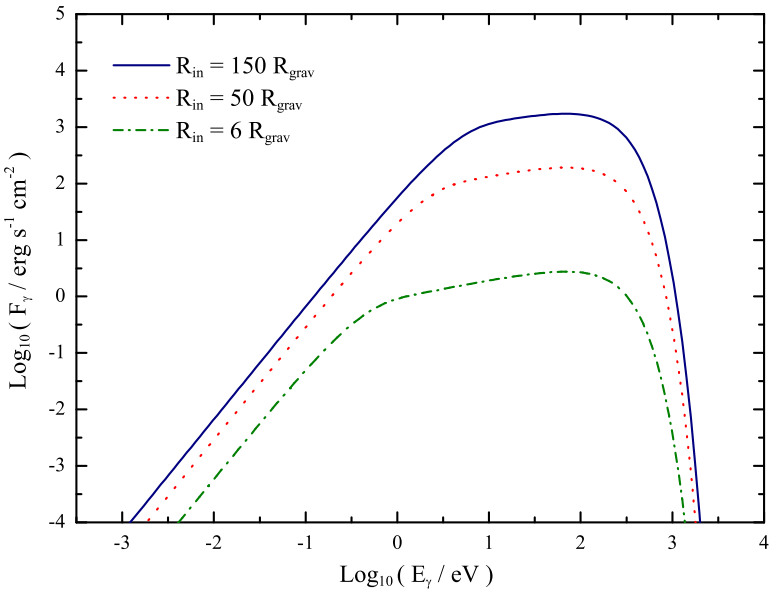

Figure 2.5: Spectral energy distribution of a "standard" geometrically thin, optically thick accretion disc as a function of the inner radius, for $M_1 = 10M_\odot$, $T(R_{\rm in}) = 10^6$ K, $\theta_{\rm d} = 30°$, and a distance to the source $d = 2$ kpc. The gravitational radius of the compact object is $R_{\rm grav} = GM_1/c^2$.

The standard model of geometrically thin, optically thick accretion disc is very successful in reproducing the soft X-ray emission of accreting binaries. It cannot, however, account for the production of hard X-rays and spectral lines observed in some systems. The presence of a "corona" of hot plasma surrounding the compact object was postulated to explain these observations.

2.1.3 *The corona*

The SED of X-ray binaries in low-hard state (see Section 2.2.1) is basically the sum of four components: a black body spectrum of temperature $kT_{\rm d} \sim 0.1$ keV, a hard power-law that cuts off at $\sim 100 - 200$ keV, a bump at $\gtrsim 10$ keV, and the Fe Kα emission line at ~ 6.4 keV.

The black body component is radiated in the accretion disc, but the hard X-rays originate in a "corona" of hot plasma around the compact object. To account for the observations, the thermal electrons in the corona must have a

mean energy $kT_e \approx 50 - 100$ keV. A fraction of the photons emitted in the disc can interact with these electrons and gain energy through inverse Compton (IC) scattering. Comptonization (multiple Compton scattering events) of low-energy photons by thermal electrons naturally produces a power-law spectrum (e.g. Titarchuk & Lyubarskij 1995).

Part of the radiation scattered in the corona is reprocessed in the disc by photoabsorption, iron fluorescence, and Compton scattering (George & Fabian 1991). The combined effect of these processes generates the "reflection bump" observed above ~ 10 keV. The iron fluorescence line arises when an inner-shell electron in a weakly ionized Fe atom absorbs an X-ray, and the vacancy is occupied by an electron of the upper energy levels. The strongest line is the Kα line (corresponding to the electron transition $2p \rightarrow 1s$) at ~ 6.40 keV. The line often appears distorted because of scattering (Torrejón et al. 2010) and strong gravitational effects (Fabian et al. 2000, Reynolds & Nowak 2003).

The typical size of the corona can be estimated from the variability timescale of the hard X-ray emission. If $t_{\rm min}$ is the shortest variability timescale, then the size of the emission region cannot be larger than $R_{\rm c} \sim ct_{\rm min}$. For galactic accreting black holes $t_{\rm min} \sim 1$ ms, then $R_{\rm c} \lesssim 300$ km; this is about ten Schwarzschild radii for a black hole of $10M_{\odot}$.

Two types of models for the corona can be found in the literature: models of "disc + corona", and Advection-Dominated Accretion Flows (ADAFs) and its extensions. In disc + corona models the corona is simply added as a separate component besides the accretion disc. In ADAF models the corona appears as a self-consistent solution of the hydrodynamic equations for an accretion flow.

In disc + corona models (see Poutanen 1998 for a review) a certain geometry is assumed for the corona. This is an important detail, since the location of the corona with respect to the disc determines the amount of feedback between the two regions. Some of the proposed geometries are depicted in Figure 2.6. In a *sandwich* configuration (e.g. Dove et al. 1997) the corona is formed by slabs that cover the disc on both sides. A *patchy* corona (e.g. Stern et al. 1995) is composed of magnetized clouds above the disc. Finally, in the *sombrero* configuration (e.g. Poutanen et al. 1997) the disc is truncated at a certain inner radius and the corona fills the region closer to the compact object. The external radius of the corona is larger than the inner radius of the disc, so the two components

spatially overlap. Whereas the disc is optically thick and geometrically thin, the corona is assumed to be optically thin and geometrically thick, with $H/R \sim 0.5 - 1$.

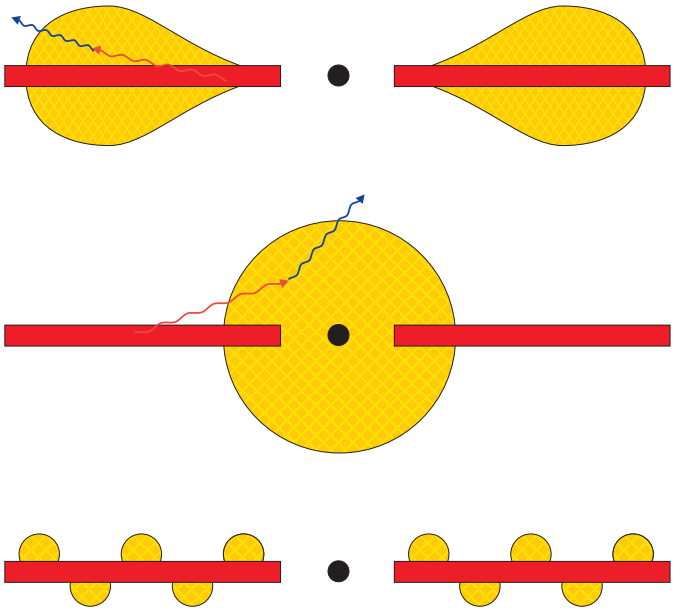

Figure 2.6: Different configurations of disc + corona: from top to bottom, a *sandwich*, *sombrero*, and *patchy* corona.

Once a geometry is chosen, the characteristics of the corona (the electron temperature T_e and the optical depth τ) and its radiative spectrum must be found solving the coupled kinetic equations for particles and radiation. Several effects add complexity to the model. For example, if T_e is large, the high-energy tail of the electron distribution is expected to deviate from a Maxwellian; this population of non-thermal particles can produce significant radiation above $m_e c^2 \sim 500$ keV. In that case, the creation of electron-positron pairs by two-photon annihilation must be taken into account (e.g. Vieyro & Romero 2012).

Advection-Dominated Accretion Flows, like the standard disc model, represent a self-consistent solution of the hydrodynamical equations for a viscous plasma in accretion. The fundamental difference between an ADAF and a thin accretion disc is that, by definition, an ADAF is radiatively inefficient. A significant fraction of the energy of the plasma is advected towards the compact object instead of being radiated. The characteristics of the ADAF solution depend

on the value of the accretion rate. The solution for $\dot{M} < \dot{M}_{\rm Edd}$[2] has been extensively applied to model the spectrum of X-ray binaries and low-luminosity AGN.

The set of equations to be solved in an ADAF model is essentially the same as in a thin disc model, except for the energy balance equation. In a thin disc all the energy released by viscous dissipation is radiated, whereas in an ADAF a fraction is allowed to be advected. The steady-state height-averaged equation for the conservation of energy reads (Narayan & Yi 1994)

$$\Sigma v_R T \frac{ds}{dR} = Q^+ - Q^-. \tag{2.17}$$

The left-hand side represents the advected entropy; s is the entropy per unit mass. The right-hand side is the difference between the power released by viscous dissipation (Q^+) and the power radiated per unit area (Q^-).

In most ADAF models the temperature of ions and electrons in the plasma is different, with $T_i \gg T_e$. This is based on the supposition that the energy dissipated by viscosity preferably heats the ions and only a small fraction is transferred to the electrons. The two species do not thermalize on relevant timescales, since they are only weakly coupled via Coulomb scattering and electrons cool much more quickly than ions (Shapiro et al. 1976). The power Q^+ can then be written as

$$Q^+ = Q_{\rm adv} + Q_{ie} \equiv f Q^+ + Q_{ie}. \tag{2.18}$$

This expression states that a fraction of the energy dissipated by viscosity is advected with the ions and the rest is transferred from ions to electrons. The parameter f fixes the amount of energy advected. If the flow is radiatively perfectly efficient, $f = 0$; if there is no cooling and all the energy is advected, $f = 1$. Equation (2.18) is more general than the usual condition of energy balance in a one-temperature accretion disc, where local energy balance is imposed so $Q^+ = Q^-$. Assuming that the radiative output is only due to the electrons and these cool completely, then

[2]The Eddington mass accretion rate is defined as $\dot{M}_{\rm Edd} = L_{\rm Edd}/c^2$, where the Eddington luminosity of an object of mass M is $L_{\rm Edd} \approx 1.3 \times 10^{38} M/M_\odot$ erg s^{-1}.

$$Q^- = Q_{ie}. \tag{2.19}$$

The expression for Q^- must account for all the relevant processes of electron cooling (synchrotron radiation, IC scattering, Bremsstrahlung, etc), appropriately corrected by absorption effects.

Finally, to find the temperature profile of the flow an equation of state for the plasma is required. The flow is radiatively inefficient, so the radiation pressure may be neglected.[3] The total pressure is thus the sum of the pressure exerted by the magnetic field and by an ideal gas of electrons and ions with different temperatures.

Narayan & Yi (1994, 1995a,b) found a solution for the set of equations of an ADAF. Its characteristics differ from those of a thin disc when f is close to unity. The main features of the solution are:

- the speed of sound is comparable to the Keplerian velocity, $c_s \sim \Omega_K R = v_K$,
- the flow is quasi spherical, $H \sim R$,
- the radial velocity is proportional to the viscosity parameter, $v_R \sim \alpha c_s^2 / v_K$, it is much larger than in a thin disc, and a considerable fraction of the free-fall velocity,
- the angular velocity is smaller than the Keplerian value, $\Omega < \Omega_K$, and
- in the inner regions $T_e \sim 10^8 - 10^9$ K and $T_i \sim 10^{11} - 10^{12}$ K.

ADAFs models have been applied to reproduce the spectrum of X-ray binaries in low-hard state, outburst, and quiescence; see e.g. Esin et al. (1997, 1998, 2001a) and Narayan et al. (1996, 1997). The radiative output of an ADAF extends from radio to X-rays/gamma rays (e.g. Mahadevan et al. 1997). Up to X-ray energies the emission is mainly determined by the cooling of thermal electrons through synchrotron, Bremsstrahlung, and inverse Compton interactions. Gamma rays may result from the decay of neutral pions created in inelastic collisions of (thermal or non-thermal) very energetic protons with low

[3] Radiation pressure cannot be neglected if the accretion rate is high, see e.g. Abramowicz et al. (1995).

energy protons. The injection of relativistic protons and electrons in the corona has been recently addressed by Vieyro & Romero (2012).

Some generalizations of the ADAF model have been developed. Blandford & Begelman (1999) introduced the so called Adiabatic Inflow-Outflow Solution (ADIOS). The set of equations in an ADIOS includes terms that account for the energy and angular momentum carried away by a wind. The authors proposed that radiatively inefficient accretion flows around neutron stars may have the characteristics of an ADIOS. Pure ADAF solutions are not possible near neutron stars, since the advected matter would eventually release its energy when impacting on the surface of the star. In an ADIOS, however, the wind reduces the matter density near the neutron star, and the flow may remain radiatively inefficient. See also Bogovalov & Kelner (2010) for a related model.

Another generalization of ADAFs are the Magnetically-Dominated Accretion Flows (MDAFs, see e.g. Meier 2005 and Fragile & Meier 2009). These are accretion flows in which the magnetic pressure dominates over thermal and radiation pressure. In an MDAF the plasma remains cool and optically thin, and is radiatively very inefficient. MDAFs may develop in the inner regions of an ADAF. In the MDAF region a closed magnetosphere funnels the plasma towards the black hole along the field lines. In the transition zone between the MDAF and the ADAF the magnetic field lines may open up to infinity. This is an interesting feature of MDAF models, since an open magnetosphere is expected to favour the launching of jets and winds.

2.1.4 *The jets*

The ejection of jets is a common feature in accreting systems. Jets carry away part of the energy and angular momentum of the accretion flow and/or the compact object in the shape of a flux of matter and electromagnetic field.

Microquasars can produce two type of outflows: continuous steady jets and discrete ejections. Continuous jets are observed during the low-hard state, whereas the ejection of blobs occurs during the transition between spectral states. Jets in microquasars are mildly relativistic, with typical bulk Lorentz factors $\Gamma_{\rm jet} \lesssim 10$. Apparent superluminal motion of the discrete ejections is observed in some sources (e.g. Mirabel & Rodríguez 1994, Tingay et al. 1995,

Orosz et al. 2001).

The power of microquasars jets is $L_{\rm jet} \approx 10^{37} - 10^{40}$ erg s^{-1} (e.g. Gallo et al. 2005, Sell et al. 2010, see also Heinz & Grimm 2005 and references therein). The most powerful jets inject enough energy in the surrounding medium as to distort it significantly. The best known example of jet-medium interaction is that of the galactic microquasar SS 433 inside the nebula W50. A system similar to SS433/W50 has been recently discovered by Pakull et al. (2010) in the galaxy NGC 7793.

It is usually accepted that the launching, acceleration, and collimation of relativistic jets is directly related to the action of a large-scale electromagnetic field. The formation of jets is studied, analytically and through numerical simulations, using the equations of Magnetohydrodynamics (MHD) in its classical or relativistic formulation. The standard MHD model of jet dynamics is presently well established, although it does not provide completely satisfactory explanations for all the observed properties of jets. Most probably, relativistic jets result from the action of several mechanisms that operate at different length scales.

The launching of relativistic jets couples the accretion disc and the compact object. Two models of jet launching have received particular attention: the Blandford-Znajek mechanism (Blandford & Znajek 1977), and the Blandford-Payne or magneto-centrifugal mechanism (Blandford & Payne 1982).

Blandford & Znajek (1977) proposed a mechanism to extract energy and momentum from a rotating black hole surrounded by a magnetosphere. Astrophysical black holes are not expected to be charged, therefore the magnetic field must be created by electric currents in the external medium - for example in an accretion disc. The efficiency of the Blandford-Znajek mechanism is related to the spin of the black hole and the configuration of the magnetosphere. Theoretical results (see e.g. Meier 2011 and references therein) indicate that jets are more likely to be launched from retrograde black holes (that rotate in opposite sense with respect to the accretion disc) because these have open magnetospheres. The jets from retrograde black holes are also more powerful. These results agree with the observations of supermassive black holes.

In black hole X-ray binaries it is not still clear whether the Blandford-Znajek mechanism is related to the jet launching. Two recent searches for correlations

between the jet properties and the spin of the black hole led to opposite conclusions. On the one hand, no correlation was found by Fender et al. (2010). Narayan & McClintock (2011), on the other hand, claim that there exists a correlation between the spin and the radio luminosity at 5 GHz in the case of *discrete* jets. Narayan & McClintock (2011) argue that the different results obtained by Fender et al. (2010) are due to the choice of another proxy for the jet power. Furthermore, they argue that no correlations should be expected for *continuous* jets, since these form relatively far from the black hole where relativistic effects are weak. Discrete jets are likely formed when the inner disc or the corona are ejected, so the launching region is nearer the black hole. Both the works of Fender et al. (2010) and Narayan & McClintock (2011), however, are based on data from a few sources for which there exist estimates (some very uncertain) of the black hole spin, so their results cannot be taken as definite for the moment.

The magneto-centrifugal mechanism of jet launching also involves a large-scale magnetic field generated by the electric currents in the disc. It is assumed that the footpoints of the magnetic field lines are anchored to the plasma, so the rotation of the disc forces the lines into co-rotation. If the angle between the field lines and the outwards radial direction is less than $\sim 60^\circ$,[4] the elements of plasma on the surface of the disc are in unstable equilibrium. When perturbed, they get accelerated away from the disc along the poloidal field lines - just like beads threaded in a rigid wire (Lyutikov 2009, Sądowski & Sikora 2010). The magneto-centrifugal mechanism has been shown to work in Schwarzschild and Kerr space-times, and also in a Newtonian gravitational field. It may then lead to the launching of jets from black holes and neutron stars but also from non-collapsed stars in young stellar objects.

Magneto-centrifugal forces accelerate the jet up to the Alfvén surface, defined as the surface where the jet bulk velocity equals the Alfvén speed. In this region the magnetic field lines stop co-rotating with the disc and wind up, developing a significant toroidal component as shown in Figure 2.7.

In the standard MHD model, further acceleration of the outflow is achieved

[4]This is the maximum angle for instability in a Schwarzschild black hole. It is slightly smaller for a Kerr black hole with spin $a = -1$, and approaches 90° for $a = 1$; a is taken positive (negative) if the black hole and the disc rotate in the same (opposite) sense.

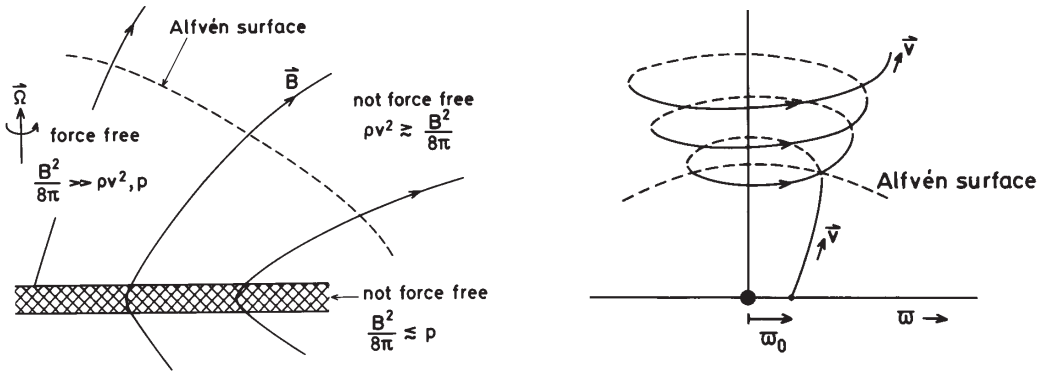

Figure 2.7: Left: jet launching region near an accretion disc. Magnetic pressure is negligible inside the disc but dominates in the disc atmosphere. In this region the plasma is approximately force-free and the flow is along the field lines. The kinetic energy density of matter dominates over magnetic energy density beyond the Alfvén surface. Right: geometry of the magnetic field lines beyond the Alfvén surface. The field lines no longer co-rotate with the disc, and start to wind up developing a significant toroidal component. The shape of the Alfvén surface is only schematic. From Spruit (2010).

by conversion of magnetic energy into bulk kinetic energy. A relevant parameter is the *magnetization* σ, defined as the ratio of the electromagnetic energy flux to the kinetic energy flux across a section of the jet. Near the launching region jets are Poynting-dominated, so the initial magnetization is $\sigma_{\rm in} \gg 1$. The maximum possible bulk Lorentz factor of the jet, corresponding to complete conversion of magnetic energy into kinetic energy, is $\Gamma_{\rm jet}^{\rm max} = \sigma_{\rm in}$.

MHD acceleration is quite efficient in non-relativistic jets: near the Alfvén surface most of the magnetic energy has converted into kinetic energy and the jet approaches its terminal velocity (e.g. Giannios 2011). This is not true, however, for relativistic jets. The efficiency of energy conversion strongly depends on the symmetry of the flow and the characteristics of the external medium.

Two-dimensional ideal MHD models predict that the acceleration efficiency depends on the shape of the jet. The bulk Lorentz factor increases as the jet propagates only when the streamlines satisfy a condition of "differential collimation": the separation between nearby flow surfaces should increase faster than their radius (Komissarov et al. 2009, Komissarov 2011). Jets with a parabolic-shaped boundary have the best acceleration rate - $\Gamma_{\rm jet}$ increases until $\sigma \sim 1$. Differential collimation of the streamlines may be achieved as the

combined effect of the radial Lorentz force exerted by the toroidal component of the magnetic field ("hoop stress") and the pressure of the external medium (e.g. Komissarov et al. 2009). In a microquasar, the confining external medium may be the corona or a slow wind expelled from the accretion disc.

Acceleration due to MHD forces is an spatially extended process because $\Gamma_{\rm jet}$ grows relatively slowly as the jet expands and advances. Indeed, after the magnetization has dropped to $\sigma \sim 1$ it only decreases logarithmically with distance. Therefore, if no other mechanism operates, the jet becomes matter-dominated at extremely large distances from the central engine (Lyubarsky 2010).

It appears unlikely that the conditions in the confining medium and the magnetic field configuration remain appropriate to sustain acceleration over such length scales. Beyond the region where standard MHD acceleration becomes inefficient, other processes may contribute to increase the bulk Lorentz factor of relativistic jets up to the large values inferred specially in AGN and GRBs. Some alternatives are reviewed in Komissarov (2011) and Meier (2011); these include energy dissipation by magnetic reconnection or magnetic instabilities, recollimation shocks, and impulsive jet ejection. Tchekhovskoy et al. (2008, 2010) found that in a collapsar the jets can suffer an abrupt re-acceleration when they break the surface of the collapsing star and become deconfined. Time-dependent numerical simulations by these authors yield Lorentz factors $\Gamma_{\rm jet} \approx 10^2 - 10^3$, in agreement with observations of long GRBs.

Relativistic jets are usually discovered because of their characteristic flat synchrotron radio spectrum. The distribution in energy of the electrons that emit the synchrotron radiation is non-thermal and follows approximately a power-law. Some mechanisms of particle acceleration that lead to the formation of a power-law spectrum are diffusive shock acceleration (also known as first-order Fermi process; Bell 1978, Drury 1983), magnetic reconnection (e.g. Zenitani & Hoshino 2001, Kowal et al. 2011), and the converter mechanism (Derishev et al. 2003).

Diffusive shock acceleration is usually quoted as the mechanism at work in jets, mainly because internal shocks are expected to develop when different regions of the jet collide. However, the internal shock model has some caveats. As discussed above, ideal MHD models predict that relativistic out-

flows remain Poynting-dominated, but for magnetizations $\sigma \gtrsim 0.1$ the efficiency of shocks to heat the plasma is greatly reduced (Kennel & Coroniti 1984). Furthermore, the magnetic field is largely parallel to the shock front, an unfavourable configuration for particle acceleration. Diffusive shock acceleration still appears to be the most efficient mechanism in the mildly relativistic jets in microquasars (Bosch-Ramon & Rieger 2011). The action of other acceleration processes, however, should not be discarded.

Whatever the acceleration mechanism is, the detection of non-thermal radiation undoubtedly reveals that there are relativistic electrons or positrons in the jets. The exact full composition of the jets, however, is unknown. Jets launched by the Blandford-Znajek mechanism start as a flux of electromagnetic field and get afterwards loaded with electron-positron pairs generated in situ. But if the jets are fed with matter from the accretion disc or the corona they may also contain baryons. There is one source, the microquasar SS 433, where the presence of hadrons in the jets has been confirmed through the detection of Doppler-shifted iron lines (Migliari et al. 2002). The same processes that accelerate electrons might be efficient as well to accelerate hadrons.[5] Indeed, the composition of cosmic rays shows that protons can be accelerated to relativistic energies. The consequences of the injection of relativistic protons in the jets of microquasars are discussed below, and are one of the topics of this thesis.

2.2 OBSERVATIONAL CHARACTERISTICS

2.2.1 *Spectral states and the role of jets*

Black hole X-ray binaries go through different spectral states, classified according to the timing and spectral characteristics of the X-ray emission. The four canonical states are (e.g. McClintock & Remillard 2006, Belloni et al. 2011) the *low-hard*, *high-soft*, *very high*, and *quiescence* states. *Intermediate* states with

[5]The same mechanism (diffusive shock acceleration) that accelerates particles in supernova remnants (SNRs) is expected to operate in jets. The presence of relativistic electrons in SNRs is inferred from the detection of non-thermal radiation, but there is also strong evidence supporting the presence of relativistic protons in two systems, Cassiopeia A and Tycho. The combined data of the gamma-ray satellite *Fermi* and the Cherenkov array VERITAS, favour a hadronic (due to decay of neutral pions created in proton-proton collisions) over a leptonic origin of the high energy and very high energy emission from these sources (Araya & Cui 2010, Morlino & Caprioli 2012).

mixed properties are also observed. These five spectral states can be briefly characterised as follows:

• **Low-hard (LH) state:** the X-ray flux follows a hard power-law $F \propto E_\gamma^{-\alpha}$ of index $\alpha \sim 0.4 - 0.9$, with an exponential cutoff at ~ 100 keV. The Fe Kα line at ~ 6.4 keV is observed in many sources. All these features can be explained in terms of Compton scattering of photons from the accretion disc in a hot corona, plus the reprocessing of some the scattered radiation in the disc. The presence of steady jets in the LH state is inferred from the flat/slightly inverted shape of the radio spectrum. The radio and X-ray emission are tightly correlated, suggesting that the jets may also contribute at X-ray energies. The typical luminosity of jets in the LH state is $\sim 10^{36-37}$ erg s^{-1}.

• **Quiescence state:** similar to a faint LH state. The X-ray spectrum is dominated by a hard power-law of very low luminosity ($\sim 10^{30-35}$ erg s^{-1}).

• **Very high (VH) state:** the X-ray spectrum is a power-law without indication of a cutoff up to ~ 100 keV. The power-law is steeper than in LH state. Some sources in VH state show quasi-periodic oscillations (QPOs). The role of jets during the VH state is not clear. In some cases the onset of the VH state coincides with the quenching of the radio emission; in other sources discrete ejections are observed during the VH state or the transition to it.

• **High-soft (HS) state:** the spectrum below ~ 10 keV is dominated by the thermal emission of an accretion disc of temperature $kT_\mathrm{d} \approx 0.5 - 1$ keV. A steep power-law tail extends into the hard X-rays. The Fe Kα line is broadened, probably because the disc extends closer to the compact object than in the LH state. The radio emission is strongly suppressed, suggesting the absence of jets.

• **Intermediate states:** XRBs spend most time in the four spectral states described above, but there are also epochs when the characteristics of the X-ray emission cannot be accounted for in terms of purely one spectral state. In such cases the source is said to be in an intermediate state. Intermediate states occur, for example, during the transition between two of the main spectral states.

Figure 2.8 shows the SEDs of several black hole XRBs in low-hard, high-soft, and very high state. The distinguishing features of each state are clearly seen.

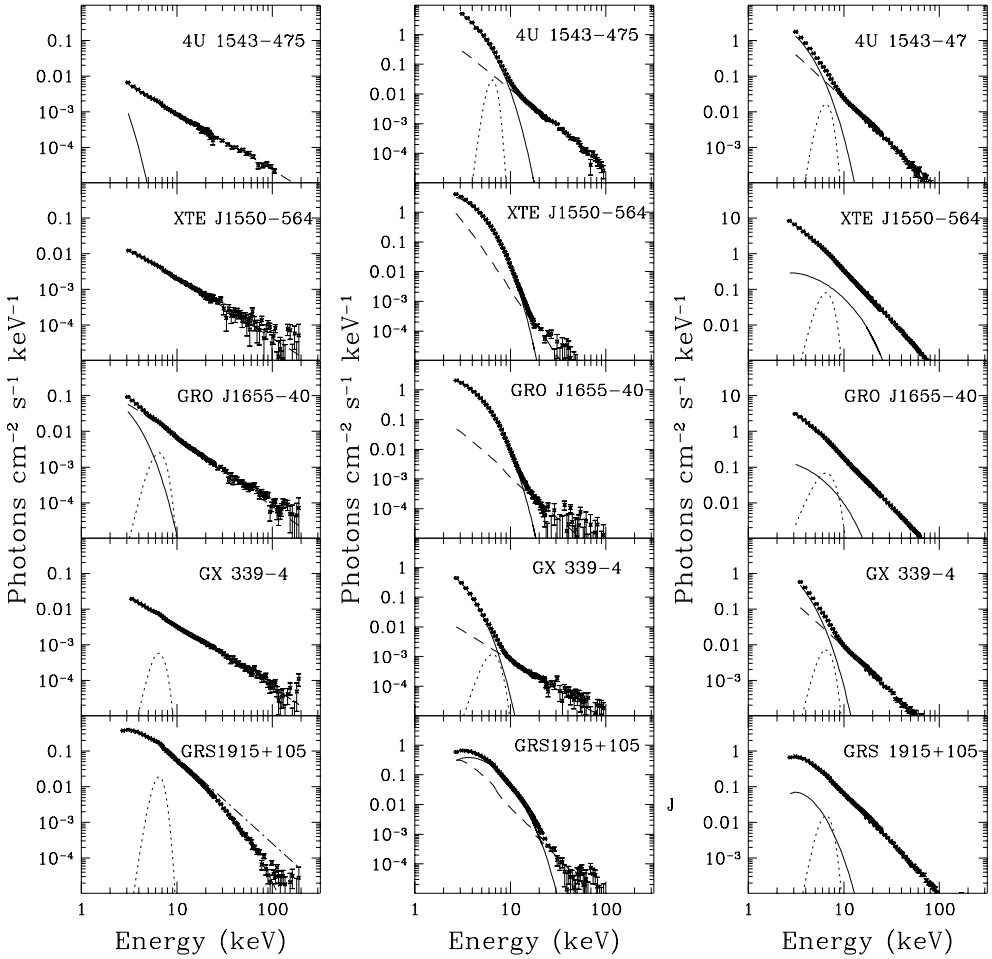

Figure 2.8: SEDs of several black hole X-ray binaries in the low-hard state (left), high-soft state (center), and very high state (right). From McClintock & Remillard (2006).

Esin et al. (1997) developed a model to explain the change between spectral states in terms of variations in the mass accretion rate. In this model the X-ray emission originates in an accretion disc and a two-temperature ADAF corona. The transition radius between the disc and the corona is a function of the accretion rate, as depicted in the left panel of Figure 2.9. The parameters are normalized to the gravitational radius of the black hole and the Eddington mass accretion rate: $r_{\rm tr} \equiv R_{\rm tr}/R_{\rm grav}$ and $\dot{m} \equiv \dot{M}/\dot{M}_{\rm Edd}$, respectively.

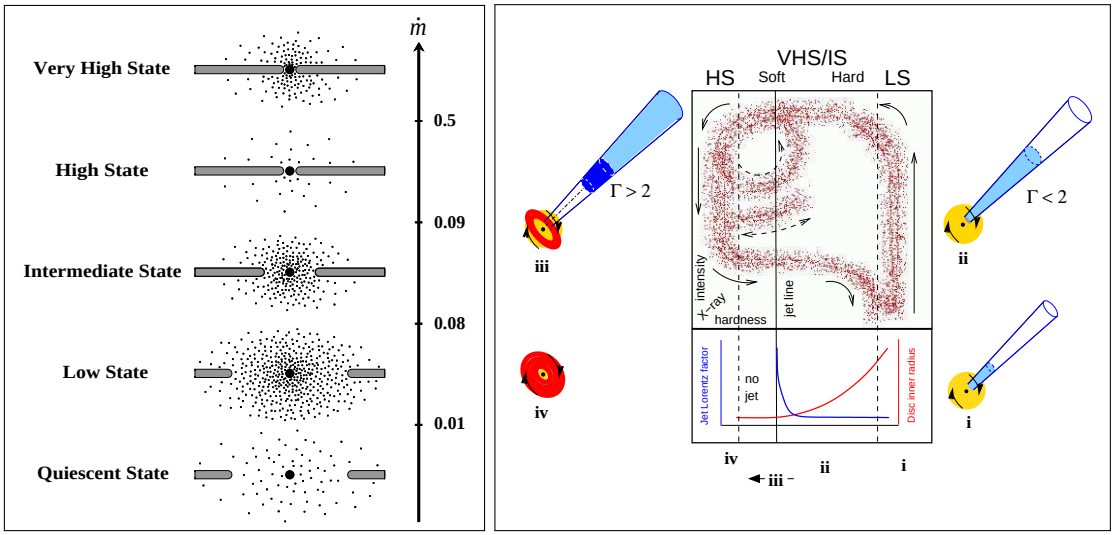

Figure 2.9: Left: structure of the accretion disc and the corona as a function of the mass accretion rate. From Esin et al. (1997). Right: hardness-intensity diagram along the complete cycle of transitions between spectral states. The value of the bulk Lorentz factor of the jet and the inner radius of the disc are plotted in the bottom panel. The configuration of the disc, corona, and jet in each phase is shown. From Fender et al. (2004b).

In quiescence the accretion rate is very low and the transition radius is large, $\dot{m} \lesssim 10^{-2}$ and $r_{\rm tr} \approx 10^{3-4}$. The radiation from the disc is negligible and the corona is radiatively very inefficient. At higher accretion rates, $10^{-2} \lesssim \dot{m} \lesssim 0.1$, the source enters the LH state. The configuration is similar but the radiative efficiency of the corona increases, whereas the disc is still very faint.

The two-temperature ADAF solution exists only for accretion rates lower than a critical value $\dot{m}_{\rm crit}(r_{\rm tr})$. The transition radius decreases as the accretion rate increases. Eventually, the disc extends up to the innermost stable orbit and the corona disappears. The corresponding value of the critical accretion rate depends on the details of the model, but it is of the order of $\dot{m}_{\rm crit} \approx 0.1$. The disappearance of the corona sets the transition from the LH to the HS state. In HS state the spectrum is dominated by the emission of the disc, plus a power-law tail from a very thin corona.

The main drawback of this model is that it cannot explain the transition to the VH state that takes place when the accretion rate approaches the Eddington limit. Esin et al. (1997) suggested that in the VH state other mechanisms of

energy dissipation (magnetic reconnection, for example) might enhance the radiative efficiency of the corona.

The model of Esin et al. (1997) does not address the role of jets. The radio emission indicates that steady, compact jets are active during the LH state and disappear in the HS state. Fender et al. (2004b) proposed that black hole XRBs follow a cycle in which the dynamics of the disc, corona, and jets are coupled. The right panel of Figure 2.9 is a hardness-intensity diagram of the cycle; each phase is associated with a spectral state. The configuration of the accretion flow and the jet during each phase is also sketched in the figure.

Steady jets are present during the quiescence and the LH states, or phase (i). The luminosity rises until it peaks when the sources enters the VH/intermediate state, or phase (ii). Phase (iii) starts still during the VH state, as the path in the hardness-intensity diagram approaches the "jet line". At this point the ejection velocity of the outflow suddenly increases. An internal shock propagates when the high velocity plasma catches up with the slow jet. These shock waves might be observed as advancing superluminal components. It is possible that the ejected fast plasma is the corona itself, pushed by the accretion disc as it approaches the black hole, giving rise to fast, large-scale events of magnetic reconnection (de Gouveia dal Pino & Lazarian 2005). Finally the jet disappears and the source enter the HS, or phase (iv). The source then returns to the LH state. The transition HS-to-LH always occurs at lower luminosities than the transition LH-to-HS.

The spectrum of jets during the LH state covers the radio band and continues up to a turnover at infrared/optical frequencies. There is, however, a hint that it could extend, at least, up to the X-rays. A clear correlation between the radio and the X-ray emission is observed during the LH state (Corbel et al. 2003, Gallo et al. 2003). The coupling can be parameterised as (Merloni et al. 2003, Falcke et al. 2004)

$$L_{\rm radio} \propto M^{0.8}\, L_{\rm X}^{0.6}. \tag{2.20}$$

This scaling law is known as the *fundamental plane* of black hole activity.[6] It remains valid up to very low accretion rates in quiescence state, but it does not apply in the HS state (Gallo et al. 2003).

Two scenarios have been proposed to explain the radio/X-ray coupling. In one case the radio emission originates in the jet and the X-rays in a radiatively inefficient corona. The non-linear relation in Eq. (2.20) arises because of the different scaling of the radio and X-ray luminosities with the accretion rate (Merloni et al. 2003). The alternative is that the jets considerably contribute, or even dominate, the X-ray emission. Markoff et al. (2001, 2003) have shown that a single synchrotron component emitted by relativistic electrons in a jet, can fit the simultaneous radio and X-ray data of the binaries XTE J1118+480 and GX 339-4. This is an interesting possibility, since it implies that the jets carry significant power in high-energy non-thermal electrons.

2.2.2 *Differences between neutron star and black hole binaries*

Low-magnetic field accreting neutron stars[7] are classified according to the shape of the path they follow in an X-ray colour diagram (e.g. van der Klis 2006). The two main types are the Z and the atoll sources.

The Z-type sources host neutron stars with magnetic fields $\lesssim 10^9$ G and accrete at a rate close to the Eddington limit. These are the brightest persistent X-ray sources observed. Z sources are also variable radio emitters; jets have been imaged in two of them, Scorpius X-1 and Circinus X-1. Atoll-type sources are low-mass X-ray binaries that accrete at lower rates than Z sources. They are faint radio sources (~ 30 times less powerful than black holes and Z-type neutron stars); no jets have been detected in any atoll source.

A comprehensive study of the radiative properties of both accreting neutron stars and black holes was carried out by Migliari & Fender (2006). Both types of sources appear to produce steady jets during states of low-hard X-ray emission. There are, however, some important differences. First, atoll-type neutron stars

[6]The fundamental plane can be also applied to X-ray observations of supermassive black holes. Its universality, however, is far from being established. See for example Gallo et al. 2012 for a critical assessment of its validity in the case of XRBs.

[7]In neutron stars with very large magnetic fields such as X-ray pulsars ($B \gtrsim 10^{11}$ G), the magnetic field disrupts the accretion flow far from the neutron star. These sources probably do not produce jets.

do not show a large suppression of the radio emission in soft state. Also no transient ejections are seen during hard to soft state transitions in neutron stars (see Miller-Jones et al. 2010 for the case of Aquila X-1). Second, the correlation between the radio and X-ray luminosities is harder, $L_{\rm radio} \propto L_{\rm X}^{1.4}$. And third, neutron star binaries are less powerful radio emitters than black holes binaries for the same value of the ratio $L_{\rm X}/L_{\rm Edd}$; this might imply that jets from neutron stars are less powerful than jets from stellar-mass black holes. Jets from neutron star XRB, however, can be very relativistic. An example is the jet in the microquasar Circinus X-1, with an inferred bulk Lorentz factor ≥ 10 (Fender et al. 2004a).

The nature of the compact object does not seem, then, to have a fundamental role in the formation of jets in XRBs. The launching of relativistic jets depends, in principle, only on the presence of an accretion disc and rotating compact object. Recently, Migliari et al. (2011) investigated if the spin of the compact object may account for the observed differences between accreting neutron stars and black holes. They found some hints that the value of the spin might be correlated with the jet power, but the results are only preliminary.

2.2.3 *Detections at high and very high energies*

Gamma-ray astronomy has experienced a breakthrough during the past few years, largely because of the improved capabilities of the new ground-based and satellite-borne instruments presently available. The high-energy gamma-ray band (HE, 30 MeV - 50 GeV) is explored with space-borne detectors. There are several active gamma-ray satellites, like the *Fermi Gamma-ray Space Telescope*, and the *Astro-rivelatore Gamma a Immagini LEggero* (*AGILE*). Observations at very high energies (VHE, $>$ 50 GeV) are carried out with terrestrial Cherenkov telescope arrays, mainly the Major Atmospheric Gamma-ray Imaging Cherenkov Telescope (MAGIC, two telescopes in La Palma, Spain), the High Energy Stereoscopic System (HESS, four telescopes in Khomas Highland, Namibia), and the Very Energetic Radiation Imaging Telescope Array System (VERITAS, four telescopes in southern Arizona, USA).

Up to date, five galactic XRBs have been detected at high or very high

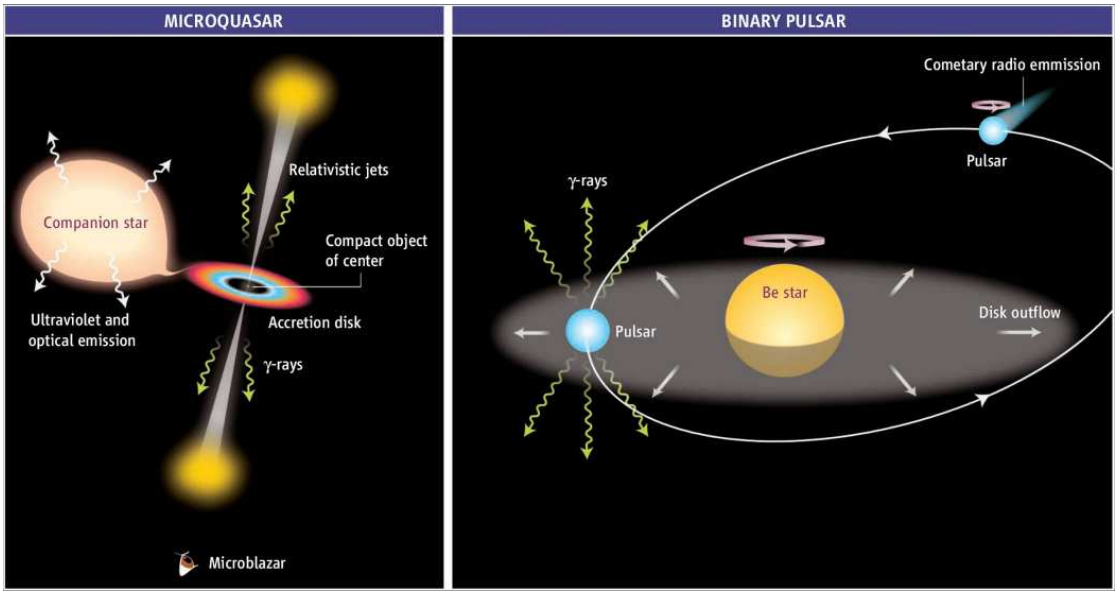

Figure 2.10: Artistic representation of a microquasar (left) and a pulsar/Be star binary system (right). In high-mass microquasars the gamma rays are produced by non-thermal particles in the jets. In pulsar/Be star binaries particles are accelerated where the pulsar wind and the disc of the star collide. From Mirabel (2006).

energies (Holder 2009, Paredes & Zabalza 2010, Paredes 2011). All of them are also radio sources and contain a massive companion star of type O or B. There are at least three other sources - HESS J0632 + 57 (Aharonian et al. 2007, Jogler et al. 2011), 1FGL J1018.6 − 5856 (Corbet et al. 2011), and AGL J2241 + 4454 (Lucarelli et al. 2010) - that are candidates to gamma-ray binaries; see for example Casares et al. 2012 for evidence supporting this scenario in HESS J0632 + 57 and AGL J2241 + 4454.

The identified gamma-ray binaries are (or are suspected to be) either high-mass microquasars or systems formed by a Be star and a non-accreting pulsar. Figure 2.10 shows a comparative sketch of the two types of binaries. In high-mass microquasars, the gamma-ray emission is thought to originate from the interaction of relativistic particles in the jets with the wind and the radiation field of the companion star. In pulsar-driven binaries the high-energy emission is expected to be produced by particles accelerated at shocks that develop where the pulsar wind and the stellar disc collide.

PSR B1259 − 63 is a confirmed pulsar gamma-ray binary (Aharonian et al.

2005). The sources LS I $+61^\circ$ 303 and LS 5039 have been detected at high and very high energies (Albert et al. 2006, Acciari et al. 2008, Abdo et al. 2009b, Jogler & Blanch 2011, Aharonian et al. 2006a, Abdo et al. 2009c), but in these the nature of the compact object remains unknown (Casares et al. 2005a,b). It is not clear either whether they are powered by accretion or pulsar-driven. Models based on both scenarios have been developed (Bosch-Ramon et al. 2006a, Dubus 2006, Romero et al. 2007), but none can completely explain the observed phenomenology. McSwain et al. (2011) searched for pulsed radio emission in LS I $+61^\circ$ 303 and LS 5039 with negative results. Recently, Massi et al. (2012) revisited radio observations of LS I $+61^\circ$ 303 and concluded that the morphology of the emitting region is consistent with that of a precessing jet, and not with the cometary tail of a pulsar.

The confirmed gamma-ray microquasars are Cygnus X-1 and Cygnus X-3. In the former the compact object is a black hole, whereas in the latter it is yet unidentified.

Gamma-ray emission at a few MeV from Cygnus X-1 was already observed with the COMPTEL instrument on board the *Compton Gamma-Ray Observatory* about a decade ago (McConnell et al. 2000). A very high-energy gamma-ray flare (79 min) was detected with MAGIC in 2006 at a 4.1σ confidence level (Albert et al. 2007). A longer ($\sim$ 1 day) flare at > 100 MeV was observed with *AGILE* in 2009 (Sabatini et al. 2010). The MAGIC detection occurred just before superior conjunction. To avoid the strong absorption in the stellar radiation field, the emission site must have been located at the border of the binary system (Bosch-Ramon et al. 2008, Romero et al. 2010a). A possible origin of the flaring emission is the interaction of relativistic protons in the jet with a clump in the wind of the companion star. Romero et al. (2010a) estimated that the time for the clump to cross the jet is of the order $\sim 10^4$ s, consistent with the rising time of the 2006 flare.

Cygnus X-3 has been detected with *AGILE* (Tavani et al. 2009, Bulgarelli et al. 2012) and *Fermi* (Abdo et al. 2009d) as a transient source. The high-energy emission detected by *Fermi* is modulated with the orbital period of the binary ($\sim$ 0.2 d), securing the association of the gamma-ray source with Cygnus X-3. *AGILE* detected gamma-ray flares from Cygnus X-3 during the X-ray soft state and a few days before episodes of strong radio emission. The

radio outburst may be associated with the ejection of discrete jets, or jet-clump collisions (Araudo et al. 2010).

2.2.4 *Modeling the spectrum of microquasars*

The radiation from microquasars covers the entire electromagnetic spectrum. In the LH state the emission from radio to infrared/optical frequencies is firmly associated with synchrotron radiation from the jets. The origin of the X-ray radiation is not so certain. Classically, it has been attributed to an ADAF corona, but the strong correlation between the radio and X-ray emission points to a significant (or dominant) contribution from the jets, at least in some objects.

The most important implication of the detection of synchrotron radiation from the jets is that these are particle accelerators. This is a strong reason to maintain that jets can be as well gamma-ray emitters.

Models for the electromagnetic emission in microquasars are an indirect way to investigate the physical conditions in the source. Comparing the theoretical spectrum with the observational data allows to constrain the characteristic parameters of the model, expected to reproduce the conditions in the emission region. Modeling the SED also serves to make predictions for unexplored energy bands, particularly gamma rays.

Usually, radiative jet models are divided into *leptonic* and *hadronic*. In leptonic (hadronic) models the bulk of the gamma-ray emission is produced in interactions initiated by relativistic electrons (protons).

In leptonic models (e.g. Markoff et al. 2001, Kaufman Bernadó et al. 2002, Bosch-Ramon et al. 2005, Bosch-Ramon et al. 2006b, Khangulyan et al. 2008) gamma rays are created by relativistic electrons in the jets mainly through inverse Compton interactions. The most important target photon field in a high-mass microquasar is the radiation field of the companion star. Inverse Compton scattering against the internal radiation field of the jet is more efficient in low-mass microquasars, where the donor star is in general too dim.

The interaction of relativistic protons in the jets with the wind of the companion star can produce photons with energies above 1 GeV through proton-proton inelastic collisions. This is the gamma-ray emission mechanism proposed in hadronic models for high-mass microquasars (e.g. Romero et al. 2003,

Romero et al. 2005). If a clump in the stellar wind crosses the jet, the temporary increase in the rate of proton-proton interactions might cause a gamma-ray flare (Owocki et al. 2009, Romero et al. 2010a).

There is a key feature that distinguishes hadronic from leptonic models: high-energy hadronic interactions lead to the production of neutrinos. Their detection would definitely prove that microquasars can accelerate protons up to relativistic energies. Detailed estimates for the flux of neutrinos from jets in microquasars, however, predict that they would be undetectable with present instruments (Reynoso & Romero 2009). The two largest and most sensitive active neutrino detectors, ANTARES and IceCube, up to now have failed to detect gamma-ray binaries or any other galactic source (Kappes 2011). The search is ongoing. It is expected that the chances of detection will improve significantly with the next-generation neutrino telescope KM3NeT, and future upgrades of IceCube.

The injection of relativistic protons in the jets brings about yet other interesting and unique effects. In general, protons reach higher energies than electrons and easily produce gamma rays above 1 GeV. As well as gamma rays, proton-proton and proton-photon collisions create energetic charged pions, muons, and electron-positron pairs. These particles can produce significant, and perhaps detectable, radiation from radio to X-rays.

2.3 SCOPE OF THIS THESIS

In this work we develop a model for the electromagnetic radiation of jets in microquasars that generalizes and improves those existing in the literature. We seek to obtain a better understanding of the physical conditions in the jets through the comparison of our results with observational data. In particular, we focus on models for jets in low-mass microquasars. This is a topic that has received little attention, overshadowed by the interest in explaining the origin of the gamma-ray emission detected from binaries with massive companions. Here we assess the detectability of low-mass microquasars at high and very high energies with the instruments available now or in the near future. These predictions are particularly relevant for the Cherenkov Telescope Array (CTA).

Under some basic suppositions, the model allows to characterize the jets in

steady state. We estimate the value of the magnetic field and the density of matter and radiation inside the jets. These fields are the targets for relativistic particles. We explore a large number of possible scenarios by varying the values of the parameters of the model.

The first generalization we introduce is that our model is lepto-hadronic: both relativistic electrons and protons are injected in the jets. As we shall show, the radiative contribution of both species of particles cannot be considered separately. The efficiency of proton interactions to produce gamma rays depends in part on the radiative spectrum of electrons at lower energies. We do not deal with the process of particle acceleration; instead, we just assume that some unspecified mechanism injects relativistic particles. The steady-state distribution in energy and space of the relativistic particles results from the interplay between energy losses, convection or escape from the source, and decay in the case of unstable species. We consider all these effects by calculating the particle distributions from an appropriate version of the transport (or kinetic) equation.

Along the thesis, two different versions of this equation are used. We start by working in the *one-zone* approximation. In this approximation the region of injection of relativistic particles is spatially narrow (compared to the length of the jet) and homogeneous. We later refine this approach by adding a convection term to the transport equation. This allows to study the injection of relativistic particles in an extended, inhomogeneous region of the jet. We do not include time dependence. The model cannot be applied to study transient phenomena such as flaring emission (with typical durations of hours).

The outcome of our model are broadband electromagnetic spectra, from radio to gamma rays. The total luminosity of the jet is the sum of many individual components that arise in the interaction of protons, electrons, pions, muons, and secondary electron-positron pairs with all the target fields. Radiation from pions and muons has been seldom or never studied before in the context of galactic jets. Depending on the values of the parameters of the model, the predicted spectral energy distributions take different and complex shapes.

We implement specific applications of the model. The initial calculations are general; we show that the observational characteristics of some unidentified high-energy sources may be reproduced by the model. Later we apply

it to fit the available broadband data from two transient[8] low-mass microquasars, GX 339-4 and XTE J1118+480. The model predicts that these sources might emit high-energy gamma rays during outbursts. We expect these results will be tested in the near future with new data from gamma-ray satellites and Cherenkov telescopes.

[8]These sources remain in the LH state typically for periods of months. It is therefore valid to apply the steady-state model developed here to study their radiative properties during this spectral state.

3

ONE-ZONE LEPTO-HADRONIC MODELS. I. THEORY

3.1 JET MODEL

The low-hard state of X-ray binaries is characterized by the presence of steady jets. We assume that the jets are launched perpendicularly to the plane of the accretion disc. We do not consider precessing jets here; the effects of precession and misalignment on the radiative spectrum of jets have been studied elsewhere (e.g. Kaufman Bernadó et al. 2002, Romero et al. 2002, Romero & Orellana 2005).

We adopt cylindrical coordinates. The z-axis is taken along the symmetry axis of the jet, that makes an angle $\theta_{\rm jet}$ with the line of sight (see Figure 3.1). The base of the jet is at a distance $z_0 = 50 R_{\rm grav}$ from the black hole, and the initial radius of the jet is $r_0 = \chi\, z_0$. The outflow expands initially as a cone of radius

$$r_{\rm jet}(z) = r_0 \left(\frac{z}{z_0} \right). \tag{3.1}$$

Following the "disk-jet symbiosis" hypothesis of Falcke & Biermann (1995) (see also Mirabel et al. 1998 and Körding et al. 2006), the total power of each jet is assumed to be proportional to the accretion power,

$$L_{\rm jet} = q_{\rm jet} L_{\rm accr}, \tag{3.2}$$

where $q_{\rm jet} < 1$ is an adimensional parameter.

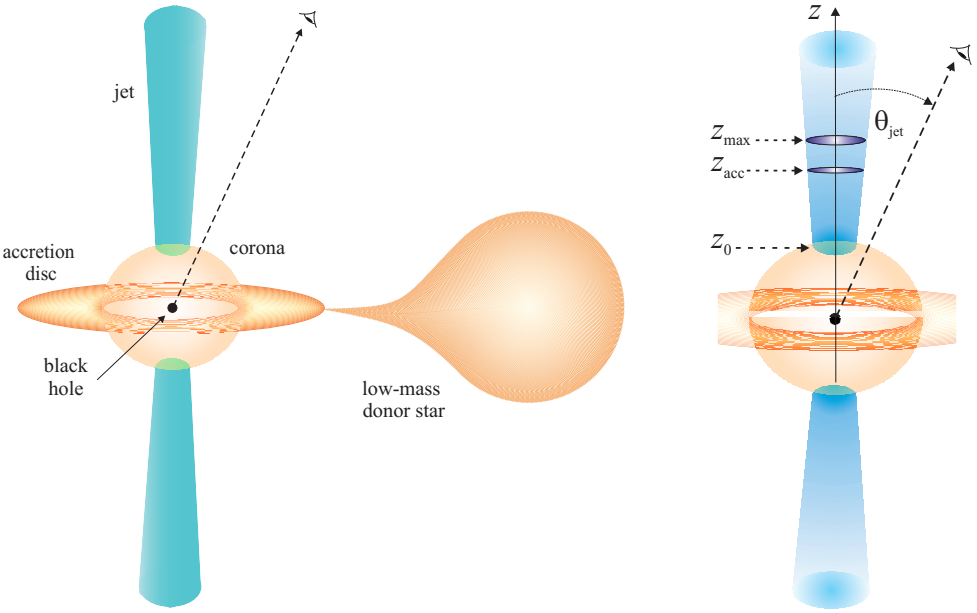

Figure 3.1: Left: components of a low-mass microquasar. Right: a detail, indicating the relevant geometrical parameters.

At any distance z from the compact object, the total energy budget of the jet can be roughly divided into magnetic energy, bulk kinetic energy, and particle internal energy[1]

$$L_{\rm jet} \approx L_{\rm B} + L_{\rm k} + L_{\rm m}. \tag{3.3}$$

Since the outflow is likely ejected by some kind of magneto-centrifugal mechanism, we assume that the outflow is energetically completely dominated by the magnetic field at the base. The value of the magnetic field $B_0 = B(z_0)$ may then be estimated equating the magnetic energy density at z_0 with the total energy density of the outflow once it has been set in motion with a bulk velocity $v_{\rm jet}$,

$$\frac{B_0^2}{8\pi} = \frac{L_{\rm jet}}{\pi r_{\rm in}^2 v_{\rm jet}}. \tag{3.4}$$

We take $r_{\rm in} = r_0 + \Delta r \approx r_0$. For $z > z_0$ the magnetic field decreases as

[1]Strictly, $L_{\rm jet} > L_{\rm jet}(z)$ since part of $L_{\rm jet}$ is dissipated as radiation.

$$B(z) = B_0 \left(\frac{z_0}{z}\right)^m, \tag{3.5}$$

with $1 \leq m \leq 2$ (e.g. Krolik 1999).

Magnetic energy is converted into bulk kinetic energy and internal energy of the plasma. The bulk Lorentz factor of the jet, $\Gamma_{\rm jet}$, increases as the outflow accelerates. The behaviour of $\Gamma_{\rm jet}$ with the distance to the black hole can be studied both analytically and numerically using the equations of the MHD (e.g. Lyubarsky 2010, Tchekhovskoy et al. 2008, 2010); a simpler approach is presented in Reynoso et al. (2011). Here we simply adopt a constant value of $\Gamma_{\rm jet}$ for all z larger than a certain $z_{\rm in} \approx z_0$.

The jet is dynamically dominated by thermal (cold) matter. If shock waves propagate through some region of the outflow, the suprathermal tail of the Maxwellian particle distribution may be accelerated up to relativistic energies by diffusion across the shock front (see, for instance, Drury 1983 and references therein). We assume that the total power $L_{\rm rel}$ injected in relativistic particles is only a small fraction of the total jet power,

$$L_{\rm rel} = q_{\rm rel} L_{\rm jet}, \tag{3.6}$$

with $q_{\rm rel} \ll 1$. This power is shared between relativistic protons and leptons

$$L_{\rm rel} = L_p + L_e. \tag{3.7}$$

We relate the energy budget of both species as

$$L_p = a\, L_e. \tag{3.8}$$

The parameter a remains free in our model but, as we are interested in jets with a relevant hadronic content, we keep $a \geq 1$ throughout.

The physical conditions for an efficient particle acceleration are not clear. For the plasma to be mechanically compressible and allow the formation of shocks, the magnetic energy density $U_{\rm B} = B^2/8\pi$ must be in sub-equipartition with the bulk kinetic energy density $U_{\rm k}$ of the plasma (see Komissarov et al. 2007 for a discussion on this topic). Therefore, the base of the acceleration

region must be located at a distance $z_{\rm acc}$ from the black hole such that

$$U_{\rm B}(z_{\rm acc}) < U_{\rm k}(z_{\rm acc}). \tag{3.9}$$

The kinetic energy density of the jet can be written as

$$U_{\rm k} = n(z) E_p^{\rm kin}, \tag{3.10}$$

where $n(z)$ is the density of thermal particles (e.g. Bosch-Ramon et al. 2006b)

$$n(z) \approx \frac{L_{\rm jet}}{\Gamma_{\rm jet} \pi r_{\rm jet}^2 v_{\rm jet} m_p c^2}, \tag{3.11}$$

and $E_p^{\rm kin}$ is the relativistic kinetic energy of a proton that moves with the jet bulk velocity

$$E_p^{\rm kin} = (\Gamma_{\rm jet} - 1) m_p c^2. \tag{3.12}$$

The presence of shocks may not suffice to accelerate particles efficiently. According to Gaisser (1990), for diffusive shock acceleration to work, the ram pressure in the acceleration region must dominate over the magnetic pressure. This condition can be written as

$$U_{\rm B}(z_{\rm acc}) < \frac{2}{3} U_{\rm m}(z_{\rm acc}), \tag{3.13}$$

where $U_{\rm m}$ is the internal matter energy density. For a cold proton-dominated jet, $U_{\rm m}$ can be calculated as in Bosch-Ramon et al. (2006b)

$$U_{\rm m} = n(z) \bar{E}_p^{\rm kin}. \tag{3.14}$$

Here $\bar{E}_p^{\rm kin}$ is the classical kinetic energy of a thermal proton

$$\bar{E}_p^{\rm kin} = \frac{1}{2} m_p v_p^2. \tag{3.15}$$

The mean velocity of the particles is taken to be equal to the lateral expansion velocity of the jet, $v_p = v_{\rm exp} = \chi v_{\rm jet}$, that is of the order of the speed of

sound in the plasma in the *comoving* or *jet reference frame*.[2] Condition (3.13) is stronger than (3.9), in the sense that if the former is fulfilled, so is the latter. In either case, the location of the innermost acceleration region can be determined demanding that the appropriate condition is satisfied,

$$U_{\rm B} = \rho\, U_{\rm (k,m)}, \tag{3.16}$$

with $\rho < 1$.

3.2 INJECTION AND ENERGY DISTRIBUTION OF RELATIVISTIC PARTICLES

The most energetic thermal particles in the jet may get accelerated up to relativistic energies by the action of one or more mechanisms. The protons and electrons injected in this way are referred to as *primary particles*. The *secondary particles* are the pions, muons, and electron-positron pairs injected as a result of the interaction of primary particles with matter and radiation.[3] The injection and cooling of primary and secondary particles occurs mainly in the same region of the jet, that we call *acceleration region*.[4]

We do not model the acceleration process, but assume that it leads to an injection spectrum of primary particles that is a power-law in energy. We parameterize the isotropic injection function (in units of $\mathrm{erg}^{-1}\ \mathrm{cm}^{-3}\ \mathrm{s}^{-1}$) in the jet reference frame as

$$Q\,(E,z) = Q_0\, E^{-\alpha}\, z^{-\beta}, \tag{3.17}$$

with $\alpha, \beta > 0$. The normalization constant Q_0 is calculated from the total power injected in each type of particle

$$L_{(e,p)} = \int_V \mathrm{d}^3 r \int_{E^{\rm min}}^{E^{\rm max}} \mathrm{d}E\, E\, Q_{(e,p)}(E,z), \tag{3.18}$$

where V is the volume of the acceleration region.

[2] This is the reference frame attached to bulk motion of the outflow.

[3] And also the electron-positron pairs created by annihilation of two photons, see Section 3.4.1.

[4] Notice that protons can still cool significantly beyond this region; see Chapters 4 and 5.

One of the problems of the theory of diffusive shock acceleration is that only suprathermal particles (those with energies significantly above their thermal energy) can cross the shock front and be efficiently accelerated. This means that some mechanism of "pre-acceleration" must operate. To take this effect into account, we adopt $E^{\rm min} \geq 2mc^2$. Aside from this constraint, the minimum energy of primary particles is a free parameter of the model.

The maximum energy that primary particles can attain is fixed by the balance of acceleration and energy losses. Particles can gain energy up to a certain value $E^{\rm max}$ for which the total cooling rate equals the acceleration rate, i.e.

$$t_{\rm acc}^{-1}\left(E_{\rm max}, z\right) = t_{\rm cool}^{-1}\left(E_{\rm max}, z\right). \tag{3.19}$$

For diffusive shock acceleration, the time for a particle to reach an energy E is approximately (e.g. Aharonian 2004)

$$t_{\rm acc} = 10\,\frac{D(E)}{v_{\rm s}^2}, \tag{3.20}$$

where $D(E)$ is the diffusion coefficient in the upstream (unshocked) region, and $v_{\rm s}$ the velocity of the upstream region in the reference frame of the shock front. The diffusion coefficient is unknown, but it can be written in terms of the minimum or Bohm diffusion coefficient $D_{\rm B}$ as

$$D(E) = \xi D_{\rm B}(E), \tag{3.21}$$

where

$$D_{\rm B}(E) = \frac{1}{3}\frac{Ec}{eB}, \tag{3.22}$$

the electron charge is e, and $\xi \geq 1$. A diffusion coefficient equal to the Bohm value implies that the mean free path of a particle is equal to its gyroradius. Replacing Eq. (3.21) into Eq. (3.20) gives

$$t_{\rm acc} = \frac{10}{3}\xi\left(\frac{c}{v_{\rm s}}\right)^2\frac{E}{eBc}. \tag{3.23}$$

Without entering into details about the value of the diffusion coefficient and the shock speed, we parameterize the acceleration rate as

$$t_{\rm acc}^{-1} = \eta e B c E^{-1}, \tag{3.24}$$

where the coefficient $\eta < 1$ characterizes the efficiency of the acceleration.

The total cooling rate is the sum of the individual contributions of all the radiative and non-radiative processes of energy loss

$$t_{\rm cool}^{-1} = \sum_i \left(t_{\rm cool}^i \right)^{-1}. \tag{3.25}$$

The expressions for the radiative cooling rates are given in Section 3.3. The non-radiative energy losses are due to the adiabatic work exerted by the relativistic particles on the walls of the expanding plasma. The adiabatic cooling rate is (e.g. Bosch-Ramon et al. 2006b)

$$t_{\rm ad}^{-1} = \frac{2}{3} \frac{v_{\rm jet}}{z}. \tag{3.26}$$

There is a further constraint on the maximum energy of the relativistic particles, since these can only remain confined if their gyroradius $r_{\rm gy}$ does not exceed the size of the acceleration region. This condition is known as the *Hillas criterion* (Hillas 1984). According to this criterion, we must then demand that

$$r_{\rm gy} = \frac{E}{eB(z)} < r_{\rm jet}(z). \tag{3.27}$$

The value of the maximum energy is the minimum between those determined from Eqs. (3.19) and (3.27).

The injection function and the maximum energy of the secondary particles depend on the specific process by which they were created. The relevant formulae are presented in Section 3.3.

A general expression for the equation that describes the evolution of the distribution of relativistic particles $N(\vec{r}, E, t)$ is given by (e.g. Ginzburg & Syrovatskii 1964, Ginzburg & Ptuskin 1976, Aharonian 2004)

$$\frac{\partial N}{\partial t} - \nabla \cdot (D \nabla N) + \nabla \cdot (\vec{v} N) + \frac{\partial}{\partial E}(bN) = -pN + f[N] + Q_{\rm inj}. \tag{3.28}$$

The second and third term on the left-hand side account for the particle transport through diffusion and convection, respectively; $D(\vec{r}, E)$ is the diffusion coefficient and $\vec{v}$ the bulk velocity of the medium. The fourth term represents the "continuous" energy losses; these are interactions in which the particle only suffers a small change in its energy. The function $b(\vec{r}, E) < 0$ is the total energy loss rate

$$b \equiv \left.\frac{dE}{dt}\right|_{\rm cool} = -E\, t_{\rm cool}^{-1}. \tag{3.29}$$

The first and second terms on the right-hand side are the "catastrophic" losses. These are processes in which a particle disappears as such, or loses a significant fraction of its initial energy in only one interaction. Particles can disappear, for example, because they decay. If $\tau_{\rm dec}$ is the mean lifetime of the particle in its rest frame and γ its Lorentz factor, then

$$p_{\rm dec} = \frac{1}{T_{\rm dec}} = \frac{1}{\gamma \tau_{\rm dec}}. \tag{3.30}$$

The functional $f[N]$ accounts for the influx of particles because of catastrophic interactions. It can be written as

$$f[N] = \sum_k \int P_k\left(E', E\right) N_k\left(E', \vec{r}, t\right) \mathrm{d}E', \tag{3.31}$$

where $P_k\left(E', E\right)$ is the probability per unit time and unit energy, of the appearance of a particle with energy E in a collision of a particle of type k and energy E'. Relativistic Bremsstrahlung and inverse Compton scattering in the Klein-Nishina regime are examples of processes that lead to catastrophic energy losses.

Finally, the last term on the right-hand side is the particle injection function $Q_{\rm inj}\left(\vec{r}, E, t\right)$. This function must account for the injection of particles through the acceleration processes, and also through the decay or annihilation of other

species. In a strict treatment, particle acceleration should be included separately as extra terms involving energy derivatives of $N(\vec{r}, E, t)$. In Eq. (3.28) these terms are replaced by the effective injection function in Eq. (3.17).

We use a simplified form of Eq. (3.28) to calculate the energy distributions of primary and secondary particles. The most important approximation we introduce is that the acceleration region is spatially thin enough to ignore the spatial derivatives in the transport equation. This is called the *one-zone* approximation. Physically, it means that the contribution to $N(E, z)$ of particles coming from other regions in the jet is neglected.

An effective term of the form

$$Q_{\rm esc} = -\frac{N}{T_{\rm esc}} \tag{3.32}$$

is added to account for the escape of particles from the acceleration region. This approach is usually known as the "leaky box". We consider a simple, energy-independent, expression for the escape time

$$T_{\rm esc} \approx \frac{\Delta z}{v_{\rm jet}}, \tag{3.33}$$

where Δz is the width of the acceleration region.

We also neglect catastrophic energy losses, so the second term on the right-hand side of Eq. (3.28) is dismissed. See Khangulyan & Aharonian (2005) for a discussion on this approximation in the case of inverse Compton energy losses. Finally, throughout this thesis we are only interested in models for jets that are globally in steady state.

Under the approximations described above, the transport equation reads

$$\frac{d}{dE}(bN) + \frac{N}{T} = Q_{\rm inj}, \tag{3.34}$$

with

$$T(E) = \left[\frac{1}{T_{\rm esc}} + \frac{1}{T_{\rm dec}(E)}\right]^{-1}. \tag{3.35}$$

The mean lifetime of protons and electrons/positrons is infinite, so the decay

term only contributes when solving for pions and muons.

The general analytic solution of Eq. (3.34) is known (e.g. Aharonian 2004)

$$N(E) = \frac{1}{b\,(E)} \int_E^{E^{\max}} \mathrm{d}E'\, Q_{\mathrm{inj}}(E') \exp\left[-\frac{\tau(E,E')}{T(E')}\right], \tag{3.36}$$

where

$$\tau(E,E') \equiv \int_E^{E'} \mathrm{d}E''\, \frac{1}{b\,(E'')}. \tag{3.37}$$

A particular case of importance is that when energy losses dominate over particle escape and decay. The solution of Eq. (3.34) then reduces to

$$N(E) \approx \left|\frac{1}{b(E)}\right| \int_E^{\infty} \mathrm{d}E'\, Q_{\mathrm{inj}}(E'). \tag{3.38}$$

If the injection function and the total energy loss rate are described by power-laws[5] of spectral indices $\alpha > 1$ and ε, respectively, then

$$N \propto E^{-(\alpha+\varepsilon)+1}. \tag{3.39}$$

The steady-state distribution of particles, therefore, does not reproduce the energy dependence of the injection function, except when $\varepsilon = 1$.

3.3 RADIATIVE PROCESSES

3.3.1 *General considerations*

Relativistic particles interact with the magnetic field, radiation, and matter in the jet to produce photons and secondary particles. For each radiative process we calculate the specific luminosity $L_\gamma(E_\gamma)$ (in units of erg s^{-1}) at photon energy E_γ. The total luminosity of the jet is the sum of these individual contributions; it is a measure of the intrinsic radiative power of the jets, not affected by inferred parameters such as the distance to the system.

[5] As we shall see, this is indeed the case for virtually all the processes considered in this thesis.

Equation (3.34) yields the particle distributions in the jet frame, attached to bulk motion of the outflow. Then, for convenience, we initially calculate the luminosities in this reference frame. The jet frame moves with velocity $v_{\rm jet}$ with respect to the *observer frame*, the reference frame fixed to the accretion disc or the compact object.

The luminosities in the observer frame are obtained applying an appropriate boost, see for example Lind & Blandford (1985). Denoting the variables in the comoving and the observer frame with primed and non-primed symbols, respectively, the luminosity transforms as

$$L_\gamma(E_\gamma) = \mathcal{D}^2\, L'_\gamma(E'_\gamma). \tag{3.40}$$

Here

$$E_\gamma = \mathcal{D} E'_\gamma \tag{3.41}$$

is the photon energy in the observer frame, and

$$\mathcal{D} = \left[\Gamma_{\rm jet}\left(1 - \beta_{\rm jet}\cos\theta_{\rm jet}\right)\right]^{-1} \tag{3.42}$$

is the Doppler factor for an approaching jet; $\theta_{\rm jet}$ is the viewing angle (see Figure 3.1) and $\beta_{\rm jet} = v_{\rm jet}/c$.

The exception to this procedure is the calculation of the luminosity from the decay of neutral pions created in proton-proton inelastic collisions. For this process it is convenient to work directly in the observer frame, where some useful parameterizations for the total inelastic cross section are available. It is necessary, then, to convert the proton distribution obtained from Eq. (3.34) to the observer frame. This can be done with the transformations given in Torres & Reimer (2011). Using the same notation convention as before, the proton distribution transforms as

$$N_p(E) = N'_p(E')\left(\frac{p}{p'}\right)\left(\frac{E}{E'}\right). \tag{3.43}$$

The transformations for energy and momentum are

$$E' = \Gamma_{\rm jet}\left(E - \beta_{\rm jet} c p \cos\theta_{\rm jet}\right) \tag{3.44}$$

and

$$p'^2 = p^2\left[\sin^2\theta_{\rm jet} + \Gamma_{\rm jet}^2\left(\cos\theta_{\rm jet} - \frac{\beta_{\rm jet}E}{\sqrt{E^2 - m^2c^4}}\right)^2\right], \tag{3.45}$$

where $E^2 = c^2p^2 + m^2c^4$. Equation (3.44) reduces to Eq. (3.41) for a massless particle. Notice that for the values of the jet bulk Lorentz factor and the viewing angle adopted throughout this thesis, the simpler transformation for the particle distribution obtained in earlier works (e.g. Purmohammad & Samimi 2001) provides accurate results.

Some relevant formulae regarding the calculation of the cooling rates and the luminosities are given below. A more detailed discussion about some interactions is presented in Appendix A; see also the books by Aharonian (2004) and Romero & Paredes (2011).

3.3.2 *Synchrotron radiation*

Charged relativistic particles emit synchrotron radiation as they move in the magnetic field of the jet. For a particle of unit charge e, energy E, and mass m in a random magnetic field, the synchrotron cooling rate is (e.g. Blumenthal & Gould 1970)

$$t_{\rm synchr}^{-1} = \frac{4}{3}\left(\frac{m_e}{m}\right)^3 \frac{c\sigma_T U_{\rm B}}{m_e c^2}\frac{E}{mc^2}. \tag{3.46}$$

Here m_e is the mass of the electron and σ_T is the Thomson cross section. The mass ratio in Eq. (3.46) makes synchrotron cooling very efficient for light particles. In particular, for a proton and an electron with the same Lorentz factor, the cooling rate is $\left(m_p/m_e\right)^3 \approx 7\times10^9$ times larger for the electron.

In the comoving reference frame, the synchrotron power per unit energy radiated by a single particle is

$$P_{\rm synchr}\left(E_\gamma, E, \alpha, \vec{r}\right) = \frac{\sqrt{3}\,e^3 B\left(\vec{r}\right)}{4\pi m c^2 h}\frac{E_\gamma}{E_{\rm c}}\int_{E_\gamma/E_{\rm c}}^{\infty} {\rm d}\zeta\, K_{5/3}(\zeta), \tag{3.47}$$

where E_γ is the energy of the emitted photon and $K_{5/3}(\zeta)$ is a modified Bessel function of the second kind.[6] The variable α is the "pitch angle", defined as the angle between the magnetic field and the particle's momentum. The function $P_{\rm synchr}$ peaks sharply near the characteristic energy

$$E_{\rm c} = \frac{3heB\sin\alpha}{4\pi mc}\left(\frac{E}{mc^2}\right)^2. \tag{3.48}$$

In general, the value of $E_{\rm c}$ is much smaller than that of the energy of the parent particle.

The total synchrotron luminosity is calculated integrating Eq. (3.47) times the distribution of particles over energy, pitch angle, and volume of the emission region

$$L_{\rm synchr}\,(E_\gamma) = E_\gamma \int_V {\rm d}^3 r \int_{\Omega_\alpha} {\rm d}\Omega_\alpha \sin\alpha \int_{E^{\rm min}}^{E^{\rm max}} {\rm d}E\, N(E,\vec{r})\, P_{\rm synchr}. \tag{3.49}$$

A power-law distribution of particles yields a synchrotron spectrum that is also a power-law. For $N \propto E^{-p}$, the synchrotron luminosity (in units of erg s^{-1}) is of the form $L_{\rm synchr} \propto E_\gamma^{-l}$ with $l = -(p-3)/2$.

3.3.3 *Relativistic Bremsstrahlung*

Bremsstrahlung radiation is produced when a relativistic charged particle is accelerated in an electrostatic field. Bremsstrahlung losses are essentially catastrophic: the particle loses almost all its energy in one interaction, and most of the emitted radiation is in the form of high-energy photons. We can, however, introduce an average continuous cooling rate. For an electron of energy E_e in a plasma of fully ionized nuclei of charge eZ and number density n_p,

$$t_{\rm Br}^{-1} = 4\,\alpha_{\rm FS}\, r_e^2 Z^2 c n_p \left[\ln\left(\frac{2E_e}{m_e c^2}\right) - \frac{1}{3}\right]. \tag{3.50}$$

where $\alpha_{\rm FS}$ is the fine structure constant and r_e the classical electron radius.

[6] A very simple analytical approximation for the integral is given in Appendix A.

The differential cross section for the emission of a photon with energy E_γ by an electron of energy $E_e \gg m_e c^2$ in the presence of a nucleus of charge eZ is (e.g. Berezinskii et al. 1990)

$$\frac{\mathrm{d}\sigma_{\mathrm{Br}}}{\mathrm{d}E_\gamma}\left(E_\gamma, E_e\right) = \frac{4\,\alpha_{\mathrm{FS}}\, r_e^2 Z^2}{E_\gamma}\left[1 + \left(1 - \frac{E_\gamma}{E_e}\right)^2 - \frac{2}{3}\left(1 - \frac{E_\gamma}{E_e}\right)\right] \times \left\{\ln\left[\frac{2E_e\left(E_e - E_\gamma\right)}{m_e c^2 E_\gamma}\right] - \frac{1}{2}\right\}. \tag{3.51}$$

The Bremsstrahlung luminosity can be directly calculated from the differential cross section and the distribution of electrons as

$$L_{\mathrm{Br}}\left(E_\gamma\right) = cE_\gamma^2 \int_V \mathrm{d}^3 r\, n_p(\vec{r}) \int_{E_e^{\min}}^{E_e^{\max}} \mathrm{d}E_e\, \frac{\mathrm{d}\sigma_{\mathrm{Br}}}{\mathrm{d}E_\gamma}\left(E_\gamma, E_e\right)\, N_e(E_e, \vec{r}). \tag{3.52}$$

3.3.4 *Proton-proton inelastic collisions*

The inelastic collision of a relativistic proton with a low-energy proton yields mesons. The reactions with the lowest energy thresholds correspond to the creation of pions

$$\begin{aligned} p + p &\rightarrow p + p + a\pi^0 + b\left(\pi^+ + \pi^-\right) \\ p + p &\rightarrow p + n + \pi^+ + a\pi^0 + b\left(\pi^+ + \pi^-\right) \\ p + p &\rightarrow n + n + 2\pi^+ + a\pi^0 + b\left(\pi^+ + \pi^-\right). \end{aligned} \tag{3.53}$$

The integers a and b are the pions multiplicities. They depend on the energy of the relativistic proton approximately as $a, b \propto E_p^{-\kappa}$ with $\kappa \sim 1/4$ (Mannheim & Schlickeiser 1994). The threshold energy for the production of a single neutral pion is

$$E_{\rm thr} = m_p c^2 + 2 m_{\pi^0} c^2 \left(1 + \frac{m_{\pi^0}}{4 m_p} \right) \approx 1.22\,{\rm GeV}, \tag{3.54}$$

where m_p and m_{π^0} are the mass of the proton and the neutral pion, respectively.

The cooling rate for a proton of energy E_p due to inelastic collisions with a target field of low-energy protons with number density n_p is (e.g. Begelman et al. 1990, Aharonian & Atoyan 2000)

$$t_{pp}^{-1} \approx c n_p K_{pp} \sigma_{pp} \left(E_p \right). \tag{3.55}$$

Here σ_{pp} is the total inelastic cross section (see Appendix A) and $K_{pp} \approx 0.5$ is the total inelasticity of the interaction. Most of the energy lost by the relativistic proton is transferred to only one or two "leading" pions. To calculate the cooling rate of charged pions due to inelastic collisions with protons we use that $\sigma_{\pi p} \approx 2/3\, \sigma_{pp}$. This approximation for the cross section was introduced by Gaisser (1990), taking into account that the proton is formed by three valence quarks whereas the pion only by two.

The main decay mode of the neutral pion is into two gamma rays[7]

$$\pi^0 \longrightarrow \gamma + \gamma. \tag{3.56}$$

Kelner et al. (2006) introduced an useful parameterization for the spectrum of gamma rays due to the decay of neutral pions created in proton-proton collisions. The formulae were obtained fitting the results of the code SIBYLL, used to study atmospheric cascades at ultra-high energies (Fletcher et al. 1994). Defining $x = E_\gamma / E_p$, the gamma-ray emissivity (in units of erg^{-1} cm^{-3} s^{-1}) is given by

$$q_\gamma^{(pp)} \left(E_\gamma, \vec{r} \right) = c\, n_p \left(\vec{r} \right) \int_{E_\gamma}^{E_p^{\rm max}} \frac{1}{E_p}\, \sigma_{pp} \left(E_p \right) N_p \left(E_p, \vec{r} \right) F_\gamma \left(x, E_p \right) {\rm d}E_p. \tag{3.57}$$

[7]The mean lifetime of the neutral pion is $\tau_{\pi^0} = (8.4 \pm 0.4) \times 10^{-17}$ s; the branching ratio of the two-photon decay mode is (98.823 ± 0.034). Data from Nakamura et al. (2010), also available online at http://pdg.lbl.gov/.

The function $F_\gamma\left(x, E_p\right)$ is the number of photons per unit energy created per proton-proton collision; see Appendix A for its full expression.

Equation (3.57) is valid for $E_p \gtrsim 100$ GeV. At lower energies, the gamma-ray emissivity can be calculated to a good accuracy using the *δ-functional formalism* (Aharonian & Atoyan 2000, Kelner et al. 2006). In this approximation all the neutral pions carry a fixed fraction of the kinetic energy of the relativistic proton, $E_\pi \approx K_\pi E_p^{\mathrm{kin}}$. The injection function of neutral pions is then

$$Q_{\pi^0}^{(pp)}\left(E_\pi, \vec{r}\right) \approx \frac{\widetilde{n}}{K_\pi}\, c\, n_p\left(\vec{r}\right)\, \sigma_{pp}\left(m_p c^2 + \frac{E_\pi}{K_\pi}\right) N_p\left(m_p c^2 + \frac{E_\pi}{K_\pi}, \vec{r}\right), \tag{3.58}$$

where $\widetilde{n}$ is the number of neutral pions created per proton-proton collision. The gamma-ray emissivity is directly calculated from $Q_{\pi^0}^{(pp)}$ as

$$q_\gamma^{(pp)}\left(E_\gamma, \vec{r}\right) = 2 \int_{E_{\min}}^{E_p^{\max}} \frac{Q_{\pi^0}^{(pp)}\left(E_\pi, \vec{r}\right)}{\sqrt{E_\pi^2 - m_{\pi^0}^2 c^4}}\, \mathrm{d}E_\pi, \tag{3.59}$$

with

$$E_{\min} = E_\gamma + \frac{m_{\pi^0}^2 c^4}{4E_\gamma}. \tag{3.60}$$

For a given value of K_π, the value of $\widetilde{n}$ is fixed demanding continuity between Eqs. (3.57) and (3.59) at $E_p = 100$ GeV.[8] As demonstrated in Aharonian & Atoyan (2000), taking $K_\pi = 0.17$ (Gaisser 1990) provides a good agreement with the results of simulations.

Once the gamma-ray emissivity is known, the luminosity is readily obtained integrating over the volume of the emission region

$$L_{pp}\left(E_\gamma\right) = E_\gamma^2 \int_V \mathrm{d}^3 r\, q_\gamma^{(pp)}\left(E_\gamma, \vec{r}\right). \tag{3.61}$$

[8] It is assumed that $\widetilde{n}$ and K_π depend only weakly on the energy of the proton.

3.3.5 *Inverse Compton scattering*

Low-energy radiation can be boosted to very high energies through inverse Compton scattering off relativistic electrons[9]

$$e + \gamma \longrightarrow e + \gamma. \tag{3.62}$$

The spectrum of photons scattered by an electron of energy $E = \gamma mc^2$ interacting with an isotropic target radiation field of energy distribution $n_{\rm ph}(\epsilon, \vec{r})$ is (e.g. Blumenthal & Gould 1970)

$$P_{\rm IC}\left(E_\gamma, E, \epsilon, \vec{r}\right) = \frac{3}{4}\frac{c\sigma_{\rm T}}{\gamma^2}\frac{n_{\rm ph}\left(\epsilon, \vec{r}\right)}{\epsilon} F_{\rm IC}\left(E_\gamma, E, \epsilon\right), \tag{3.63}$$

where E_γ is the final energy of the photon and $F_{\rm IC}$ is an adimensional function given in Appendix A. Defining $\kappa = \epsilon E / m_e^2 c^4$, the allowed energy range for the scattered photons is

$$\epsilon \leq E_\gamma \leq \frac{4E\kappa}{1 + 4\kappa}. \tag{3.64}$$

The classical or Thomson regime corresponds to $\kappa \ll 1$. In this regime the electron loses only a small fraction of its energy per collision. For $\kappa \gg 1$ - in the quantum or Klein-Nishina regime - the electron transfers almost all its energy to the photon. In spite of this, IC scattering in the Klein-Nishina regime is not an efficient cooling process - the cross section drops abruptly for $\kappa \gg 1$, strongly suppressing the rate of collisions.

To calculate the IC cooling rate, Eq. (3.63) must be integrated over the initial and final energy of the photons:

$$t_{\rm IC}^{-1} = \frac{1}{E}\int_{\epsilon_{\rm min}}^{\epsilon_{\rm max}} {\rm d}\epsilon \int_{\epsilon}^{E_\gamma^{\rm max}(\kappa)} {\rm d}E_\gamma \, \left(E_\gamma - \epsilon\right) P_{\rm IC}. \tag{3.65}$$

In the Thomson limit it reduces to the well-known expression

[9] Inverse Compton scattering off protons can be treated in exactly the same way as lepton IC, but we do not consider it here. Inelastic collisions with radiation are a more efficient cooling mechanism than IC for protons and pions.

$$t_{\rm IC,Th}^{-1} = \frac{4}{3}\frac{c\sigma_T\, U_{\rm ph}}{m_e^2 c^4}\, E. \tag{3.66}$$

This is identical to the synchrotron cooling rate for an electron if the magnetic energy density is replaced by the energy density $U_{\rm ph}$ of the target photon field.

For an isotropic distribution of target photons, the total IC luminosity is given by

$$L_{\rm IC}\left(E_\gamma\right) = E_\gamma^2 \int_V {\rm d}^3 r \int_{E_{\rm e}^{\rm min}}^{E_{\rm e}^{\rm max}} {\rm d}E_{\rm e} \int_{\epsilon_{\rm min}}^{\epsilon_{\rm max}} {\rm d}\epsilon\, N\left(E_{\rm e}, \vec{r}\right) P_{\rm IC}. \tag{3.67}$$

In low-mass microquasars we expect that only the photon fields generated inside the jets provide relevant targets for IC scattering. Among these, the most important is the synchrotron radiation field of primary electrons. We estimate the energy distribution of synchrotron photons in the *local approximation* introduced by Ghisellini et al. (1985)

$$n_{\rm synchr}\left(\epsilon, z\right) \approx \frac{\varepsilon_{\rm synchr}\left(\epsilon, z\right)}{\epsilon}\frac{r_{\rm jet}(z)}{c}, \tag{3.68}$$

where $\varepsilon_{\rm synchr}\left(\epsilon, z\right)$ is the synchrotron power per unit energy per unit volume. In the particular case when particles scatter their own synchrotron radiation field, the process is called *synchrotron self-Compton* (SSC).

3.3.6 *Proton-photon inelastic collisions*

The inelastic collision of a photon with a high-energy proton yields mesons and leptons. The interaction channels with the lowest energy thresholds correspond to the production of the lightest particles: pions (*photomeson production*) and electron-positron pairs (*photopair production*).

Electron-positron pairs are directly injected through the reaction

$$p + \gamma \rightarrow p + e^- + e^+. \tag{3.69}$$

In the rest frame of the proton, the photon threshold energy for the creation of a pair is $\epsilon_{\rm thr}^{\prime(e)} = 2m_e c^2 \approx 1$ MeV.

Photomeson production becomes possible when the energy of the photon in the rest frame of the proton is larger than

$$\epsilon_{\rm thr}^{\prime(\pi)} = m_{\pi^0} c^2 \left(1 + \frac{m_{\pi^0}}{2m_p}\right) \approx 145\,{\rm MeV}, \tag{3.70}$$

There are two main channels of pion production:

$$p + \gamma \rightarrow p + a\pi^0 + b\left(\pi^+ + \pi^-\right) \tag{3.71}$$

and

$$p + \gamma \rightarrow n + \pi^+ + a\pi^0 + b\left(\pi^+ + \pi^-\right). \tag{3.72}$$

The integer coefficients a and b are, as before, the pion multiplicities.

The cooling rate for a proton of energy $E_p = \gamma_p m_p c^2$ in an isotropic photon distribution $n_{\rm ph}$ can be conveniently parameterized as (e.g. Begelman et al. 1990)

$$t_{p\gamma}^{(i)\,-1} = \frac{c}{2\gamma_p^2} \int_{\epsilon_{\rm thr}^{\prime(i)}/2\gamma_p}^{\infty} {\rm d}\epsilon\, \frac{n_{\rm ph}\left(\epsilon\right)}{\epsilon^2} \int_{\epsilon_{\rm thr}^{\prime(i)}}^{2\epsilon\gamma_p} {\rm d}\epsilon^{\prime}\, \sigma_{p\gamma}^{(i)}\left(\epsilon^{\prime}\right)\, K_{p\gamma}^{(i)}\left(\epsilon^{\prime}\right) \epsilon^{\prime}, \tag{3.73}$$

where $i = e, \pi$ denotes the interaction channel, and $\epsilon^{\prime}$ is the energy of the photon in the rest frame of the proton. Simple parameterizations for the inelasticities $K_{p\gamma}^{(i)}$ and the cross sections $\sigma_{p\gamma}^{(i)}$ are presented in Appendix A.[10] The cross section for pair production is about two orders of magnitude larger than that for pion production. The inelasticity $K_{p\gamma}^{(e)}$, however, is very low, so the proton only loses a small fraction of its energy per collision. As a result, the cooling is completely dominated by pion production if the energy of the photons exceeds $\epsilon_{\rm thr}^{\prime(\pi)}$.

Kelner & Aharonian (2008) provide simple analytical expressions for the spectrum of gamma rays due to decay of neutral pions created in proton-photon collisions. In terms of the distributions of relativistic protons and target

[10] To calculate the cooling rate of charged pions due to inelastic collisions with photons we again assume that $\sigma_{\pi\gamma} \approx 2/3\sigma_{p\gamma}$.

photons, the gamma-ray emissivity can be written as

$$q_\gamma^{(p\gamma)}\left(E_\gamma\right) = \int_{E_p^{\min}}^{E_p^{\max}} \mathrm{d}E_p \int_{\epsilon_{\mathrm{thr}}^{\prime(\pi)}/2\gamma_p}^{\infty} \mathrm{d}\epsilon\, \frac{1}{E_p}\, N_p(E_p)\, n_{\mathrm{ph}}(\epsilon)\, \Phi\left(\eta,\, x\right). \tag{3.74}$$

Here $\eta = 4\epsilon E_p / m_p^2 c^4$ and $x = E_\gamma / E_p$. The function $\Phi\left(\eta,\, x\right)$ was obtained fitting the numerical results of SOPHIA, a Monte Carlo code for the simulation of photohadronic interactions (Mücke et al. 2000). The full expression for $\Phi\left(\eta,\, x\right)$ is given in Appendix A.

Atoyan & Dermer (2003) found a simpler expression for the emissivity in the δ-functional approximation. Using that $E_\gamma \approx 0.1 E_p$, the gamma-ray emissivity results

$$q_\gamma^{(p\gamma)}\left(E_\gamma\right) \approx 20 N_p\left(10E_\gamma\right) \omega_{p\gamma}^{(\pi)}\left(10E_\gamma\right) n_{\pi^0}\left(10E_\gamma\right), \tag{3.75}$$

where n_{π^0} is the mean number of neutral pions crated per collision (see Appendix A) and $\omega_{p\gamma}^{(\pi)}$ is the collision rate,

$$\omega_{p\gamma}^{(\pi)} = \frac{c}{2\gamma_p^2} \int_{\epsilon_{\mathrm{thr}}^{\prime(\pi)}/2\gamma_p}^{\infty} \mathrm{d}\epsilon\, \frac{n_{\mathrm{ph}}\left(\epsilon\right)}{\epsilon^2} \int_{\epsilon_{\mathrm{thr}}^{\prime(\pi)}}^{2\epsilon\gamma_p} \mathrm{d}\epsilon^\prime\, \sigma_{p\gamma}^{(\pi)}\left(\epsilon^\prime\right)\, \epsilon^\prime. \tag{3.76}$$

The gamma-ray luminosity can be directly calculated from the emissivity as

$$L_{p\gamma}\left(E_\gamma\right) = E_\gamma^2 \int_V \mathrm{d}^3 r\, q_\gamma^{(p\gamma)}\left(E_\gamma, \vec{r}\right). \tag{3.77}$$

3.4 ABSORPTION

3.4.1 *Photon-photon annihilation*

The production of electron-positron pairs by annihilation of two photons

$$\gamma + \gamma \rightarrow e^+ + e^-, \tag{3.78}$$

plays a double role: it is a source of secondary pairs and a mechanism of photon absorption. This process is possible only above the kinematic energy threshold

$$\epsilon E_\gamma (1 - \cos\theta) \geq 2 m_e^2 c^4, \tag{3.79}$$

where E_γ and ϵ are the energies of the photons, and θ is the collision angle in the observer frame. The annihilation cross section is (Gould & Schréder 1967)

$$\sigma_{\gamma\gamma}(\beta) = \frac{3}{16}\,\sigma_{\rm T}\left(1-\beta^2\right)\left[\left(3-\beta^4\right)\ln\left(\frac{1+\beta}{1-\beta}\right) - 2\beta\left(2-\beta^2\right)\right]. \tag{3.80}$$

Here $\beta = \left(1-\gamma_e^{-2}\right)^{1/2}$ and γ_e is the Lorentz factor of the electron (positron) in the center of momentum frame. It is related to the energy of the photons and the collision angle as

$$(1-\beta^2) = \frac{2 m_e^2 c^4}{(1-\cos\theta)\epsilon E_\gamma} \qquad 0 \leq \beta < 1. \tag{3.81}$$

We define the optical depth $\tau_{\gamma\gamma}\left(E_\gamma, R\right)$ as the probability that a photon of energy E_γ annihilates against another photon of the target radiation field $n_{\rm ph}(\epsilon, \vec{r})$, after traversing a distance R. It is given by (e.g. Gould & Schréder 1967)

$$\tau_{\gamma\gamma}(E_\gamma, R) = \frac{1}{2}\int_0^R {\rm d}\ell \int_{\epsilon_{\rm thr}}^{\infty} {\rm d}\epsilon \int_{-1}^{u_{\rm max}} {\rm d}u\,(1-u)\,\sigma_{\gamma\gamma}(E_\gamma, \epsilon, u)\,n_{\rm ph}(\epsilon, \vec{r}), \tag{3.82}$$

where $u = \cos\theta$ and ℓ is a spatial variable along the path of the photon. The integration limits are

$$\epsilon_{\rm thr} = \frac{m_e^2 c^4}{E_\gamma}, \tag{3.83}$$

and

$$u_{\max} = 1 - \frac{2m_e^2c^4}{\epsilon E_\gamma}. \tag{3.84}$$

Because of the narrowness of the pair production cross section, a gamma ray of energy E_γ can effectively be absorbed by photons with energy in a narrow band centered at $\epsilon \approx 4m_e^2c^4/E_\gamma$.

The luminosities must be corrected to take into account the probability that the photons are absorbed on their way to the observer. In the initial applications of the model we only consider the absorption due to photon-photon annihilation in the internal radiation field of the jet, in particular the synchrotron field of primary protons.[11] The energy distribution of target photons is then given by Eq. (3.68).

In order to obtain the corrected (or absorbed) luminosity, an overall coefficient is applied to the "primary" luminosity

$$L_\gamma^{\rm abs}(E_\gamma) = \exp\left[-\tau_{\gamma\gamma}(E_\gamma)\right]\, L_\gamma(E_\gamma)\,. \tag{3.85}$$

Here $\tau_{\gamma\gamma}(E_\gamma) = \lim_{R\to\infty}\tau_{\gamma\gamma}(E_\gamma, R)$.

Notice that, although we do not consider it in this work, the absorption of radiation by interaction with matter may also be of importance, specially for extragalactic sources. At low energies ($E_\gamma \lesssim 1$ keV) the dominant mechanisms of absorption are scattering off dust and, for $E_\gamma > 13.6$ eV, photoionization. Direct Compton scattering and pair creation in photon-nuclei collisions become relevant above $E_\gamma \approx 1$ keV.

3.5 INJECTION OF SECONDARY PARTICLES

We are interested in the radiative output of all species of secondary particles: charged pions, muons, and electron-positron pairs. The corresponding luminosities are obtained with the formulae of Section (3.3), with the appropriate changes in the values of the mass of the particles and, in some cases, the cross sections. The missing piece of information are, then, the energy distributions of the secondary particles. To calculate them it is necessary to know the injection

[11] In Chapter 5 we also include the radiation field of the accretion disc as a target.

functions.

Proton-proton and proton-photon inelastic collisions inject charged pions. Their mean decay channels are

$$\begin{aligned} \pi^+ &\rightarrow \mu^+ + \nu_\mu, \\ \pi^- &\rightarrow \mu^- + \overline{\nu}_\mu, \end{aligned} \tag{3.86}$$

with a branching ratio (99.98770 ± 0.00004) (Nakamura et al. 2010). Muons decay with a probability almost equal to unity into a neutrino, an antineutrino, and an electron/positron:[12]

$$\begin{aligned} \mu^+ &\rightarrow e^+ + \nu_\mathrm{e} + \overline{\nu}_\mu \\ \mu^- &\rightarrow e^- + \overline{\nu}_\mathrm{e} + \nu_\mu. \end{aligned} \tag{3.87}$$

We do not study the emission of neutrinos. For detailed predictions of the neutrino flux from microquasars the reader is referred to Reynoso & Romero (2009).

If the cooling of pions and muons before decay is neglected, the injection function of electron-positron pairs can be easily estimated in the δ-functional approximation as in Atoyan & Dermer (2003). Assuming that each charged pion takes an energy $E_\pi \approx 0.2 E_p$, and that this energy is equally distributed among the decay products, the energy of each electron/positron is $E_e \approx 0.05 E_p$. The injection function of pairs is then

$$Q_{e^\pm}\left(E_{e^\pm}\right) = 20 N_p\left(20E_e\right) \omega_{p\gamma}^{(\pi)}\left(20E_e\right) n_{\pi^\pm}\left(20E_e\right), \tag{3.88}$$

where $n_{\pi^\pm}$ is the mean number of charged pions created per proton-photon collision and $\omega_{p\gamma}^{(\pi)}$ is the collision rate.

[12]The decay of charged pions and muons is a weak process. The mean lifetime of these particles - $\tau_{\pi^\pm} = (2.6033 \pm 0.0005) \times 10^{-8}$ s and $\tau_\mu = (2.197034 \pm 0.000021) \times 10^{-6}$ s - is then several orders of magnitude larger than that of the neutral pion, whose decay is purely electromagnetic.

When the conditions in the jet are such that the characteristic timescales of energy loss are shorter than the decay time, the cooling of pions and muons cannot be ignored. As a result, the injection spectrum of their decay products is modified with respect to that calculated ignoring the cooling. Then, for example, to calculate the injection function of muons we must first obtain the energy distribution of charged pions from Eq. (3.36). This, in turn, requires the knowledge of the pion injection function. The same applies to the calculation of the spectrum of electron-positron pairs injected in the decay of muons. Some relevant expressions are given below.

The injection function of charged pions in proton-proton collisions is given in Kelner et al. (2006),

$$Q_{\pi^\pm}^{(pp)}\left(E_\pi, \vec{r}\right) = c\, n_p(\vec{r}) \int_{E_\pi / E_p^{\max}}^{1} \mathrm{d}x\, \frac{1}{x}\, N_p\left(\frac{E_\pi}{x}, \vec{r}\right) \sigma_{pp}\left(\frac{E_\pi}{x}\right) F_\pi^{(pp)}\left(x, \frac{E_\pi}{x}\right). \tag{3.89}$$

The function $F_\pi^{(pp)}$ (see Appendix A) is related to the number of pions per unit energy interval created per proton-proton collision

$$\mathrm{d}N_\pi = \frac{1}{E_p}\, F_\pi^{(pp)}\left(x, E_p\right) \mathrm{d}E_\pi = F_\pi^{(pp)}\left(x, E_p\right) \mathrm{d}x, \tag{3.90}$$

where $x = E_\pi / E_p$.

The injection function for charged pions created in proton-photon interactions was estimated by Atoyan & Dermer (2003) in the δ-functional approximation. Assuming that each pion takes an energy $E_\pi \approx E_p/5$, the injection function results

$$Q_{\pi^\pm}^{(p\gamma)}\left(E_\pi, \vec{r}\right) \approx 5 N_p\left(5E_\pi\right) \omega_{p\gamma}^{(\pi)}\left(5E_\pi\right) n_{\pi^\pm}\left(5E_\pi\right). \tag{3.91}$$

As in Eq. (3.75), $\omega_{p\gamma}^{(\pi)}$ is the collision rate and $n_{\pi^\pm}$ the mean number of charged pions produced per proton-photon collision.

The injection of muons through the decay of charged pions was studied, for example, by Lipari et al. (2007). The spectra of left-handed and right-handed μ^- created in the decay of a π^- are

$$\frac{dn_{\pi^- \to \mu_L^-}}{dE_\mu}(E_\mu, E_\pi) = \frac{r_\pi(1-x)}{E_\pi\, x(1-r_\pi)^2}\, \mathcal{H}[x - r_\pi] \tag{3.92}$$

$$\frac{dn_{\pi^- \to \mu_R^-}}{dE_\mu}(E_\mu, E_\pi) = \frac{(x - r_\pi)}{E_\pi\, x(1-r_\pi)^2}\, \mathcal{H}[x - r_\pi], \tag{3.93}$$

where $x = E_\mu / E_\pi$, $r_\pi = (m_\mu / m_\pi)^2$ and $\mathcal{H}$ is the Heaviside function. Because of CP invariance

$$\frac{dn_{\pi^- \to \mu_R^-}}{dE_\mu} = \frac{dn_{\pi^+ \to \mu_L^+}}{dE_\mu} \tag{3.94}$$

and

$$\frac{dn_{\pi^- \to \mu_L^-}}{dE_\mu} = \frac{dn_{\pi^+ \to \mu_R^+}}{dE_\mu}. \tag{3.95}$$

The muon injection function is then

$$\begin{aligned} Q_{\mu_L^-, \mu_R^+}(E_\mu) = \int_{E_\mu}^{E^{(\max)}} \frac{\mathrm{d}E_\pi}{T_{\mathrm{dec}}^{\pi^\pm}(E_\pi)} \Bigg\{ & N_{\pi^-}(E_\pi)\, \frac{dn_{\pi^- \to \mu_L^-}}{dE_\mu}(E_\mu, E_\pi) + \\ & N_{\pi^+}(E_\pi)\, \frac{dn_{\pi^+ \to \mu_R^+}}{dE_\mu}(E_\mu, E_\pi) \Bigg\}, \end{aligned} \tag{3.96}$$

where $N_{\pi^\pm}$ are the pion energy distributions and $T_{\mathrm{dec}}^{\pi^\pm}$ is the decay time of the charged pions in the jet frame, respectively. Using Eq. (3.95), Eq. (3.96) simplifies to

$$Q_{\mu_L^-, \mu_R^+}(E_\mu) = \int_{E_\mu}^{E^{(\max)}} \mathrm{d}E_\pi\, \frac{N_\pi(E_\pi)}{T_{\mathrm{dec}}^{\pi^\pm}(E_\pi)}\, \frac{dn_{\pi^- \to \mu_L^-}}{dE_\mu}(E_\mu, E_\pi), \tag{3.97}$$

where $N_\pi = N_{\pi^+} + N_{\pi^-}$. Analogous considerations lead to

$$Q_{\mu_R^-, \mu_L^+}(E_\mu) = \int_{E_\mu}^{E^{(\max)}} \mathrm{d}E_\pi\, \frac{N_\pi(E_\pi)}{T_{\mathrm{dec}}^{\pi^\pm}(E_\pi)}\, \frac{dn_{\pi^- \to \mu_R^-}}{dE_\mu}(E_\mu, E_\pi). \tag{3.98}$$

To calculate the spectrum of electron-positron pairs from muon decay we follow Schlickeiser (2002). For an electron (or positron) of energy E_e the injection function is

$$Q_{e^\pm}^{(\mu)}(E_e) = \frac{m_e c^2}{2} \int_{m_e c^2}^{E_e'^{\max}} \mathrm{d}E_e' \, \frac{P(E_e')}{\sqrt{E_e'^2 - m_e^2 c^4}} \int_{E_\mu^-}^{E_\mu^+} \mathrm{d}E_\mu \, \frac{Q_\mu(E_\mu)}{\sqrt{E_\mu^2 - m_\mu^2 c^4}}. \tag{3.99}$$

Here Q_μ is the total muon injection function, E_e' is the energy of the electron (positron) in the rest frame of the muon, and P is the decay spectrum (particles per unit energy) in the same frame

$$P(E_e') = \frac{2E_e'^2}{(E_e'^{\max})^3} \left[3 - \frac{2E_e'}{E_e'^{\max}} \right]. \tag{3.100}$$

The maximum energy of the electron (positron) is $E_e'^{\max} = 104 m_e c^2$; the other integration limits are

$$E_\mu^\pm = \frac{m_\mu}{m_e^2 c^2} \left(E_e \, E_e' \pm \sqrt{E_e^2 - m_e^2 c^4} \sqrt{E_e'^2 - m_e^2 c^4} \right). \tag{3.101}$$

We consider two process of direct creation of electron-positron pairs: photopair production and photon-photon annihilation.

The direct injection of pairs in proton-photon collisions was studied, for example, by Chodorowski et al. (1992), Mastichiadis et al. (2005), and Kelner & Aharonian (2008). An expression for the pair injection function in the δ-functional approximation is given in Mastichiadis et al. (2005)

$$Q_{e^\pm}^{(p\gamma)}(E_e) \approx 2 \frac{m_p}{m_e} N_p \left(\frac{m_p}{m_e} E_e \right) \omega_{p\gamma}^{(e)} \left(\frac{m_p}{m_e} E_e \right), \tag{3.102}$$

where $\omega_{p\gamma}^{(e)}$ is the reaction rate, see Eq. (3.76).

The latter source of electron-positron pairs is the annihilation of two photons. Under the conditions $\epsilon \ll m_e c^2 \lesssim E_\gamma$, the pair emissivity that results from the interaction of two isotropic photon distributions n_γ and n_{ph} can be approximated by the following expression (Aharonian et al. 1983, see also Böttcher & Schlickeiser 1997)

$$Q_{e^\pm}^{(\gamma\gamma)}(E_e) = \frac{3}{32}\frac{c\,\sigma_T}{m_e c^2}\int_{\gamma_e}^{\infty} d\epsilon_\gamma \int_{\frac{\epsilon_\gamma}{4\gamma_e(\epsilon_\gamma-\gamma_e)}}^{\infty} d\omega\, \frac{n_\gamma(\epsilon_\gamma)}{\epsilon_\gamma^3}\,\frac{n_{ph}(\omega)}{\omega^2}\left\{\frac{4\epsilon_\gamma^2}{\gamma_e(\epsilon_\gamma-\gamma_e)}\times\right.$$
$$\left.\ln\left[\frac{4\gamma_e\omega(\epsilon_\gamma-\gamma_e)}{\epsilon_\gamma}\right] - 8\epsilon_\gamma\omega + \frac{2(2\epsilon_\gamma\omega-1)\epsilon_\gamma^2}{\gamma_e(\epsilon_\gamma-\gamma_e)} - \left(1-\frac{1}{\epsilon_\gamma\omega}\right)\frac{\epsilon_\gamma^4}{\gamma_e^2(\epsilon_\gamma-\gamma_e)^2}\right\}. \tag{3.103}$$

Here $\gamma_e = E_e/m_e c^2$ is the Lorentz factor of the electron, and $\epsilon_\gamma = E_\gamma/m_e c^2$ and $\omega = \epsilon/m_e c^2$ are the adimensional photon energies. The spectrum is symmetric around $E_e = E_\gamma/2$. For $\epsilon E_\gamma \gg m_e^2 c^4$ the interaction is catastrophic: one of the produced particles takes most of the energy of the gamma ray.

3.6 OVERALL PICTURE

Before proceeding to the applications, we briefly review the overall picture developed in the previous sections. Figure 3.2 shows a general sketch of the situation.

Two jets are launched from the surroundings of a black hole, perpendicularly to the plane of the accretion disc ($z = 0$). They expand as a cone as they propagate; the symmetry axis of the cone (the $z-$axis) makes an angle θ_{jet} with the line of sight of the observer.

The outflows are magnetically dominated near the base, at $z \sim z_0$. As they propagate, the bulk kinetic energy of the plasma increases at the expense of the magnetic energy density. We estimate the value of the magnetic field at the base of the jet assuming that the outflow is magnetically dominated in the launching region.

At some distance $z = z_{acc}$ from the black hole shock waves develop in the jets. In this region, a fraction of the thermal plasma - both electrons and protons - is accelerated up to relativistic energies, likely by a diffusive mechanism. The particle spectrum at injection is a power-law in energy. The total power injected in relativistic particles is $L_{rel} = q_{rel} L_{jet}$, with $q_{rel} \ll 1$. This

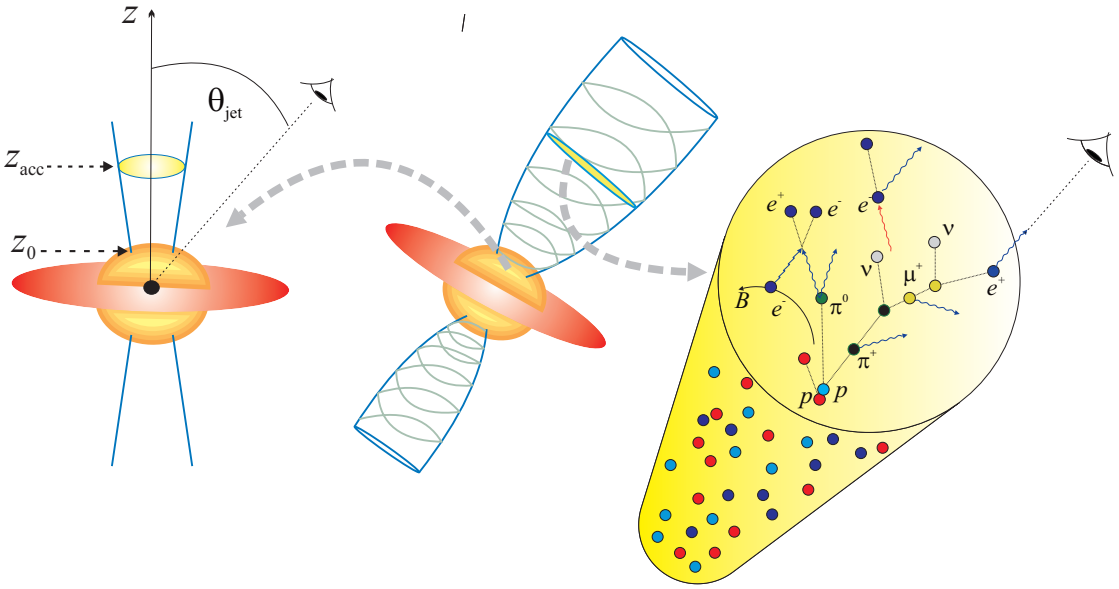

Figure 3.2: Sketch of the jet at different spatial scales.

power is shared between protons and electrons, $L_{\rm rel} = L_e + L_p$, with $L_p = aL_e$ and $a \geq 1$, since we are interested in jets with a high content of relativistic protons.

The steady-state distribution of relativistic particles depends on the injection spectrum, on the cooling processes (radiative and non-radiative), and the rate of escape from the acceleration region (and the rate of decay for the unstable species). We calculate the particle distributions solving a simple version of the kinetic equation that takes all these effects into account.

The interaction of the primary protons and electrons with the thermal particles (through proton-proton inelastic collisions and relativistic Bremsstrahlung), photons (through proton-photon collisions and inverse Compton scattering), and magnetic field (through synchrotron radiation) in the jet produce electromagnetic radiation. Hadronic interactions also inject charged pions, muons, and electron-positron pairs. We calculate the steady-state energy distribution and the radiative spectrum of all these particles in the same manner as for primary protons and electrons.

The final product of our calculations are broadband spectral energy distributions, duly corrected by absorption. In the next chapters we present some general results and apply the model to reproduce the observational spectrum

of specific sources, also making predictions for their gamma-ray emission.

4

ONE-ZONE LEPTO-HADRONIC MODELS. II. APPLICATIONS

4.1 GENERAL MODELS

As an initial application of the model presented in the previous chapter, we explore the parameter space with the aim of studying the cooling of particles and to obtain some general spectral energy distributions. The values adopted for the basic parameters of the model are listed in Table 4.1.

The accretion power is $L_{\rm accr} = \dot{M}c^2 \approx 1.7 \times 10^{39}$ erg s^{-1}; this corresponds to a mass accretion rate $\dot{M} = 3 \times 10^{-8} M_\odot$ yr^{-1}, as estimated by Markoff et al. (2001) for the low-mass microquasar XTE J1118+480. A fraction $q_{\rm jet} = 0.1$ of the accretion power goes to the outflows. The jets are injected at a distance $z_0 = 50 R_{\rm schw}$ from the black hole, with an initial radius $r_0 = 0.1 z_0$. The value of the magnetic field at z_0 is high, $B_0 = 2 \times 10^7$ G.

We assume that the acceleration region is located close to the base of the jet, so $z_{\rm acc} = z_0$. It extends up to $z_{\rm max} = 5 z_{\rm acc}$. The magnetic energy density in this region is in equipartition with respect to the bulk kinetic energy density, so the constraint in Eq. (3.16) is not fulfilled. Particle acceleration through a Fermi-like mechanism, however, may still take place under these conditions although likely not mediated by diffusion through shock fronts but by magnetic reconnection events, see e.g. de Gouveia Dal Pino et al. (2010) and Kowal et al. (2011). This process also leads to a power-law energy distribution of particles at injection.

In the acceleration region, a fraction $q_{\rm rel} = 0.1$ of the jet power is transferred

to relativistic particles. We consider several values for the proton-to-lepton power ratio and the acceleration efficiency, $a = 1 - 10^3$ and $\eta = 10^{-4} - 10^{-1}$, respectively. The injection function for primary particles is given by Eq. (3.17) with $\beta = 1$ and $\alpha = 1.5$ (*hard* injection) or $\alpha = 2.2$ (*soft* injection). Values of the spectral index in the range $\alpha = 2.0 - 2.2$ are predicted by the theory of acceleration in strong (with high Mach number), non-relativistic shocks (e.g. Drury 1983). Spectral indices $\alpha \approx 1.5$ or harder may arise as a result of diffusive acceleration mediated by relativistic shocks (e.g. Stecker et al. 2007, Summerlin & Baring 2012). As it has been shown by Drury (2012), hard particle injection spectra (as hard as $\alpha \sim 1$ for a test particle) may also be produced by a Fermi-like acceleration mechanism at magnetic reconnection sites.

Table 4.1: Values of the parameters for some general models.

Parameter	Symbol	Value
Mass of the black hole	$M_{\rm BH}$	$8 M_\odot$
Accretion power	$L_{\rm accr}$	1.7×10^{39} erg s^{-1} [(1)]
Disk-jet coupling constant	$q_{\rm jet}$	0.1
Jet bulk Lorentz factor	$\Gamma_{\rm jet}$	1.5
Viewing angle	$\theta_{\rm jet}$	30°
Base of the acceleration region	$z_{\rm acc}$	1.18×10^8 cm
End of the acceleration region	$z_{\rm max}$	$5\, z_{\rm acc}$
Magnetic field at z_0	B_0	2×10^7 G
Magnetic field decay index	m	1
Fraction of jet power in relativistic particles	$q_{\rm rel}$	0.1
Hadron-to-lepton power ratio	a	$1 - 10^3$
Particle injection spectral index	α	1.5/2.2
Acceleration efficiency	η	$10^{-4} - 0.1$
Minimum energy of primary particles	$E^{\rm min}_{(p,e)}$	$2 - 100\ m_{(p,e)}c^2$

[(1)] Typical value for the LMMQ XTE J1118+480 in outburst (Markoff et al. 2001).

We do not take into account neither the cooling nor the radiative contribution of pions and muons, but we do include that of electron-positron pairs created in proton-photon collisions. The injection function of pairs directly created in photopair interactions is given by Eq. (3.102). Since the energy losses of pions and muons are ignored, for the injection of pairs in photomeson inter-

actions we use Eq. (3.88).

Figure 4.1 shows the cooling rates for protons and electrons at the base of the jet for a set of representative parameters. The main cooling channel for electrons is always synchrotron radiation; for protons, adiabatic losses dominate at low energies and synchrotron losses above ~ 100 TeV. For comparison, we plot the cooling rates for $a = 1$ (equal power in protons and electrons) and $a = 10^3$ (proton-dominated case). Notice that the proton-photon and the IC cooling rates increase as a decreases, because the target photon field - the synchrotron field of electrons - is more dense.

The maximum energies are fixed by the balance of the acceleration and cooling rates, without any constraint due to the size of the acceleration region. Depending on the value of η, the maximum energy of electrons is in the range 100 MeV - 5 GeV, and that of protons approximately between 5×10^{14} eV and 10^{16} eV. As it can be seen from Figure 4.2, which shows the evolution of $E^{\max}(z)$, particles cool rapidly after leaving the acceleration region.

Figure 4.3 shows the energy distributions of protons and electrons in a model with $a = 1$, $\eta = 0.1$, and $\alpha = 2.2$. Synchrotron losses are absolutely dominant for electrons. Since $t_{\rm sy}^{-1} \propto E$, the spectral index of the electron distribution is softer than that of the injection function: $N_e \propto E_e^{-(\alpha+1)}$ as predicted by Eq. (3.39). The adiabatic cooling rate does not depend on energy, so the proton distribution repeats the behaviour of the injection function, $N_e \propto E_p^{-\alpha}$. Notice that, strictly, for $\eta = 1$ adiabatic losses dominate over synchrotron losses for $E_p \lesssim 10^3$ TeV. A change in the slope of the distribution from α to $\alpha + 1$ occurs around this energy, but it is hardly noticeable in Figure 4.3 because the break energy is very near the cutoff.

Figures 4.4 and 4.5 show the spectral energy distributions calculated for different values of the model parameters. In Figure 4.4 the spectral index of the injection function has the canonical value $\alpha = 2.2$, whereas in Figure 4.5 we consider a harder injection with $\alpha = 1.5$. For each case, we show four representative spectra obtained by varying the value of the remaining parameters within a physically reasonable range. The main contributions to the SEDs are always due to synchrotron radiation of leptons and protons. The relative importance of each contribution depends on the value of the ratio $a = L_p/L_e$. The proton synchrotron spectra are hardly affected by changes in a, peak-

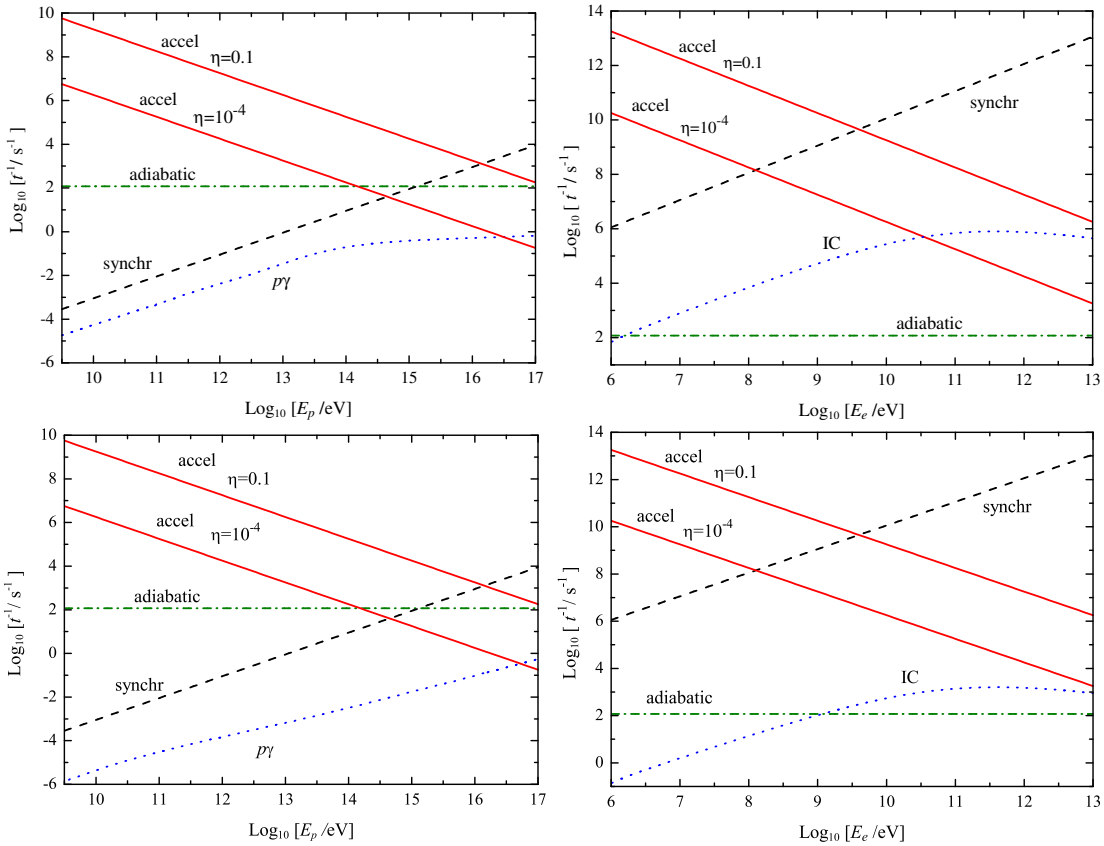

Figure 4.1: Acceleration and cooling rates at the base of the jet for protons (left) and electrons (right), for $\alpha = 2.2$, $a = 1$ (top) and $a = 10^3$ (bottom). The proton-photon ($p\gamma$) cooling rate is the sum of the photomeson and photopair cooling rates.

ing at $\sim 10^{35-36}$ erg s^{-1} for $E_\gamma \sim 10^{8-9}$ eV; electron synchrotron luminosities range from $\sim 10^{34}$ erg s^{-1} for a completely proton-dominated jet ($a = 10^3$) to $\sim 10^{37}$ erg s^{-1} in the case of equipartition ($a = 1$). In fact, synchrotron energy losses are so strong that the electrons radiate almost all their available energy budget.

The efficiency of the acceleration η fixes the maximum particle energy and therefore has a direct effect on the high-energy cutoff of the SEDs. Synchrotron spectra extend up to $E_\gamma \sim 10^{12}$ eV in the case of protons, and up to $E_\gamma \sim 10^9$ eV in the case of leptons, for $\eta = 0.1$; when a poor acceleration efficiency $\eta = 10^{-4}$ is considered, only energies of about three orders of magnitude smaller are reached. In the same way, modifying the minimum particle energy accordingly changes the low-energy cutoff of the spectra.

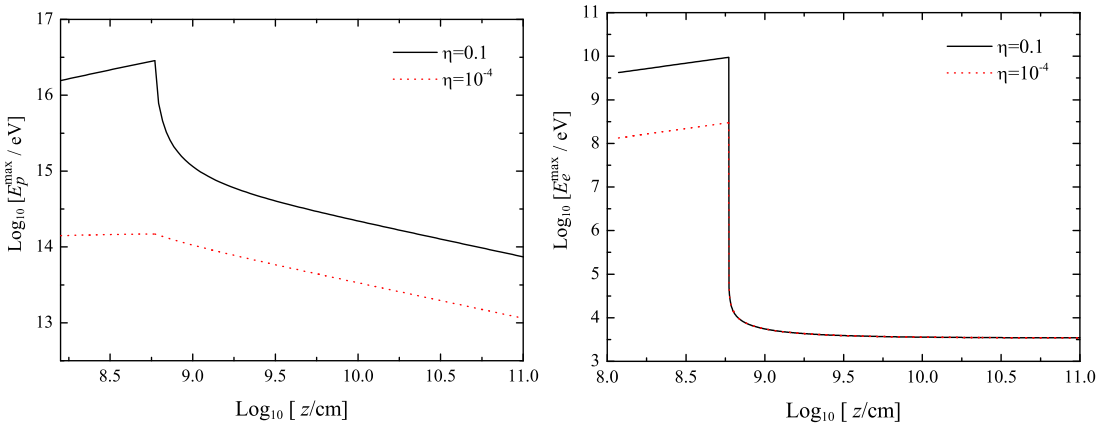

Figure 4.2: Evolution of the maximum kinetic energy of protons (left panel) and electrons (right panel) with the distance z to the compact object. Outside the acceleration region particles cool rapidly due to adiabatic and synchrotron losses.

The IC contribution is always negligible, and for $a > 1$ IC luminosities are below $\sim 10^{30}$ erg s^{-1} as the leptonic content of the jet is reduced. The gamma-ray luminosity due to the decay of neutral pions created in proton-photon collisions yields a very hard energy tail to the SEDs, peaking at energies $E_\gamma \sim 10^{14-15}$ eV. The peak value of this component is sensitive to a, since the target photons for $p\gamma$ collisions are provided by the electron synchrotron radiation field. Luminosities as large as 10^{35-36} erg s^{-1} can be reached at very high energies. Synchrotron radiation from electron-positron pairs produced in $p\gamma$ interactions can be important in those models with relatively low hadronic content, as it can be seen from the different SEDs in Figures 4.4 and 4.5. In general, these contributions have luminosities not too different from those obtained from the decay of neutral pions, but they cover a lower energy range.

Internal photon-photon absorption might be important in some of the models. In particular, TeV gamma rays can be efficiently absorbed by infrared synchrotron photons. This might initiate an electromagnetic cascade in the emission region in those cases where there are significant photon fields at low energies, as it may happen in blazars (e.g. Blandford & Levinson 1995). In microquasars, however, a strong magnetic field can quench a pure IC cascade. This is because the synchrotron losses for the first few generations of pairs are so strong, that they cannot produce photons energetic enough to sustain the electromagnetic avalanche (Khangulyan et al. 2008, Pellizza et al. 2010).

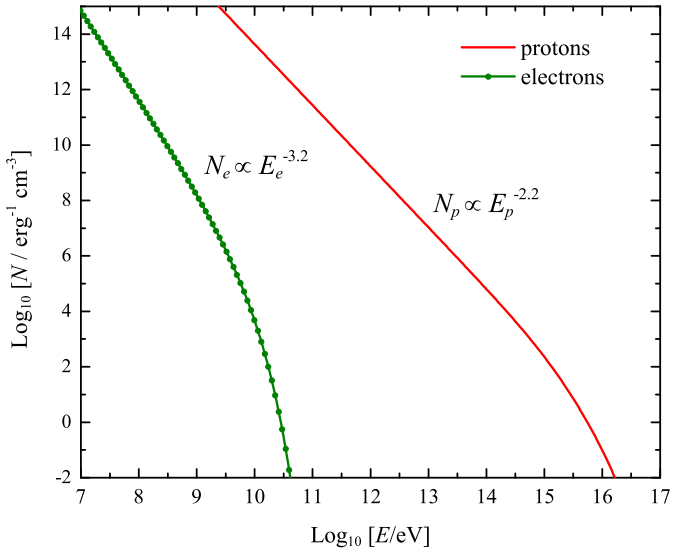

Figure 4.3: Energy distributions of primary particles at the base of the jet, for $a = 1$, $\eta = 0.1$, and $\alpha = 2.2$. The proton distribution keeps the spectral index of the injection function, but the electron distribution is softer due to the strong synchrotron losses.

The photon absorption, nonetheless, might change the gamma-ray spectrum depending on the specific model. This, in turn, can yield a variety of slopes in the spectra observed by *Fermi*, *AGILE*, or other instruments sensitive in the MeV-GeV energy range (see, e.g., Aharonian et al. 2008 for a discussion in the context of extragalactic jets).

We calculate the attenuation factor $\exp(-\tau_{\gamma\gamma})$ for a photon emitted at the base of the acceleration region at an angle $\theta_{\rm jet}$ with the line of sight, in the different models presented above. The target photon field is the synchrotron photon field of primary electrons. Some results are shown in Figure 4.6. In all cases with significant leptonic synchrotron emission, the radiation is completely suppressed above 10 GeV.[1] For proton-dominated models, which are characterized by a prominent proton synchrotron peak, the attenuation is quite moderate.

In Figure 4.7 we present two spectral energy distributions modified by the effects of photon-photon absorption. The top panel corresponds to a case with strong attenuation ($a = 1$). The internal opacity to gamma-ray propagation results in a significant softening of the spectrum between ~ 10 MeV and ~ 10 GeV, with a cutoff beyond the latter energy. This is consistent with the

[1]Notice, however, that neutrino propagation is not affected by absorption effects.

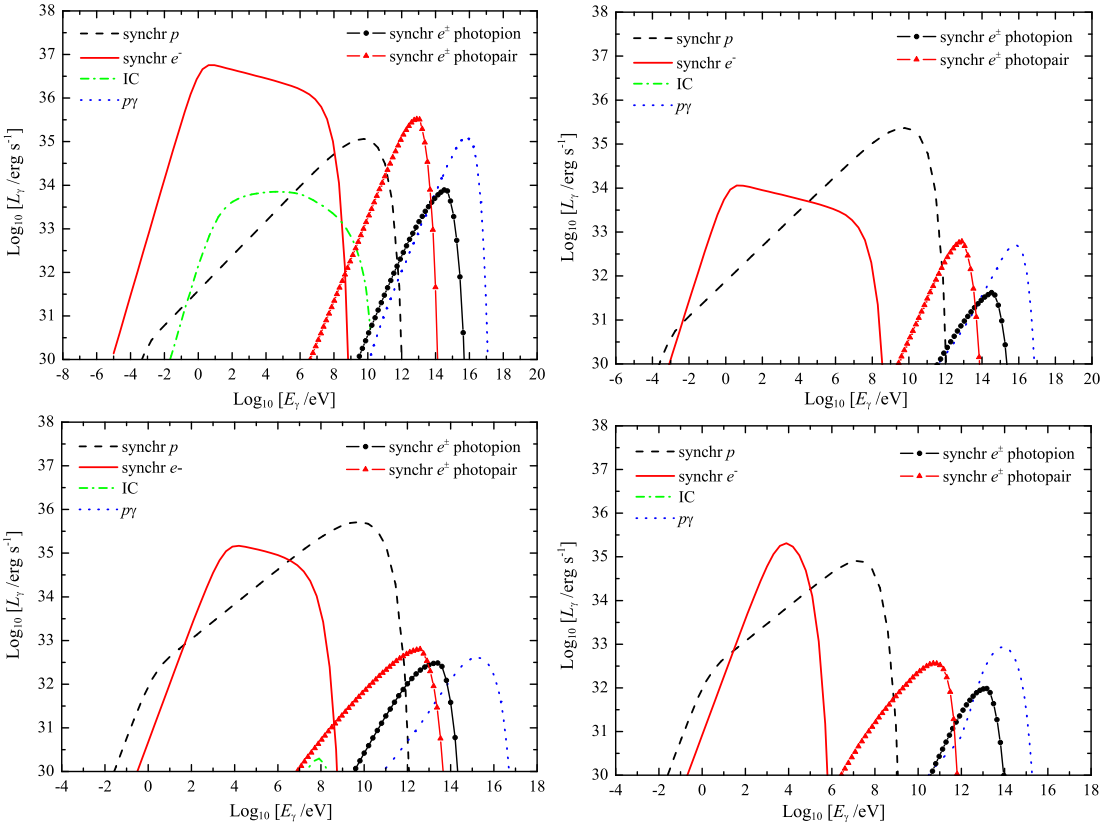

Figure 4.4: Spectral energy distributions for different values of the parameters in the case of a particle injection index $\alpha = 2.2$. Top left: $E^{\rm min} = 2mc^2$, $\eta = 0.1$, $a = 1$. Top right: $E^{\rm min} = 2mc^2$, $\eta = 0.1$, $a = 10^3$. Bottom left: $E^{\rm min} = 100mc^2$, $\eta = 0.1$, $a = 100$. Bottom right: $E^{\rm min} = 100mc^2$, $\eta = 10^{-4}$, $a = 100$.

type of very soft spectra observed by *EGRET* in some variable halo sources (e.g. Thompson et al. 2000, Grenier 2001, Romero et al. 2004). In the bottom panel of the same figure, we show the SED for a proton-dominated microquasar, which is basically not modified by absorption effects.

In all cases, the emission at TeV energies is either suppressed or relatively weak. The detection of these sources with current Cherenkov telescopes appears possible for nearby objects (∼2-6 kpc), see Figure 4.7, or if very high acceleration efficiencies could be achieved in proton-dominated cases.[2]

From our results it is clear that proton low-mass microquasars can be sig-

[2] A high acceleration efficiency would move the high-energy cutoff of the synchrotron peak into the TeV regime.

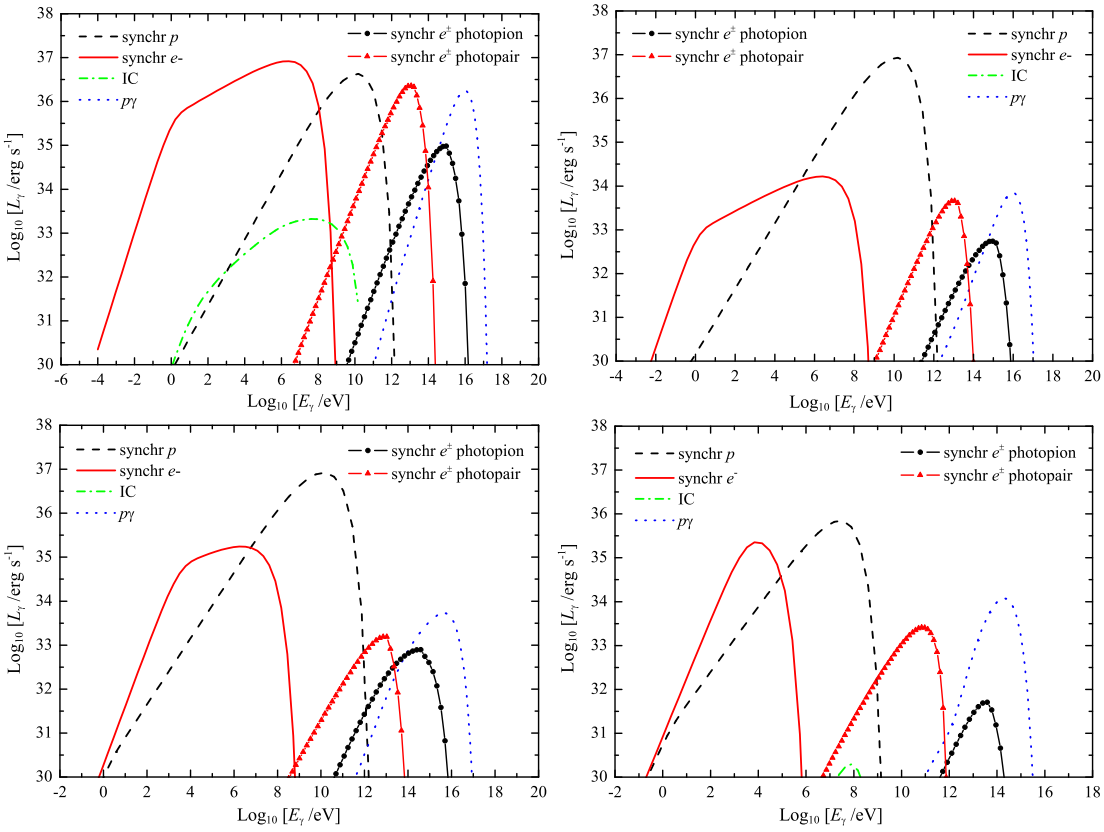

Figure 4.5: Spectral energy distributions obtained for different values of the parameters in the case of a particle injection index $\alpha = 1.5$. Top left: $E^{\min} = 2mc^2$, $\eta = 0.1$, $a = 1$. Top right: $E^{\min} = 2mc^2$, $\eta = 0.1$, $a = 10^3$. Bottom left: $E^{\min} = 100mc^2$, $\eta = 0.1$, $a = 100$. Bottom right: $E^{\min} = 100mc^2$, $\eta = 10^{-4}$, $a = 100$.

nificant gamma-ray sources in the MeV-GeV range, and perhaps in some cases even at TeV energies. According to the ratio a of primary protons to leptons, we obtain different types of low-energy counterparts. Such counterparts range from sources with radio luminosities of $10^{29} - 10^{30}$ erg s^{-1} and strong X-ray emission (e.g. the model shown in the left upper panel of Figure 4.5), up to sources with weak luminosities dominated by proton synchrotron emission between 100 MeV and 100 GeV (e.g. the model shown in the right upper panel of Figure 4.5). The satellites *Fermi* and *AGILE*, with energy windows in the range 100 MeV $-$ 300 GeV and 30 MeV $-$ 50 GeV, respectively, are especially suitable for the detection of these objects. Actually, we suggest that many of the unidentified *EGRET* sources detected off the galactic plane around the galac-

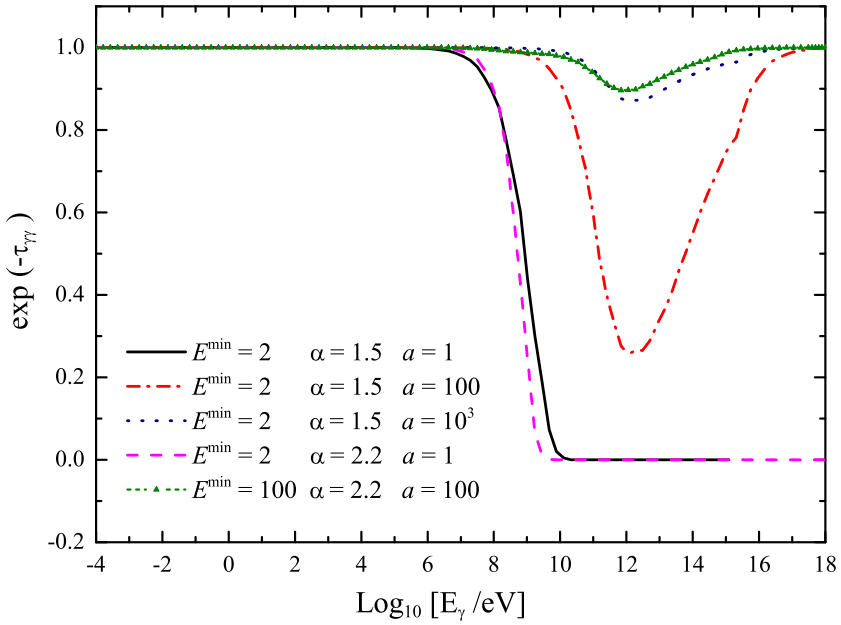

Figure 4.6: Attenuation factor for a photon emitted at $z = z_{\rm acc}$ at an angle $\theta_{\rm jet}$ with the line of sight, for different models of a proton microquasar. In all cases the acceleration efficiency is $\eta = 0.1$, and the minimum particle energy is indicated in units of the rest mass.

tic center, might be proton microquasars. Variability, one of the outstanding properties of these sources (Nolan et al. 2003), can be easily introduced in our model through a variable accretion rate, precessing jets, or internal shocks (in this latter case, there would be very rapid variability, superposed to longer variations with timescales from hours to days). Low-threshold, ground-based gamma-ray Cherenkov telescope arrays like HESS II, MAGIC II, or the future CTA, could also detect hadronic LMMQs at $E \geq 100$ GeV. In particular, the tail of the proton synchrotron peak from models with large values of a might be detectable, displaying a soft spectra. So, observations of LMMQs with Cherenkov telescopes can be useful to constrain the parameter a.

An additional prediction of our model is the production of high-energy ($E > 1$ TeV) neutrinos, with luminosities in the range $10^{33} - 10^{35}$ erg s^{-1}. In the cases of the highest luminosities, if the microquasar is located not too far away (say, around 2 kpc as it is the case of XTE J1118+480) the expected flux could be similar to those estimated for HMMQs (e.g. Levinson & Waxman 2001, Romero et al. 2003, Christiansen et al. 2006, Aharonian et al. 2006b). We notice

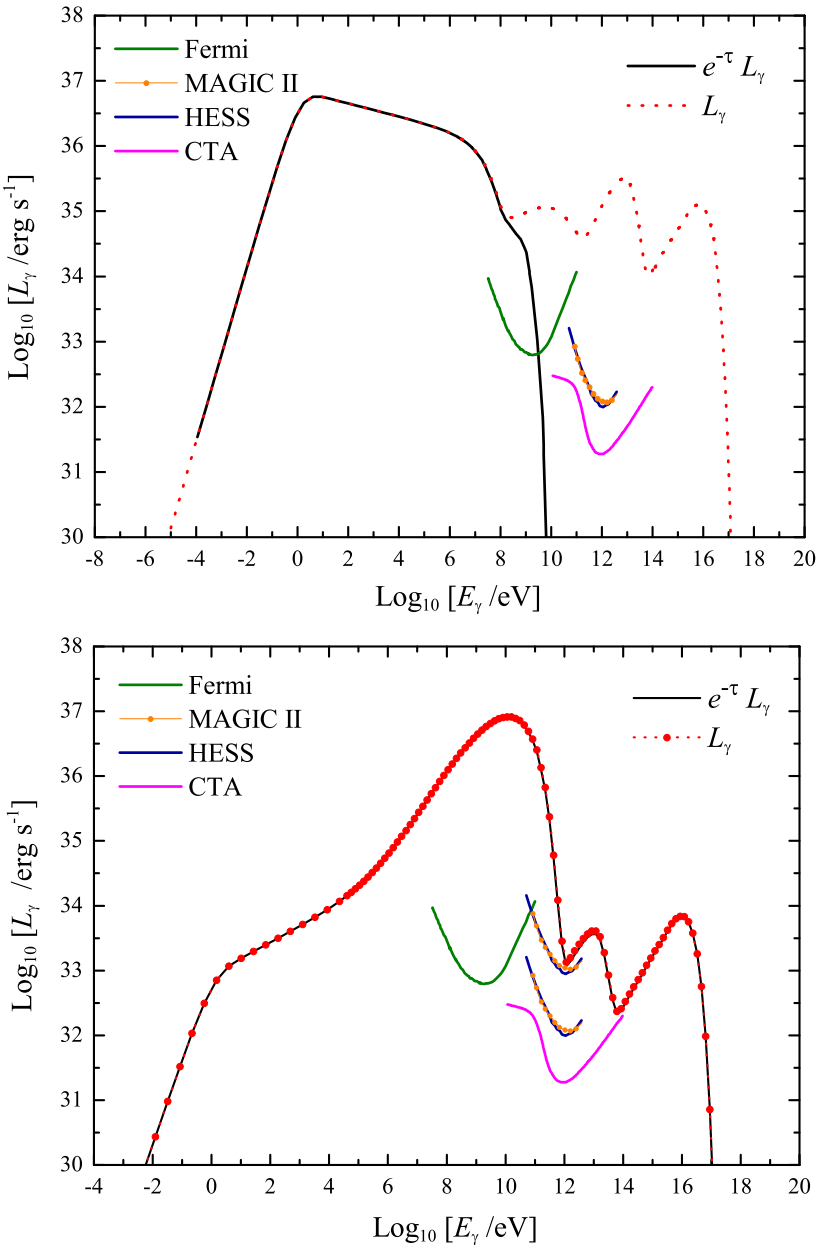

Figure 4.7: Spectral energy distributions attenuated by internal absorption in two different jet models with $E^{\mathrm{min}} = 2mc^2$ and $\eta = 0.1$. Top panel: $\alpha = 2.2$ and $a = 1$. Bottom panel: $\alpha = 1.5$ and $a = 10^3$. In the case $a = 1$ the emission above ~ 10 GeV is completely suppressed. On the contrary, for $a = 10^3$ the production SED is basically unmodified. The sensitivities of *Fermi* (5σ, one-year sky survey exposure), HESS (5σ, 50 h exposure), MAGIC II (50 h exposure), and the predicted for CTA (50 h exposure) are indicated. In the bottom panel, the HESS and MAGIC II sensitivity curves are plotted for sources at 2 kpc (higher sensitivity) and 6 kpc (lower sensitivity).

that heavily absorbed sources are precisely those with the highest neutrino luminosities, so a correlation between gamma-ray and neutrino fluxes should not necessarily be expected.

4.2 ON THE NATURE OF THE AGILE TRANSIENT GALACTIC SOURCES

The Gamma-Ray Imaging Detector (GRID) aboard the satellite *AGILE* has detected several non-identified variable sources likely of galactic origin (Pittori et al. 2009). These include the strong source 1AGL J2022+4032 (formerly AGL J2021+4029) located in the Cygnus region, with the center of gravity of the error box at $l = 78.37^\circ$ and $b = 2.04^\circ$ (Longo et al. 2008), the variable source 1AGL J1412-6149 in the Musca region (error box centered at $l = 312.3^\circ$ and $b = -0.43^\circ$; Pittori et al. 2008), and the high galactic latitude transient AGL J0229+2054, with the error box centered at $l = 151.7^\circ$ and $b = -36.4^\circ$ (Bulgarelli et al. 2008).[3]

1AGL J2022+4032 showed some significant re-brightening after its discovery (Chen et al. 2008, Giuliani et al. 2008, Tavani et al. 2008). Simultaneous X-ray observations with the instrument SuperAGILE did not show any counterpart in the 20-60 keV band. A steady and weak source was detected within the large error box by *Swift*/BAT (15-55 keV, see Ajello et al. 2008), but there is no clear relationship. Additional X-ray observations have been performed with *XMM-Newton*, without adding new clues (Pandel et al. 2008). Radio observations with the Very Large Array have shown no clear counterpart (Cheung 2008a,b), either. VERITAS detected no emission above 300 GeV after 7 hours of exposure in 2009 (Hui 2010), supporting the hypothesis of the transient nature of the source.

Concerning 1AGL J1412-6149, a potential archival X-ray counterpart has been claimed on the basis of *BeppoSAX* observations dating from January 2001 (Orlandini et al. 2008). Also a high-mass pulsar X-ray binary, MAXI J1409-619, is located within the *AGILE* error box of 1AGL J1412-6149 (see Orlandini et al. 2012 and references therein).

[3]For 1AGL J2022+4032 and 1AGL J1412-6149, the coordinates of the center of the error box have been updated to the values reported in the First *AGILE* catalogue of high-confidence gamma-ray sources (Pittori et al. 2009).

The gamma-ray transient AGL J0229+2054 might be a halo galactic source or a blazar (the AGN 1ES 0229+200 is at 61.3 arcmin from the GRID error box centroid). There is also a radio source, CRATES J023030+211241, within the *AGILE* error box. No follow-up of the *AGILE* observation of this source is reported in the literature, except for a negative detection at X-ray energies (2-10 keV) with the *Rossi X-ray Timing Explorer* (*RXTE*) (Markwardt & Swank 2008). AGL J0229+2054 is not included in the First *AGILE* catalogue of high-confidence gamma-ray sources (Pittori et al. 2009).

The fact that these sources are highly variable implies that the high-energy radiation should be produced in a compact region. The absence of detection with SuperAGILE means that the ratio of gamma-ray to X-ray luminosities should be $L_\gamma / L_X \gg 1$. These characteristics recall those of the population of variable *EGRET* sources found in the galactic plane and in the galactic halo (Romero 2001, Grenier 2001, 2004, Nolan et al. 2003). Actually, the *AGILE* detections in the Cygnus region and the Musca region partially overlap with the location error box of the sources 3EG J2020+4017 and 3EG J1410-6147, respectively. It has been proposed that the unidentified variable gamma-ray sources sources at MeV-GeV energies might be high-mass microquasars with the emission dominated by inverse Compton up-scattering of UV stellar photons from the hot donor star (Kaufman Bernadó et al. 2002, Bosch-Ramon et al. 2005). The donor star on the galactic plane could be strongly obscured, rendering difficult its detection. These models, however, predict a significant production of X-rays, something that is at odds with the new *AGILE*/GRID and SuperAgile observations. Grenier et al. (2005) proposed that the variable high-latitude unidentified sources might be old, low-mass microquasars expelled long ago from the galactic plane or from globular clusters (see Mirabel et al. 2001). They also showed that external Compton models cannot account for the energetics required by the observations. As we have shown in Section 4.1, "proton" microquasars with low-mass donor stars might explain the halo *EGRET* sources through proton synchrotron radiation and photomeson production.

In what follows we explore the possibility that microquasars with proton-dominated jets can produce spectral energy distributions that satisfy all the constraints imposed by the *AGILE* observations. The model is the same as for the general applications presented in Section 4.1, but now we include proton-

proton interactions and the cooling and radiative contribution of pions and muons.

The values of the characteristic parameters of the jet are listed in Table 4.2. The jet power is $L_{\rm jet} = 10^{37}$ erg s^{-1}; a 10% of this power is transferred to the relativistic particles. As before, the acceleration region is thin and located at the base of the jet.

Table 4.2: Values of the parameters for a microquasar model of the *AGILE* transient sources.

Parameter	Symbol	Value
Mass of the black hole	$M_{\rm BH}$	$10 M_\odot$
Jet power	$L_{\rm jet}$	1×10^{37} erg s^{-1}
Jet bulk Lorentz factor	$\Gamma_{\rm jet}$	1.5
Viewing angle	$\theta_{\rm jet}$	30°
Base of the acceleration region	$z_{\rm acc}$	7.5×10^7 cm$^{(*)}$
End of the acceleration region	$z_{\rm max}$	$5\, z_{\rm acc}$
Magnetic field at z_0	B_0	8×10^6 G
Magnetic field decay index	m	1
Jet content of relativistic particles	$q_{\rm rel}$	0.1
Hadron-to-lepton power ratio	a	10^3
Particle injection spectral index	α	1.5
Acceleration efficiency	η	$0.01 - 0.1$
Minimum energy primary particles	$E^{\rm min}_{(p,e)}$	$2 m_{(p,e)} c^2$

$^{(*)}$ $z_{\rm acc} = z_0 = 50 R_{\rm grav}$.

The magnetic field in the acceleration region is high, $B_0 \approx 10^7$ G. This produces the immediate cooling of primary electrons and significant cooling of protons. In Figures 4.8 and 4.9 we show the cooling rates for both primary electrons and protons at the base of the acceleration region, as well as the cooling and decay rates of secondary muons and pions in the jet frame. The maximum energies of the primary particles are obtained equating the cooling rates and the acceleration rate. For comparison, we adopt two different values for the acceleration efficiency, $\eta = 0.1$ and $\eta = 0.01$. We see that electrons, even for such a high acceleration efficiency, reach only energies below 10 GeV, whereas protons can attain much higher energies, well into the PeV band.

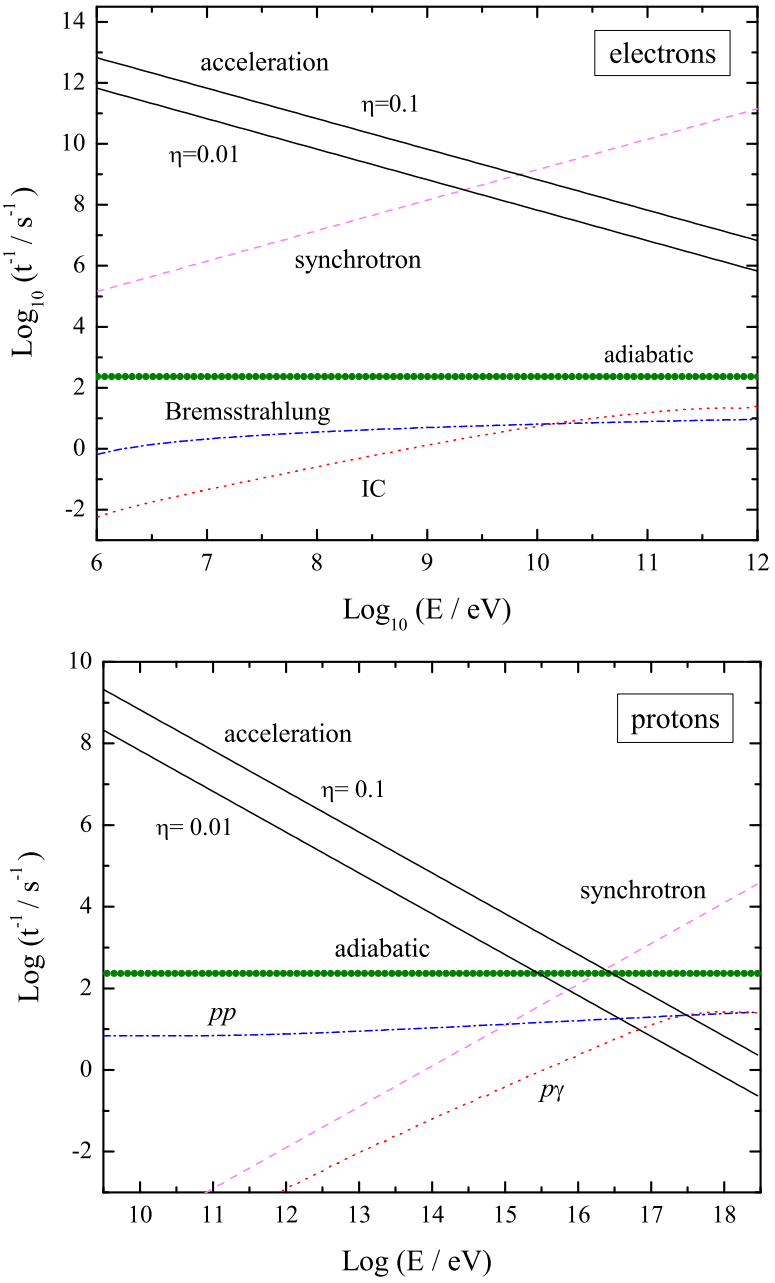

Figure 4.8: Acceleration and cooling rates at the base of the jet for primary protons and electrons in a proton-dominated microquasar model for the *AGILE* transient sources, calculated for $a = 1000$ and $\alpha = 1.5$. The value of the magnetic field is $B_0 = 8 \times 10^6$ G and the acceleration efficiency η is indicated.

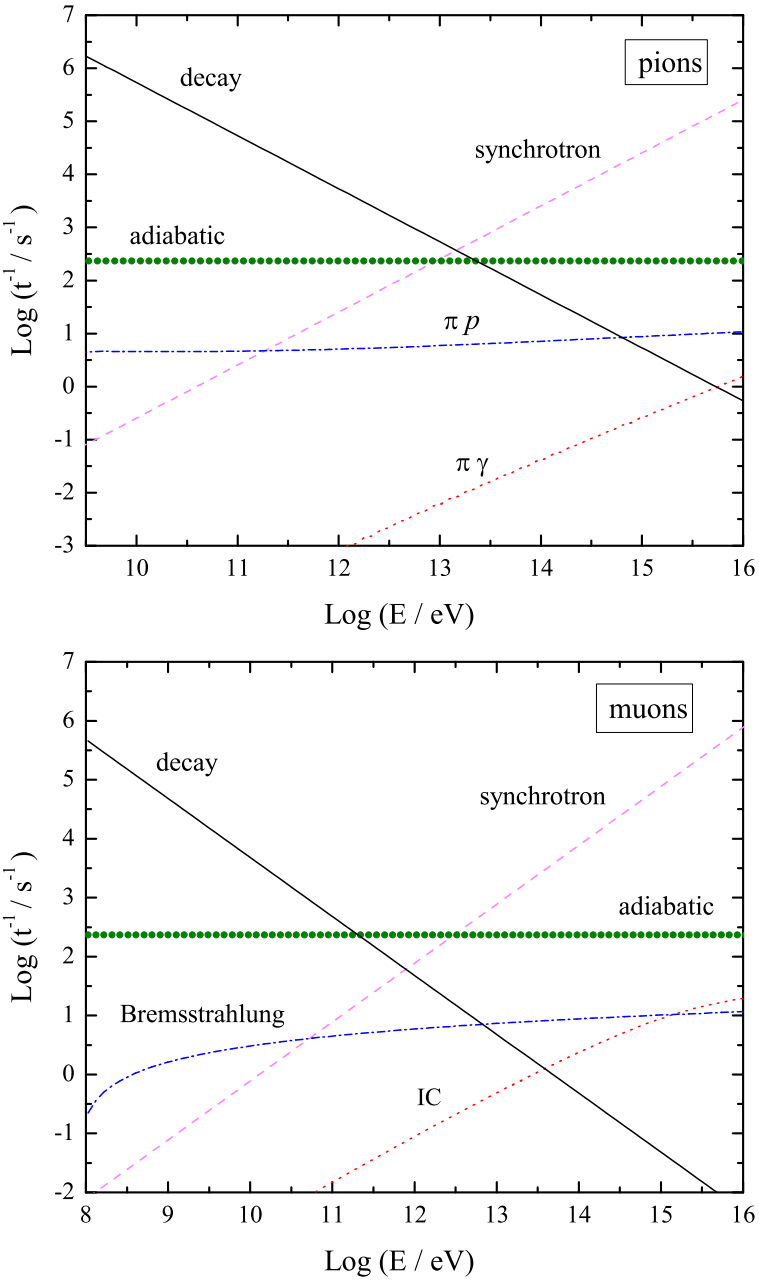

Figure 4.9: Acceleration, cooling, and decay rates at the base of the jet for secondary pions and muons in a proton-dominated microquasar model for the *AGILE* transient sources, calculated for $a = 1000$ and $\alpha = 1.5$. The value of the magnetic field is $B_0 = 8 \times 10^6$ G.

The calculated total luminosity of the jet includes the contributions of synchrotron emission from all types of primary and secondary particles, IC emission from all leptons in the electron synchrotron radiation field of the emission region, photopair and photomeson production by both protons and pions, inelastic collisions between relativistic protons in the jet and the cold material that forms most of the same outflow, and relativistic Bremsstrahlung from electrons and muons.

Figure 4.10 shows the spectral energy distribution calculated for a proton dominated jet with $a = 1000$ and a hard particle injection function with spectral index $\alpha = 1.5$. We show the different contributions from all significant cooling processes for primary and secondary particles, in the case of two different acceleration efficiencies $\eta = 0.1$ (top panel) and $\eta = 0.01$ (bottom panel). Synchrotron radiation is the dominant cooling channel for leptons; Bremsstrahlung and IC losses are negligible. In both cases the peak of the SED is determined by proton synchrotron radiation, followed by pion synchrotron emission. For the higher efficiency the synchrotron peak is sharper, reaching almost 10^{35} erg s^{-1}. In the case of a lower efficiency, the peak is slightly above 10^{34} erg s^{-1}. In the first case most of the emission is concentrated in the range $10^8 - 10^{12}$ eV, whereas in the second it is between 10^8 and 10^{10} eV, with a soft slope beyond 10^9 eV. In both cases there is a high ratio L_γ / L_X, in accordance with what is inferred from *AGILE* observations. Soft X-rays, due mainly to electron synchrotron radiation, are at the level of 10^{32} erg s^{-1}. The hard X-ray component is dominated by muon synchrotron emission. Contrary to models with equipartition ($a = 1$) in relativistic particles, photomeson production is not significant in strongly proton-dominated jets, since the synchrotron field is relatively weak. Internal photon absorption and the injection of secondary pairs through photon-photon annihilation are also negligible for the same reason.

The quoted luminosities correspond to the flux reported by *AGILE* and the upper X-ray limits of SuperAGILE, for a source at a distance of the order of $\sim 0.3 - 0.4$ kpc. An accurate determination of the distance can be used to constrain the energy budget of the jets. Depending on the position of the cutoff of the proton synchrotron luminosity, sources with these characteristics would be easily detected with a very soft spectrum at TeV energies by HESS, MAGIC II, or CTA.

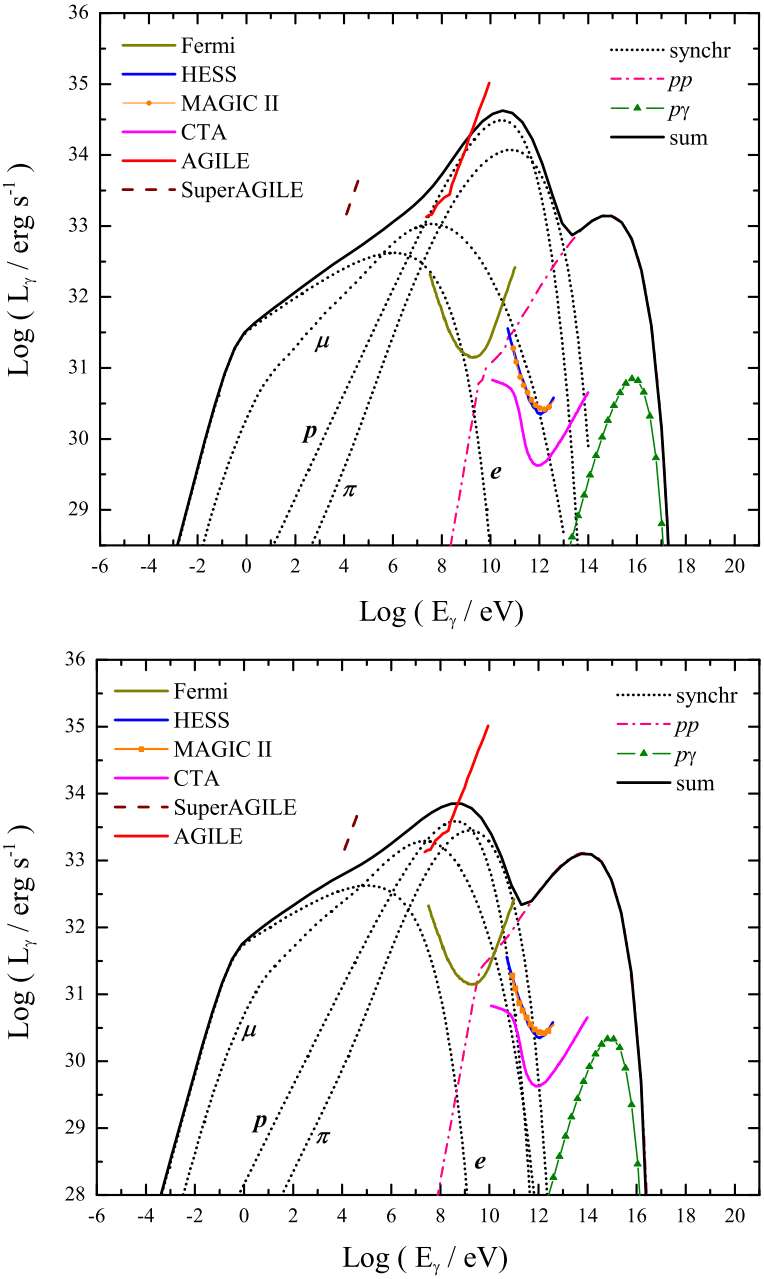

Figure 4.10: Spectral energy distributions in a proton-dominated microquasar model ($a = 1000$) for the *AGILE* transient sources. Each panel corresponds to a different acceleration efficiency ($\eta = 0.1$ on the top, $\eta = 0.01$ on the bottom). The integral sensitivities for a source at 0.3 kpc of *Fermi* (5σ, one-year sky survey exposure), *AGILE*/GRID (2 d exposure), SuperAGILE (2 d exposure), HESS (5σ, 50 h exposure), MAGIC II (50 h exposure), and the expected for CTA (50 h exposure) are indicated.

A crucial feature of a synchrotron proton-dominated jet is that a very strong magnetic field is necessary to produce detectable radiation in gamma rays. This means that the acceleration region should be located very close to the compact object (at $\sim 10^8$ cm in our models). Intrinsic absorption is then not very important since the low energy fields, which are responsible for the opacity to gamma-ray propagation, are weak. In models with a high content of primary electrons these effects, at the base of the jet, are very significant leading to a complete suppression of all emission above $\sim$ 100 GeV, as seen in Section 4.1. Such models produce a huge amount of X-rays, something that is not observed in the unidentified MeV-GeV sources.

We introduce a hard injection spectrum in order to achieve a strong contrast between leptonic and hadronic peaks. A softer injection would reduce the L_γ / L_X ratio. We notice that the losses in the high magnetic field strongly affect the overall leptonic particle spectrum. Observations with the LAT instrument of the *Fermi* satellite may allow to determine the photon spectrum of these sources in the range 100 MeV $-$ 100 GeV.

In summary, we propose that lepto-hadronic jets from nearby low-mass microquasars can explain the unidentified variable *AGILE* sources. This model assumes a strong component of relativistic primary protons and takes into account all radiative processes that might occur at the base of the jets. The predicted SEDs are in accordance with what we know about these objects. The jet model is independent of the nature of the donor star, so it could explain both low- and high-latitude galactic sources.[4] *Fermi* observations will allow us to better constrain the spectral features, then making it possible to infer more accurately the actual conditions in the sources.

POST SCRIPTUM Since we proposed the association of the *AGILE* source 1AGL J2022+4032 with a proton microquasar (Romero & Vila 2009), a gamma-ray pulsar, LAT PSR J2021+4026, was detected with *Fermi* inside the *AGILE* error box (Abdo et al. 2009a). Initially, the association between the two sources was considered highly unlikely by Chen et al. (2011), on the basis of a vari-

[4] Although in a high-mass binary the interaction of relativistic protons with the radiation field and the wind from the companion star may modify the high-energy region of the SEDs with respect to the results presented here.

ability analysis performed on the *AGILE* data. Gamma-ray emission variable on timescales from weeks to months in the range $100 - 400$ MeV had never been observed before in pulsars, and appeared difficult to be explained by theoretical models. Chen et al. (2011) favoured instead the model presented here. Shortly afterwards, however, gamma-ray flares (lasting from days to weeks) were observed for the first time in the Crab pulsar with *AGILE* and *Fermi* (Abdo et al. 2011, Tavani et al. 2011). The flares are not associated with the pulsed emission but with the emission of the pulsar wind nebula. No simultaneous variations in the X-ray flux were observed with SuperAGILE. These discoveries add support to the possible association between LAT PSR J2021+4026 and 1AGL J2022+4032. To the knowledge of the author of this thesis, however, there is no definite identification to date neither of 1AGL J2022+4032, nor of the other two *AGILE* sources considered here.

4.3 A MODEL FOR THE BROADBAND EMISSION OF THE MICROQUASAR GX 339-4

4.3.1 *Characterization of the source*

The low-mass microquasar GX 339-4 was discovered in 1972 by the satellite *OSO–7* (Markert et al. 1973). Since then, it has been extensively observed at all wavelengths from radio to X-rays and detected in all the canonical spectral states of X-ray binaries.

Little is known with certainty about the characteristics of the binary system. Based on modulations in the optical photometry, Callanan et al. (1992) inferred an orbital period of 14.8 h, later confirmed by Buxton & Vennes (2003). Optical spectroscopic measurements and the analysis of long-term X-ray light curves showed no evidence of this modulation, revealing instead a periodicity of $\sim$1.75 days (Hynes et al. 2003, Levine & Corbet 2006). The first estimates of the distance to GX 339-4 placed the system at $d \sim 1.3 - 4$ kpc, see Zdziarski et al. (1998) and references therein. This result was later revised by Zdziarski et al. (2004), who concluded that the minimum distance lay in the range 6.7 kpc $\leq d_{\rm min} \leq$ 9.4 kpc. They favoured a location in the galactic bulge at $\sim$ 8 kpc. A distance as large as $d > 15$ kpc, however, cannot be completely ruled out (Hynes et al. 2004).

The emission in the optical band is dominated by the accretion flow (Imamura et al. 1990), preventing direct observation of the secondary star even when the system is going through the very low X-ray luminosity state. The first detection of the companion star was made by Hynes et al. (2003) during an X-ray outburst in 2002. The mass and spectral type have not been firmly established yet. According to Hynes et al. (2004), an orbital period of $\sim$1.7 days implies a companion with a low density of ~ 0.06 g cm^{-3}. This may correspond to a low-mass subgiant of spectral type G or F, depending on the assumed distance. Muñoz-Darias et al. (2008) suggested that the star is in particular a "stripped-giant", in which mass loss is due to the burning of a Hydrogen shell. This model predicts that its mass is in the range $0.166M_\odot < M_2 < 1.1M_\odot$. The mass of the compact object is then constrained to be $M_{\rm BH} > 6M_\odot$ or even $M_{\rm BH} > 8.6M_\odot$, for a mass of the secondary near the lower or upper limit, respectively. These values strongly support the idea that the compact object is a black hole (see also Hynes et al. 2003).

GX 339-4 has been observed in radio, infrared, optical, and X-ray wavelengths, sometimes simultaneously or quasi–simultaneously (Hannikainen et al. 1998, Wilms et al. 1999, Nowak et al. 2002, Homan et al. 2005). The source goes through all the spectral states of X-ray binaries: low-hard, high-soft, very high, intermediate state, and quiescence. It frequently displays outbursts associated with state transitions, episodes during which the X-ray luminosity can reach peaks of $L_{\rm X} = 10^{37-38}$ erg s^{-1} for an assumed distance of 6 kpc (Homan et al. 2005, Yu et al. 2007). It was after the X-ray outburst of 2002 that Gallo et al. (2004) imaged for the first time a relativistic radio jet on $\sim 10^3$ AU scales in the system (see also Corbel et al. 2000). The detection of the jet confirmed that GX 339-4 is a microquasar.

There is some evidence supporting the presence of a hot corona in GX 339-4, in particular the possible detection of the Fe Kα line; see for example Dunn et al. (2008). Corbel et al. (2003), however, found that the radio and X-ray fluxes display a tight correlation of the form $F_{\rm R} \propto F_{\rm X}^{0.7}$. This suggests that the emission in both bands might have a common origin in synchrotron radiation produced by non-thermal electrons in the jet, and not in the corona (Corbel & Fender 2002, Corbel et al. 2003). This idea was explored by Markoff et al. (2003, 2005), who applied a purely leptonic jet model to fit the observations.

They showed that synchrotron radiation of relativistic electrons in the base of a jet can explain both the radio and X-ray spectra, and reproduce the observed correlation.

4.3.2 *Broadband observations and constraints on the model parameters*

We apply the lepto-hadronic, one-zone jet model presented in the previous chapter to fit the broadband electromagnetic spectrum of GX 339-4. As before, we take into account the cooling and radiative contribution of all species of secondary particles. We introduce some changes with respect to the model used to study the *AGILE* transient sources. Now we parameterize the jet power directly in terms of the Eddington accretion power as

$$L_{\rm jet} = \frac{1}{2} q_{\rm jet} L_{\rm Edd}, \tag{4.1}$$

where $L_{\rm Edd} \approx 1.3 \times 10^{38} (M_{\rm BH}/M_{\odot})$ erg s^{-1}. The factor $1/2$ accounts for the existence of a counterjet of equal power. We also consider different values m =1.2, 1.5, 1.8, and 2 for the decay index of the magnetic field, see Eq. (3.5).

The most important modification concerns the location of the acceleration region. Instead of placing it at the base of the jet, we determine $z_{\rm acc}$ demanding that the magnetic energy density is in sub-equipartition with respect to the bulk kinetic energy density or the matter internal energy density of the outflow; see Eqs. (3.9) to (3.16). Then, once a value for $\rho < 1$ is chosen, $z_{\rm acc}$ is calculated from the condition

$$U_{\rm B}(z_{\rm acc}) = \rho\, U_{\rm (k,m)}(z_{\rm acc}). \tag{4.2}$$

GX 339-4 was extensively observed simultaneously in radio and X-rays during the low-hard state in 1997, 1999, and 2002.[5] For some of these observations, simultaneous near infrared (NIR) and optical data are also available. The 1997 and 1999 radio observations were carried out with the Australia Telescope Compact Array (ATCA) and the Molonglo Observatory Synthesis Telescope

[5] A new outburst occurred in 2010. Simultaneous broadband data taken during this episode are presented, for example, in Cadolle Bel et al. (2010, 2011), and Gandhi et al. (2011). These data are not analysed here.

(MOST), and are described in detail in Corbel et al. (2000). The radio, NIR and optical data from 2002 are presented in Homan et al. (2005). The X-ray data were collected with *RXTE* and are compiled in Wilms et al. (1999), Nowak et al. (2002), Corbel et al. (2003), and Homan et al. (2005). We refer the reader to these works for model assumptions and other details of the data extraction in each case; no further data reductions were performed here.[6−7] Additional information on each particular data set is presented in Table 4.3.

Obs1, Obs2, and Obs5 in Table 4.3 correspond to the end of the low-hard state, when the source was highly luminous. Assuming a conservative value $d = 6$ kpc for the distance, the observed X-ray fluxes yield luminosities of up to $L_X \approx 10^{37}$ erg s^{-1}. This places some constraints on the value of the parameters that determine the energetics in our model. Only a small fraction of the jet power is carried by relativistic particles, otherwise the outflow could not be confined; we fixed $q_{\rm rel} = 0.1$ in Eq. (4.1). In a model with equipartition between hadrons and leptons ($a = 1$), half of this energy is given to relativistic electrons. If the observed X-ray flux is due to electron synchrotron radiation, this implies at least a total jet power $L_{\rm jet} \approx 2 \times 10^{38}$ erg s^{-1}. This is a significant fraction of the Eddington luminosity of a black hole of $M_{\rm BH} = 6M_\odot$, $L_{\rm Edd} \approx 7.8 \times 10^{38}$ erg s^{-1}. If part of the accretion power is radiated outside the jet and part advected onto the black hole, the accretion rate required to account for the observations must be very near the Eddington limit.

An accretion model that could apply to powerful sources or high luminosity states has been proposed by Bogovalov & Kelner (2005, 2010). They showed that, along with the standard thin disc solution of Shakura & Sunyaev (1973), there exists another accretion regime in which the accretion disc is radiatively very inefficient, even for high accretion rates. In this solution, known as the "dissipationless disc model", a magnetized plasma falls onto a central object. Angular momentum is removed from the system not by viscosity effects, but

[6]The data were extracted with the help of the ADS's Dexter Data Extraction Applet and a script prepared by the author.

[7]Calibration and data reduction algorithms have been updated since the data presented here were reduced. Reprocessing the data might result in changes in the slope of the X-ray spectrum. However, we do not intend to perform detailed fits to the spectrum but to show that the observations can be accounted for by a lepto-hadronic jet model, as an alternative to purely leptonic models. Using the same data allows to compare the results of our model with those of previous works.

Table 4.3: Broadband observations of the microquasar GX 339-4 in outburst, between 1997 and 2002.

Observation	Date (y/m/d)	X-ray flux (10^{-9} erg cm^{-2} s^{-1})			Radio flux (mJy)		
		3-9 keV	9-20 keV	20-200 keV	0.8 GHz	4.8 GHz	8.6 GHz
Obs1	1997/02/03	1.06	1.02	4.95	7.0	-	9.1
Obs2	1999/04/02	0.49	0.48	2.75	-	4.8	5.1
Obs3	1999/06/25	0.059	0.052	<0.29	-	0.14	0.34
Obs4	1999/08/28[a]	0.037	<0.01	<0.17	-	-	0.35
		X-ray flux (10^{-9} erg cm^{-2} s^{-1})	IR/optical magnitudes			Radio flux (mJy)	
		$3-300$ keV	m_H	m_I	m_V	4.8 GHz	
Obs5	2002/03/22	15.1	11.7	14.1	15.6	13.3	

[a] Radio data from 1999/09/01.

X-ray data were collected with the Proportional Counter Array (PCA) and High Energy X-ray Timing Experiment (HXTE) instruments of the satellite *RXTE*. The HXTE measurements are normalized to PCA flux levels. Optical and IR photometry was obtained with the Yale-AURA-Lisbon-Ohio State (YALO) telescope. The radio flux density at 0.8 GHz was obtained with MOST, and at 8.6 GHz and 4.8 GHz with ATCA. From Corbel et al. (2000), Nowak et al. (2002), Corbel et al. (2003), and Homan et al. (2005).

it is carried away by matter itself (see also the ADIOS model of Blandford & Begelman 1999 for early ideas regarding this accretion regime). In fact, the dissipationless disc model predicts that the mass advection rate vanishes at the position of the compact object, and so all the infalling matter is ejected. In this way, most of the accretion power could be directly channeled into the jets. This model could account for the observations of very powerful jets and low-luminosity discs in extreme systems such as SS 433 or M87. Other radiatively inefficient models, such as ADAFs and MDAFs, are more suitable for low accretion rates.

GX 339-4 was also detected during the low luminosity phase of the low-hard state in 1999 (Obs3 and Obs4). The X-ray luminosity is $L_X \approx 10^{34}$ erg s^{-1}. Applying the same energetic considerations as above, the minimum jet power required is now $L_{\rm jet} \approx 2 \times 10^{35}$ erg s^{-1}, a fraction $q_{\rm jet} \approx 3 \times 10^{-4}$ of the Eddington luminosity of the black hole.

The observed spectrum in the X-ray band is quite hard, $L_X \propto E_\gamma^{-l}$ with $l \approx 0.3$. If the X-rays originate in electron synchrotron radiation, from the slope of the observed spectrum it is possible to estimate the spectral index p of the steady-state parent particle distribution, $N \propto E^{-p}$. They are related as

$$l = -\frac{p}{2} + \frac{3}{2}. \tag{4.3}$$

This yields $p \approx 2.4$. Since particles cool, the index p is not the same as that of the electron injection function, $Q \propto E^{-\alpha}$. In particular $p = \alpha + 1$ in the case of dominant synchrotron losses. The particle injection spectrum must therefore be quite hard, with a power-law index smaller than the typically assumed $\alpha = 2.0 - 2.2$ predicted by the theory of acceleration in strong, non-relativistic shocks. Here we fixed $\alpha = 1.5$, consistent with relativistic shock acceleration.

The values of the relevant parameters of the model are summarized in Table 4.4. We performed least-squares fits to the observational data. The parameters $q_{\rm jet}$, a, η, $E^{\rm min}$, and ρ were allowed to vary subject to the constraints discussed above, whereas the rest of the parameters were kept fixed. The quality of the fits was quantified through the value of its chi-squared

$$\chi^2 = \sum \frac{(F_{\rm obs} - F_{\rm m})^2}{\Delta F_{\rm obs}^2}. \tag{4.4}$$

Here $F_{\rm obs}$ is the observed flux, $F_{\rm m}$ is the value predicted by the model, and $\Delta F_{\rm obs}$ is the uncertainty associated with every observational point. The best fit for a given set of fixed parameters was found minimizing χ^2.

The fits were performed applying the *Pattern Search* algorithm (Audet & Dennis 2003, Kolda et al. 2003). This algorithm does not require the explicit calculation of derivatives and is relatively robust. It is also a convenient method since it allows to impose constraints on the search domain; in this way we could restrict the solutions to the physically meaningful range of values of the free parameters as discussed above. The Nelder-Mead method (Nelder & Mead 1965, Lagarias et al. 1998) was used to accelerate convergence. Special care was taken to avoid local minima by restarting the optimization process from multiple initial values of the free parameters in the allowed domain.

Table 4.4: Values of the parameters in a model for the microquasar GX 339-4.

Parameter	Symbol	Value
Distance	d	6 kpc
Black hole mass	$M_{\rm BH}$	$6M_\odot$
Viewing angle	$\theta_{\rm jet}$	30°
Jet bulk Lorentz factor	$\Gamma_{\rm jet}$	2
Jet injection point	z_0	4.5×10^7 cm$^{(*)}$
Ratio r_0/z_0	χ	0.1
Ratio $2L_{\rm jet}/L_{\rm Edd}$	$q_{\rm jet}$	$\geq 10^{-4}$
Ratio $L_{\rm rel}/L_{\rm jet}$	$q_{\rm rel}$	0.1
Ratio L_p/L_e	a	≥ 1
Magnetic field decay index	m	$1-2$
Ratio $U_B/U_{\rm k}$ at $z_{\rm acc}$	ρ	$0.1-1$
Particle injection index	α	1.5
Minimum particle energy	$E^{\rm min}$	$\geq 2\,mc^2$
Acceleration efficiency	η	$10^{-4}-0.1$

$^{(*)}$ $z_0 = 50R_{\rm grav}$.

4.3.3 *Best-fit spectral energy distributions*

Figures 4.11, 4.12, and 4.13 show the best fits obtained for two sets of simultaneous radio and X-ray data taken on February 3rd 1997 and April 2nd 1999 (Obs1 and Obs2 in Table 4.3, respectively), when the source was in a luminous low-hard state. In Figures 4.11 and 4.12 the location of the acceleration region $z_{\rm acc}$ was determined demanding that $U_{\rm B} = \rho U_{\rm k}$, whereas in the case of Figure 4.13 the condition $U_{\rm B} = \rho U_{\rm m}$ was applied. The values of the best-fit parameters are listed in Table 4.5.

Each SED corresponds to a different value of the magnetic field decay index m. This parameter strongly determines the shape of the spectrum, since it fixes the value of the field along the jet and consequently $z_{\rm acc}$. Larger values of m yield $z_{\rm acc}$ closer to the jet base where the magnetic field is stronger.

The SEDs in Figures 4.11 and 4.12 all correspond to Obs1. The best fit is obtained for $m = 1.2$. The X-ray data range is always covered by the synchrotron emission of primary electrons, but as m grows, synchrotron radiation of secondary pairs begins to dominate at radio wavelengths. This diminishes the quality of the fit. The slope of the X-ray spectrum also gets worse modelled as m increases, indicating that the injection index should be harder than the assumed value $\alpha = 1.5$.

Between ~ 1 GeV and ~ 1 TeV, the emission is dominated by synchrotron self-Compton radiation and synchrotron emission of protons and secondary particles; at higher energies the contributions of proton-proton and proton-photon interactions are the dominant ones. All these processes become more relevant when $z_{\rm acc}$ is nearer the jet base, since the magnetic field is stronger and enhances the synchrotron radiation of protons, muons, and charged pions. Also the matter and photon densities are larger, providing denser targets for proton-proton and proton-photon collisions, and SSC scattering. The contribution of secondary pairs from photon-photon annihilation is significantly increased for large values of m due to this effect as well.[8] In all cases the best fits favour large minimum particle energies, $E_{\rm min} \approx 100 mc^2$. A powerful jet ($q_{\rm jet} \approx 0.8 - 0.9$) and equipartition of energy between primary protons and lep-

[8] We considered the synchrotron and the inverse Compton radiation fields of primary electrons (both in the local approximation) as targets for photon-photon annihilation.

Table 4.5: Values of the best fit parameters in a model for the microquasar GX 339-4.

Model	Obs	Parameter [units]										
		α	m	$E_{\min}$ $[mc^2]$	$q_{\rm jet}$	a	η	ρ	$z_{\rm acc}$ $[R_{\rm grav}]$	$B(z_{\rm acc})$ [G]	$\dot{N}_{e^+}$ $[{\rm s}^{-1}]$	χ^2_ν
A	Obs1	1.5	1.2	97.4	0.9	1.5	0.1	0.1	9.7×10^4	8.4×10^3	3.8×10^{38}	1.42
B	Obs1	1.5	1.5	99.2	0.8	1.4	0.08	0.75	1.4×10^2	1.5×10^7	8.6×10^{40}	2.0
C	Obs1	1.5	1.8	96.3	0.8	1.6	0.03	0.5	1.4×10^2	1.4×10^7	8.4×10^{40}	3.1
D	Obs1	1.5	2.0	92.4	0.75	1.4	0.03	0.75	85.5	2.3×10^7	1.3×10^{41}	3.3
E	Obs1	1.5	1.8	15.0	1.00	1.5	0.1	0.1	1×10^4	5.0×10^3	4.5×10^{40}	0.8
F	Obs2	1.5	2.0	11.5	0.73	2.7	0.1	0.1	3.5×10^3	1.2×10^4	3.0×10^{40}	0.98
G	Obs3	1.5	2.0	2.0	6.4×10^{-3}	2.0	3×10^{-3}	0.4	3×10^3	3.6×10^3	1.4×10^{35}	0.15
H	Obs4	1.5	2.0	2.0	6.3×10^{-3}	2.0	1×10^{-4}	0.15	4.9×10^3	1.4×10^3	7.5×10^{34}	0.15
I	Obs3	2.2	2.0	25.2	6.6×10^{-3}	2.0	0.1	0.4	2×10^2	3.1×10^3	2.4×10^{37}	0.8
J	Obs5	1.5	2.0	92.7	1.0	1.0	0.1	0.1	6×10^3	4×10^3	1×10^{42}	6.2

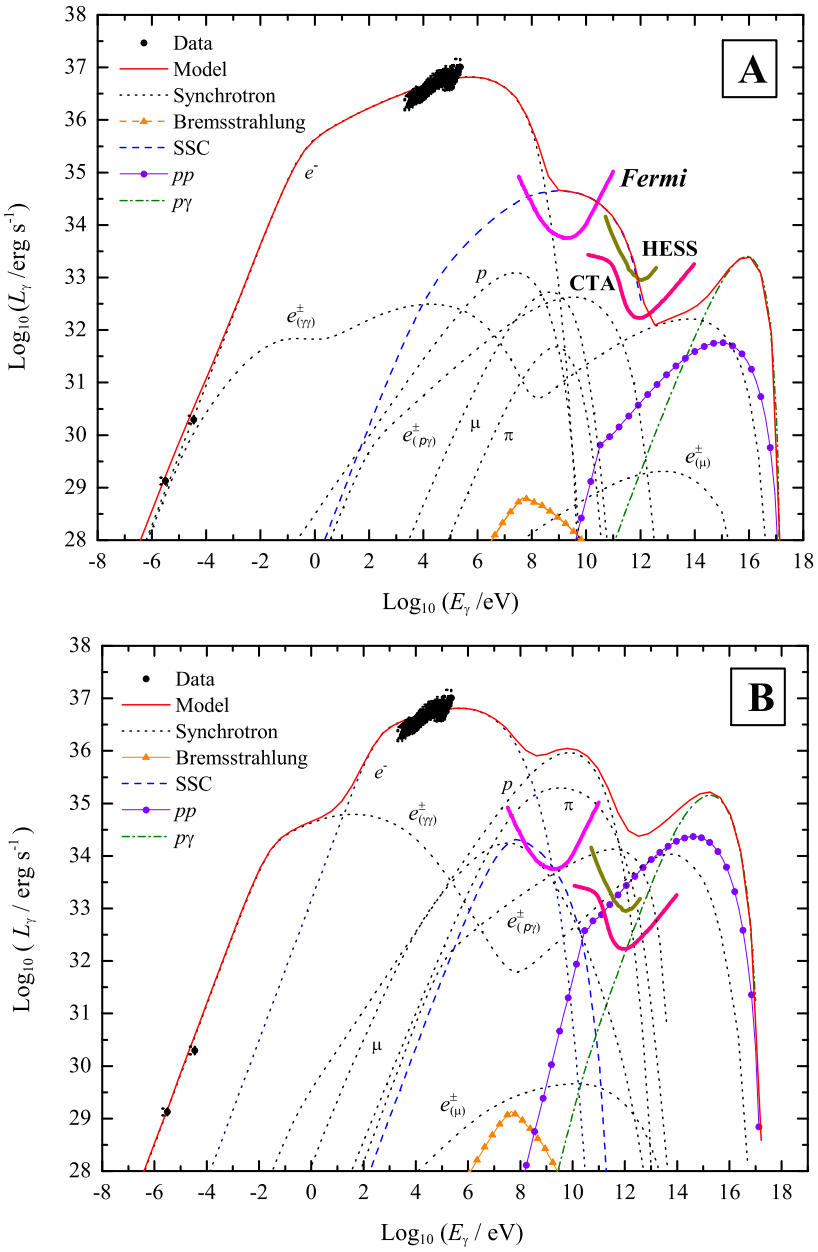

Figure 4.11: Best-fit spectral energy distributions for Obs1 of GX 339-4, for different values of the magnetic field decay index: $m = 1.2$ (model A) and $m = 1.5$ (model B). See Tables 4.4 and 4.5 for the values of the rest of the parameters. The position $z_{\rm acc}$ of the acceleration region was determined demanding that $U_{\rm B} < U_{\rm k}$. The subindices $(\gamma\gamma)$, $(p\gamma)$, and (μ) indicate pairs created through photon-photon annihilation, photopair production, and muon decay, respectively. The thick lines are the sensitivity limits of *Fermi* (5σ, one-year sky survey exposure), HESS (5σ, 50 h exposure), and CTA (50 h exposure).

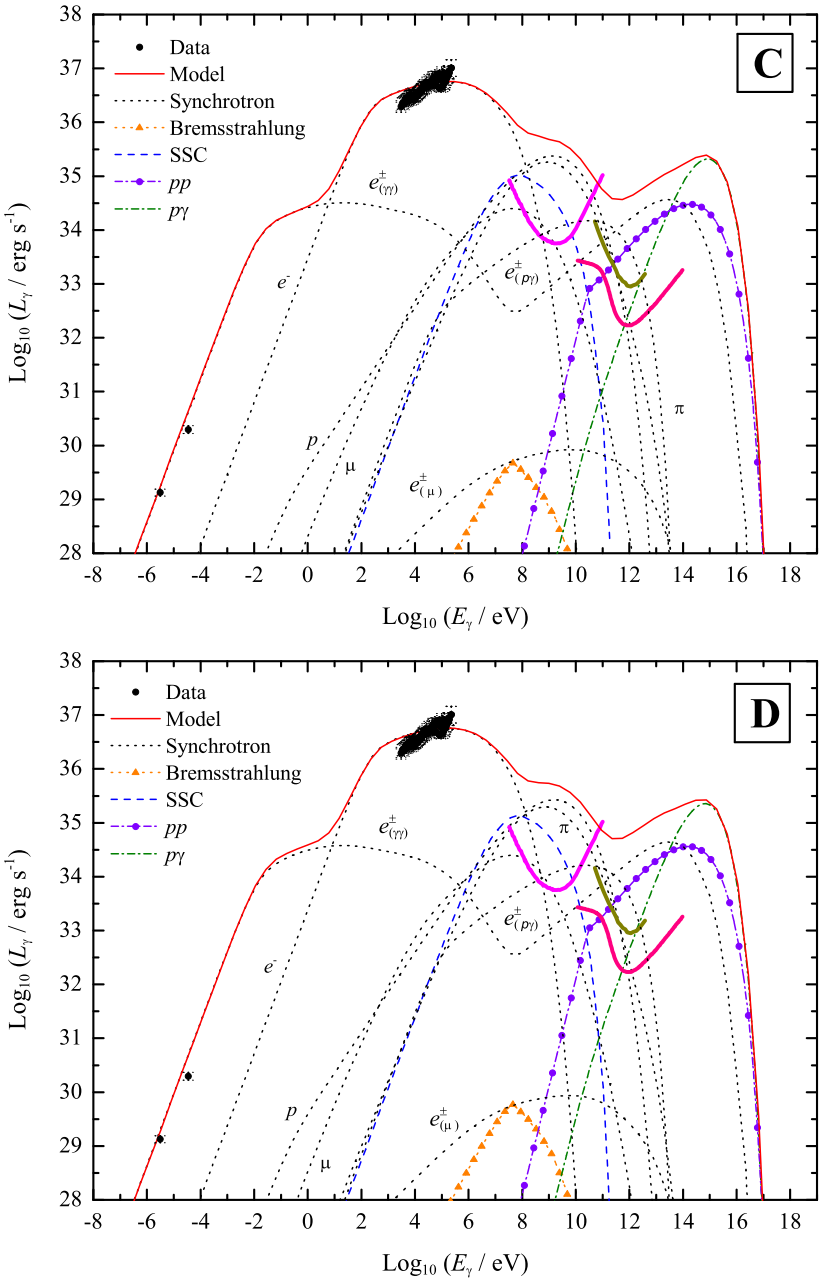

Figure 4.12: Best-fit spectral energy distributions for Obs1 of GX 339-4, for different values of the magnetic field decay index: $m = 1.8$ (model C) and $m = 2.0$ (model D). See Tables 4.4 and 4.5 for the values of the rest of the parameters. The position $z_{\rm acc}$ of the acceleration region was determined demanding that $U_{\rm B} < U_{\rm k}$. The subindices $(\gamma\gamma)$, $(p\gamma)$, and (μ) indicate pairs created through photon-photon annihilation, photopair production, and muon decay, respectively. The thick lines are the sensitivity limits of *Fermi*, HESS, and CTA, see Figure 4.11.

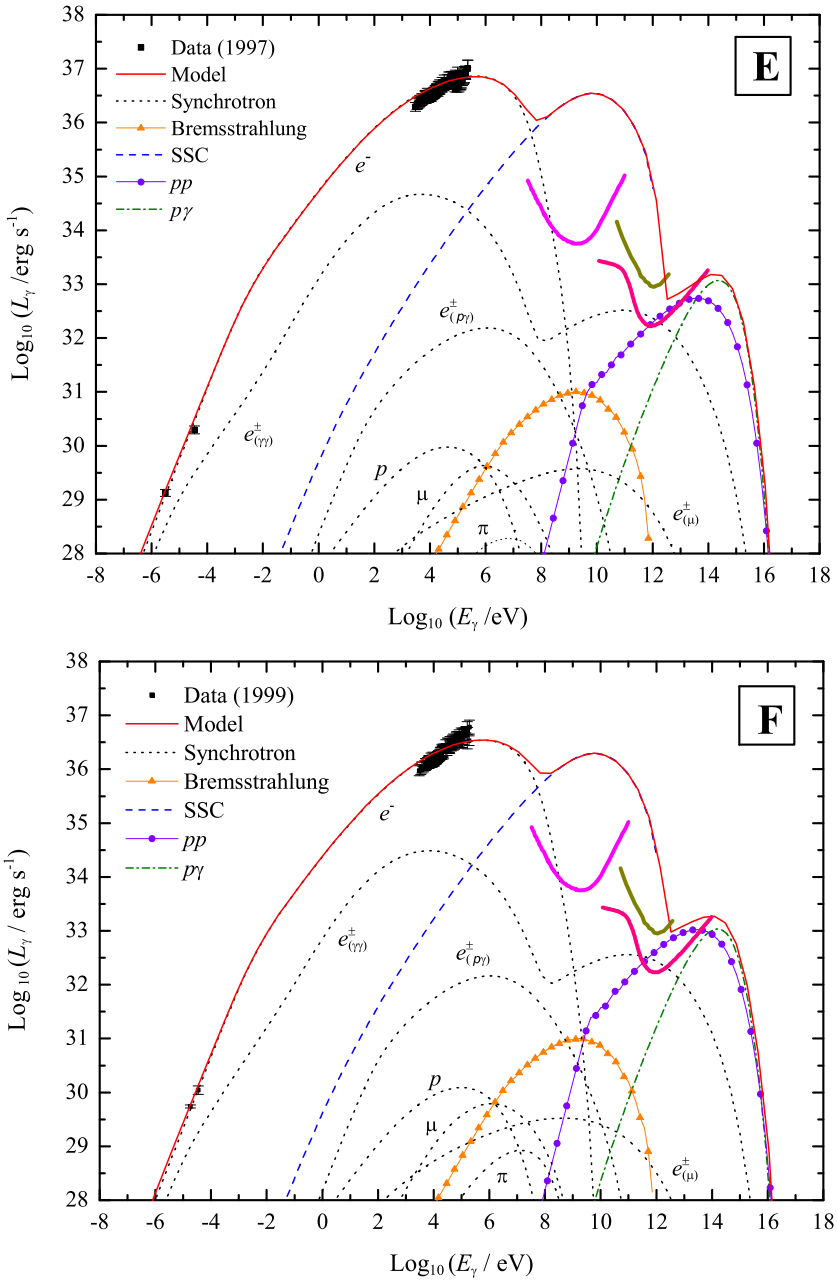

Figure 4.13: Best-fit spectral energy distributions for Obs1 (Model E) and Obs2 (Model F) of GX 339-4. See Tables 4.4 and 4.5 for the values of the parameters. The position $z_{\rm acc}$ of the base of the acceleration region is calculated from the condition $U_{\rm B} < U_{\rm m}$.

tons ($a \approx 1$) are also required, since the power injected in electrons needs to be as large as possible to account for the X-ray observations.

Models E and F in Figure 4.13 correspond to fits of Obs1 and Obs2, respectively. In both cases, $z_{\rm acc}$ was calculated demanding that $U_{\rm B} < U_{\rm m}$. For the same m and ρ, this condition gives larger values of $z_{\rm acc}$ and weaker magnetic fields. Now the best fits are obtained for large values of m. These sets of parameters reproduce the slope of the X-ray spectrum for the same value of the injection index better than the models of Figures 4.11 and 4.12.

Figure 4.14 shows two model fits to low-luminosity low-hard state observations of GX 339-4, carried out in 1999 (Obs3 and Obs4). Simultaneous observations in the optical band are also available for Obs3, but we postpone the analysis of these data until the next section. The radio and X-ray emission is due to primary electrons; all radiative contributions of protons and secondary particles are negligible. The jet power required to account for the data is now only a fraction $q_{\rm jet} \approx 6 \times 10^{-3}$ of the Eddington luminosity. The best fit models are obtained for low values of the acceleration efficiency and minimum particle energy.

For each model we also calculate the synchrotron emission of thermal electrons at the base of the jet. For an electron energy $E_e \approx 2 m_e c^2$ and a magnetic field $B_0 \approx 10^6 - 10^7$ G, the peak of the spectrum is at $E_\gamma \approx 10$ eV. The luminosity of this component, however, is below or just above the jet emission. This contribution is not significant in the relevant energy bands. The results of the fits are therefore not affected.

4.3.4 *Spectral correlations*

The analysis of simultaneous radio and X-ray observations from 1997-1999, led Corbel et al. (2003) to find that the fluxes in both energy bands are tightly correlated. In particular, the radio flux at 8.6 GHz is related the 3-9 keV integrated X-ray flux as $F_{\rm R} \propto \Delta F_{\rm X}^{\delta}$, with $\delta \sim 0.7$. This correlation suggests a common origin in the jet[9] (synchrotron radiation). According to Markoff et al. (2003), if all

[9] Alternative models to explain the radio/X-rays correlation have been suggested. Markoff et al. (2005) presented fits to simultaneous radio and X-ray data of GX 339-4 obtained applying a corona model. Furthermore, in Heinz & Sunyaev (2003) it is shown that for an ADAF-like boundary condition, the radio flux from the base of the jet scales with the black hole mass and

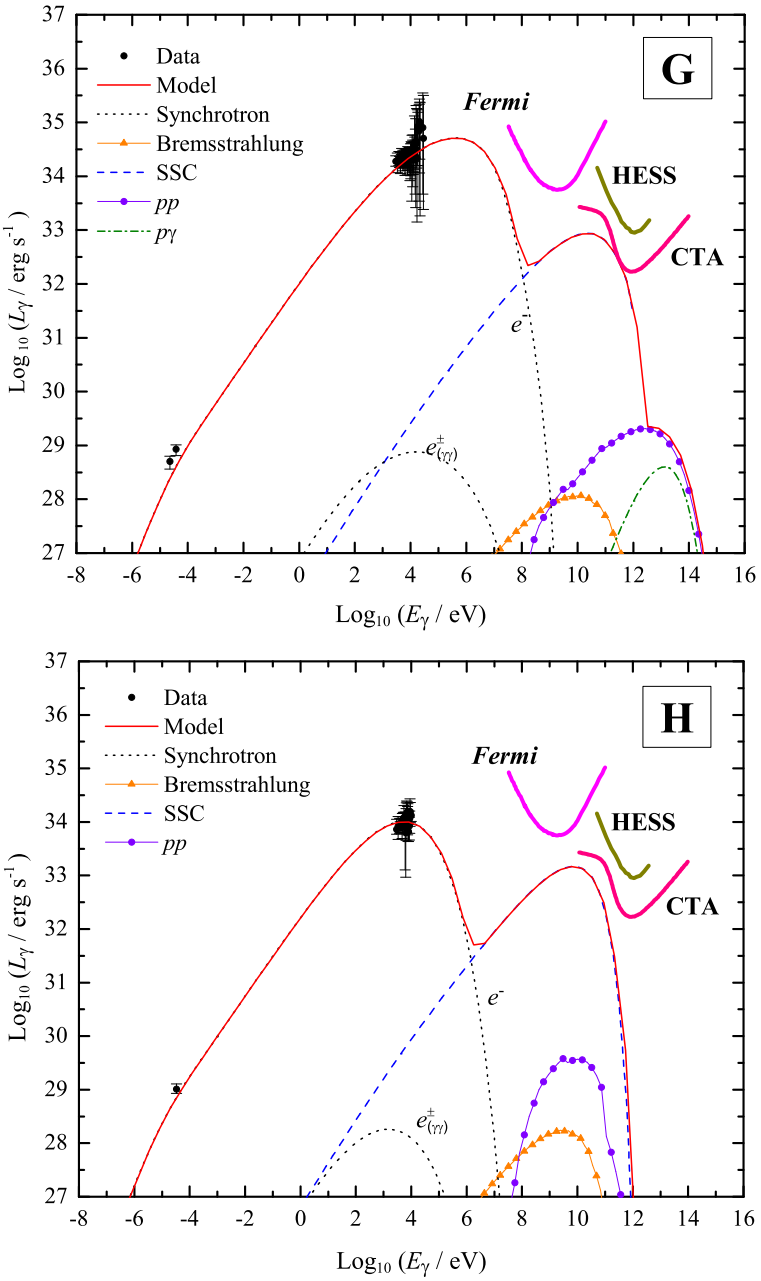

Figure 4.14: Best-fit SEDs for Obs3 (model G) and Obs4 (model H) of GX 339-4. The decay index of the magnetic field is $m = 2$ and the position $z_{\rm acc}$ of the acceleration region was determined demanding that $U_{\rm B} < U_{\rm m}$. See Tables 4.4 and 4.5 for the values of the rest of the parameters. The sensitivity limits of *Fermi*, HESS, and CTA are indicated. Optical data in model G (not shown, see Figure 4.16) were not included in the fit.

model parameters except the jet power are kept frozen, the correlation index δ is given by

$$\delta = \frac{17/12 - 2/3\delta_{\rm R}}{17/12 - 2/3\delta_{\rm X}}. \tag{4.5}$$

Here $\delta_{\rm X}$ is the spectral index of the X-ray region of the synchrotron spectrum ($F_{\rm X} \propto \nu^{\delta_{\rm X}}$) and $\delta_{\rm R}$ that of the synchrotron radio flux ($F_{\rm R} \propto \nu^{\delta_{\rm R}}$).

In our model the radio and X-ray emission is due to synchrotron radiation of electrons. We find a value of the radio spectral index $\delta_{\rm R} \sim 0.33$, which corresponds to the low energy part of the spectrum from a particle distribution with a low-energy cutoff. The value of the X-ray spectral index is $\delta_{\rm X} \sim -0.8$, as expected for an injection function $Q_e \propto E^{-1.5}$ (notice that electrons are strongly cooled due to synchrotron losses after injection, see Section 3.3.2). These values yield $\delta \sim 0.6$, in reasonable agreement with the result of Corbel et al. (2003). Figure 4.15 shows the correlation curves predicted by our model for cases A, E, F, and G, together with the data from Corbel et al. (2003). The model results are in reasonable agreement with the observations.

Simultaneously with the radio and X-ray observations of Obs3 and Obs5, GX 339-4 was also detected at NIR and optical wavelengths (Markoff et al. 2003, Homan et al. 2005). The NIR/optical flux is also strongly correlated to the X-ray flux.

From the analysis of data from the same epoch as Obs5, Homan et al. (2005) showed that the flux density in the NIR H-band and the $3 - 100$ keV bolometric X-ray flux correlate as $F_H \propto \Delta F_{\rm X}^{\delta}$, with $\delta = 0.53$. A similar correlation was found between the optical V-band and I-band flux densities and the integrated X-ray flux, with correlation indices $\delta = 0.44$ and $\delta = 0.48$, respectively. These correlations disappear when the source leaves the low-hard state. The H-band emission, however, rises and decays faster than the optical during the transition, whereas the slope between the I and V bands remains constant. As pointed out by Homan et al. (2005), this may indicate a different origin for the NIR and optical emission during the low-hard state.

The correlations between the radio/X-ray and NIR/X-ray fluxes suggest that the emission in the three ranges must originate in the jet. This is further

the accretion rate, independently of the assumed jet model.

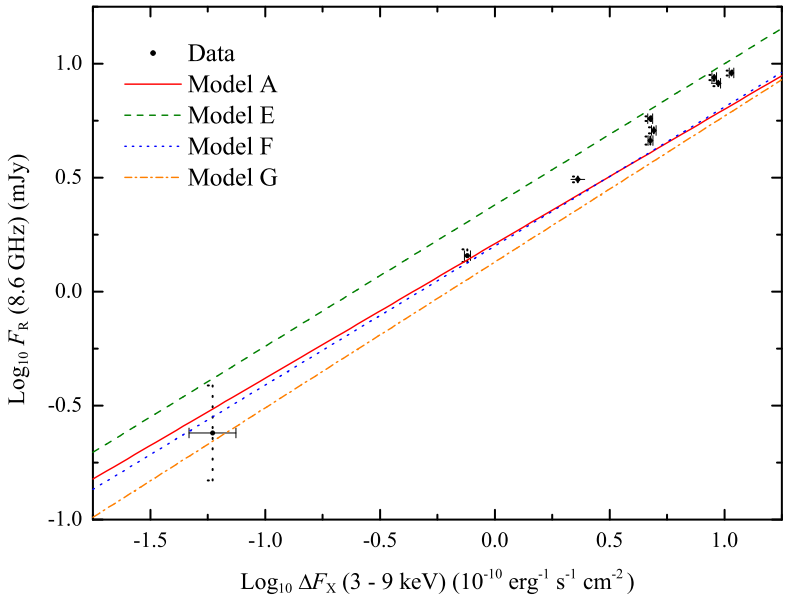

Figure 4.15: Radio/X-ray flux correlations in GX 339-4. The different curves correspond to models A, E, F, and G. In each case, the slope was calculated as in Markoff et al. (2003), and to determine the intercept we used corresponding SEDs in Figures 4.11, 4.12, 4.13, and 4.14. The model correlation index is $\delta \sim 0.6$, whereas that of the 1997-1999 observational data is $\delta \sim 0.7$ (Corbel et al. 2003).

supported by the fact that the NIR flux extrapolates back to the radio data (see also Corbel et al. 2003). Direct or reprocessed emission from an accretion disc can be ruled out due to the shape of the NIR/optical spectrum and the short decay time scales. Furthermore, the NIR and radio fluxes are quenched when the disc begins to contribute significantly to the X-ray emission. Homan et al. (2005) conclude that the NIR emission probably originates in the jet, and approximately coincides with the position of the break of the synchrotron spectrum. The optical flux may be due to thermal and/or non-thermal reprocessed radiation from the accretion disc or star, or from a region of the jet different from where the NIR emission is produced.

These ideas are further supported by the recent results of Coriat et al. (2009), who presented an analysis of five years of observations of GX 339-4 (from 2002 to 2007, a period that comprises five outbursts). They found a strong IR/X-ray correlation over four decades in flux during the low-hard state. The correlation index, however, is not unique: a break appears at bolometric (3-100 keV) X-ray

fluxes $\sim 1.1 \times 10^{-10}$ erg s^{-1} cm^{-2} ($L_X \sim 6 \times 10^{-4} L_{Edd}$ for $M_{BH} = 6 M_\odot$ and $d = 6$ kpc). Coriat et al. (2009) argue that this break can be explained attributing the X-ray emission to SSC radiation from the jet (see also Nowak et al. 2005, where it is suggested that models more complex than a single jet synchrotron component maybe needed to explain the correlations). They find no clear evidence of a similar break in the V-band/X-ray correlation, and suggest that the optical emission in the low-hard state is dominated by the outer part of the accretion disc, and not by the jet.

This correlation is not peculiar of GX 339-4, but it seems to be a signature of low-mass black hole X-ray binaries. Russell et al. (2006) analysed radio, NIR, optical, and X-ray data from 16 sources (including extragalactic systems in the Large Magellanic Cloud). Their results agree with those of Homan et al. (2005) for GX 339-4. They estimate that the jet contribution to the NIR emission during the low-hard state is $\sim 90\%$, but only $\sim 50\%$ to the I and V bands.

We attempt to fit the NIR/optical data, when available, using our jet model. Figure 4.16 shows the best-fit models obtained for Obs3 (the data in the optical band are now plotted) and Obs5. In the case of Obs5, the radio, NIR, optical, and X-ray data are reasonably well reproduced with a hard particle injection spectral index $\alpha = 1.5$. In the case of Obs3, the whole data set at optical frequencies cannot be accounted for with a single synchrotron component. However, adopting a softer particle injection spectral index $\alpha = 2.2$, it is possible to obtain models models where the synchrotron turnover occurs in the optical.[10] The rise in the spectrum at higher energies, however, cannot be fitted. This emission must have a different origin, for example in an accretion disc (Markoff et al. 2003).

4.3.5 *Absorption effects*

In order to assess the effect of photon self-absorption by photon-photon annihilation, we calculated the attenuation parameter $\exp(-\tau_{\gamma\gamma})$. As targets, we considered the synchrotron and the inverse Compton radiation fields of primary electrons. As it can be seen from Figure 4.17, contrary to some of the models in Section 4.1, internal attenuation is almost negligible. This is because

[10] Synchrotron radiation of thermal electrons from the base of the jet is not relevant in these models either.

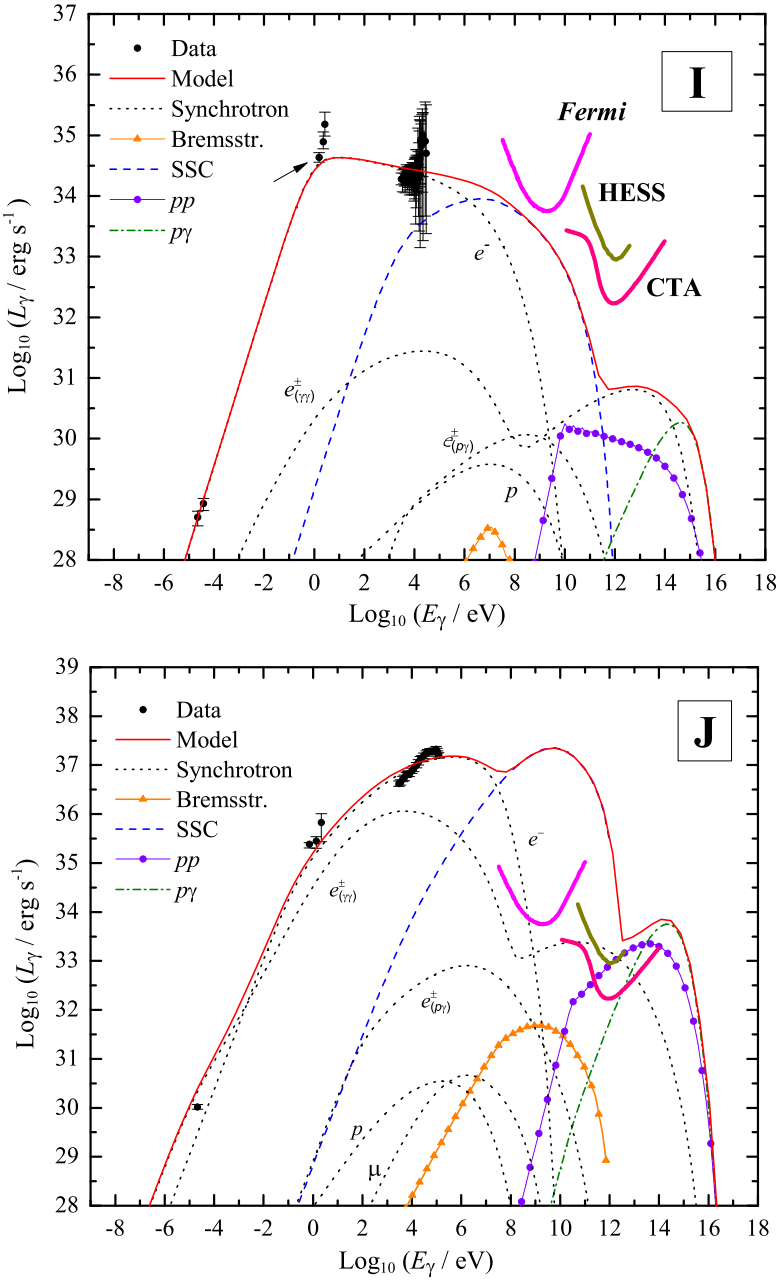

Figure 4.16: Best-fit SEDs for Obs3 (model I) and Obs5 (model J) of GX 339-4. In model I, the arrow indicates the only point in the optical band that was included in the fit. The decay index of the magnetic field is $m = 2$. The position $z_{\rm acc}$ of the acceleration region was determined demanding that $U_{\rm B} < U_{\rm k}$ in Model I and $U_{\rm B} < U_{\rm m}$ in Model J. See Tables 4.4 and 4.5 for the values of the rest of the parameters. The sensitivity limits of *Fermi*, HESS, and CTA are indicated.

the volume of the emission region is larger, and so the density of the target photon field is low. The production spectrum is not appreciably modified in any case.

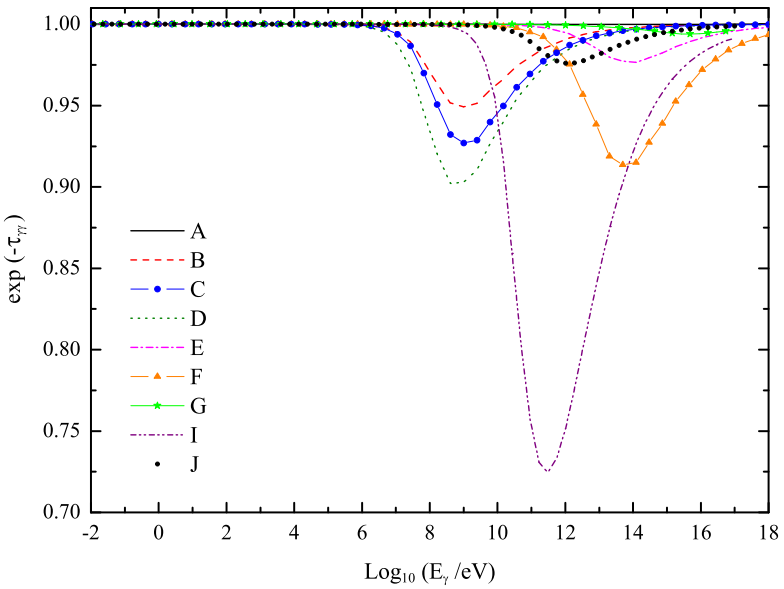

Figure 4.17: Attenuation factor as a function of energy for a photon emitted at $z = z_{\rm acc}$ at an angle $\theta_{\rm jet}$ with the line of sight, due to photon-photon annihilation in the internal radiation field of the jet. Absorption is negligible in all cases and does not modify the production spectrum.

4.3.6 *Positron production rate*

Measurements carried out with the INTEGRAL Spectrometer (SPI) instrument of the *INTEGRAL* satellite have allowed to complete a detailed map of an extended region of emission line at 511 keV in the Galaxy (Weidenspointner et al. 2008, Bouchet et al. 2010), see Figure 4.18. These observations confirm the diffuse (rather than point-like) distribution of the line, with bright emission from the galactic bulge and a clear, extended ($|l| \lesssim 200^\circ$, $|b| \lesssim 10^\circ$) disc component. The bulge-to-disc flux ratio is within the range $0.25 - 0.7$ (Bouchet et al. 2010).

The initial results of Weidenspointner et al. (2008) pointed to an asymmetry in the disc component: the flux from the region of negative galactic longitudes ($-50^\circ < l < 0^\circ$) appeared to be 1.8 times larger than that from the corresponding region of positive longitudes. Since the same type of asymmetry

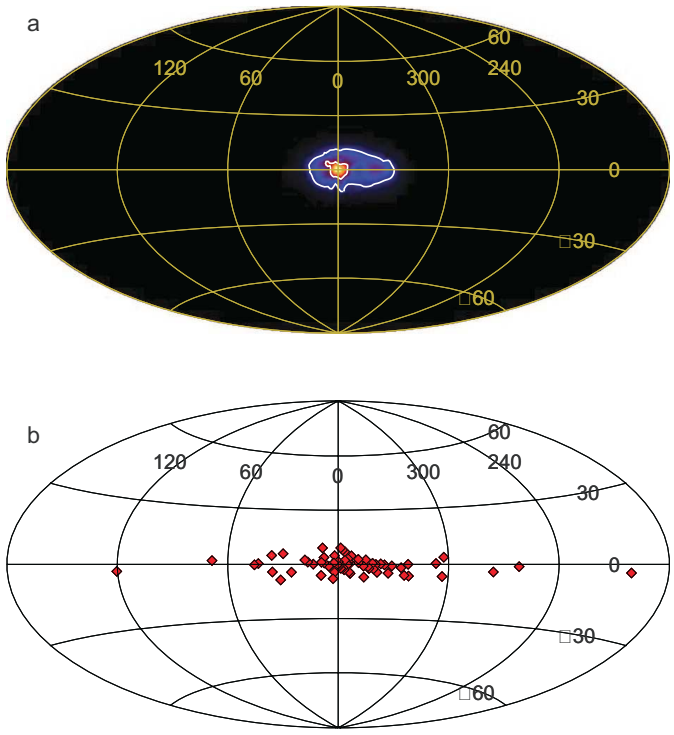

Figure 4.18: Spatial distribution of (**a**) the line emission at 511 keV and (**b**) of low-mass X-ray binaries with emission above 20 keV, as seen by the instruments SPI and IBIS of the satellite *INTEGRAL*, respectively. From Weidenspointner et al. (2008).

was observed in the spatial distribution of hard LMXBs (those that show appreciable emission above 20 keV) detected with *INTEGRAL*, Weidenspointner et al. (2008) suggested that LMXBs might be the main sources of positrons. As new *INTEGRAL* observations became available, these results were revised by Bouchet et al. (2010); they found no asymmetry in the line emission from the galactic disc to within statistical errors.

Different types of positron sources have been suggested in the literature, including pulsars, the massive black hole at the galactic center, microquasars, nucleosynthesis events, and extended processes like cosmic ray nuclear reactions and dark matter decay. The fact that both bulge and disc emission are clear, seems to disfavour the latter two possibilities. Furthermore, Bouchet et al. (2010) suggested that the widened longitudinal extension of the disc emission points to a population of old stars as the main source of positrons in the galaxy. Microquasars, in particular those with a low-mass donor star, appear then as

an appealing possibility. Along with electromagnetic radiation, the creation of electron-positron pairs is a necessary result of relativistic particle interactions. As we have seen, they are injected, for example, through photon-photon annihilation and as a by-product of hadronic interactions. The estimates of Guessoum et al. (2006) already shown that the association between microquasars and galactic positron sources is likely at least on energetic grounds. Here, we explore the possibilities for electron-positron production in more self-consistent models for microquasar jets.

We calculated the positron injection rate predicted by our model. According to Heinz (2008), the number of injected positrons per unit time can be roughly estimated as

$$\dot{N}_{e^+} \approx \frac{L_{e^\pm}}{2\Gamma_{\rm jet}\bar{\gamma}_e m_e c^2}. \tag{4.6}$$

In this expression $L_{e^\pm}$ is the total luminosity injected in pairs and $\bar{\gamma}_e$ is the mean Lorentz factor of the positrons when they leave the source.

It is reasonable to expect that positrons have almost completely cooled when they reach the end of the jet, and thus $\bar{\gamma}_e$ is of the order of the jet bulk Lorentz factor, $\bar{\gamma}_e \sim \Gamma_{\rm jet} = 2$. In our case, the most relevant process of pair production is photon-photon annihilation. The predicted positron injection rates $\dot{N}_{e^+}$ are shown in Table 4.5; they range from $\sim 10^{35}$ s^{-1} to 10^{42} s^{-1} in the models that correspond to the brightest X-ray luminosities. Bouchet et al. (2010) estimate that the positron production rate required to account for the observed flux from the disc is $\sim 0.8 \times 10^{43}$ s^{-1}. There are about ≥ 100 LMXB in the Galaxy (Liu et al. 2007) and, although not detected yet, possibly most of them produce jets. Even if many of them are less powerful than the jet in GX 339-4, the added contributions might account for the observed flux at 511 keV. Our estimations show that the proposed association between LMXB and the annihilation line emission is indeed feasible at least in energetic terms. In this way, there may be no need to resort to other more exotic explanations, such as annihilation of dark matter.

4.3.7 *Conclusions*

To sum up, we have shown that, under certain general conditions, the model developed here is capable of explaining the observed radio and X-ray spectrum of the low-mass microquasar GX 339-4. The data from high X-ray luminosities states require a powerful jet with a large leptonic content. In fact, all the fits yield $a \sim 1$, what means that as much energy is given to the primary relativistic electrons as it is allowed by the constraints imposed. The hadronic contribution to the spectrum in cases A and E is undetectable with the present gamma-ray instruments. In the other models, synchrotron radiation of protons and secondary muons and pions, and at higher energies the contribution of pp interactions, could be detectable by *Fermi* and HESS (and in the future by CTA), respectively. For the low-luminosity observations (models G and H), the predicted emission above ~ 100 MeV is too faint to be detected with the present gamma-ray telescopes. We have also calculated fits to simultaneous radio, NIR/optical, and X-ray observations from 1999 and 2002 (models I and J). For these sets of parameters, the break in the synchrotron spectrum occurs approximately in the NIR and the lowest-energy data were reasonably fit. The rising shape of the spectrum at optical wavelengths, however, could not be reproduced. This component is likely to originate mostly outside the jet, probably in the accretion disc.

In all models the spectrum is essentially of leptonic origin. In this sense, the results do not differ from those of previous works like those of Markoff et al. (2003, 2005). Our model, however, besides making predictions for the emission in the high and very high-energy bands, introduces some refinements over the previous scenarios adopted for this source. The particle distributions are calculated self-consistently taking into account the effect of energy losses on the injection spectrum. We also calculate the radiation emitted by secondary particles produced in hadronic interactions, and that of the electron-positron pairs from photon-photon annihilation. The importance of photon self-absorption is assessed as well, although it turns out not to be relevant since the emission region is in a zone of low radiation density.

We have also shown that the pair injection rate is significant enough, if this kind of model is solid in general for low-mass microquasars, to account for

the observed line emission at 511 keV, according to the lower limit given by Bouchet et al. (2010). If the proposed association between hard low-mass X-ray binaries and the electron-positron annihilation line flux can be proved, other explanations such as annihilation of dark matter could result unnecessary.

5

INHOMOGENEOUS JET MODEL

In this chapter, we generalize the one-zone jet model to treat the injection and cooling of relativistic particles in a spatially extended, inhomogeneous region, and study its consequences on the radiative output of the jet. We begin by presenting some general results. Then, as an application, we fit the observational data from the low-mass X-ray binary XTE J1118+480, a very well studied black hole candidate in the galactic halo. The spectral energy distribution of this source in the low-hard state displays a thermal component at UV frequencies, attributed to the emission from an accretion disc. We then add a simple disc model to our representation of the system. We also consider the radiation from the disc as a target for inverse Compton scattering off relativistic electrons and for photon-photon annihilation.

5.1 JET MODEL

The basic jet model is the same as in Chapter 3; we briefly summarize it below. We parameterize the accretion power $L_{\rm accr}$ in terms of the Eddington luminosity of the black hole as

$$L_{\rm accr} \equiv \dot{M}c^2 = q_{\rm accr}\, L_{\rm Edd} \approx 1.3 \times 10^{38} q_{\rm accr} \left(\frac{M_{\rm BH}}{M_\odot}\right) {\rm erg\,s^{-1}}, \qquad (5.1)$$

where $\dot{M}$ is the mass accretion rate, $M_{\rm BH}$ is the mass of the black hole, $M_\odot$ is the solar mass, and $q_{\rm accr}$ is an adimensional parameter.

A fraction of the accreted matter is ejected via two symmetrical jets, each

carrying a power

$$L_{\rm jet} = \frac{1}{2} q_{\rm jet}\, L_{\rm accr} \tag{5.2}$$

with $q_{\rm jet} < 1$. The outflows are launched at a distance z_0 from the black hole, and propagate up to $z = z_{\rm end}$ with a constant bulk Lorentz factor $\Gamma_{\rm jet}$. The symmetry axis of the jet makes an angle $\theta_{\rm jet}$ with the line of sight of the observer. Figure 5.1 shows a sketch of the situation.

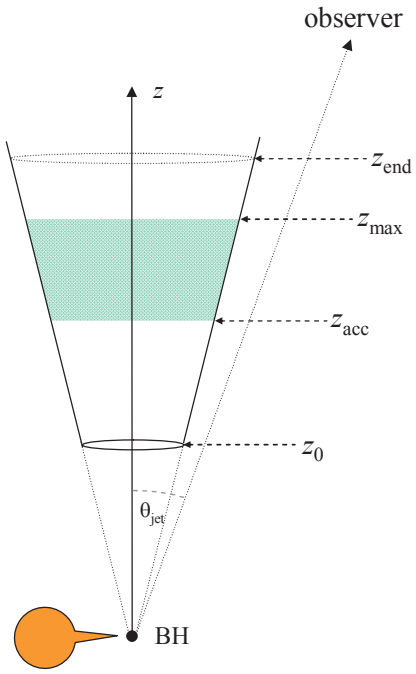

Figure 5.1: Detail of the jet and the acceleration region (not to scale). Some relevant geometrical parameters are indicated.

As before, the value of the magnetic field $B_0 = B(z_0)$ is estimated assuming that the flow is magnetically dominated in the launching region, see Eq. (3.4). We apply the prescription in Eq. (3.5) with $m > 1$ to calculate $B(z)$ for $z > z_0$.

The region of the jet where the relativistic particles are accelerated extends from $z = z_{\rm acc}$ up to $z = z_{\rm max}$. The position of the base of the acceleration region is determined demanding that

$$U_{\rm B}(z_{\rm acc}) = \rho\, U_{\rm k}(z_{\rm acc}), \tag{5.3}$$

with $\rho < 1$. The fraction of the jet power that is transferred to relativistic electrons and protons is $q_{\rm rel} \ll 1$; the ratio of the power injected in protons to the power injected in electrons is $a \geq 1$.

In the jet reference frame, we adopt an injection function for primary particles that is a power-law in energy times an exponential cutoff

$$Q(E,z) = Q_0\, E^{-\alpha} \exp\left[-E/E_{\rm max}(z)\right]\, f(z). \tag{5.4}$$

The step-like function $f(z)$ fixes the effective size of the acceleration region

$$f(z) = 1 - \frac{1}{1+\exp[-(z-z_{\rm max})]} \approx \begin{cases} 1 & z \leq z_{\rm max} \\ 0 & z > z_{\rm max}. \end{cases} \tag{5.5}$$

The cutoff energy $E_{\rm max}(z)$ is calculated from the balance of the acceleration and the cooling rates, and the normalization constant Q_0 from the total power in protons or electrons as in Eq. (3.18).

Since the acceleration region is extended, the simple version of the kinetic equation in the one-zone jet model must be generalized to account for the transport of particles and the spatial variation of the parameters that govern the interactions (the magnetic field, the radiation fields, and the density of thermal particles). We neglect diffusion, but add a convective term; the convection velocity is of the order of the jet bulk velocity, $\vec{v}_{\rm conv} \approx v_{\rm jet}\,\hat{z}$. Under these assumptions, Eq. (3.28) now reads

$$v_{\rm conv}\frac{\partial N}{\partial z} + \frac{\partial}{\partial E}\left(bN\right) + \frac{N}{T_{\rm dec}} = Q. \tag{5.6}$$

Notice that the convection term has replaced the effective term that represented the removal of particles due to escape.

We solve Eq. (5.6) numerically by the method of finite differences. The domain of the partial differential equation is discretized into a non-uniform grid in order to accommodate the wide range of values of z and E. The linear system of equations thus obtained is sparse, and can solved efficiently with state of the art numerical routines (Davis 2004a,b).

The treatment of the cooling and radiation from primary and secondary par-

ticles is identical to that in the previous chapters. Here, however, we add the IC radiation field of primary electrons as an internal target for proton-photon collisions and photon-photon annihilation. As we calculate the emission from an extended region of the jet, the appropriate general expression for the luminosity corrected by absorption is

$$L_\gamma\left(E_\gamma\right) = \int_V \mathrm{d}^3 r \, \exp\left[-\tau_{\gamma\gamma}(E_\gamma, \vec{r})\right] q_\gamma\left(E_\gamma, \vec{r}\right). \tag{5.7}$$

5.2 ACCRETION DISC MODEL

5.2.1 *Basic model*

We assume that the accretion disc is perpendicular to the jets and extends from an inner radius $R_{\rm in}$ to an outer radius $R_{\rm out}$ about the plane $z = 0$; see Figure 5.2 for an scheme.

We adopt a radial profile for the temperature consistent with that of a standard optically thick, geometrically thin accretion disc (see Section 2.1.2)

$$T(R) = \frac{T_{\rm max}}{a_0}\left(\frac{R_{\rm in}}{R}\right)^{3/4}\left(1-\sqrt{\frac{R_{\rm in}}{R}}\right)^{1/4}. \tag{5.8}$$

The maximum temperature of the disc, $T_{\rm max}$, is reached at $R_{\rm max} = (49/36)R_{\rm in}$, and $a_0 = 6^{3/2}/7^{7/4} \approx 0.49$.

Every annulus of the disc radiates as a black body at the local temperature $T(R)$. The observed flux at energy E_γ is then

$$F_{\rm d}(E_\gamma) = 2\pi\frac{\cos\theta_{\rm d}}{d^2}\int_{R_{\rm in}}^{R_{\rm out}} B(E_\gamma, R)\, R\, dR, \tag{5.9}$$

where

$$B(E_\gamma, R) = \frac{2}{c^2 h^3}\frac{E_\gamma^3}{\exp\left[E_\gamma/kT(R)\right]-1} \tag{5.10}$$

is the Planck function and $\theta_{\rm d} = \theta_{\rm jet}$ is the inclination angle of the disc with respect to the line of sight. Both viewing angles are equal since we take the

disc to be perpendicular to the jet.

The power per unit area emitted by a black body is $D(R) = \sigma_{SB} T(R)^4$. The total luminosity of the disc is then calculated integrating $D(R)$ over the two faces of the disc,

$$L_d = 2 \times 2\pi\sigma_{SB} \int_{R_{in}}^{R_{out}} T(R)^4 \, R \, dR \approx \frac{4\pi}{3} \sigma_{SB} \left(\frac{T_{max}}{a_0} \right)^4 R_{in}^2. \tag{5.11}$$

The approximation is valid for $R_{out} \gg R_{in}$.

In steady state, a half of the gravitational energy lost by the infalling matter is radiated in the disc, so

$$L_d = \frac{1}{2} \frac{G M_{BH} \dot{M}}{R_{in}} = \frac{1}{2} \frac{R_{grav}}{R_{in}} \dot{M} c^2. \tag{5.12}$$

Eqs. (5.11) and (5.12) provide an estimation of the accretion power

$$\dot{M} c^2 = \frac{8\pi}{3} \sigma_{SB} \left(\frac{T_{max}}{a_0} \right)^4 \frac{R_{in}^3}{R_{grav}}. \tag{5.13}$$

5.2.2 *Interaction with the disc radiation field*

The radiation field of the disc provides a target for IC scattering off the relativistic leptons in the jet. Besides, the high-energy photons emitted in the jets can be absorbed by disc photons to create electron-positron pairs.

The radiation field of the disc is not isotropic in the jet frame. The photon-photon optical depth and the spectrum from IC interactions must be calculated using the full cross sections (not averaged over the collision angle), and taking into account the geometry of the disc-jet system.

To calculate the IC luminosity we must start from the most general expression for the emissivity per unit solid angle Ω_s in the jet reference frame

$$q_\gamma^{\rm IC}\left(E_\gamma,\Omega_{\rm s},\vec{r}\right)=2\pi c\int_{R_{\rm in}}^{R_{\rm out}}R\,{\rm d}R\int_0^\infty{\rm d}\epsilon\oint{\rm d}\Omega\int_{E^{\rm min}}^{E^{\rm max}}{\rm d}E\oint{\rm d}\Omega_e\,\left(1-\beta\cos\psi\right)\times$$
$$N\left(E,\Omega_e,\vec{r}\right)\,n_{\rm ph}\left(\epsilon,\Omega,\vec{r},R\right)\,\frac{{\rm d}\sigma_{\rm IC}}{{\rm d}E_\gamma{\rm d}\Omega_{\rm s}}. \tag{5.14}$$

Here $\mathrm{d}\sigma_{\rm IC}/\mathrm{d}E_\gamma\mathrm{d}\Omega_{\rm s}$ is the double differential IC cross section, ψ is the collision angle between the particle and the disc photon, $N\left(E,\Omega_e,\vec{r}\right)$ is the particle energy distribution, and $\beta=\sqrt{1-1/\gamma^2}$, where γ is the Lorentz factor of the particle. The function $n_{\rm ph}\left(\epsilon,\Omega,\vec{r},R\right)$ (in units of $\mathrm{erg}^{-1}\ \mathrm{cm}^{-3}\ \mathrm{cm}^{-2}$) is the number density of disc photons per unit energy at position $\vec{r}$, that were emitted per unit area of the disc at radius R around the solid angle Ω.

Equation (5.14) can be simplified under some appropriate assumptions, see for example Dermer & Schlickeiser (1993). We develop them in Appendix A. Here we only present the details of the calculation of the disc radiation field.

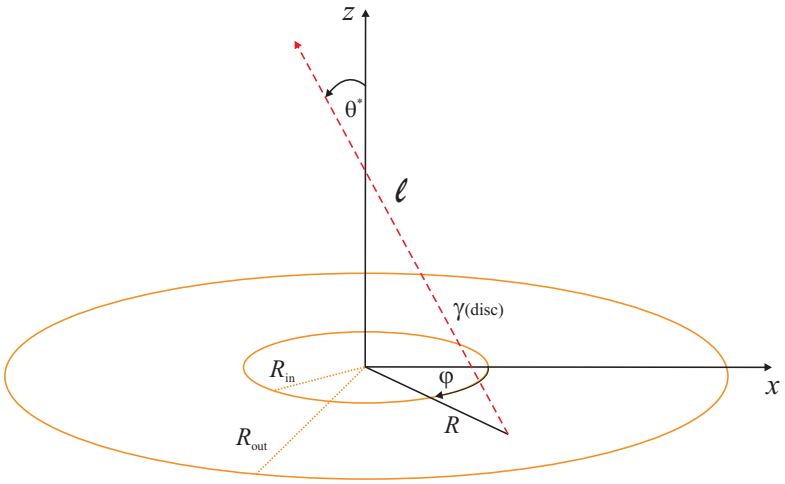

Figure 5.2: Sketch of the accretion disc. Some geometrical parameters relevant to the calculation of the inverse Compton emissivity with the disc radiation field as target are indicated.

We are interested in the number density of photons per unit energy per unit solid angle at height z on the jet axis, that were emitted per unit area at radius R in the accretion disc. In a reference frame fixed to the disc (where the

variables are denoted with starred symbols), this quantity can be written as

$$n_{\rm ph}\left(\epsilon^*, \Omega^*, z, R\right) = \frac{1}{\pi \ell^2 c}\, \dot{n}_{\rm ph}\left(\epsilon^*, R\right) \frac{1}{2\pi}\, \delta\left(\mu^* - \bar{\mu}^*\right). \tag{5.15}$$

Here $\ell^2 = z^2 + R^2$ and $\bar{\mu}^* = \cos\theta^* = z/\ell$, see Figure 5.2. The delta functional appears because the polar angle of the direction of motion of the disc photon is fixed once the values of R and z are chosen. The emissivity of photons per unit disc area at radius R is $\dot{n}_{\rm ph}\left(\epsilon^*, R\right)$.

To insert it in the expression for the IC emissivity, Eq. (5.15) must be first transformed to the jet frame. The transformation is easily done using that the ratio $n_{\rm ph}/\epsilon^2$ is a relativistic invariant. This yields

$$n_{\rm ph}\left(\epsilon, \Omega, z, R\right) = \frac{1}{2\pi^2 \ell^2 c}\, \dot{n}_{\rm ph}\left(\epsilon^*, R\right)\, \delta\left(\mu - \bar{\mu}\right), \tag{5.16}$$

where the photon energy and the cosine of the polar angle in both frames are related as

$$\epsilon^* = \Gamma_{\rm jet} \epsilon \left(1 + \beta_{\rm jet}\, \mu\right) \tag{5.17}$$

and

$$\bar{\mu} = \frac{\bar{\mu}^* - \beta_{\rm jet}}{1 - \beta_{\rm jet}\, \bar{\mu}^*}. \tag{5.18}$$

Finally, we must provide an expression for $\dot{n}_{\rm ph}\left(\epsilon^*, R\right)$. To keep the calculations as simple as possible, we approximated the radiation field of the disc at fixed R as monoenergetic at energy $\bar{\epsilon}^* = 2.7kT(R)$. This is the mean energy of the photons emitted by a black body of temperature $T(R)$. Then, the disc emissivity per unit area can be estimated as

$$\dot{n}_{\rm ph}\left(\epsilon^*, R\right) \approx \frac{1}{\epsilon^*}\, D(R)\, \delta(\epsilon^* - \bar{\epsilon}^*) = \frac{1}{\epsilon^*}\, \sigma_{\rm SB} T(R)^4\, \delta(\epsilon^* - \bar{\epsilon}^*). \tag{5.19}$$

The optical depth due to photon-photon absorption in the radiation field of the disc is given by the generalized form of Eq. (3.82) that includes the full

angular dependency of the parameters. For a photon with energy E_γ emitted at height z on the jet axis with polar angle Φ

$$\tau_{\gamma\gamma}(E_\gamma, z, \Phi) = \int_0^\infty \mathrm{d}\lambda \int_{\epsilon_{\rm thr}}^\infty \mathrm{d}\epsilon \oint \mathrm{d}\Omega\,(1-\cos\theta)\,\sigma_{\gamma\gamma}(E_\gamma, \epsilon, \theta)\,n_{\rm ph}(\epsilon, \vec{r}, \Omega). \tag{5.20}$$

Here $n_{\rm ph}$ is the energy distribution of the disc radiation (that we approximate as monoenergetic as before) and $\sigma_{\gamma\gamma}$ is the annihilation cross section, see Eq. (3.80). The variable λ is the length of the path traversed by the jet photon until the interaction point and θ is the collision angle. These and other relevant geometrical variables are indicated in Figure 5.3.

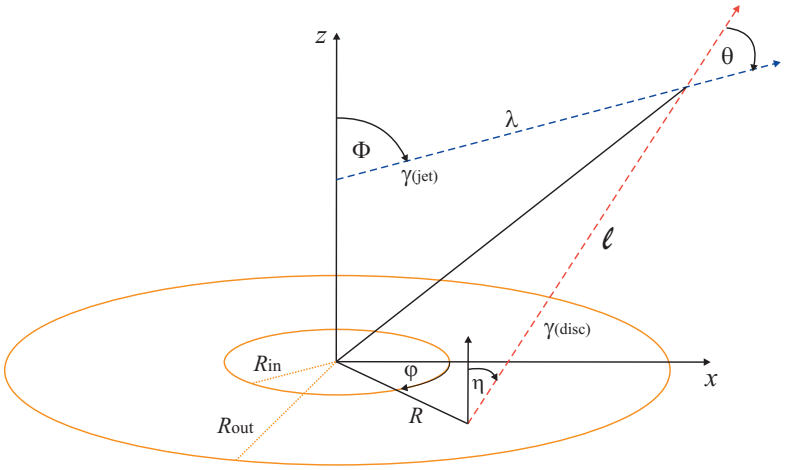

Figure 5.3: Sketch of the accretion disc. The geometrical parameters relevant to the calculation of the optical depth in the radiation field of the accretion disc are indicated.

It is convenient to perform the integration over the surface of the disc instead that over the solid angle. The differential $\mathrm{d}\Omega$ is related to the differential of area $\mathrm{d}A = R\mathrm{d}R\mathrm{d}\varphi$ on the disc as

$$\mathrm{d}\Omega = \frac{\cos\eta\, R\,\mathrm{d}R\,\mathrm{d}\varphi}{\ell^2}. \tag{5.21}$$

After some lengthy algebra, the variables ℓ, $\cos\eta$, and $\cos\theta$ can be written in terms of R, φ, z, and λ. The expressions are given, for example, in Becker & Kafatos (1995); we develop them in further detail in Appendix A.

5.3 GENERAL RESULTS

We present the results of four representative models with different values of some of the parameters. These general models do not include the accretion disc. In all cases we fixed $M_{\rm BH} = 10 M_\odot$, $z_0 = 50\, R_{\rm grav}$, $r_0 = 0.1\, z_0$, $z_{\rm end} = 10^{12}$ cm, $\theta_{\rm jet} = 30^\circ$, $q_{\rm accr} = 0.1$, $q_{\rm jet} = 0.1$, $q_{\rm rel} = 0.1$, $\eta = 0.1$, and $E_{\rm min} = 10\, m_{(e,p)} c^2$. The parameters specific to each model are listed in Table 5.1.

5.3.1 *Cooling rates*

In Figures 5.4 and 5.5 we plot the cooling rates for primary electrons and protons in Model A of Table 5.1. They are calculated at $z = z_{\rm acc}$ (base of the acceleration region), $z = z_{\rm max}$ (top of the acceleration region), and $z = z_{\rm end}$ ("end" of the jet).

Synchrotron radiation dominates the cooling of electrons near the base of the acceleration region. Further away from the black hole this process gradually becomes less relevant at lower energies. The maximum energy of electrons, however, is always determined by the balance of the synchrotron cooling rate and the acceleration rate. Synchrotron self-Compton energy losses are in general much smaller and the cooling due to relativistic Bremsstrahlung is negligible.

Adiabatic energy losses are the most important for protons all along the jet. Notice that the cooling due to proton-photon interactions is completely negligible at large z because the density of the target photon field is very low.

5.3.2 *Particle injection and energy distributions*

Figure 5.6 shows the dependence of the injection function on energy and z for primary electrons and protons in Model A. The injection is confined to the region $z < z_{\rm max} = 10^{10}$ cm. As expected from the cooling rates in Figures 5.4 and 5.5, protons reach energies much higher than electrons. The maximum energy of electrons is determined by the synchrotron losses, and so it grows with z as the magnetic field decreases. For protons adiabatic losses are the main cooling channel, and the maximum proton energy decreases with z.

The steady state particle distributions calculated from Eq. (5.6) are plotted

Table 5.1: Values of the parameters of four representative models of inhomogeneous jet.

Parameter (symbol)	Model A	Model B	Model C	Model D
Magnetic field decay index (m)	1.5	2.0	1.5	1.5
Ratio U_B/U_k at z_acc (ρ)	0.9	0.9	0.5	0.1
Base of the acceleration region (z_acc)	1.8×10^8 cm	1.2×10^8 cm	3.2×10^8 cm	1.6×10^9 cm
End of the acceleration region (z_max)	10^{10} cm	10^{10} cm	10^{11} cm	10^{10} cm
Ratio L_p/L_e (a)	1	100	1	1
Power relativistic protons (L_p)	3.2×10^{35} erg s^{-1}	6.4×10^{35} erg s^{-1}	3.2×10^{35} erg s^{-1}	3.2×10^{35} erg s^{-1}
Power relativistic electrons (L_e)	3.2×10^{35} erg s^{-1}	6.4×10^{33} erg s^{-1}	3.2×10^{35} erg s^{-1}	3.2×10^{35} erg s^{-1}
Particle injection spectral index (α)	1.5	1.5	1.5	2.2

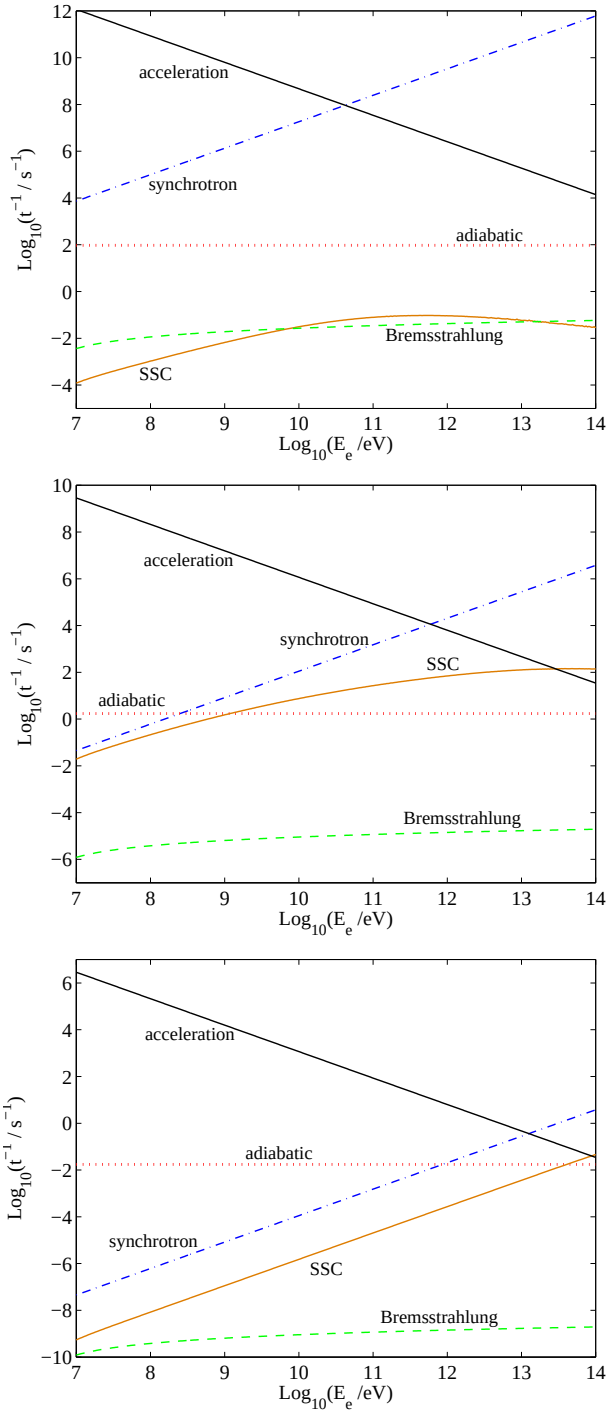

Figure 5.4: Cooling and acceleration rates for relativistic electrons for Model A (see Table 5.1) at the base (top) and the top (center) of the acceleration region, and at the "end" of the jet (bottom).

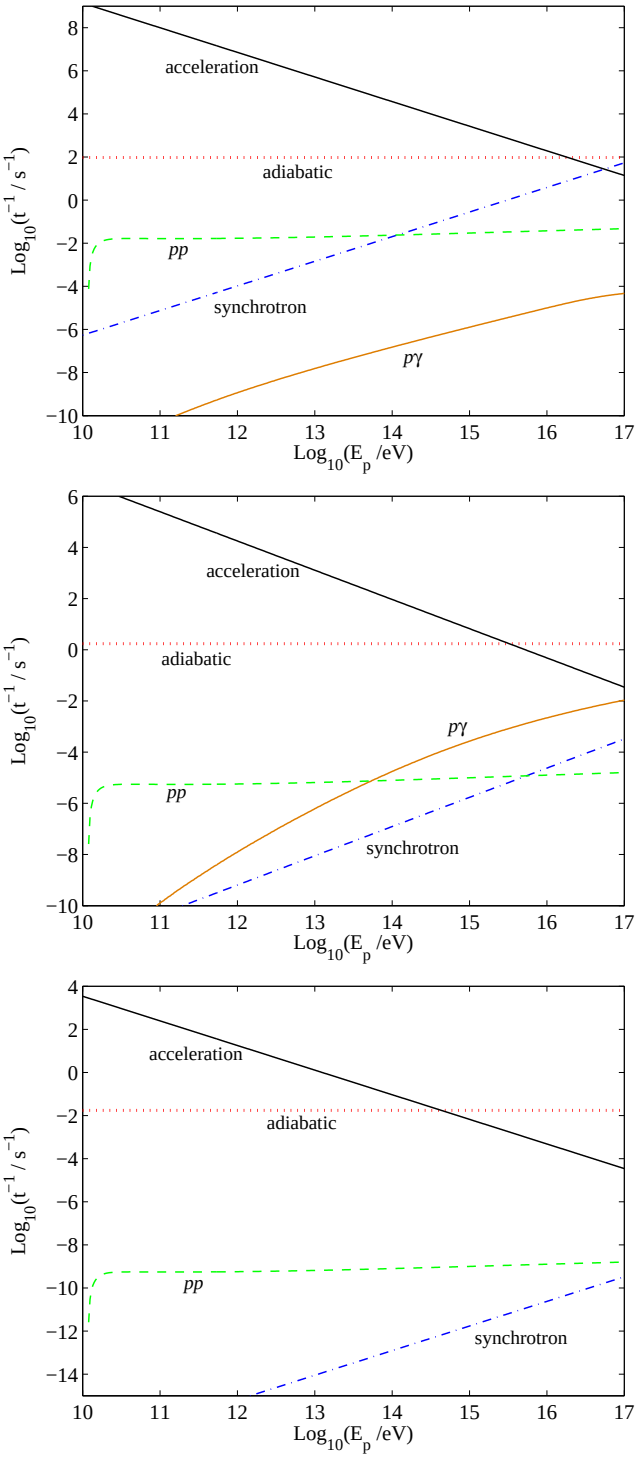

Figure 5.5: The same as in Fig. 5.4 but for relativistic protons. The abbreviations "pp" and "$p\gamma$" stand for proton-proton and proton-photon, respectively.

in Figure 5.7. Notice that the most energetic electrons quickly disappear after the injection is switched off - they cool and accumulate at lower energies. Since the cooling times are much longer for protons than for electrons, the behaviour of the proton distribution is quite different. The number of the most energetic protons also decreases for $z > z_{\rm max}$, but there are plenty of high-energy protons outside the acceleration region. It is interesting to note that in one-zone models (where there is no convection term in the transport equation, or it is replaced by an escape term) the particle distributions would be zero in those regions where $Q(E, z) \approx 0$.

5.3.3 *Spectral energy distributions*

Figures 5.8 and 5.9 show the spectral energy distributions obtained for the four models of Table 5.1. Very different spectral shapes result.

In Model A the power injected in relativistic protons is large ($a = 1$). The jet emission up to ~ 1 TeV is synchrotron and IC radiation of primary electrons, reaching luminosities of $\sim 10^{36}$ erg s^{-1} at ~ 10 MeV. The very high-energy tail of the spectrum is due to proton-proton and proton-photon interactions.

In Model B most of the energy is transferred to relativistic protons ($a = 100$). The synchrotron radiation of primary electrons is greatly reduced, and so are all other interactions that have this photon field as target (proton-photon collisions and IC scattering). Furthermore, in this model $m = 2$ and the magnetic field strength decreases rapidly with z. This also contributes to quench the synchrotron emissivity. Notice that the radiative output of proton-proton collisions is only slightly affected compared to that of Model A.

The only difference between Model C and Model A is the extent of the acceleration region. In Model C the base of the region is shifted to slightly larger z and extends up to 10^{11} cm. This "spread" in the spatial distribution of the relativistic particles affects the proton-proton gamma-ray spectrum. The more extended the acceleration region, the less radiatively efficient this process is.

Finally, in Model D the injection spectral index of the relativistic particles is changed from $\alpha = 1.5$ to $\alpha = 2.2$. This turns the electron synchrotron spectrum from hard to relatively soft. The same happens with the emission

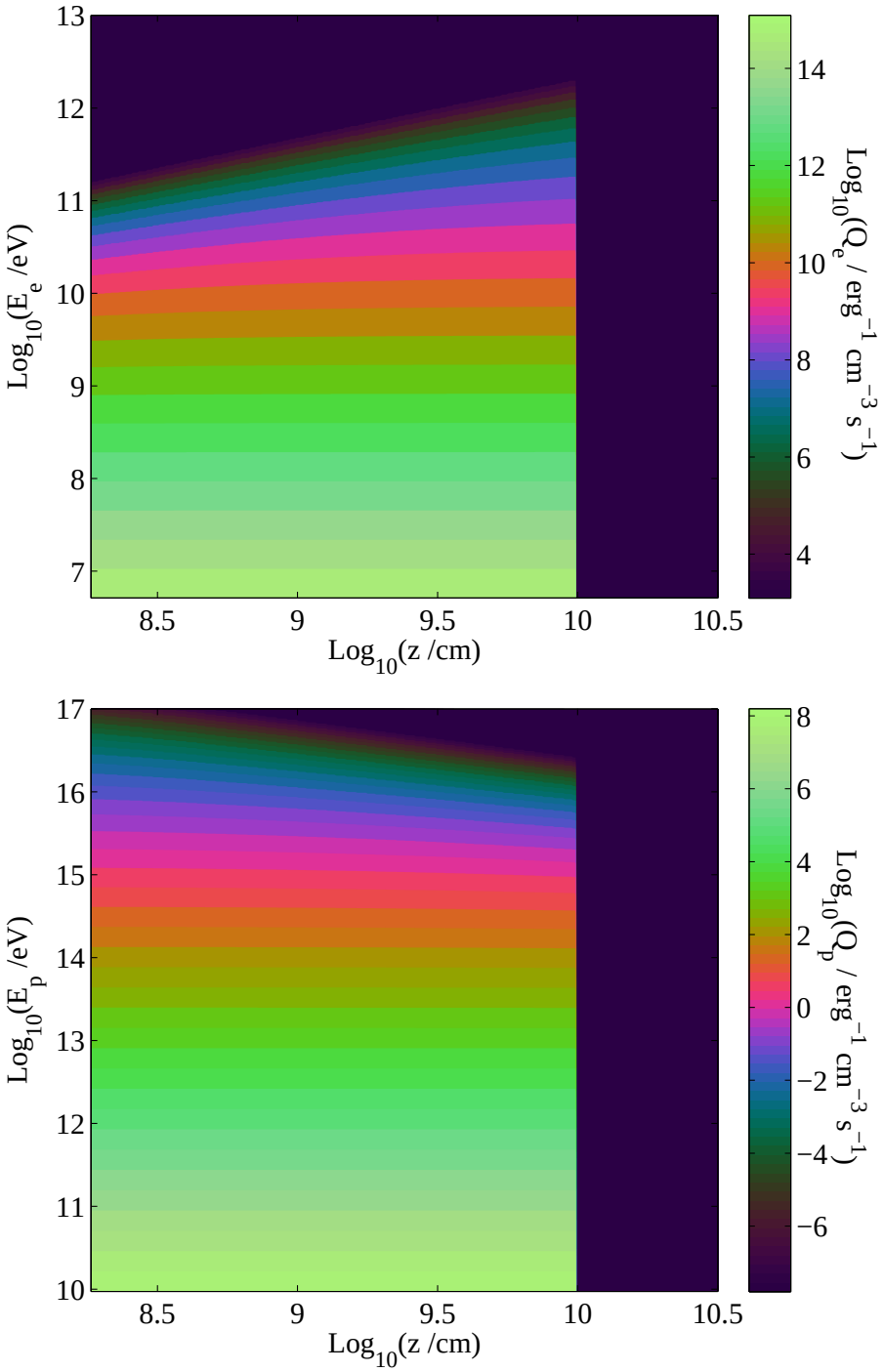

Figure 5.6: Injection function of relativistic electrons (top) and protons (bottom) for Model A (see Table 5.1). All color maps are chosen to have monotonous luminance (McNames 2006, Green 2011) in order to ease interpretation.

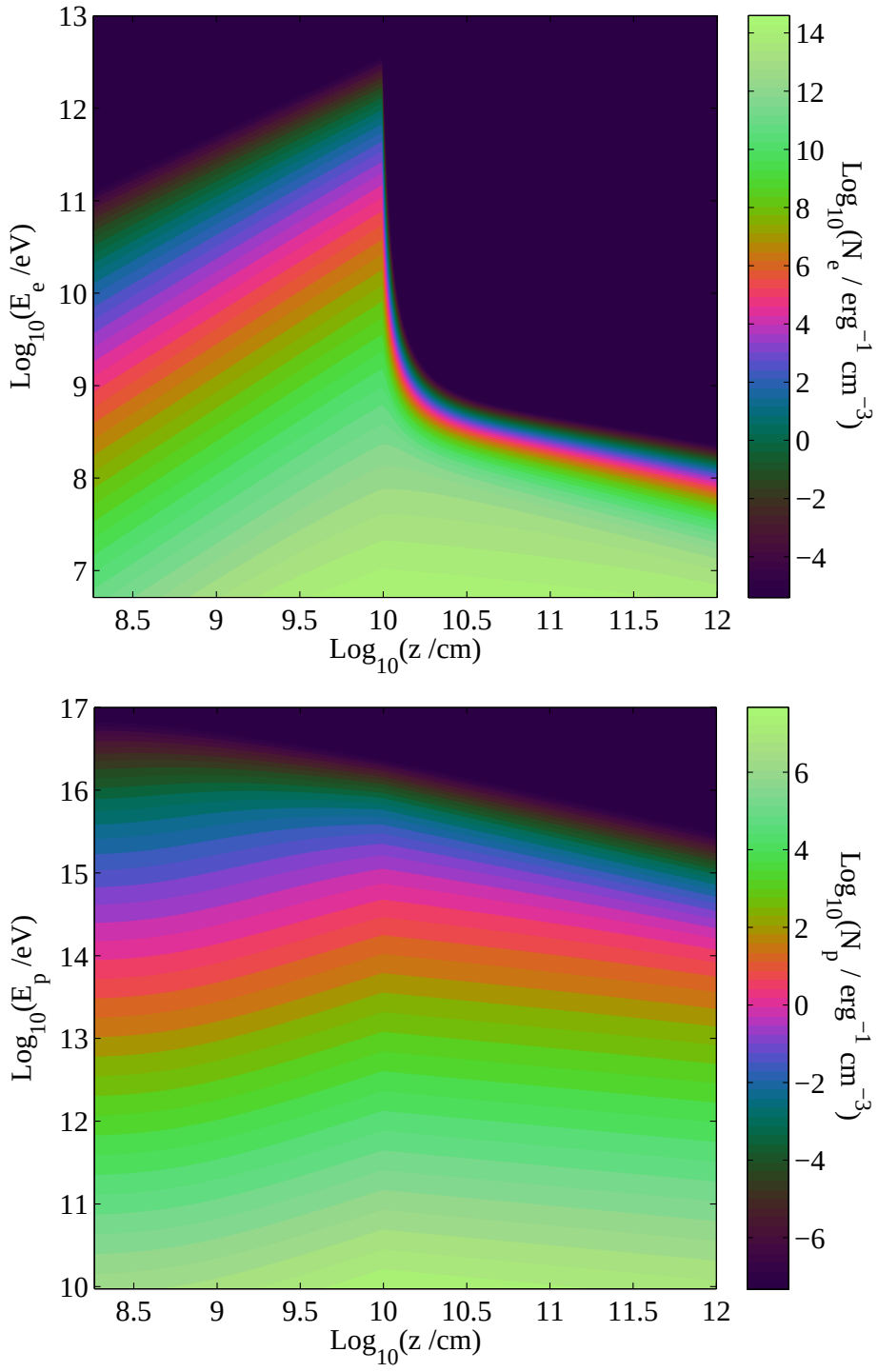

Figure 5.7: Energy distribution of relativistic electrons (top) and protons (bottom) for Model A (see Table 5.1).

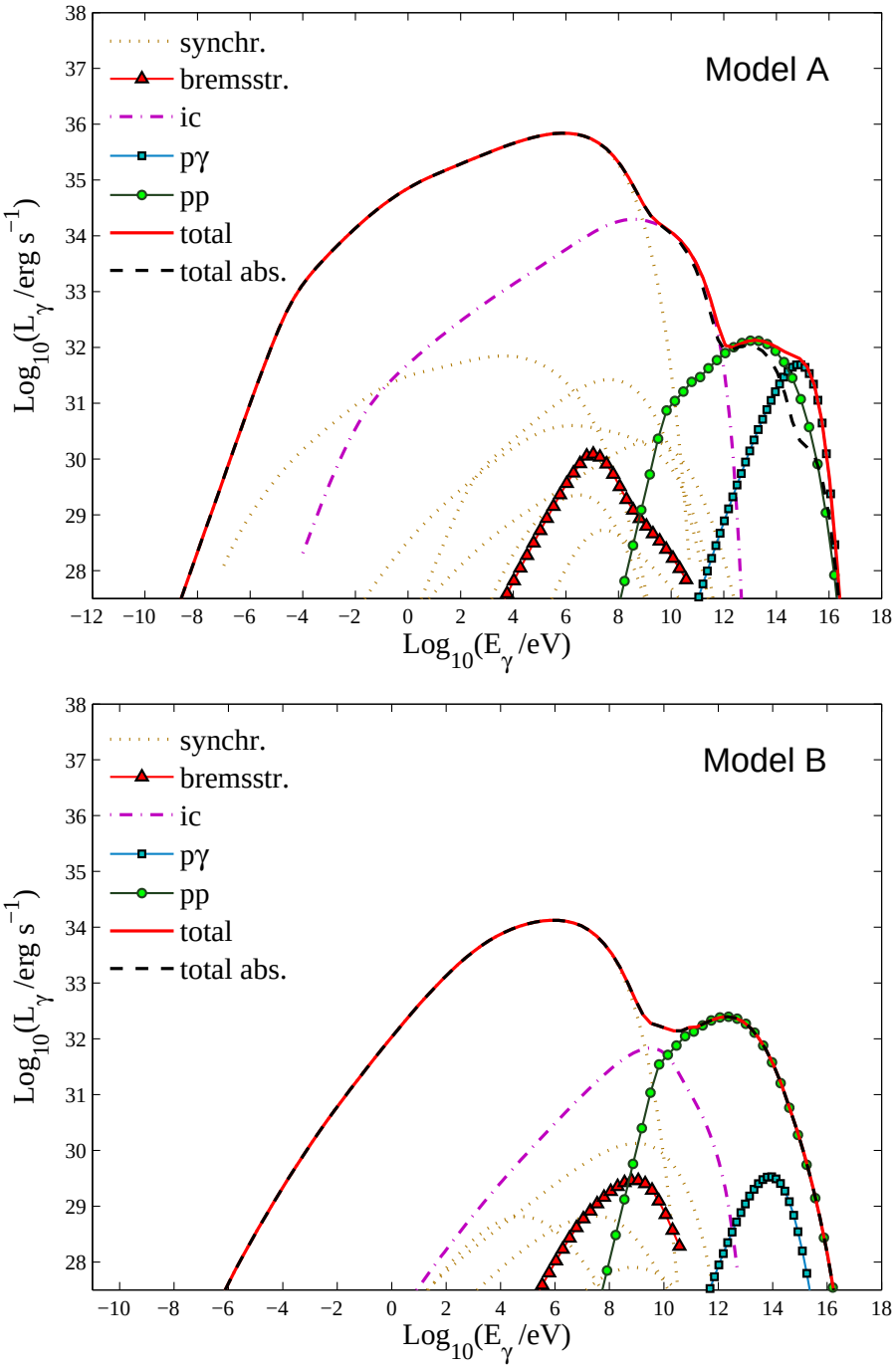

Figure 5.8: Spectral energy distributions for models A and B of Table 5.1. The various curves labelled "synchr." correspond to the synchrotron radiation of primary electrons (the most luminous component), protons, and secondary particles (pions, muons and electron-positron pairs).

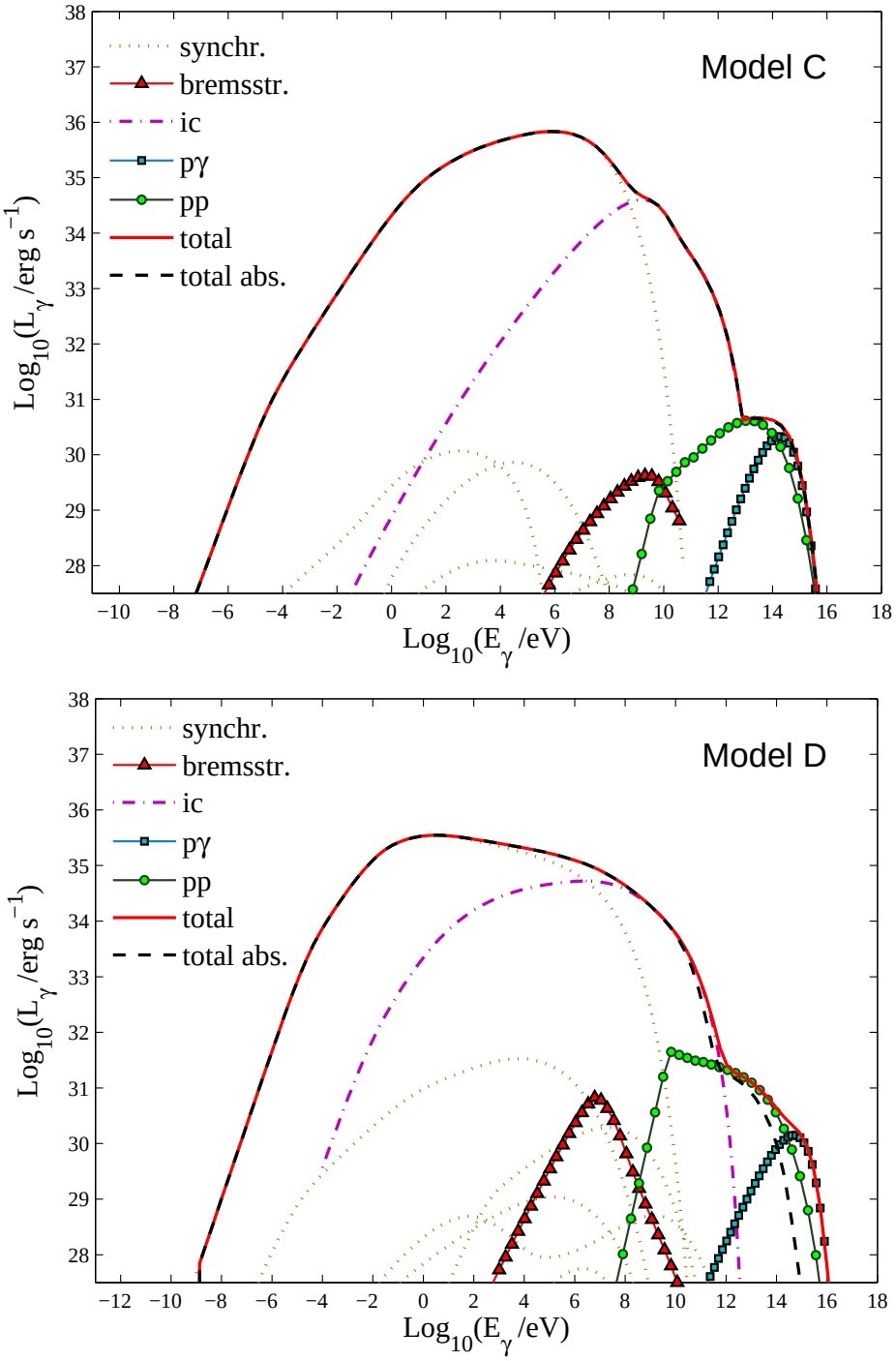

Figure 5.9: Same as in Figure 5.8 for models C and D.

due to proton-proton collisions.

Bremsstrahlung and synchrotron radiation of secondary particles do not contribute significantly to the SED in any model.

The total luminosity corrected by absorption in the internal radiation field of the jet is also plotted for every model in Figures 5.8 and 5.9. The effect of absorption is only noticeable at very high energies in Models A and D, where the acceleration region is less extended and the photon density is larger.

These four models do not exhaust the possible parameter space that can be explored. To calculate the SEDs of Models A to D, we chose a set of fixed parameters and studied the effects of varying the rest of them. Modifying other parameters, such as $q_{\rm accr}$ or η, would introduce further interesting changes in the spectrum, including higher gamma-ray luminosities. This is clearly exemplified by the SEDs calculated to fit the spectrum of XTE J1118+480 presented below.

5.4 THE LOW-MASS MICROQUASAR XTE J1118+480

5.4.1 *Characteristic parameters and observations*

XTE J1118+480 is an X-ray binary in the galactic halo. It hosts a low-mass donor star ($M_* \approx 0.37 M_\odot$) and a black hole of mass $M_{\rm BH} \approx 8.53 M_\odot$ (Gelino et al. 2006).

The estimated distance to XTE J1118+480 is $d \approx 1.72$ kpc (Gelino et al. 2006). The source is located at high galactic latitude ($b = +62^\circ$) in a region of low interstellar absorption along the line of sight. This peculiarity of its position allows to obtain very clean observations. It is possible that the system was born in the galactic plane and received a kick during the supernova explosion that led to the formation of the black hole, or it could have formed in a globular cluster in the halo and ejected later (Mirabel et al. 2001).

XTE J1118+480 is a transient XRB, spending long periods in quiescence. Since it was first detected in 2000 (Remillard et al. 2000), two outbursts have been observed: at the time of its discovery and in 2005. The source was extensively monitored at different wavelengths during the two episodes, and on both occasions the spectrum showed the characteristics of the low-hard state. No outflows have been directly imaged, but the presence of jets can be inferred

from the radio-to-infrared/optical emission (Fender et al. 2001).

The outburst of 2000 lasted for $\sim$ 7 months. Observational data with very complete spectral coverage are presented and analysed in Hynes et al. (2000), McClintock et al. (2001), Esin et al. (2001b), and Chaty et al. (2003). As shown in Chaty et al. (2003), the SED did not change significantly over a period of about 3 months. The second outburst started in January 2005 (Zurita et al. 2005, Pooley 2005, Remillard et al. 2005) and lasted for 1-2 months (Zurita et al. 2006). Radio-to-X-rays data from this epoch are presented in Hynes et al. (2006) and Zurita et al. (2006).

The radio-to-X-rays spectrum of XTE J1118+480 in outburst has been explained as the sum of the black body emission of a thin accretion disc and synchrotron radiation from non-thermal electrons in a jet. See, for example, the works of Markoff et al. (2001), Maitra et al. (2009), and Brocksopp et al. (2010). Other authors replace the contribution of the jet by that of a hot, optically thin ADAF, see Esin et al. (2001b) and Yuan et al. (2005). ADAF models, however, underpredict the observed radio and UV emission.

We apply our inhomogeneous jet model to fit the broadband data from the two known outbursts of XTE J1118+480. Differentiating from previous works, we explore the consequences of the injection of non-thermal protons and secondary particles in an extended region of the jet. We also consider the effects of internal and external absorption on the jet emission.

Table 5.2 shows a brief log of the observations used for the fits. The data from the 2000 outburst are taken from McClintock et al. (2001), whereas for the 2005 outburst we use the data published in Maitra et al. (2009).[1] We refer the reader to these works for details on the instrumental techniques and the reduction process. The UV/X-ray spectrum of the 2000 outburst displays a "dip" in the energy range 0.15-2.5 keV. According to Esin et al. (2001b) this feature might be caused by absorption in a region of partially ionized gas interposed in the line of sight. We exclude this energy band from the fits.

[1]The data were extracted with the help of the ADS's Dexter Data Extraction Applet and a script prepared by the author.

Table 5.2: Log of the observational data of XTE J1118+480 used in the fits.

Observation date	Instrument	Range
2000 April 18	Ryle Telescope	15.2 GHz
	UKIRT[(a)]	1-5 μm
	HST[(b)]	1155-10250 Å
	EUVE[(c)]	0.1-0.17 keV
	Chandra	0.24-7 keV
	RXTE - PCA[(d)]	2.5-25 keV
	RXTE - HEXTE[(e)]	15-200 keV
2005 January 23	Ryle Telescope	15.2 GHz
	UKIRT	J, H, K-band
	Liverpool Telescope	V, B-band
	RXTE	3-70 keV

[(a)] United Kingdom Infrared Telescope
[(b)] *Hubble Space Telescope*
[(c)] *Extreme Ultraviolet Explorer*
[(d)] *Rossi X-Ray Timing Explorer* - Proportional Counter Array
[(e)] *Rossi X-Ray Timing Explorer* - High Energy X-ray Timing Experiment

5.5 FITS OF THE SED OF XTE J1118+480 IN LOW-HARD STATE

5.5.1 *Parameters of the model*

In Table 5.3 are listed the values of the model parameters that were kept fixed during the fit. Some of them, as the black hole mass and the distance to Earth, were inferred from observations; we took their values from the literature on the source. The rest are parameters we have no information about for XTE J1118+480 (such as the bulk Lorentz factor), or they are specific to our model. For them we adopt typical values for other microquasars, or simply estimates.

The parameters in Table 5.4 were varied to obtain the best fits. The inner radius $R_{\rm in}$ and the temperature $T_{\rm max}$ determine the spectrum of the accretion disc and the value of $q_{\rm accr}$, that follows from Eqs. (5.2) and (5.13). The rest of the parameters of the jet model (see Table 5.5) are calculated from the fixed and free parameters using the equations of Section 5.1.

5.5.2 *Best-fit spectral energy distributions*

Figure 5.10 shows the best-fit SEDs for the 2000 and 2005 outbursts of XTE J1118+480. We obtained $\chi^2_\nu = 1.99$ and $\chi^2_\nu = 0.56$ for the chi-squared per degree of freedom, respectively.[2] The best-fit parameters are listed in Tables 5.3 to 5.5.

The value of the maximum temperature of the disc is in agreement with previous works, see for example McClintock et al. (2001), Markoff et al. (2001), Chaty et al. (2003), and Maitra et al. (2009). In the case of the 2000 outburst $T_{\rm max}$ is tightly constrained by the data, that clearly indicates the position of the peak of the multicolor black body component. There is no agreement in the value of the inner radius of the disc reported in the literature. This parameter is not well constrained by the observations, and depends on other details of the model as we discuss below.

We emphasize that our disc model is simple. We do not include effects such as irradiation of the outer disc (e.g. Dubus et al. 1999) or the transition to an ADAF in the surroundings of the black hole. We do not attempt, therefore, to constrain tightly any characteristic parameter of the disc, but just to account

[2] We applied the same optimization methods as in Chapter 4.

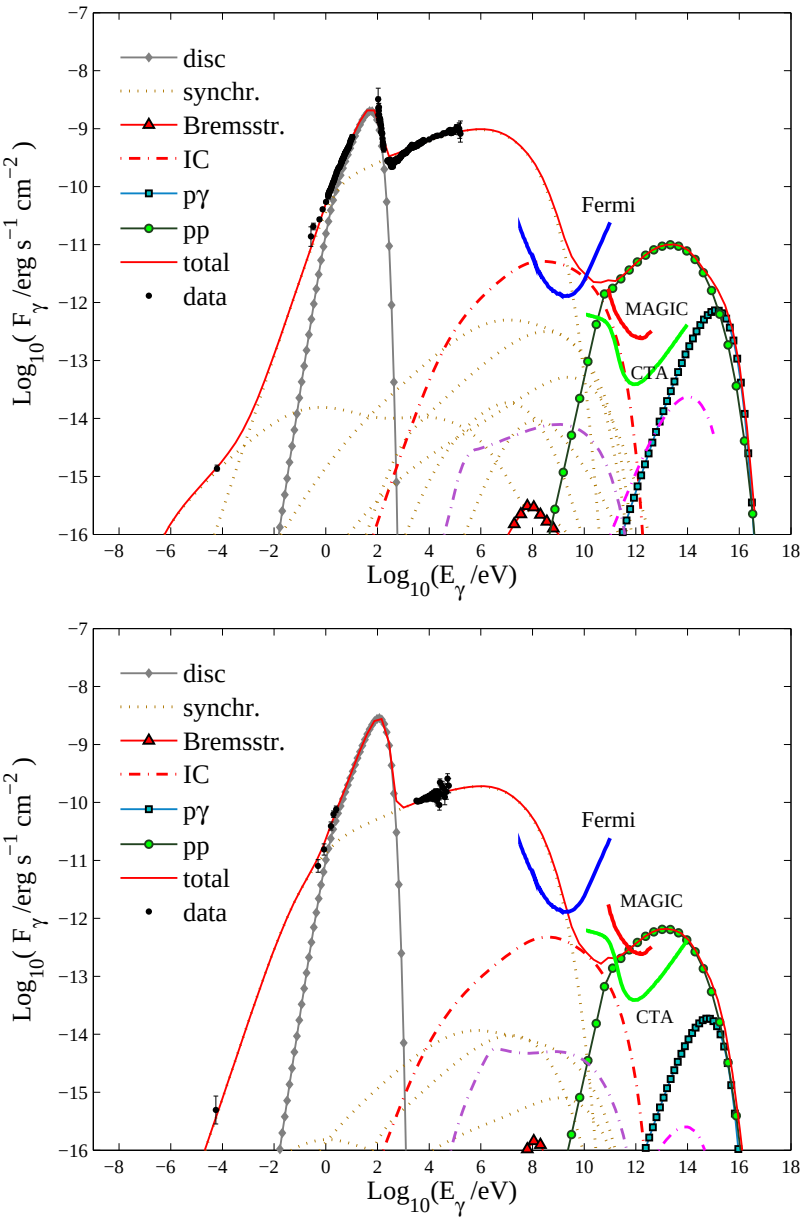

Figure 5.10: Best fit SEDs for the outbursts of 2000 (top) and 2005 (bottom) of XTE J1118+480. The various dotted curves labelled under the legend "synchr." correspond to the synchrotron radiation of primary electrons (the most luminous component), protons, and secondary particles (pions, muons and electron-positron pairs). The dash-dotted curves labelled "IC" correspond to the SSC luminosity of primary electrons (red), and the external IC luminosities of primary electrons (violet) and muons (magenta). Also shown are the sensitivity curves of *Fermi*-LAT (1 yr exposure, 5σ), MAGIC II (50 h exposure), and CTA (50 h exposure).

Table 5.3: Values of the fixed parameters in an inhomogeneous jet model for the microquasar XTE J1118+480.

Parameter	Symbol	Value
Distance to Earth	d	1.72 kpc$^{(a)}$
Black hole mass	$M_{\rm BH}$	$8.5 M_\odot$ $^{(a)}$
Disc outer radius	$R_{\rm out}$	$7 \times 10^4 R_{\rm grav}$ $^{(b)}$
Jet viewing angle	$\theta_{\rm jet}$	30°
Jet bulk Lorentz factor	$\Gamma_{\rm jet}$	2
Jet injection distance	z_0	$50 R_{\rm grav}$
Jet termination distance	$z_{\rm end}$	10^{12} cm
Jet initial radius	r_0	$0.1 z_0$
Ratio $L_{\rm rel}/L_{\rm jet}$	$q_{\rm rel}$	0.1
Magnetic field decay index	m	1.5
Particle injection spectral index	α	1.5
Acceleration efficiency	η	0.1

$^{(a)}$ Gelino et al. (2006)
$^{(b)}$ Chaty et al. (2003)

roughly for the thermal component observed in the SED.

The typical accretion power of XRBs in the LH state is $L_{\rm accr} \approx 0.01 - 0.1 L_{\rm Edd}$. The value of $q_{\rm accr} \approx 0.08$ we obtain from for the 2005 outburst is within this range. It is higher for the 2000 outburst, $q_{\rm accr} \approx 0.22$, mainly because the disc inner radius is larger. Once $T_{\rm max}$ and $\theta_{\rm d}$ are fixed, $R_{\rm in}$ determines the normalization of the spectrum. The maximum temperature of the disc for the 2000 outburst is well constrained; the inclination angle, however, is unknown. The best-fit value of $R_{\rm in}$ then depends on the value chosen for $\theta_{\rm d}$, that we took equal to 30°.[3] Given the strong dependence of the accretion power on $R_{\rm in}$ (see Eq. 5.13), small variations in this parameter yield significant changes in $q_{\rm accr}$.

[3]There are estimates of the orbital inclination for XTE J1118+480, see e.g. Gelino et al. (2006). However, there is no compelling reason to assume that the disc lies in the orbital plane of the binary. See, for example, Maccarone (2002), Butt et al. (2003), and Romero & Orellana (2005) for a discussion on misaligned microquasars.

Table 5.4: Best-fit values of the free parameters in an inhomogeneous jet model for the microquasar XTE J1118+480.

Parameter	Symbol	Value	
		2000	2005
Disc inner radius	$R_{\rm in}$	$164\,R_{\rm grav}$	$44\,R_{\rm grav}$
Disc maximum temperature	$T_{\rm max}$	22.4 eV	46.5 eV
Ratio $L_{\rm jet}/L_{\rm accr}$	$q_{\rm jet}$	0.16	0.16
Ratio $U_B/U_{\rm k}$ at $z_{\rm acc}$	ρ	0.5	0.85
Ratio L_p/L_e	a	12.2	25.5
End of acceleration region	$z_{\rm max}$	8.2×10^{9} cm	1.5×10^{10} cm
Minimum energy primary protons and electrons	$E_{\rm min}$	$86\,m_{(p,e)}c^2$	$150\,m_{(p,e)}c^2$

According to our modeling, there are no great differences in the physical conditions in the jets during the two outbursts. The radio and X-ray emission is fitted by the synchrotron spectrum of primary electrons, plus some contribution at low energies of secondary pairs created through photon-photon annihilation. The IR-optical-UV range has significant contribution from the accretion disc. The synchrotron emission of secondary particles is negligible (except in the case mentioned above), as well as Bremsstrahlung radiation of primary electrons. The IC scattering off the jet photon field by primary electrons contributes in a narrow energy range about $\sim$ 10 GeV in the case of the 2000 outburst. The SED above $\sim$ 1 GeV is completely dominated by gamma rays from the decay of neutral pions created in proton-proton collisions.

The attenuation factor $e^{-\tau_{\gamma\gamma}}$ as a function of energy and z is plotted in Figure 5.11. The main source of absorbing photons is the accretion disc. The internal radiation field of the jet only adds a "bump" at high energies, mainly due to absorption in the synchrotron field of primary electrons, see Figure 5.12. The optical depth is large only near the base of the acceleration region. Gamma rays with energies 10 GeV $\leq E_\gamma \leq$ 1 TeV are mostly absorbed in this zone. The development of electromagnetic cascades, however, is suppressed by the high magnetic field, see Pellizza et al. (2010).

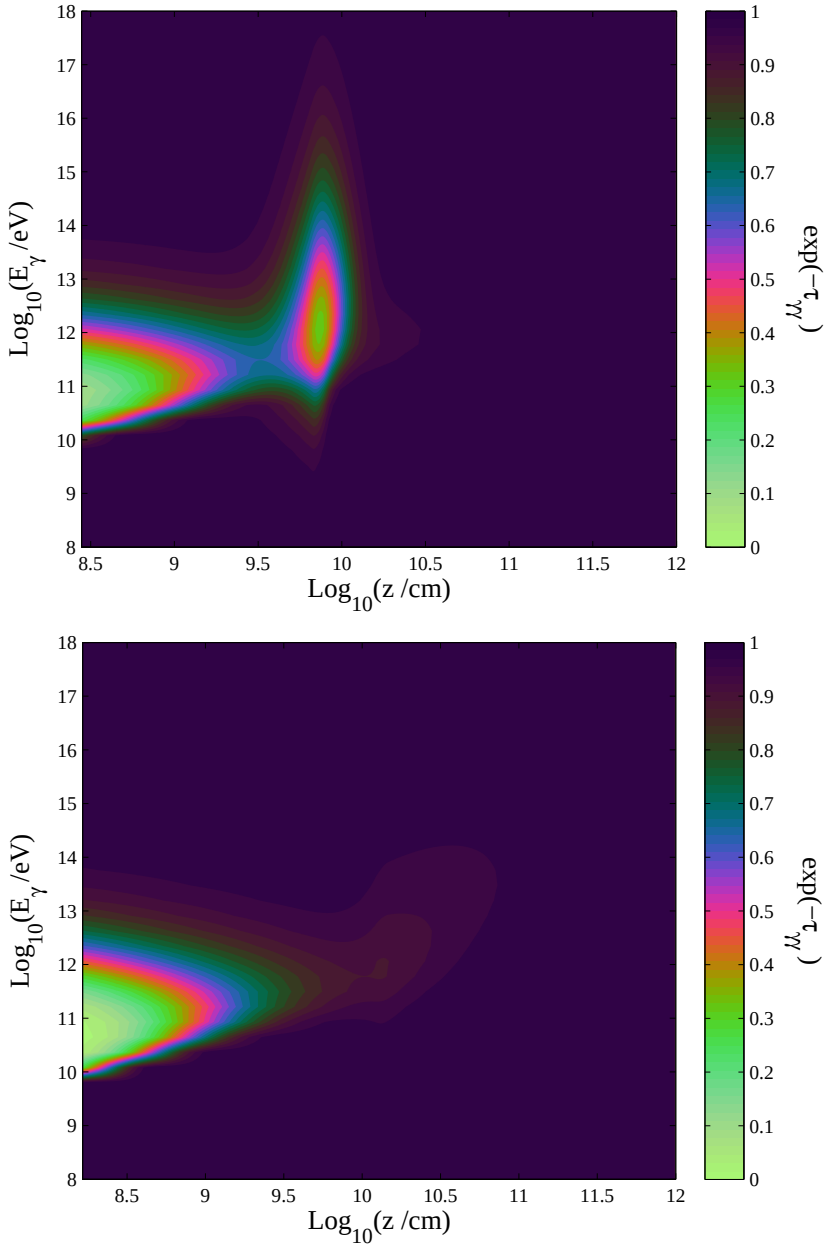

Figure 5.11: Total attenuation factor $\exp(-\tau_{\gamma\gamma})$ due to photon-photon annihilation for the best-fit SEDs of the 2000 (top) and 2005 (bottom) outbursts of XTE J1118+480.

Table 5.5: Best-fit values of the free parameters in an inhomogeneous jet model for the microquasar XTE J1118+480 (continued).

Parameter	Symbol	Value	
		2000	2005
Accretion power	$L_{\rm accr}$	2.6×10^{38} erg s^{-1}	9.9×10^{37} erg s^{-1}
Jet power	$L_{\rm jet}$	2.1×10^{37} erg s^{-1}	8.1×10^{36} erg s^{-1}
Power relativistic protons	L_p	1.9×10^{36} erg s^{-1}	7.8×10^{35} erg s^{-1}
Power relativistic electrons	L_e	1.6×10^{35} erg s^{-1}	3.1×10^{34} erg s^{-1}
Magnetic field jet base	B_0	1.3×10^{7} G	7.9×10^{6} G
Base of the acceleration region	$z_{\rm acc}$	2.8×10^{8} cm	1.6×10^{8} cm

The total luminosities are unmodified by absorption. The reason is that there are many high-energy protons that produce gamma rays through proton-proton collisions outside the acceleration region. This radiation escapes unabsorbed since the density of disc photons is low at high z.

The sensitivity curves of *Fermi*-LAT, MAGIC II, and the predicted for CTA are also plotted in Figure 5.10. According to our results, a future outburst of the source with emission levels comparable to those of 2000 and 2005, would be detectable in gamma rays by ground-based observatories like MAGIC II and CTA. In the context of the model presented here, observations at very high energies would help to constrain the hadronic content of the jets, since above ~ 100 GeV the predicted emission is completely due to proton-proton interactions.

The detectability in the *Fermi* band depends basically on the position of the synchrotron cutoff. We fixed $\eta = 0.1$ for the acceleration efficiency; this yields a large maximum energy for the electrons, and the synchrotron emission extends into the MeV energy range. Observations with *Fermi*, then, could help to investigate the efficiency of particle acceleration in jets of microquasars like XTE J1118+480.

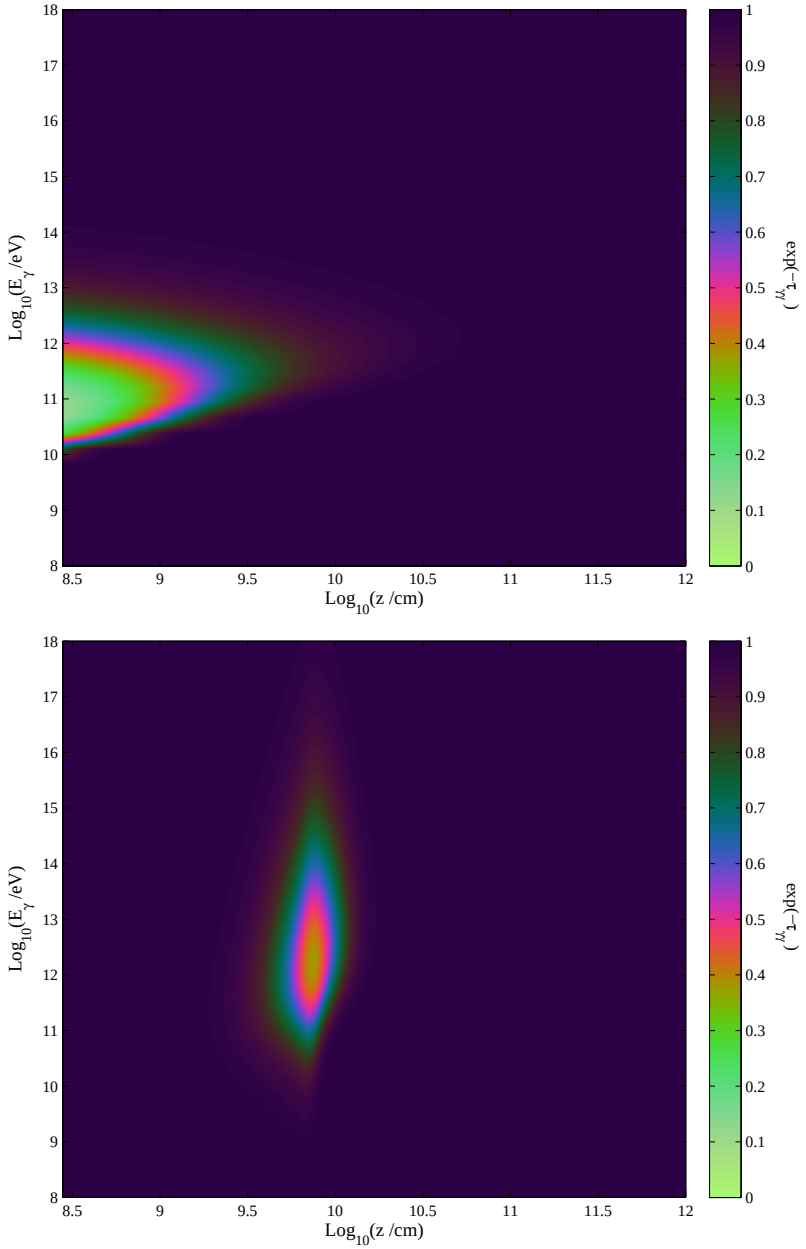

Figure 5.12: Total attenuation factor $\exp(-\tau_{\gamma\gamma})$ due to photon-photon annihilation in the radiation field of the accretion disc (top) and the internal radiation field of the jet (bottom), for the best-fit parameters of the 2000 outburst of XTE J1118+480.

6

CONCLUSIONS

The important thing is not to stop questioning. Curiosity has its own reason for existing.

Albert Einstein

In the last ten years there has been a major breakthrough in observational gamma-ray astronomy. The volume and quality of the data have substantially increased since the deployment of the present generation of gamma-ray satellites and terrestrial Cherenkov telescopes. The number of high and very high energy sources (many of unidentified type) has grown from the < 300 listed in the Third EGRET Catalog (Hartman et al. 1999) to about 2000, over 1800 of them in the Second *Fermi*-LAT Catalog (Nolan et al. 2012, see also Vandenbroucke 2010). This calls for an effort to build models to explain, at least, which type of particle interactions yield the observed spectra, reproduce their characteristics, and, through it, gain insight into the physical conditions in the sources. Such has been the fundamental motivation of this thesis, in what concerns relativistic jets.

Along this work we developed a lepto-hadronic model for the radiation from jets in microquasars. We adopted the following general conceptual picture of the source. Two mildly relativistic jets are launched from the vicinities of an accreting stellar-mass black hole. The ejection mechanism is of magnetohydrodynamical origin, so the outflows are energetically dominated by the magnetic field near the launching region. Magnetic energy gradually converts

into bulk kinetic energy as the jets propagate. At some distance from the central engine, shock waves develop in the jet. These shocks mediate the acceleration of a fraction of the thermal electrons *and* protons up to relativistic energies. The acceleration of protons is efficient, and at least as much power is injected in relativistic protons as in electrons. Non-thermal protons and electrons (as well as the charged by-products of hadronic collisions) cool by interaction with matter, photons, and magnetic field, emitting electromagnetic radiation at all energies from radio to gamma rays. The produced electromagnetic spectrum might be modified by absorption before reaching the observer. Within this global picture, we explored a large number of particular scenarios and obtained broadband electromagnetic spectral energy distributions with very different characteristics.

We have attempted to add as much detail and self-consistency to the model as possible. The model contains a number of parameters that determine the physical conditions in the jets and the distribution of relativistic particles. For these parameters we took, when available, estimates inferred from observations. The values of other parameters (such as the position of the acceleration region and the spectral index of the particle injection function) were chosen to account, in an affective manner, for the main constraints imposed by the physics of particle acceleration and the dynamics of the outflow. Our modeling of the source is, nevertheless, by no means free of limitations. The most important one is, perhaps, related to the magnetic field. This is a key feature of the model, and many of the results depend on our assumptions about the value of the magnetic field in the jet launching region and how it decays further away from the compact object. We have made simple and reasonable assumptions on this point, but they might require further refinement in the light of future insights and observational data.

The model was developed in stages of increased complexity. We gradually generalized some assumptions, refined the treatment of particle transport, and included new interaction processes. The initial models were "one-zone"; the compact, homogeneous acceleration region was placed at the base of the jet. We later considered a location further away from the black hole, in regions where the kinetic energy density dominates over the magnetic energy density. Magnetohydrodynamical models predict that this condition favours the forma-

tion of shock waves. Finally, we progressed to study the injection and cooling of relativistic particles in a spatially extended, inhomogeneous region of the jet. This implied the introduction of a more general version of the transport equation that accounted for particle convection.

The very first one-zone models did not include interactions with matter; this was added for the applications in Chapter 4 starting with the model for the *AGILE* sources. At this stage we also included the radiative contribution of charged pions and muons. For the model of GX 339-4, we calculated as well the synchrotron radiation of pairs injected in proton-proton collisions, muon decay, and photon-photon annihilation. As the model was conceived for jets in low-mass microquasars, throughout the thesis we neglected the interaction between the jet and the radiation and the wind from the companion star. For the modeling of the SED of XTE J1118+480 in Chapter 5, however, we added the radiation field of the disc as a target for inverse Compton scattering and gamma-ray absorption.

In its current version, the model is suited to the study of low-mass microquasars, but there are a number of specific improvements that would allow a broader application. For example, by considering the interaction between the relativistic particles in the jets with the radiation and the wind from the companion star (see for example Perucho & Bosch-Ramon 2012),[1] the model could be applied to high-mass microquasars.

With some further modifications, the same jet model can be also applied to active galactic nuclei and gamma-ray bursts. The main modifications concern the calculation of the particle distributions. These sources have outflows with very high bulk Lorentz factors, so all the relativistic effects must be carefully taken into account. The transport equation, for example, must be modified to a covariant version. Besides, in environments where the radiation field is ultra dense (like in the jets of long gamma-ray bursts), the coupling among the kinetic equations for particles and photons cannot be ignored. A further generalization of the transport equation includes time dependence, allowing the study of flares.

We have shown that the spectral energy distributions from microquasar jets might be complex and take a variety of shapes depending on the conditions in

[1] This would require, as well, the introduction of a model for the stellar wind.

the source. We have tried to cover a large number of scenarios, always within a physically meaningful range for the values of the model parameters.

The general results of this thesis can be summarized as follows:

• Relativistic jets from low-mass X-ray binaries with a content of non-thermal electrons and protons radiate along the whole electromagnetic spectrum. Under some particular conditions, they might emit high and very high energy gamma rays at levels detectable with presently operative instruments.

• From radio to X-rays the emission is of leptonic origin, predominantly due to synchrotron radiation. In the context of our model, the synchrotron luminosity is a good proxy for the power injected in relativistic electrons, since these cool almost completely through this channel. It also provides information about the acceleration mechanism, because the spectral index and the maximum energy of the particles can be inferred from the slope and the cutoff energy of the synchrotron spectrum.

• In particle "equipartition" models ($a \sim 1$) with a high acceleration efficiency ($\eta = 0.1$), there is significant synchrotron self Compton emission between ~ 1 MeV and ~ 0.1 TeV.

• In proton-dominated models ($a > 1$), the spectrum above ~ 1 GeV is of hadronic origin.

• If the acceleration region is near the base of the jet (where the magnetic field is stronger), the synchrotron radiation of relativistic protons is significant at energies $\sim 1 - 10$ GeV. The peak luminosity of this component may be as large as $10^{34} - 10^{36}$ erg s^{-1}. The position of the proton synchrotron peak depends on the acceleration efficiency parameter η.

• The radiation above ~ 10 GeV is emitted by the products of proton-proton and proton-photon inelastic collisions: neutral pions that decay into two gamma rays and energetic secondary electron-positron pairs that cool by synchrotron radiation.

• Proton-proton and proton-photon inelastic collisions inject charged pions and muons. For values of the magnetic field as those we adopted ($\sim 10^6 - 10^7$ G

at the base of the jet), the cooling of these particles before decay cannot be neglected. We have shown in Chapter 4, Section 4.2, that muons in particular can produce significant synchrotron radiation at X-ray energies.

• The strong cooling of pions and muons modifies their energy distribution at decay, consequently affecting the energy spectrum of their decay products. This is particularly relevant when making predictions for the neutrino emission from microquasars, as demonstrated by Reynoso & Romero (2009).

• The high and very high energy gamma-ray spectrum, although of hadronic origin, is coupled to the leptonic content of the jets. This is because the efficiency of photohadronic interactions and the optical depth due to photon-photon annihilation depend on the density of the electron synchrotron radiation. This photon field plays in our model a role similar to that of the radiation field of the companion star in models for high-mass microquasars.

• Gamma rays can escape the source without significant absorption if the emission region is located in a zone of the jet where the internal radiation field has low density. In one-zone models this is possible if the relativistic particles are injected at large distances from the black hole, where the magnetic field is significantly lower that in the jet base and the internal radiation field is diluted because the outflow has expanded. In models for extended jets, absorption can be avoided even if the acceleration region is relatively near the jet base. As we have shown in Chapter 5, leptonic emission is confined mostly to the acceleration region; the most energetic electrons rapidly cool where the injection vanishes. Plenty of energetic protons, however, leave the acceleration region and inject gamma rays (by decay of neutral pions created in proton-proton collisions) in zones with low internal (and eventually external) photon density.

We performed three concrete applications of the jet model. Two of them are fits to observations of very well studied low-mass microquasars, GX 339-4 and XTE J1118+480. We make predictions for the high and very high energy gamma-ray spectrum during outbursts, a question not addressed in previous works about these sources. From the three applications of the model we conclude:

• Low-mass microquasars might be the counterpart of some of the galactic transient gamma-ray sources detected with the satellite *AGILE*. A salient characteristic of the observed spectra, namely the lack of simultaneous detection at X-rays with SuperAGILE, can be reproduced in proton-dominated jet models. The luminosities predicted by these "X-ray quiet" models are of the order of the measured with *AGILE* ($\sim 10^{34}$ erg s^{-1} at $\sim$ 100 MeV) if the sources are nearby, at distances of $\sim 300 - 400$ pc. In such case, the results of the models indicate that these systems would be readily detected at high and very high energies, although this could be complicated because of their variable behaviour on timescales of 1-2 d.

• The broadband spectral energy distribution of the low-mass microquasar GX 339-4 may be satisfactorily reproduced by the model, both during outburst and low-luminosity hard X-ray states. The radio-to-X-ray emission is synchrotron radiation from non-thermal electrons, in agreement with the results of previous works (e.g. Markoff et al. 2003, 2005) and as inferred from the spectral correlations (Corbel et al. 2003). The model predicts detectable gamma-ray emission during outbursts with similar characteristics to the observed in the past. The typical duration of these episodes was of some months, so observations with Cherenkov telescopes are feasible. GX 339-4 entered again in outburst in 2010; we expect to count with data at gamma rays from this event in the very near future.

• The existence of a population of positrons in the galactic halo is revealed by the detection of the annihilation line at 0.511 MeV with the satellite *INTEGRAL*. Adopting the same values of the model parameters that provided the best fits to the observed SED of GX 339-4, we estimated the positron production rate of jets from microquasars. The results indicate that the added contribution of all low-mass microquasars might be enough to account for the minimum positron injection rate necessary to explain the observed flux at 0.511 MeV. Please note that this conclusion is based on estimates of the positron injection for a source with a luminosity similar to that of GX 339-4 in outburst, and assuming that a large fraction of the known low-mass XRBs are able to produce jets.

• The broadband spectral energy distribution of the halo low-mass micro-

quasar XTE J1118+480 during the outbursts of 2000 and 2005, may be satisfactorily reproduced by the model as well. Simultaneous data from radio to X-rays are well explained as the sum of synchrotron radiation from non-thermal electrons in the jet and the emission of an optically thick accretion disc. According to our results, a luminous outburst of this source may be detected with *Fermi* and MAGIC, and in the future with CTA.

• Interestingly, in the three applications of the jet model a hard particle injection was required to reproduce the characteristic of the observed spectrum of the sources. Values of the injection spectral index $\alpha = 1.5 - 1.8$ such as those we adopted, are expected to arise from diffusive acceleration mediated by relativistic shocks.

To date, no low-mass X-ray binaries have been detected at high-energies. There is one *Fermi* gamma-ray source, 1FGL J1227.9-4852, that might be the counterpart of the bright low-mass X-ray binary XSS J12270-4859, but the association is still unclear (Falanga et al. 2010, Hill et al. 2011). No low-mass X-ray binaries have been detected with Cherenkov telescopes, either. Their observation is further complicated because in general they are transient sources. Negative detections of four low-mass microquasars with HESS are reported in Chadwick et al. (2005). Three of them, however, were in the high-soft state; there are no available simultaneous X-ray data for the fourth source, GX 339-4, but it was apparently in a low-luminosity state.

We expect that this situation changes in the very near future. The detection (or not) of low-mass XRBs at high and very high energies will provide very valuable information. The most favourable situation would be, undoubtedly, to have at our disposal simultaneous observations in X-rays and high and very high energy gamma rays. We have shown that the same observational data may be satisfactorily reproduced adopting different values of the model parameters. For example, proton-dominated as well as lepton-dominated jets might yield SEDs with similar characteristics at $\sim 0.1 - 10$ GeV. Observations with *Fermi* and *AGILE*, then, would be most useful to put constraints on the model parameters when complemented with data from Cherenkov telescopes. Such simultaneous spectral coverage is nowadays possible. Together with the much improved quality of the data, it will allow to remove part of the inherent

degeneracy of the modeling.

In this context, and in spite of its limitations, the type of models developed in this thesis are timely. We expect that, when confronted with observations, they result adequate to reproduce the radiative spectrum from microquasar jets and contribute to a better understanding of these objects.

BIBLIOGRAPHY

Abdo, A. A., Ackermann, M., Ajello, M., et al. 2011, Science, 331, 739

Abdo, A. A., Ackermann, M., Ajello, M., et al. 2009a, Science, 325, 840

Abdo, A. A., Ackermann, M., Ajello, M., et al. 2009b, Astrophys. J., 701, L123

Abdo, A. A., Ackermann, M., Ajello, M., et al. 2009c, Astrophys. J. Lett., 706, L56

Abdo, A. A., Ackermann, M., Ajello, M., et al. 2009d, Science, 326, 1512

Abramowicz, M. A., Chen, X., Kato, S., Lasota, J.-P., & Regev, O. 1995, Astrophys. J., 438, L37

Acciari, V. A., Beilicke, M., Blaylock, G., et al. 2008, Astrophys. J., 679, 1427

Aharonian, F., Akhperjanian, A. G., Aye, K.-M., et al. 2005, Astron. Astroph., 442, 1

Aharonian, F., Akhperjanian, A. G., Bazer-Bachi, A. R., et al. 2006a, Astron. Astroph., 460, 743

Aharonian, F., Anchordoqui, L., Khangulyan, D., & Montaruli, T. 2006b, J. Phys. Conf. Ser., 39, 408

Aharonian, F. A. 2004, Very High Energy Cosmic Gamma Radiation, 1st edn. (World Scientific Publishing, Singapore)

Aharonian, F. A., Akhperjanian, A. G., Bazer-Bachi, A. R., et al. 2007, Astron. Astroph., 469, L1

Aharonian, F. A. & Atoyan, A. M. 2000, Astron. Astroph., 362, 937

Aharonian, F. A., Atoyan, A. M., & Nagapetian, A. M. 1983, Astrofizika, 19, 323

Aharonian, F. A., Khangulyan, D., & Costamante, L. 2008, Mon. Not. R. Astron. Soc., 387, 1206

Ajello, M., Greiner, J., & Gehrels, G. K. N. 2008, The Astronomer's Telegram, 1497, 1

Albert, J., Aliu, E., Anderhub, H., et al. 2006, Science, 312, 1771

Albert, J., Aliu, E., Anderhub, H., et al. 2007, Astrophys. J. Lett., 665, L51

Anguelov, V. & Vankov, H. 1999, J. Phys. G Nucl. Partic., 25, 1755

Araudo, A., Bosch-Ramon, V., & Romero, G. E. 2010, in 25th Texas Symposium on Relativistic Astrophysics, PoS(Texas 2010)184

Araya, M. & Cui, W. 2010, Astrophys. J., 720, 20

Atoyan, A. M. & Dermer, C. D. 2003, Astrophys. J., 586, 79

Audet, C. & Dennis, J. E. J. 2003, SIAM Journal of Optimization, 13, 889

Balbus, S. A. & Hawley, J. F. 1991, Astrophys. J., 376, 214

Becker, P. A. & Kafatos, M. 1995, Astrophys. J., 453, 83

Bednarek, W. & Giovannelli, F. 2007, Astron. Astroph., 464, 437

Begelman, M. C., Rudak, B., & Sikora, M. 1990, Astrophys. J., 362, 38

Bell, A. R. 1978, Mon. Not. R. Astron. Soc., 182, 147

Belloni, T. M., Motta, S. E., & Muñoz-Darias, T. 2011, Bulletin of the Astronomical Society of India, 39, 409

Belmont, R., Malzac, J., & Marcowith, A. 2008, Astron. Astroph., 491, 617

Beloborodov, A. M. 1999, in Astronomical Society of the Pacific Conference Series, Vol. 161, High Energy Processes in Accreting Black Holes, ed. J. Poutanen & R. Svensson, 295

Berezinskii, V. S., Bulanov, S. V., Dogiel, V. A., & Ptuskin, V. S. 1990, Astrophysics of cosmic rays (North-Holland, Amsterdam)

Blandford, R. D. & Begelman, M. C. 1999, Mon. Not. R. Astron. Soc., 303, L1

Blandford, R. D. & Levinson, A. 1995, Astrophys. J., 441, 79

Blandford, R. D. & Payne, D. G. 1982, Mon. Not. R. Astron. Soc., 199, 883

Blandford, R. D. & Znajek, R. L. 1977, Mon. Not. R. Astron. Soc., 179, 433

Blumenthal, G. R. & Gould, R. J. 1970, Rev. Mod. Phys., 42, 237

Bodaghee, A., Tomsick, J. A., Rodriguez, J., & James, J. B. 2012, Astrophys. J., 744, 108

Bogovalov, S. V. & Kelner, S. R. 2005, Astronomy Reports, 49, 57

Bogovalov, S. V. & Kelner, S. R. 2010, Int. J. Mod. Phys. D, 19, 339

Bordas, P., Bosch-Ramon, V., Paredes, J. M., & Perucho, M. 2009, Astron. Astroph., 497, 325

Bosch-Ramon, V. & Khangulyan, D. 2009, Int. J. Mod. Phys. D, 18, 347

Bosch-Ramon, V., Khangulyan, D., & Aharonian, F. A. 2008, Astron. Astroph., 489, L21

Bosch-Ramon, V., Paredes, J. M., Romero, G. E., & Ribó, M. 2006a, Astron. Astroph., 459, L25

Bosch-Ramon, V., Perucho, M., & Bordas, P. 2011, Astron. Astroph., 528, id.A89

Bosch-Ramon, V. & Rieger, F. M. 2011, ArXiv e-prints, arXiv:1110.1534 [astro-ph.HE]

Bosch-Ramon, V., Romero, G. E., & Paredes, J. M. 2005, Astron. Astroph., 429, 267

Bosch-Ramon, V., Romero, G. E., & Paredes, J. M. 2006b, Astron. Astroph., 447, 263

Böttcher, M. & Schlickeiser, R. 1997, Astron. Astroph., 325, 866

Bouchet, L., Roques, J. P., & Jourdain, E. 2010, Astrophys. J., 720, 1772

Brocksopp, C., Jonker, P. G., Maitra, D., et al. 2010, Mon. Not. R. Astron. Soc., 404, 908

Bulgarelli, A., Tavani, M., Chen, A. W., et al. 2012, Astron. Astroph., 538, A63

Bulgarelli, A., Tavani, M., Pucella, G., et al. 2008, The Astronomer's Telegram, 1641, 1

Butt, Y. M., Maccarone, T. J., & Prantzos, N. 2003, Astrophys. J., 587, 748

Buxton, M. & Vennes, S. 2003, Mon. Not. R. Astron. Soc., 342, 105

Cadolle Bel, M., Kuulkers, E., Ibarra, A., et al. 2010, The Astronomer's Telegram, 2573, 1

Cadolle Bel, M., Rodriguez, J., D'Avanzo, P., et al. 2011, Astron. Astroph., 534, A119

Cadolle Bel, M., Sizun, P., Goldwurm, A., et al. 2006, Astron. Astroph., 446, 591

Callanan, P. J., Charles, P. A., Honey, W. B., & Thorstensen, J. R. 1992, Mon. Not. R. Astron. Soc., 259, 395

Casares, J., Ribas, I., Paredes, J. M., Martí, J., & Allende Prieto, C. 2005a, Mon. Not. R. Astron. Soc., 360, 1105

Casares, J., Ribó, M., Ribas, I., et al. 2005b, Mon. Not. R. Astron. Soc., 364, 899

Casares, J., Ribó, M., Ribas, I., et al. 2012, Mon. Not. R. Astron. Soc., 421, 1103

Chadwick, P. M., Dickinson, H. J., Latham, I. J., Nolan, S. J., & Osborne, J. L. 2005, in International Cosmic Ray Conference, Vol. 4, International Cosmic Ray Conference, 263

Chaty, S., Haswell, C. A., Malzac, J., et al. 2003, Mon. Not. R. Astron. Soc., 346, 689

Chen, A., Caraveo, P., Giuliani, A., et al. 2008, The Astronomer's Telegram, 1585, 1

Chen, A. W., Piano, G., Tavani, M., et al. 2011, Astron. Astroph., 525, A33

Cheung, C. C. 2008a, The Astronomer's Telegram, 1584, 1

Cheung, C. C. 2008b, The Astronomer's Telegram, 1589, 1

Chodorowski, M. J., Zdziarski, A. A., & Sikora, M. 1992, Astrophys. J., 400, 181

Christiansen, H. R., Orellana, M., & Romero, G. E. 2006, Phys. Rev. D, 73, 063012

Churchwell, E., Babler, B. L., Meade, M. R., et al. 2009, Publ. Astron. Soc. Pac., 121, 213

Coleiro, A. & Chaty, S. 2011, in Astronomical Society of the Pacific Conference Series, ed. L. Schmidtobreick, M. R. Schreiber, & C. Tappert, Vol. 447, 265

Coppi, P. S. 1999, in Astronomical Society of the Pacific Conference Series, Vol. 161, High Energy Processes in Accreting Black Holes, ed. J. Poutanen & R. Svensson, 375

Coppi, P. S. & Blandford, R. D. 1990, Mon. Not. R. Astron. Soc., 245, 453

Corbel, S. & Fender, R. P. 2002, Astrophys. J. Lett., 573, L35

Corbel, S., Fender, R. P., Tzioumis, A. K., et al. 2000, Astron. Astroph., 359, 251

Corbel, S., Nowak, M. A., Fender, R. P., Tzioumis, A. K., & Markoff, S. 2003, Astron. Astroph., 400, 1007

Corbet, R. H. D., Cheung, C. C., Kerr, M., et al. 2011, The Astronomer's Telegram, 3221, 1

Coriat, M., Corbel, S., Buxton, M. M., et al. 2009, Mon. Not. R. Astron. Soc., 400, 123

Davis, T. A. 2004a, ACM Transactions on Mathematical Software, 30, 165

Davis, T. A. 2004b, ACM Transactions on Mathematical Software, 30, 196

de Gouveia dal Pino, E. M. & Lazarian, A. 2005, Astron. Astroph., 441, 845

de Gouveia Dal Pino, E. M., Piovezan, P. P., & Kadowaki, L. H. S. 2010, Astron. Astroph., 518, A5

Derishev, E. V., Aharonian, F. A., Kocharovsky, V. V., & Kocharovsky, V. V. 2003, Phys. Rev. D, 68, 043003

Dermer, C. D. & Schlickeiser, R. 1993, Astrophys. J., 416, 458

Done, C., Gierliński, M., & Kubota, A. 2007, The Astronomy and Astrophysics Review, 15, 1

Dove, J. B., Wilms, J., Maisack, M., & Begelman, M. C. 1997, Astrophys. J., 487, 759

Drury, L. O. 1983, Reports on Progress in Physics, 46, 973

Drury, L. O. 2012, Mon. Not. R. Astron. Soc., 2661

Dubus, G. 2006, Astron. Astroph., 456, 801

Dubus, G., Lasota, J.-P., Hameury, J.-M., & Charles, P. 1999, Mon. Not. R. Astron. Soc., 303, 139

Dunn, R. J. H., Fender, R. P., Körding, E. G., Cabanac, C., & Belloni, T. 2008, Mon. Not. R. Astron. Soc., 387, 545

Esin, A. A., McClintock, J. E., Drake, J. J., et al. 2001a, Astrophys. J., 555, 483

Esin, A. A., McClintock, J. E., Drake, J. J., et al. 2001b, Astrophys. J., 555, 483

Esin, A. A., McClintock, J. E., & Narayan, R. 1997, Astrophys. J., 489, 865

Esin, A. A., Narayan, R., Cui, W., Grove, J. E., & Zhang, S.-N. 1998, Astrophys. J., 505, 854

Fabian, A. C., Iwasawa, K., Reynolds, C. S., & Young, A. J. 2000, Publ. Astron. Soc. Pac., 112, 1145

Falanga, M., de Martino, D., Bonnet-Bidaud, J. M., et al. 2010, in Proceedings of the 8th INTEGRAL Workshop "The Restless Gamma-ray Universe" (INTEGRAL 2010). September 27-30 2010. Dublin Castle, Dublin, Ireland, id. 54

Falcke, H. & Biermann, P. L. 1995, Astron. Astroph., 293, 665

Falcke, H., Körding, E., & Markoff, S. 2004, Astron. Astroph., 414, 895

Fender, R., Wu, K., Johnston, H., et al. 2004a, Nature, 427, 222

Fender, R. P., Belloni, T. M., & Gallo, E. 2004b, Mon. Not. R. Astron. Soc., 355, 1105

Fender, R. P., Gallo, E., & Russell, D. 2010, Mon. Not. R. Astron. Soc., 406, 1425

Fender, R. P., Hjellming, R. M., Tilanus, R. P. J., et al. 2001, Mon. Not. R. Astron. Soc., 322, L23

Fletcher, R. S., Gaisser, T. K., Lipari, P., & Stanev, T. 1994, Phys. Rev. D, 50, 5710

Fragile, P. C. & Meier, D. L. 2009, Astrophys. J., 693, 771

Frank, J., King, A., & Raine, D. 2002, Accretion Power in Astrophysics, 3rd edn. (Cambridge University Press, Cambridge, UK)

Frontera, F., Palazzi, E., Zdziarski, A. A., et al. 2001, Astrophys. J., 546, 1027

Gaisser, T. K. 1990, Cosmic rays and particle physics, 1st edn. (Cambridge and New York, Cambridge University Press)

Galeev, A. A., Rosner, R., & Vaiana, G. S. 1979, Astrophys. J., 229, 318

Gallo, E., Corbel, S., Fender, R. P., Maccarone, T. J., & Tzioumis, A. K. 2004, Mon. Not. R. Astron. Soc., 347, L52

Gallo, E., Fender, R., Kaiser, C., et al. 2005, Nature, 436, 819

Gallo, E., Fender, R. P., & Pooley, G. G. 2003, Mon. Not. R. Astron. Soc., 344, 60

Gallo, E., Miller, B., & Fender, R. 2012, ArXiv e-prints, arXiv:1203.4263 [astro-ph.HE]

Gandhi, P., Blain, A. W., Russell, D. M., et al. 2011, Astrophys. J. Lett., 740, L13

Gelino, D. M., Balman, Ş., Kızıloğlu, Ü., et al. 2006, Astrophys. J., 642, 438

George, I. M. & Fabian, A. C. 1991, Mon. Not. R. Astron. Soc., 249, 352

Ghisellini, G., Maraschi, L., & Treves, A. 1985, Astron. Astroph., 146, 204

Giannios, D. 2011, Journal of Physics Conference Series, 283, 012015

Gierlinski, M., Zdziarski, A. A., Done, C., et al. 1997, Mon. Not. R. Astron. Soc., 288, 958

Ginzburg, V. & Syrovatskii, S. 1964, Origin of Cosmic Rays, 1st edn. (Macmillan, New York)

Ginzburg, V. L. & Ptuskin, V. S. 1976, Rev. Mod. Phys., 48, 161

Giuliani, A., Caraveo, P., Chen, A., et al. 2008, The Astronomer's Telegram, 1547, 1

Gould, R. J. & Schréder, G. P. 1967, Phys. Rev., 155, 1404

Green, D. A. 2011, Bulletin of the Astronomical Society of India, 39, 289

Grenier, I. A. 2001, in Astrophysics and Space Science Library, Vol. 267, The Nature of Unidentified Galactic High-Energy Gamma-Ray Sources, ed. A. Carramiñana, O. Reimer, & D. J. Thompson, 51–63

Grenier, I. A. 2004, in Astrophysics and Space Science Library, Vol. 304, Cosmic Gamma-Ray Sources, ed. K. S. Cheng & G. E. Romero, 47

Grenier, I. A., Kaufman Bernadó, M. M., & Romero, G. E. 2005, Astrophys. Space Sci., 297, 109

Grimm, H.-J. 2003, PhD thesis, Fakultät für Physik der Ludwig-Maximilians-Universität München

Guessoum, N., Jean, P., & Prantzos, N. 2006, Astron. Astroph., 457, 753

Hannikainen, D. C., Hunstead, R. W., Campbell-Wilson, D., & Sood, R. K. 1998, Astron. Astroph., 337, 460

Hartman, R. C., Bertsch, D. L., Bloom, S. D., et al. 1999, Astrophys. J. Suppl. S., 123, 79

Heinz, S. 2008, International Journal of Modern Physics D, 17, 1947

Heinz, S. & Grimm, H. J. 2005, Astrophys. J., 633, 384

Heinz, S. & Sunyaev, R. A. 2003, Mon. Not. R. Astron. Soc., 343, L59

Herrero, A., Kudritzki, R. P., Gabler, R., Vilchez, J. M., & Gabler, A. 1995, Astron. Astroph., 297, 556

Hill, A. B., Szostek, A., Corbel, S., et al. 2011, Mon. Not. R. Astron. Soc., 415, 235

Hillas, A. M. 1984, Annu. Rev. Astron. Astrophys., 22, 425

Holder, J. 2009, ArXiv e-prints, arXiv:0912.4781 [astro-ph.HE]

Homan, J., Buxton, M., Markoff, S., et al. 2005, Astrophys. J., 624, 295

Huarte-Espinosa, M., Frank, A., & Blackman, E. 2011, in Jets at all Scales, Proceedings of the International Astronomical Union, Vol. 275, 87

Hui, C. M. 2010, in Astronomical Society of the Pacific Conference Series, Vol. 426, 2009 Snowbird Particle Astrophysics and Cosmology Workshop (SNOWPAC 2009), ed. D. B. Kieda & P. Gondolo, 35

Hynes, R. I., Mauche, C. W., Haswell, C. A., et al. 2000, Astrophys. J. Lett., 539, L37

Hynes, R. I., Robinson, E. L., Pearson, K. J., et al. 2006, Astrophys. J., 651, 401

Hynes, R. I., Steeghs, D., Casares, J., Charles, P. A., & O'Brien, K. 2003, Astrophys. J. Lett., 583, L95

Hynes, R. I., Steeghs, D., Casares, J., Charles, P. A., & O'Brien, K. 2004, Astrophys. J., 609, 317

Imamura, J. N., Kristian, J., Middleditch, J., & Steiman-Cameron, T. Y. 1990, Astrophys. J., 365, 312

Jogler, T. & Blanch, O. 2011, ArXiv e-prints, arXiv:1110.1681 [astro-ph.HE]

Jogler, T., Munar-Adrover, P., Ribó, M., & Paredes, J. M. 2011, ArXiv e-prints, arXiv:1110.1682 [astro-ph.HE]

Kappes, A. 2011, ArXiv e-prints, arXiv:1110.6840 [astro-ph.HE]

Kaufman Bernadó, M. M., Romero, G. E., & Mirabel, I. F. 2002, Astron. Astroph., 385, L10

Kelner, S. R. & Aharonian, F. A. 2008, Phys. Rev. D, 78, 034013

Kelner, S. R., Aharonian, F. A., & Bugayov, V. V. 2006, Phys. Rev. D, 74, 034018

Kennel, C. F. & Coroniti, F. V. 1984, Astrophys. J., 283, 710

Khangulyan, D. & Aharonian, F. 2005, in American Institute of Physics Conference Series, Vol. 745, High Energy Gamma-Ray Astronomy, ed. F. A. Aharonian, H. J. Völk, & D. Horns, 359–364

Khangulyan, D., Aharonian, F., & Bosch-Ramon, V. 2008, Mon. Not. R. Astron. Soc., 383, 467

King, A. 2006, in Compact Stellar X-Ray Sources, ed. W. H. G. Lewin & M. van der Klis, Cambridge Astrophysics (Cambridge University Press, Cambridge, UK), p. 507

Kolda, T. G., Lewis, R. M., & Torczon, V. 2003, SIAM Review, 45, 385

Komissarov, S. S. 2011, Memor. Soc. Astronom. Ital., 82, 95

Komissarov, S. S., Barkov, M. V., Vlahakis, N., & Königl, A. 2007, Mon. Not. R. Astron. Soc., 380, 51

Komissarov, S. S., Vlahakis, N., Königl, A., & Barkov, M. V. 2009, Mon. Not. R. Astron. Soc., 394, 1182

Körding, E. G., Fender, R. P., & Migliari, S. 2006, Mon. Not. R. Astron. Soc., 369, 1451

Kowal, G., de Gouveia Dal Pino, E. M., & Lazarian, A. 2011, Astrophys. J., 735, 102

Krolik, J. H. 1999, Active Galactic Nuclei: from the central black hole to the galactic environment, 1st edn. (Princeton University Press, Princeton)

Kusunose, M. & Mineshige, S. 1995, Astrophys. J., 440, 100

Lagarias, J. C., Reeds, J. A., Wright, M. H., & Wright, P. E. 1998, SIAM Journal of Optimization, 9, 112

Levine, A. M. & Corbet, R. 2006, The Astronomer's Telegram, 940, 1

Levinson, A. & Waxman, E. 2001, Phys.l Rev. Lett., 87, 171101

Lind, K. R. & Blandford, R. D. 1985, Astrophys. J., 295, 358

Lipari, P., Lusignoli, M., & Meloni, D. 2007, Phys. Rev. D, 75, 123005

Liu, Q. Z., van Paradijs, J., & van den Heuvel, E. P. J. 2006, Astron. Astroph., 455, 1165

Liu, Q. Z., van Paradijs, J., & van den Heuvel, E. P. J. 2007, Astron. Astroph., 469, 807

Longo, F., Chen, A., Vercellone, S., et al. 2008, The Astronomer's Telegram, 1492, 1

Lucarelli, F., Verrecchia, F., Striani, E., et al. 2010, The Astronomer's Telegram, 2761, 1

Lynden-Bell, D. 1969, Nature, 223, 690

Lyubarsky, Y. E. 2010, Mon. Not. R. Astron. Soc., 402, 353

Lyutikov, M. 2009, Mon. Not. R. Astron. Soc., 396, 1545

Maccarone, T. J. 2002, Mon. Not. R. Astron. Soc., 336, 1371

Mahadevan, R., Narayan, R., & Krolik, J. 1997, Astrophys. J., 486, 268

Maitra, D., Markoff, S., Brocksopp, C., et al. 2009, Mon. Not. R. Astron. Soc., 398, 1638

Malzac, J., Belmont, R., & Fabian, A. C. 2009, Mon. Not. R. Astron. Soc., 400, 1512

Mannheim, K. & Schlickeiser, R. 1994, Astron. Astroph., 286, 983

Markert, T. H., Canizares, C. R., Clark, G. W., et al. 1973, Astrophys. J. Lett., 184, L67

Markoff, S., Falcke, H., & Fender, R. 2001, Astron. Astroph., 372, L25

Markoff, S., Nowak, M., Corbel, S., Fender, R., & Falcke, H. 2003, Astron. Astroph., 397, 645

Markoff, S., Nowak, M. A., & Wilms, J. 2005, Astrophys. J., 635, 1203

Markwardt, C. B. & Swank, J. H. 2008, The Astronomer's Telegram, 1645, 1

Massi, M., Ros, E., & Zimmermann, L. 2012, ArXiv e-prints, arXiv:1203.4621 [astro-ph.HE]

Mastichiadis, A., Protheroe, R. J., & Kirk, J. G. 2005, Astron. Astroph., 433, 765

Maximon, L. 1968, J. Res. Natl. Bur. Stand., 72B, 79

McClintock, J. & Remillard, R. 2006, in Compact Stellar X-Ray Sources, ed. W. H. G. Lewin & M. van der Klis, Cambridge Astrophysics (Cambridge University Press, Cambridge, UK), p. 157

McClintock, J. E., Haswell, C. A., Garcia, M. R., et al. 2001, Astrophys. J., 555, 477

McConnell, M. L., Ryan, J. M., Collmar, W., et al. 2000, Astrophys. J., 543, 928

McNames, J. 2006, Signal Processing Magazine, IEEE, 23, 82

McSwain, M. V., Ray, P. S., Ransom, S. M., et al. 2011, Astrophys. J., 738, 105

Meier, D. L. 2005, Astrophys. Space Sci., 300, 55

Meier, D. L. 2011, in IAU Symposium, Vol. 275, IAU Symposium, ed. G. E. Romero, R. A. Sunyaev, & T. Belloni, 13–23

Melrose, D. B. 1980, Plasma astrohysics. Nonthermal processes in diffuse magnetized plasmas - Vol.1: The emission, absorption and transfer of waves in plasmas (Gordon and Breach, New York)

Merloni, A., Heinz, S., & Di Matteo, T. 2003, Mon. Not. R. Astron. Soc., 345, 1057

Migliari, S., Fender, R., & Méndez, M. 2002, Science, 297, 1673

Migliari, S. & Fender, R. P. 2006, Mon. Not. R. Astron. Soc., 366, 79

Migliari, S., Miller-Jones, J. C. A., & Russell, D. M. 2011, Mon. Not. R. Astron. Soc., 415, 2407

Miller-Jones, J. C. A., Sivakoff, G. R., Altamirano, D., et al. 2010, Astrophys. J. Lett., 716, L109

Mirabel, I. F. 2006, Science, 312, 1759

Mirabel, I. F. 2007, in VI Microquasar Workshop: Microquasars and Beyond, ed. T. Belloni

Mirabel, I. F., Dhawan, V., Chaty, S., et al. 1998, Astron. Astroph., 330, L9

Mirabel, I. F., Dhawan, V., Mignani, R. P., Rodrigues, I., & Guglielmetti, F. 2001, Nature, 413, 139

Mirabel, I. F. & Rodríguez, L. F. 1998, Nature, 392, 673

Mirabel, I. F. & Rodríguez, L. F. 1994, Nature, 371, 46

Mirabel, I. F. & Rodríguez, L. F. 1999, Annu. Rev. Astron. Astrophys., 37, 409

Mirabel, I. F., Rodríguez, L. F., Cordier, B., Paul, J., & Lebrun, F. 1992, Nature, 358, 215

Morlino, G. & Caprioli, D. 2012, Astron. Astroph., 538, A81

Muñoz-Darias, T., Casares, J., & Martínez-Pais, I. G. 2008, Mon. Not. R. Astron. Soc., 385, 2205

Mücke, A., Engel, R., Rachen, J. P., Protheroe, R. J., & Stanev, T. 2000, Comput. Phys. Commun., 124, 290

Nakamura, K., Hagiwara, K., Hikasa, K., et al. 2010, J. Phys. G Nucl. Partic., 37, 075021

Narayan, R., Barret, D., & McClintock, J. E. 1997, Astrophys. J., 482, 448

Narayan, R. & McClintock, J. E. 2011, Mon. Not. R. Astron. Soc. Lett., L362

Narayan, R., McClintock, J. E., & Yi, I. 1996, Astrophys. J., 457, 821

Narayan, R. & Yi, I. 1994, Astrophys. J., 428, L13

Narayan, R. & Yi, I. 1995a, Astrophys. J., 444, 231

Narayan, R. & Yi, I. 1995b, Astrophys. J., 452, 710

Nelder, J. A. & Mead, R. 1965, The Computer Journal, 7, 308

Nolan, P. L., Abdo, A. A., Ackermann, M., et al. 2012, Astrophys. J. Suppl. S., 199, 31

Nolan, P. L., Tompkins, W. F., Grenier, I. A., & Michelson, P. F. 2003, Astrophys. J., 597, 615

Nowak, M. A., Wilms, J., & Dove, J. B. 2002, Mon. Not. R. Astron. Soc., 332, 856

Nowak, M. A., Wilms, J., Heinz, S., et al. 2005, Astrophys. J., 626, 1006

Orlandini, M., Frontera, F., Bassani, L., Landi, R., & Sguera, V. 2008, The Astronomer's Telegram, 1419, 1

Orlandini, M., Frontera, F., Masetti, N., Sguera, V., & Sidoli, L. 2012, Astrophys. J., 748, 86

Orosz, J. A., Kuulkers, E., van der Klis, M., et al. 2001, Astrophys. J., 555, 489

Orosz, J. A., McClintock, J. E., Aufdenberg, J. P., et al. 2011, Astrophys. J., 742, 84

Owocki, S. P., Romero, G. E., Townsend, R. H. D., & Araudo, A. T. 2009, Astrophys. J., 696, 690

Pakull, M. W., Soria, R., & Motch, C. 2010, Nature, 466, 209

Pandel, D., Kaaret, P., & Lang, C. C. 2008, The Astronomer's Telegram, 1595, 1

Paredes, J. M. 2011, ArXiv e-prints, arXiv:1101.4843 [astro-ph.HE]

Paredes, J. M. & Zabalza, V. 2010, ArXiv e-prints, arXiv:1001.4473 [astro-ph.HE]

Pellizza, L. J., Orellana, M., & Romero, G. E. 2010, International Journal of Modern Physics D, 19, 671

Perucho, M. & Bosch-Ramon, V. 2012, Astron. Astroph., 539, A57

Pittori, C., Verrecchia, F., Chen, A. W., et al. 2009, Astron. Astroph., 506, 1563

Pittori, C., Verrecchia, F., Santolamazza, P., et al. 2008, The Astronomer's Telegram, 1394, 1

Pooley, G. G. 2005, The Astronomer's Telegram, 385, 1

Poutanen, J. 1998, in Theory of Black Hole Accretion Disks, ed. M. A. Abramowicz, G. Bjornsson, & J. E. Pringle, Cambridge Contemporary Astrophysics (Cambridge University Press, Cambridge, UK), 100

Poutanen, J., Krolik, J. H., & Ryde, F. 1997, Mon. Not. R. Astron. Soc., 292, L21

Poutanen, J. & Svensson, R. 1996, Astrophys. J., 470, 249

Purmohammad, D. & Samimi, J. 2001, Astron. Astroph., 371, 61

Reid, M. J., McClintock, J. E., Narayan, R., et al. 2011, Astrophys. J., 742, 83

Remillard, R., Garcia, M., Torres, M. A. P., et al. 2005, The Astronomer's Telegram, 384, 1

Remillard, R., Morgan, E., Smith, D., & Smith, E. 2000, IAU Circ., 7389, 2

Reynolds, C. S. & Nowak, M. A. 2003, Phys. Rep., 377, 389

Reynoso, M. M., Medina, M. C., & Romero, G. E. 2011, Astron. Astroph., 531, A30

Reynoso, M. M. & Romero, G. E. 2009, Astron. Astroph., 493, 1

Rodriguez, J., Corbel, S., & Tomsick, J. A. 2003, Astrophys. J., 595, 1032

Romero, G., Sunyaev, R., & Belloni, T., eds. 2010, Proceedings IAU Symposium No. 275 "Jets at All Scales", Vol. 6 (Cambridge University Press)

Romero, G. E. 2001, in Astrophysics and Space Science Library, Vol. 267, The Nature of Unidentified Galactic High-Energy Gamma-Ray Sources, ed. A. Carramiñana, O. Reimer, & D. J. Thompson, 65–80

Romero, G. E., Christiansen, H. R., & Orellana, M. 2005, Astrophys. J., 632, 1093

Romero, G. E., Del Valle, M. V., & Orellana, M. 2010a, Astron. Astroph., 518, A12

Romero, G. E., Grenier, I. A., Kaufman Bernado, M. M., Mirabel, I. F., & Torres, D. F. 2004, in ESA Special Publication, Vol. 552, 5th INTEGRAL Workshop on the INTEGRAL Universe, ed. V. Schoenfelder, G. Lichti, & C. Winkler, 703

Romero, G. E., Kaufman Bernadó, M. M., & Mirabel, I. F. 2002, Astron. Astroph., 393, L61

Romero, G. E., Okazaki, A. T., Orellana, M., & Owocki, S. P. 2007, Astron. Astroph., 474, 15

Romero, G. E. & Orellana, M. 2005, Astron. Astroph., 439, 237

Romero, G. E. & Paredes, J. M. 2011, Introducción a la Astrofísica Relativista, 1st edn. (Publicacions i Edicions de la Universitat de Barcelona, Barcelona)

Romero, G. E., Torres, D. F., Kaufman Bernadó, M. M., & Mirabel, I. F. 2003, Astron. Astroph., 410, L1

Romero, G. E., Vieyro, F. L., & Vila, G. S. 2010b, Astron. Astroph., 519, A109

Romero, G. E. & Vila, G. S. 2009, Astron. Astroph., 494, L33

Russell, D. M., Fender, R. P., Hynes, R. I., et al. 2006, Mon. Not. R. Astron. Soc., 371, 1334

Sabatini, S., Tavani, M., Striani, E., et al. 2010, Astrophys. J. Lett., 712, L10

Salpeter, E. E. 1964, Astrophys. J., 140, 796

Sams, B. J., Eckart, A., & Sunyaev, R. A. 1996, Nature, 382, 47

Sądowski, A. & Sikora, M. 2010, Astron. Astroph., 517, A18

Schlickeiser, R. 2002, Cosmic ray astrophysics (Springer, Berlin)

Schneider, P. 1993, Astron. Astroph., 278, 315

Sell, P. H., Heinz, S., Calvelo, D. E., et al. 2010, Astrophys. J. Lett., 719, L194

Shakura, N. I. & Sunyaev, R. A. 1973, Astron. Astroph., 24, 337

Shapiro, S. L., Lightman, A. P., & Eardley, D. M. 1976, Astrophys. J., 204, 187

Soria, R., Pakull, M. W., Broderick, J. W., Corbel, S., & Motch, C. 2010, Mon. Not. R. Astron. Soc., 409, 541

Spencer, R. E. 1979, Nature, 282, 483

Spruit, H. C. 1988, Astron. Astroph., 194, 319

Spruit, H. C. 2010, Lecture Notes in Physics, Vol. 794, Theory of Magnetically Powered Jets (Springer-Verlag Berlin), 233

Stecker, F. W., Baring, M. G., & Summerlin, E. J. 2007, Astrophys. J. Lett., 667, L29

Stern, B. E., Poutanen, J., Svensson, R., Sikora, M., & Begelman, M. C. 1995, Astrophys. J., 449, L13

Summerlin, E. J. & Baring, M. G. 2012, Astrophys. J., 745, 63

Tavani, M., Bulgarelli, A., Piano, G., et al. 2009, Nature, 462, 620

Tavani, M., Bulgarelli, A., Vittorini, V., et al. 2011, Science, 331, 736

Tavani, M., Piano, G., Chen, A., et al. 2008, The Astronomer's Telegram, 1848, 1

Tchekhovskoy, A., McKinney, J. C., & Narayan, R. 2008, Mon. Not. R. Astron. Soc., 388, 551

Tchekhovskoy, A., Narayan, R., & McKinney, J. C. 2010, New Astron., 15, 749

Thompson, D. J., Bertsch, D. L., Hartman, R. C., Collmar, W., & Johnson, W. N. 2000, in American Institute of Physics Conference Series, Vol. 510, American Institute of Physics Conference Series, ed. M. L. McConnell & J. M. Ryan, 479–483

Tingay, S. J., Jauncey, D. L., Preston, R. A., et al. 1995, Nature, 374, 141

Titarchuk, L. & Lyubarskij, Y. 1995, Astrophys. J., 450, 876

Torrejón, J. M., Schulz, N. S., Nowak, M. A., & Kallman, T. R. 2010, Astrophys. J., 715, 947

Torres, D. F. & Reimer, A. 2011, Astron. Astroph., 528, L2

Tsuneta, S. & Naito, T. 1998, Astrophys. J. Lett., 495, L67

van der Klis, M. 2006, in Compact Stellar X-Ray Sources, ed. W. H. G. Lewin & M. van der Klis, Cambridge Astrophysics (Cambridge University Press, Cambridge, UK), 39

Vandenbroucke, J. 2010, ArXiv e-prints, arXiv:1012.0849 [astro-ph.HE]

Vieyro, F. L. 2012, PhD thesis, Facultad de Ciencias Astronómicas y Geofísicas, Universidad Nacional de La Plata

Vieyro, F. L. & Romero, G. E. 2012, in preparation

Vila, G. S. & Aharonian, F. A. 2009, in Compact Objects and their Emission, ed. G. E. Romero & P. Benaglia, Asociación Argentina de Astronomía, Book Series (Editorial Paideia, La Plata, Argentina), 1–38

Vurm, I. & Poutanen, J. 2009, Astrophys. J., 698, 293

Weidenspointner, G., Skinner, G., Jean, P., et al. 2008, Nature, 451, 159

Wilms, J., Nowak, M. A., Dove, J. B., Fender, R. P., & Di Matteo, T. 1999, Astrophys. J., 522, 460

Yu, W., Lamb, F. K., Fender, R., & van der Klis, M. 2007, Astrophys. J., 663, 1309

Yuan, F., Cui, W., & Narayan, R. 2005, Astrophys. J., 620, 905

Zdziarski, A. A., Gierliński, M., Mikołajewska, J., et al. 2004, Mon. Not. R. Astron. Soc., 351, 791

Zdziarski, A. A., Poutanen, J., Mikolajewska, J., et al. 1998, Mon. Not. R. Astron. Soc., 301, 435

Zel′Dovich, Y. B. 1964, Sov. Phys. Dokl., 9, 195

Zenitani, S. & Hoshino, M. 2001, Astrophys. J., 562, L63

Zurita, C., Rodríguez, D., Rodríguez-Gil, P., et al. 2005, The Astronomer's Telegram, 383, 1

Zurita, C., Torres, M. A. P., Steeghs, D., et al. 2006, Astrophys. J., 644, 432

A

RADIATIVE PROCESSES

This appendix contains a more extensive discussion on some of the radiative processes introduced in Section 3.3. All the missing formulae relevant to the calculation of the luminosities are also collected here. The reader interested in more details is referred to Vila & Aharonian (2009) and Romero & Paredes (2011).

A.1 SYNCHROTRON RADIATION

A simple analytical expression for the synchrotron power per unit energy is given in Melrose (1980). The integral in Eq. (3.47) can be approximated as

$$x \int_x^\infty \mathrm{d}\zeta \, K_{5/3}(\zeta) \approx 1.85 \, x^{1/3} e^{-x}. \tag{A.1}$$

As seen in Figure A.1, this approximation is in excellent agreement with the exact expression over the range $0.1 \leq x \leq 10$.

In general, the energy of the synchrotron photons is much lower than the energy of the parent particle. But in certain astrophysical environments, such as pulsar magnetospheres, synchrotron radiation can take place near the quantum threshold. In this limit, the production of electron-positron pairs in a magnetic field by high-energy photons

$$\gamma + B \longrightarrow e^+ + e^-. \tag{A.2}$$

is also possible (e.g. Anguelov & Vankov 1999). The classical treatment of

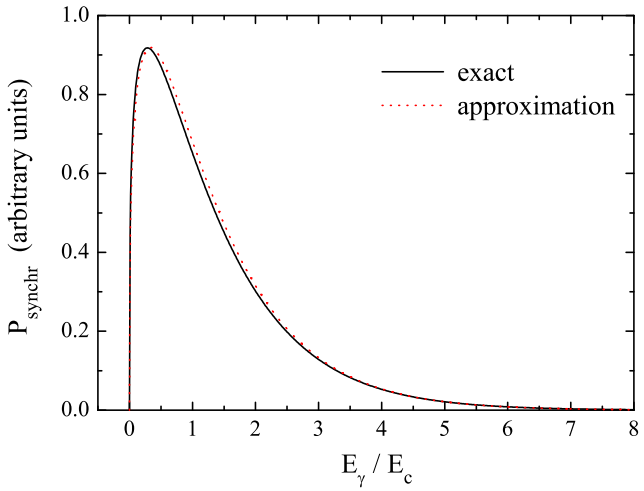

Figure A.1: Synchrotron power radiated by a single charged particle. Solid line: exact calculation. Dashed line: approximation of Eq. (A.1).

synchrotron radiation (e.g. Blumenthal & Gould 1970) is valid only in the regime

$$\frac{E}{m_e c^2}\frac{B}{B_{\rm cr}} << 1, \tag{A.3}$$

where $B_{\rm cr} = m_e^2 c^3/e\hbar \approx 4.4 \times 10^{13}\,{\rm G}$ is the critical value of the magnetic field, above which quantum effects become relevant.

A.2 PROTON-PROTON INELASTIC COLLISIONS

Inelastic collisions of protons and nuclei yield pions, kaons, and hyperons, that then decay to produce high-energy photons and leptons. The main channel of gamma-ray production is the decay of neutral pions

$$\pi^0 \rightarrow \gamma + \gamma. \tag{A.4}$$

The number of photons per unit energy injected by the decay of a monoenergetic distribution of neutral pions of energy E_π is a constant

$$\frac{dN_\gamma}{dE_\gamma} = \frac{2}{\sqrt{E_\pi^2 - m_{\pi^0}^2 c^4}}. \tag{A.5}$$

The allowed interval of photon energies is centered around $E_\gamma = 0.5 m_{\pi^0} c^2$,

$$\frac{m_{\pi^0} c^2}{2} \sqrt{\frac{1-\beta_\pi}{1+\beta_\pi}} \leq E_\gamma \leq \frac{m_{\pi^0} c^2}{2} \sqrt{\frac{1+\beta_\pi}{1-\beta_\pi}}. \tag{A.6}$$

Here $\beta_\pi = v_\pi / c$ and v_π is the velocity of the π^0 in the laboratory frame. For an arbitrary energy distribution of neutral pions, the gamma-ray spectrum is the superposition of contributions given by Eq. (A.5) for different values of E_π. This results in a spectrum with a maximum at $E_\gamma = 0.5 m_{\pi^0} c^2 \approx 67.5$ MeV, independently of the shape of the pion distribution and, therefore, that of the parent protons.

Kelner et al. (2006) presented simple analytical formulae for the cross section and energy spectra of the products of inelastic proton-proton collisions, obtained fitting the results of simulations performed mainly with the SIBYLL code. For a proton of energy E_p, the number of photons per unit energy created per collision can be parameterized as

$$F_\gamma\left(x, E_p\right) = B_\gamma \frac{\ln x}{x} \left[\frac{1 - x^{\beta_\gamma}}{1 + k_\gamma x^{\beta_\gamma}\left(1 - x^{\beta_\gamma}\right)}\right]^4 \times \left[\frac{1}{\ln x} - \frac{4\beta_\gamma x^{\beta_\gamma}}{1 - x^{\beta_\gamma}} - \frac{4 k_\gamma \beta_\gamma x^{\beta_\gamma}\left(1 - 2x^{\beta_\gamma}\right)}{1 + k_\gamma x^{\beta_\gamma}\left(1 - x^{\beta_\gamma}\right)}\right], \tag{A.7}$$

where $x = E_\gamma / E_p$. For proton energies in the range $0.1\,\text{TeV} \leq E_p \leq 10^5$ TeV, fits to the results of SIBYLL yield

$$B_\gamma = 1.30 + 0.14L + 0.011L^2, \tag{A.8}$$

$$\beta_\gamma = \left(1.79 + 0.11L + 0.008L^2\right)^{-1}, \tag{A.9}$$

$$k_\gamma = \left(0.801 + 0.049L + 0.014L^2\right)^{-1}, \tag{A.10}$$

where $L = \ln\left(E_p/1\,\mathrm{TeV}\right)$. The function $F_\gamma\left(x, E_p\right)$ includes, along with the contribution to the gamma-ray spectrum from the π^0 decay, that from the decay of the η-meson. Around $x \sim 0.1$, the contribution to the gamma-ray spectrum from the η-mesons is about 25%.

From Eq. (A.7) it is possible to obtain the gamma-ray emissivity from Eq. (3.57). The inelastic proton-proton cross section $\sigma_{\mathrm{inel}}\left(E_p\right)$ can be accurately approximated as (Kelner et al. 2006)

$$\sigma_{\mathrm{inel}}\left(E_p\right) = \left(34.3 + 1.88L + 0.25L^2\right)\left[1 - \left(\frac{E_{\mathrm{th}}}{E_p}\right)^4\right]^2 \mathrm{mb}, \tag{A.11}$$

where $E_{\mathrm{th}} = m_p + 2m_\pi + m_\pi^2/2m_p = 1.22\,\mathrm{GeV}$ is the threshold energy of the proton for the production of a single π^0. As seen in Figure A.2, this expression correctly describes the cross section near the threshold and fits the experimental data and SIBYLL simulations up to at least $E_p \sim 10^4$ TeV.

Equation (3.57) is valid for $E_p \gtrsim 100$ GeV. To calculate the emissivity of low-energy photons, Kelner et al. (2006) suggested a simple approach based on the δ-functional approximation (see also Aharonian & Atoyan 2000). It is assumed that the neutral pion takes a fixed fraction $K_\pi \approx 0.17$ of the kinetic energy of the relativistic proton. The injection function of neutral pions is then given by

$$\begin{aligned} Q_{\pi^0}^{(pp)}\left(E_\pi\right) &= \widetilde{n}\, c\, n_p \int \delta\left(E_\pi - K_\pi E_{\mathrm{kin}}\right) \sigma_{pp}\left(E_p\right) N_p\left(E_p\right)\, \mathrm{d}E_p \\ &= \frac{\widetilde{n}}{K_\pi}\, c\, n_p\, \sigma_{pp}\left(m_p c^2 + \frac{E_\pi}{K_\pi}\right) N_p\left(m_p c^2 + \frac{E_\pi}{K_\pi}\right), \end{aligned} \tag{A.12}$$

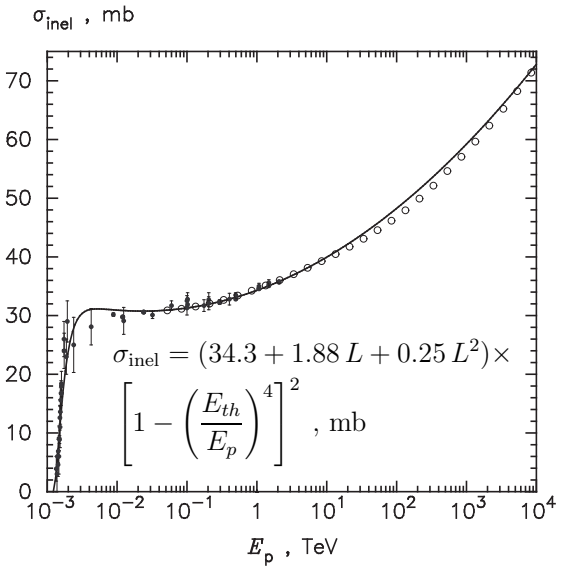

Figure A.2: Inelastic cross section for proton-proton collisions. The filled circles are experimental data and the empty circles the results of the code SIBYLL. From Kelner et al. (2006).

where $\widetilde{n}$ is the number of neutral pions created per proton-proton collision. The gamma-ray emissivity is then calculated from Eq. (3.59). Since for $E_p \lesssim 100$ GeV the cross section is essentially constant, the shape of the photon spectrum in the δ-functional formalism is similar to the shape of the parent proton spectrum, shifted in energy by a factor K_π.

Kelner et al. (2006) also obtained an expression for the injection function of charged pions in proton-proton collisions, see Eq. (3.89). The mean number of charged pions with energy $E_{\pi^\pm}$ created per collision is given by Eq. (3.90), where the function

$$F_\pi^{(pp)}\left(x, E_p\right) = 4\alpha B_\pi x^{\alpha-1}\left(\frac{1-x^\alpha}{1+rx^\alpha(1-x^\alpha)}\right)^4 \times \left(\frac{1}{1-x^\alpha}+\frac{r(1-2x^\alpha)}{1+rx^\alpha(1-x^\alpha)}\right)\left(1-\frac{m_\pi c^2}{xE_p}\right)^{1/2}. \quad \text{(A.13)}$$

Here $x = E_{\pi^\pm}/E_p$, $B_\pi = a' + 0.25$, $a' = 3.67 + 0.83L + 0.075L^2$, $r = 2.6/\sqrt{a'}$,

and $\alpha = 0.98/\sqrt{a'}$.

A.3 INVERSE COMPTON SCATTERING

In the rest frame of the electron, the exact differential cross section for inverse Compton scattering is given by the Klein-Nishina formula (e.g. Blumenthal & Gould 1970)

$$\frac{d\sigma}{d\Omega} = \frac{1}{2} r_e^2 \left(\frac{\epsilon'_\gamma}{\epsilon'}\right)^2 \left(\frac{\epsilon'}{\epsilon'_\gamma} + \frac{\epsilon'_\gamma}{\epsilon'} - \sin^2\theta'\right). \tag{A.14}$$

Here ϵ' and ϵ'_γ are the photon energies before and after the scattering in the electron rest frame, respectively, and θ' is the angle between the momenta of the incident and scattered photon in the same reference frame.[1] The final photon energy is fixed by ϵ' and θ',

$$\epsilon'_\gamma = \frac{\epsilon'}{1 + (\epsilon'/m_e c^2)\,(1 - \cos\theta')}. \tag{A.15}$$

Figure A.3 shows the angle-averaged total cross section $\sigma_{\rm IC}$ in the laboratory frame. It depends only on the product of the energies of the colliding particles $\kappa_0 = \epsilon E_e / m_e^2 c^4$ (e.g. Coppi & Blandford 1990),

$$\sigma_{\rm IC} = \frac{3\sigma_{\rm T}}{8\kappa_0}\left[\left(1 - \frac{2}{\kappa_0} - \frac{2}{\kappa_0^2}\right)\ln\left(1 + 2\kappa_0\right) + \frac{1}{2} + \frac{8}{\kappa_0} - \frac{1}{2\left(1 + 2\kappa_0\right)^2}\right]. \tag{A.16}$$

In the non-relativistic regime ($\kappa_0 \ll 1$) it reduces to the Thomson cross section, $\sigma_{\rm IC} \sim \sigma_{\rm T}(1 - 2\kappa_0)$, whereas in the ultra-relativistic or Klein-Nishina limit ($\kappa_0 \gg 1$) it decreases abruptly, $\sigma_{\rm IC} \sim (3\sigma_{\rm T}/8)\kappa_0^{-1}\ln(4\kappa_0)$.

According to Blumenthal & Gould (1970), the spectrum of photons scattered by an electron of energy $E_{\rm e} = \gamma_{\rm e} m_{\rm e} c^2$ in an isotropic target radiation field of density $n_{\rm ph}(\epsilon)$ is

[1] In this section, primed symbols indicate quantities measured in the rest frame of the incident electron.

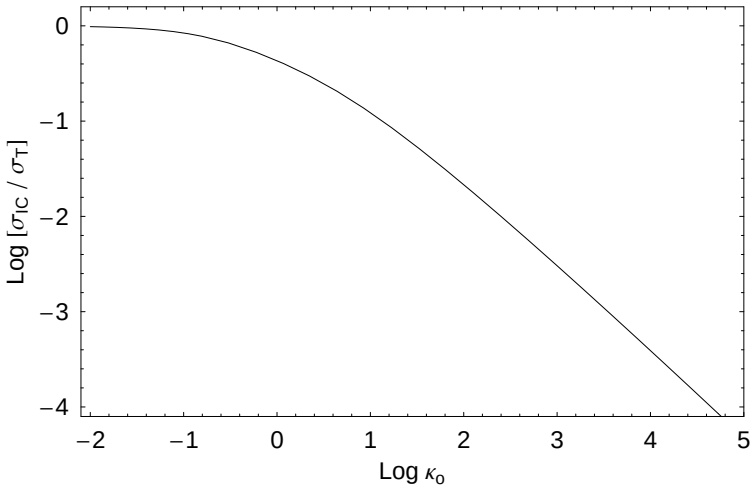

Figure A.3: Total cross section for inverse Compton scattering in an isotropic radiation field.

$$P_{\mathrm{IC}}\left(E_\gamma, E_\mathrm{e}, \epsilon\right) = \frac{3\sigma_\mathrm{T} c}{4\gamma_\mathrm{e}^2} \frac{n_\mathrm{ph}(\epsilon)}{\epsilon} F_{\mathrm{IC}}\left(q\right). \tag{A.17}$$

Here σ_T is the Thomson cross section and the function $F_{\mathrm{IC}}\left(q\right)$ is given by

$$F_{\mathrm{IC}}\left(q\right) = 2q \ln q + \left(1+2q\right)\left(1-q\right) + \frac{1}{2}\left(1-q\right)\frac{\left(q\Gamma_\mathrm{e}\right)^2}{\left(1+\Gamma_\mathrm{e} q\right)}, \tag{A.18}$$

where

$$\Gamma_\mathrm{e} = \frac{4\epsilon\gamma_\mathrm{e}}{m_\mathrm{e} c^2} \tag{A.19}$$

and

$$q = \frac{E_\gamma}{\Gamma_\mathrm{e} E_\mathrm{e}\left(1 - E_\gamma / E_\mathrm{e}\right)}. \tag{A.20}$$

The limit $\Gamma_\mathrm{e} \ll 1$ corresponds to Thomson scattering, but Eq. (A.17) is valid for all Γ_e - even deep into the Klein-Nishina regime - as long as $\gamma_\mathrm{e} \gg 1$. In terms of the parameter Γ_e, the allowed range of energies for the scattered photons is

$$\epsilon \leq E_\gamma \leq \frac{\Gamma_\mathrm{e}}{1+\Gamma_\mathrm{e}} E_\mathrm{e}. \tag{A.21}$$

When the target radiation field (and/or the electron distribution) is not isotropic, to calculate the inverse Compton emissivity (number of photons with energy ϵ_s scattered into solid angle Ω_s per unit volume per unit time) in the jet frame we must start from the most general expression,

$$q_\gamma\left(\epsilon_s,\Omega_s,\vec{r}\right)=c\int_0^\infty \mathrm{d}\epsilon \oint \mathrm{d}\Omega \int_{E^{\min}}^{E^{\max}} \mathrm{d}E \oint \mathrm{d}\Omega_e \left(1-\beta_e\cos\psi\right) \frac{\mathrm{d}\sigma}{\mathrm{d}\epsilon_s \mathrm{d}\Omega_s}\times N\left(E,\Omega_e,\vec{r}\right)\, n_{\mathrm{ph}}\left(\epsilon,\Omega,\vec{r}\right). \quad \text{(A.22)}$$

Here $N\left(E,\Omega_e,\vec{r}\right)$ and $n_{\mathrm{ph}}\left(\epsilon,\Omega,\vec{r}\right)$ are the electron and photon distributions (in units of $\mathrm{erg}^{-1}\ \mathrm{cm}^{-3}\ \mathrm{sr}^{-1}$), respectively, $\mathrm{d}\sigma/\mathrm{d}\epsilon_s\mathrm{d}\Omega_s$ is the double differential IC cross section, and ψ is the collision angle. In terms of the angular coordinates of the direction of motion of the colliding particles, $\cos\psi$ may be written as

$$\cos\psi=\mu\,\mu_e+\left(1-\mu^2\right)^{1/2}\left(1-\mu_e^2\right)^{1/2}\cos\left(\phi-\phi_e\right), \quad \text{(A.23)}$$

where $\mu=\cos\theta$ and $\mu_e=\cos\theta_e$.

Equation (A.22) can be simplified introducing some approximations. In the rest frame of the electron, the directions of motion of the incident photons are confined to a cone of half-angle $\sim 1/\gamma_e$ along the direction of motion of the electron, where γ_e is the Lorentz factor of the electron in the jet frame. When $\gamma_e \gg 1$, $\mu' \approx \beta_e \approx 1$, so the collision is almost head-on in the rest frame of the electron. Furthermore, in the jet frame the scattered photons are beamed into a cone of half-angle $\sim 1/\gamma_e$ along the direction of motion of the electron. Then, for relativistic electrons $\Omega_s \approx \Omega_e$. Under these approximations, the double differential cross section in the jet frame can be written as (Dermer & Schlickeiser 1993)

$$\frac{\mathrm{d}\sigma}{\mathrm{d}\epsilon_s\mathrm{d}\Omega_s}=\delta\left(\Omega_s-\Omega_e\right)\frac{\pi r_e^2}{\gamma_e\,\epsilon'}\left(y+\frac{1}{y}+\frac{\epsilon_s^2}{\gamma_e^2\epsilon'^2y^2}-\frac{2\epsilon_s}{\gamma_e\epsilon' y}\right), \quad \text{(A.24)}$$

where

$$\epsilon'=\gamma_e\epsilon\left(1-\beta_e\cos\psi\right) \quad \text{(A.25)}$$

is the energy of the incident photon in the rest frame of the electron, the variable $y \equiv 1 - \epsilon_s/E$, and the energy of the scattered photon is in the range

$$\frac{\epsilon'}{2\gamma_e} \leq \epsilon_s \leq \frac{2\gamma_e \epsilon'}{1 + 2\epsilon'/m_e c^2}. \tag{A.26}$$

Inserting Eq. (A.26) into Eq. (A.22) yields

$$q_\gamma\left(\epsilon_s, \Omega_s, \vec{r}\right) = c \int_{E^{\min}}^{E^{\max}} \mathrm{d}E \oint \mathrm{d}\Omega \int_{\epsilon^{\min}}^{\epsilon^{\max}} \mathrm{d}\epsilon \left(1 - \beta_e \cos\psi\right) \frac{\mathrm{d}\sigma}{\mathrm{d}\epsilon_s} \times N\left(E, \Omega_s, \vec{r}\right) n_{\mathrm{ph}}\left(\epsilon, \Omega, \vec{r}\right). \tag{A.27}$$

Now

$$\cos\psi = \mu\,\mu_s + \left(1 - \mu^2\right)^{1/2} \left(1 - \mu_s^2\right)^{1/2} \cos\left(\phi - \phi_s\right), \tag{A.28}$$

and we have defined

$$\frac{\mathrm{d}\sigma}{\mathrm{d}\epsilon_s} = \frac{\pi r_e^2}{\gamma_e\,\epsilon'} \left(y + \frac{1}{y} + \frac{\epsilon_s^2}{\gamma_e^2 \epsilon'^2 y^2} - \frac{2\epsilon_s}{\gamma_e \epsilon' y}\right). \tag{A.29}$$

The integration limits $\epsilon^{\max,\min}$ are fixed by Eq. (A.25)

$$\epsilon^{\min} = \frac{2\epsilon_s}{\left(1 - \beta_e \cos\psi\right)}, \tag{A.30}$$

$$\epsilon^{\max} = \frac{\epsilon_s/2\gamma_e}{(\gamma_e - \epsilon_s/m_e c^2)(1 - \beta_e \cos\psi)}. \tag{A.31}$$

If the system has azimuthal symmetry we can fix $\phi_s = 0$; furthermore, if the electron distribution is isotropic in the jet frame, $N\left(E, \Omega_s, \vec{r}\right) = N\left(E, \vec{r}\right)/4\pi$. Then,

$$q_\gamma\left(\epsilon_s, \Omega_s, \vec{r}\right) = \frac{c}{4\pi} \int_{E^{min}}^{E^{max}} dE \oint d\Omega \int_{\epsilon^{min}}^{\epsilon^{max}} d\epsilon \left(1 - \beta_e \cos\psi\right) \frac{d\sigma}{d\epsilon_s} \times N\left(E, \vec{r}\right) n_{ph}\left(\epsilon, \Omega, \vec{r}\right), \quad \text{(A.32)}$$

where

$$\cos\psi = \mu\,\mu_s + \left(1-\mu^2\right)^{1/2}\left(1-\mu_s^2\right)^{1/2}\cos\phi. \quad \text{(A.33)}$$

As we discussed in Chapter 5, the number density of photons per unit energy per unit solid angle at height z on the jet axis, that were emitted per unit area at radius R in the accretion disc, can be written as

$$n_{ph}\left(\epsilon^*, \Omega^*, z, R\right) = \frac{1}{\pi \ell^2 c}\, \dot{n}_{ph}\left(\epsilon^*, R\right) \frac{1}{2\pi}\, \delta\left(\mu^* - \bar{\mu}^*\right). \quad \text{(A.34)}$$

This expression is valid in a reference frame fixed to the disc, where the variables are denoted with starred symbols. The variables $\ell^2 = z^2 + R^2$ and $\bar{\mu}^* = \cos\theta^* = z/\ell$ are defined in Figure A.4.

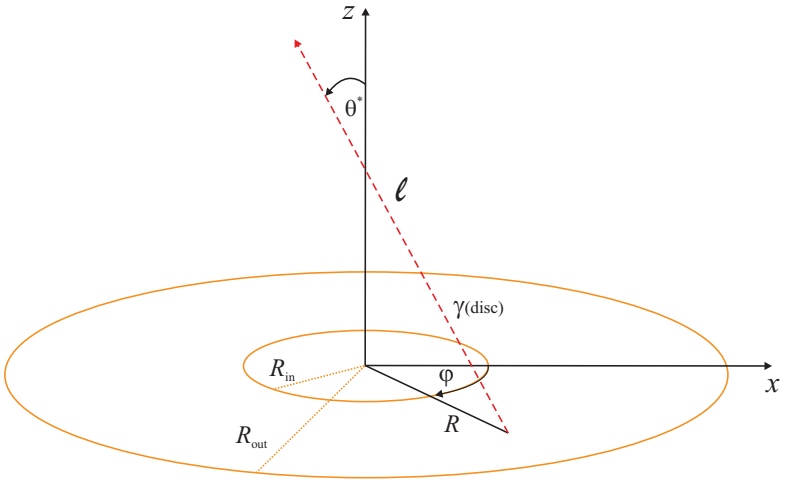

Figure A.4: Geometrical parameters relevant to the calculation of the inverse Compton emissivity with the disc radiation field as target.

The emissivity of photons per unit disc area at radius R is $\dot{n}_{ph}\left(\epsilon^*, R\right)$. Approximating the disc emission as monoenergetic at energy $\bar{\epsilon}^* = 2.7kT(R)$, we

obtain

$$\dot{n}_{\rm ph}\left(\epsilon^*, R\right) \approx \frac{1}{\epsilon^*}\,\sigma_{\rm SB} T(R)^4\,\delta(\epsilon^* - \bar{\epsilon}^*). \tag{A.35}$$

Before inserting it in Eq. (A.32), the radiation field of the disc must be transformed to the jet frame. The transformation is done using that the ratio $n_{\rm ph}/\epsilon^2$ is a relativistic invariant. This yields

$$n_{\rm ph}\left(\epsilon, \Omega, R\right) = \frac{1}{2\pi^2\ell^2 c}\,\dot{n}_{\rm ph}\left(\epsilon^*, R\right)\,\delta\left(\mu - \bar{\mu}\right), \tag{A.36}$$

where the photon energy and the cosine of the polar angle in both frames are related as

$$\epsilon^* = \Gamma_{\rm jet}\epsilon\left(1 + \beta_{\rm jet}\,\mu\right), \tag{A.37}$$

$$\bar{\mu} = \frac{\bar{\mu}^* - \beta_{\rm jet}}{1 - \beta_{\rm jet}\,\bar{\mu}^*}. \tag{A.38}$$

Inserting Eq. (A.36) into Eq. (A.32), the final result is

$$q_\gamma\left(\epsilon_{\rm s}, \Omega_{\rm s}, \vec{r}\right) = \frac{c}{4\pi}\int_{E^{\rm min}}^{E^{\rm max}} {\rm d}E \int_0^{2\pi} {\rm d}\phi \int_{R_{\rm min}}^{R_{\rm max}} R\,{\rm d}R\,\left(1 - \beta_e\cos\psi\right)\,\frac{{\rm d}\sigma}{{\rm d}\epsilon_{\rm s}}\,N\left(E, \vec{r}\right)\times \frac{\sigma_{\rm SB}T^4(R)}{2\pi^2\ell^2 c}\,\frac{1}{\bar{\epsilon}^*\Gamma_{\rm jet}\left(1 + \beta_{\rm jet}\bar{\mu}\right)}, \tag{A.39}$$

with

$$\cos\psi = \bar{\mu}\,\mu_{\rm s} + \left(1 - \bar{\mu}^2\right)^{1/2}\left(1 - \mu_{\rm s}^2\right)^{1/2}\cos\phi. \tag{A.40}$$

A.4 PROTON-PHOTON INELASTIC COLLISIONS

The cross sections for interactions of high-energy hadrons with photons are small compared to those of matter-matter interactions. However, in some astrophysical environments, radiation density is larger than matter density and

photohadronic processes may become relevant.

The production of mesons in proton-photon interactions has been studied in detail by Mücke et al. (2000), who developed the Monte Carlo code SOPHIA to simulate photohadronic collision events. Atoyan & Dermer (2003) introduced a simplified approach, in which the cross section and the inelasticity in the proton rest frame are written as the sum of two steps functions,[2]

$$\sigma_{p\gamma}^{(\pi)}(\epsilon') \approx \begin{cases} 340\,\mu\text{barn} & 200\,\text{MeV} \leq \epsilon' \leq 500\,\text{MeV} \\ 120\,\mu\text{barn} & \epsilon' > 500\,\text{MeV} \end{cases}$$

$$K_{p\gamma}^{(\pi)}(\epsilon') \approx \begin{cases} 0.2 & 200\,\text{MeV} \leq \epsilon' \leq 500\,\text{MeV} \\ 0.6 & \epsilon' > 500\,\text{MeV}, \end{cases}$$

where ϵ' is the photon energy in the rest frame of the proton. These two energy ranges correspond to the single-pion and multiple pion production channels, respectively. The spectra are calculated in the δ-functional approximation in the energy of pions and photons. In the single-pion production channel, each π^0 is produced with an energy $E_\pi \approx K_1 E_p$ and this energy is equally distributed among the products of its decay, thus yielding

$$E_\gamma \approx \frac{1}{2} K_1 E_p = 0.1 E_p. \tag{A.41}$$

In the multiple-pion production channel almost all the energy lost by the proton is equally distributed among three leading pions π^0, π^+, and π^-. The mean energy of each pion is then $E_\pi \approx K_2 E_p/3$, and the energy of the photons results the same as in the single-pion production channel.

If p_1 and $p_2 = 1 - p_1$ are the probabilities of the $p\gamma$ collision taking place through the single-pion and multiple-pion channel, respectively, and $\xi_{pn} \approx 0.5$ is the probability of conversion of a proton into a neutron per interaction, the mean number of neutral pions created per collision is

$$n_{\pi^0} = p_1 \left(1 - \xi_{pn}\right) + p_2. \tag{A.42}$$

[2]See Begelman et al. (1990) for a more accurate approximation.

We can define define a mean inelasticity

$$\overline{K}_{p\gamma}^{(\pi)}\left(\gamma_p\right) = \frac{1}{t_{p\gamma}^{(\pi)}\left(\gamma_p\right)}\,\omega_{p\gamma}^{(\pi)}\left(\gamma_p\right), \tag{A.43}$$

where the cooling time and the collision rate are given in Eqs. (3.73) and (3.76), respectively. Then the probabilities $p_{1,2}$ can be calculated from the relation

$$\overline{K}_{p\gamma}^{(\pi)}\left(E_p\right) = p_1 K_1 + \left(1 - p_1\right) K_2. \tag{A.44}$$

The emissivity of π^0 in the δ-functional approximation is

$$\begin{aligned} Q_{\pi^0}^{(\pi)}\left(E_\pi\right) &= \int \mathrm{d}E_p\, N_p\left(E_p\right)\omega_{p\gamma}^{(\pi)}\left(E_p\right)\, n_{\pi^0}\left(E_p\right)\delta\left(E_\pi - 0.2E_p\right) \\ &= 5N_p\left(5E_\pi\right)\omega_{p\gamma}^{(\pi)}\left(5E_\pi\right) n_{\pi^0}\left(5E_\pi\right), \end{aligned} \tag{A.45}$$

where N_p is the energy distribution of relativistic protons. Taking into account that each neutral pion gives two photons, the photon emissivity results

$$\begin{aligned} q_\gamma\left(E_\gamma\right) &= 2\int \mathrm{d}E_\pi\, Q_{\pi^0}^{(\pi)}\left(E_\pi\right)\delta\left(E_\gamma - 0.5E_\pi\right) \\ &= 20N_p\left(10E_\gamma\right)\omega_{p\gamma}^{(\pi)}\left(10E_\gamma\right) n_{\pi^0}\left(10E_\gamma\right). \end{aligned} \tag{A.46}$$

If the energy losses of charged pions and muons are neglected, the emissivity of secondary pairs can be estimated in the same way. Both in the single-pion and in the multiple-pion channel each charged pion has an energy $E_\pi \approx 0.2E_p$. This energy is equally distributed among the products of meson decay, hence the energy of each electron (positron) is, on average, $E_{e^\pm} \approx 0.05E_p$. The mean number of charged pions created per proton-photon collision is

$$n_{\pi^\pm} = \xi_{pn} p_1 + 2p_2, \tag{A.47}$$

and since only one lepton is produced in each decay, the emissivity of pairs is

approximately given by

$$Q_{e^\pm}\left(E_{e^\pm}\right) = 20N_p\left(20E_{e^\pm}\right)\omega_{p\gamma}^{(\pi)}\left(20E_{e^\pm}\right)n_{\pi^\pm}\left(20E_{e^\pm}\right). \tag{A.48}$$

Kelner & Aharonian (2008) introduced new simple analytical parameterizations for the gamma-ray spectrum from photohadronic interactions. Given the distributions of relativistic protons $N_p(E_p)$ and target photons $n_{\rm ph}(\epsilon)$, the gamma-ray emissivity can be written as

$$q_\gamma\left(E_\gamma\right) = \int_{E_p^{\rm min}}^{E_p^{\rm max}} {\rm d}E_p \int_{\epsilon_{\rm thr}'^{(\pi)}/2\gamma_p}^{\infty} {\rm d}\epsilon\, \frac{1}{E_p}\, N_p(E_p)\, n_{\rm ph}(\epsilon)\, \Phi\left(\eta,\, x\right). \tag{A.49}$$

Here $\eta = 4\epsilon E_p/m_p^2c^4$ and $x = E_\gamma/E_p$. Using numerical results obtained with the code SOPHIA, the function $\Phi\left(\eta,\, x\right)$ can be approximated with an accuracy better than 10% by a simple analytical formula. Let us define $x_\pm$ as

$$x_\pm = \frac{1}{2(1+\eta)}\left[\eta + r^2 \pm \sqrt{\left(\eta - r^2 - 2r\right)\left(\eta - r^2 + 2r\right)}\right]. \tag{A.50}$$

Then, in the range $x_- < x < x_+$,

$$\Phi_\gamma\left(\eta,\, x\right) = B_\gamma\, \exp\left\{-s_\gamma\left[\ln\left(\frac{x}{x_-}\right)\right]^{\delta_\gamma}\right\}\left[\ln\left(\frac{2}{1+y^2}\right)\right]^{2.5+0.4\ln(\eta/\eta_0)}, \tag{A.51}$$

where

$$y = \frac{x - x_-}{x_+ - x_-} \tag{A.52}$$

and

$$\eta_0 = 2\frac{m_\pi}{m_p} + \frac{m_\pi^2}{m_p^2} \approx 0.313. \tag{A.53}$$

For $x < x_-$, the spectrum is independent of x,

$$\Phi_\gamma(\eta, x) = B_\gamma \left[\ln 2\right]^{2.5+0.4\ln(\eta/\eta_0)}, \tag{A.54}$$

and finally $\Phi_\gamma(\eta, x) = 0$ for $x > x_+$. The parameters B_γ, s_γ and δ_γ are functions of η. For values of $1.1\,\eta_0 < \eta < 100\,\eta_0$, these functions are tabulated in Kelner & Aharonian (2008).

At energies below the threshold for photomeson production, the main channel of proton-photon interaction is the direct production of electron-positron pairs. The cross section for pair production is often referred to as Bethe-Heitler cross section. Useful approximations for this cross section are given in Maximon (1968) (see also Chodorowski et al. 1992)

$$\sigma_{p\gamma}^{(e)}(x') \approx \begin{cases} \dfrac{2\pi}{3}\alpha_{\rm FS} r_e^2 \left(\dfrac{x'-2}{x'}\right)^3 \left(1 + \dfrac{1}{2}\eta + \dfrac{23}{40}\eta^2 + \ldots\right) & x' \lesssim 4 \\ \alpha_{\rm FS} r_e^2 \left\{\dfrac{28}{9}\ln(2x') - \dfrac{218}{27} + \left(\dfrac{2}{x'}\right)^2 \left[6\ln(2x') - \dfrac{7}{2} + \ldots\right]\right\} & x' \gtrsim 4. \end{cases} \tag{A.55}$$

Here $\eta = (x'+2)/(x'-2)$ and $x' = \epsilon'/m_e c^2$. Analytical fits for the inelasticity are given in Begelman et al. (1990). For $x' < 1000$,

$$K_{p\gamma}^{(e)}(x') \approx \frac{m_e}{m_p}\frac{4}{x'}\left[1 + 0.3957\ln\left(x'-1\right) + 0.1\ln^2\left(x'-1\right) + 0.0078\ln^3\left(x'-1\right)\right], \tag{A.56}$$

whereas for $x' > 1000$,

$$K_{p\gamma}^{(e)}(x') \approx \frac{m_e}{m_p}\frac{4}{x'}\left[\frac{-8.78 + 5.513\ln(x') - 1.612\ln^2(x') + 0.668\ln^3(x')}{3.1111\ln(2x') - 8.0741}\right]. \tag{A.57}$$

The cross section in Eq. (A.55) is two orders of magnitude larger than that for pion production, but only a small fraction of the proton energy ($\leq 2m_e/m_p$)

is lost in the interaction. Instead, in the pion creation channel, the proton transfers a 10% or more of its energy to the secondary products. As a result, despite having a smaller cross section, π-meson production becomes a more important channel of cooling for protons with energies above the corresponding energy threshold.

The spectrum of pairs created through photopair production has been studied, for example, by Chodorowski et al. (1992) and Mastichiadis et al. (2005). The emissivity of pairs in the δ-functional approximation is calculated as before. In this case the inelasticity can be approximated by its value at the threshold, $K_{p\gamma}^{(e)} = 2m_e/m_p$. Therefore, the pair injection function results

$$\begin{aligned} Q_{e^\pm}^{(p\gamma)}(E_e) &= 2\int \mathrm{d}E_p N_p\left(E_p\right)\omega_{p\gamma}^{(e)}\left(E_p\right)\delta\left(E_e - \frac{m_e}{m_p}E_p\right) \\ &= 2\,\frac{m_p}{m_e}\,N_p\left(\frac{m_p}{m_e}E_e\right)\omega_{p\gamma}^{(e)}\left(\frac{m_p}{m_e}E_e\right). \end{aligned} \tag{A.58}$$

See also Kelner & Aharonian (2008) for a more detailed treatment.

A.5 Optical depth by photon-photon annihilation in the radiation field of the accretion disc

The general expression for the optical depth for a photon with energy E_γ created at an arbitrary position $\vec{r}_\gamma = (R_\gamma, \varphi_\gamma, z_\gamma)$ due to photon-photon annihilation is given by

$$\tau_{\gamma\gamma}(E_\gamma, \vec{r}_\gamma) = \int_0^\infty \mathrm{d}\lambda \int_{\epsilon_{\mathrm{thr}}}^\infty \mathrm{d}\epsilon \oint \mathrm{d}\Omega\,(1-\cos\theta)\,\sigma_{\gamma\gamma}(E_\gamma, \epsilon, \theta)\,n_{\mathrm{ph}}(\epsilon, \vec{r}, \Omega). \tag{A.59}$$

Here n_{ph} is the energy distribution of the target radiation field (the accretion disc radiation field in the case we are interested in) and $\sigma_{\gamma\gamma}$ is the annihilation cross section. The variable λ is the length of the path traversed by the jet photon until the interaction point and θ is the collision angle. All the relevant geometrical parameters are defined in Figure A.5.

It is convenient to perform the integration over the area of the disc instead of over solid angle. The relation between the element of solid angle and the element of area $\mathrm{d}A = R\,\mathrm{d}R\,\mathrm{d}\varphi$ in cylindrical coordinates is

$$\mathrm{d}\Omega = \frac{\cos\eta\, R\,\mathrm{d}R\,\mathrm{d}\varphi}{\ell^2}. \tag{A.60}$$

Here η is the angle between the normal to the disc and the direction of motion of the disc photon, and ℓ is the distance between the interaction point and the point of emission of the disc photon.

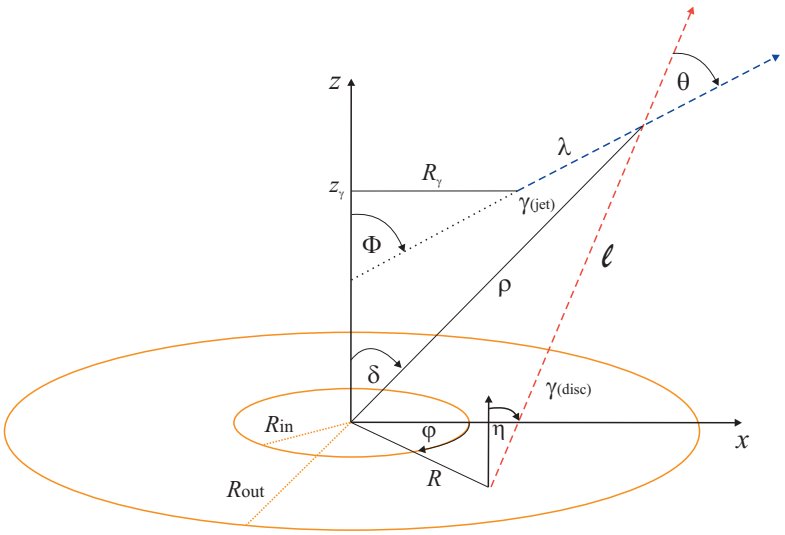

Figure A.5: Sketch of the accretion disc. The geometrical parameters relevant to the calculation of the optical depth in the radiation field of the accretion disc are indicated.

Since the system has azimuthal symmetry, we can assume that the jet photon propagates in the (x, z) plane (so $\varphi_\gamma = 0$) and its trajectory makes an angle Φ with the z-axis. In this case, the variables ℓ, $\cos\eta$, and $\cos\theta$ can be written as (e.g. Becker & Kafatos 1995)

$$\ell^2 = \rho^2 + R^2 - 2\rho R \sin\delta\cos\varphi, \tag{A.61}$$

$$\cos\theta = \frac{\rho\cos(\delta - \Phi) - R\cos\varphi\cos\Phi}{\ell}, \tag{A.62}$$

$$\cos\eta = \frac{\rho\cos\delta}{\ell}. \tag{A.63}$$

The parameters ρ and δ are related to z_γ, R_γ, Φ, and λ as

$$\rho^2 = R_\gamma^2 + z_\gamma^2 + \lambda^2 + 2\lambda\left(R_\gamma\sin\Phi + z_\gamma\cos\Phi\right), \tag{A.64}$$

$$\sin\delta = \frac{R_\gamma + \lambda\sin\Phi}{\rho}, \tag{A.65}$$

$$\cos\delta = \frac{z_\gamma + \lambda\cos\Phi}{\rho}. \tag{A.66}$$

For simplicity, we calculated the optical depth for photons created on the jet axis, so we set $R_\gamma = 0$.

B

NON-THERMAL RADIATION FROM BLACK HOLE CORONAE

As discussed in Chapter 2, the hard X-ray emission from X-ray binaries is generally thought to originate in a corona of hot plasma that surrounds the compact object, and partially overlaps spatially with the accretion disc. The hard X-rays are produced by the Compton up-scattering of photons from the accretion disc off the thermal electrons in the corona. This mechanism satisfactorily explains the hard power-law shape of the SED up to energies of $\sim 100 - 200$ keV. Further evidence of the presence of the corona is the detection in some XRBs of the Fe Kα emission line at ~ 6.4 keV.

In microquasars, the radio/X-rays correlations observed in some sources suggest a significant (possibly dominant) contribution of synchrotron radiation from the jets to the hard X-ray spectrum. In this PhD thesis we adopted the view that the broadband SED of microquasars is dominated by non-thermal emission from the jets,[1] and largely explored the predictions of this scenario.

The corona, however, might also be a site of efficient particle acceleration. This is interesting, since it implies the possibility of non-thermal radiation from XRBs that do not produce jets. A suggested mechanism to heat the corona is the magnetic reconnection of field loops attached to the accretion disc (Galeev et al. 1979). Violent reconnection may lead to the formation of shocks, as in the solar corona. A non-thermal particle population might then arise in the corona as the result of diffusive shock acceleration (e.g. Spruit 1988, Schneider 1993). Direct Fermi acceleration by converging magnetic winds is also a possibility

[1] Plus thermal radiation from an accretion disc, if observed.

(Tsuneta & Naito 1998, Kowal et al. 2011). This is interesting, since it implies the possibility of non-thermal radiation from XRBs that do not produce jets.

The effects of a non-thermal population of electrons in a hot corona were considered, for example, by Kusunose & Mineshige (1995) and more recently by Belmont et al. (2008) and Vurm & Poutanen (2009). The results of the injection of non-thermal protons and secondary pions and muons in a magnetized corona has not been comprehensively studied so far. Here we present detailed calculations of the radiative output of non-thermal particles in a simplified model of magnetized corona. The reader is referred to Romero et al. (2010b) for the full version of the work, and to Vieyro (2012) for further refinements and expansion of the model.

Figure B.1 shows a sketch of the main components of the system. We assume a spherical corona with a radius R_c and an accretion disc that penetrates the corona up to $R_p < R_c$. For simplicity, we consider the corona to be homogeneous and in a steady state.

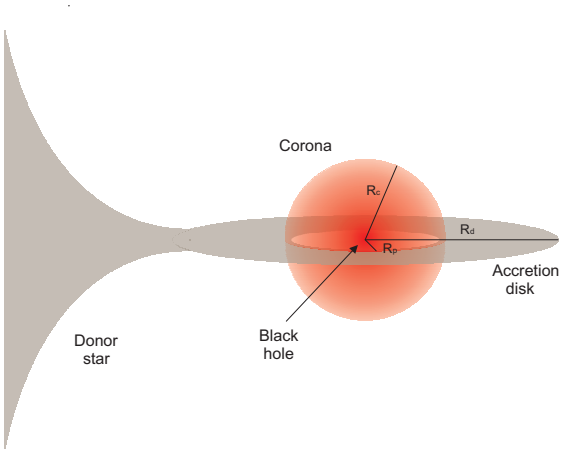

Figure B.1: Sketch of the corona, the accretion disc, and the donor star (not to scale). The author thanks Florencia Vieyro for the picture.

We take the luminosity of the corona to be 1% of the Eddington luminosity of a 10 $M_\odot$ black hole; this yields $L_c = 1.3 \times 10^{37}$ erg s^{-1}. For the remaining parameters of the model we adopted typical values inferred for Cygnus X-1 in low-hard state, see Poutanen et al. (1997). The complete list of parameters (adopted and derived) is shown in Table B.1.

The jet power in microquasars is related to the magnetic field at the base

Table B.1: Values of the parameters in the non-thermal corona model.

Parameter [units]	Symbol	Value
Black hole mass [$M_\odot$]	$M_{\rm BH}$	$10^{(1)}$
Characteristic temperature of the accretion disc [keV]	$kT_{\rm d}$	0.1
Radius of the corona [cm]	$R_{\rm c}$	$5.2 \times 10^{7(1,2)}$
Ratio of the inner disc radius to the corona radius	$R_{\rm p}/R_{\rm c}$	$0.9^{(1)}$
Covering fraction of the corona	$D(1+S)$	$0.08^{(1)}$
Temperature of the thermal electrons [K]	T_e	10^9
Temperature of the thermal ions [K]	T_i	10^{12}
Number density of the thermal plasma [cm^{-3}]	n_i, ne	6.2×10^{13}
Cutoff energy of the power-law X-ray spectrum [keV]	$E_{\rm c}$	150
Index of the power-law X-ray spectrum	δ	1.6
Normalization constant of the power-law X-ray spectrum [erg$^{3/5}$ cm^{-3}]	$A_{\rm ph}$	2.6×10^{12}
Acceleration efficiency	η	10^{-2}
Magnetic field in the corona [G]	$B_{\rm c}$	5.7×10^5
Advection velocity [c]	v	0.1
Relativistic hadrons-to-leptons power ratio	a	1 - 100

(1) Typical value for Cygnus X-1 in the low-hard state (Poutanen et al. 1997).
(2) $R_{\rm c} = 35 R_{\rm grav}$.

of the jet, since the jet launching mechanism is likely of magnetic origin. The corona and the jet launching region are thought to be regions with similar properties in the standard jet-disk symbiosis model (Malzac et al. 2009). In fact, the corona itself might be ejected in form of discrete outflows during a spectral transition (Rodriguez et al. 2003). For Cygnus X-1 and similar systems, the jet kinetic power is of the same order of the luminosity of the corona. Then, to obtain an estimate of the mean magnetic field B in the corona, we demand equipartition between the magnetic energy density $U_{\rm B} = B^2/8\pi$, and the energy density of the radiation field (see e.g. Bednarek & Giovannelli 2007 and references therein)

$$\frac{B^2}{8\pi} = \frac{L_{\rm c}}{4\pi R_{\rm c}^2 c}, \tag{B.1}$$

where $L_{\rm c}$ is the total luminosity of the corona. For $L_{\rm c} = 1.3 \times 10^{37}$ erg s^{-1} and $R_{\rm c} = 5.2 \times 10^7$ cm, we obtain $B = 5.7 \times 10^5$ G.

ADAF models predict that the corona consists of a two-temperature plasma, with an electron temperature $T_e \approx 10^9$ K and an ion temperature $T_i \approx 10^{12}$ K (Narayan & Yi 1995a,b). The kinetic energy density of the thermal component of the corona is then

$$U_{\rm th} = \frac{3}{2} n_e k T_e + \frac{3}{2} n_i k T_i, \tag{B.2}$$

where n_i and n_e are the ion and electron number densities, respectively. We assume equipartition between the magnetic and the thermal kinetic energy densities to estimate the density of the thermal plasma. From $U_{\rm th} = U_{\rm B}$, we obtain $n_i \sim n_e = 6.2 \times 10^{13}$ cm^{-3} for a corona mainly composed of hydrogen.

The hard X-ray emission of the corona is characterized by a power-law with an exponential cutoff at $\sim 100 - 200$ keV, as observed in several X-ray binaries in the low-hard state; see Chapter 2, Section 2.2.1. We parameterize the photon energy density (in units of erg^{-1} cm^{-3}) for this spectral component as

$$n_{\rm ph}(E) = A_{\rm ph} E^{-\delta} e^{-E/E_{\rm c}}. \tag{B.3}$$

In accordance with the well-studied case of Cygnus X-1 (e.g. Poutanen et al.

1997), we adopt $\delta = 1.6$ and $E_c = 150$ keV. The normalization constant A_{ph} can be obtained from L_c,

$$\frac{L_c}{4\pi R_c^2 c} = \int_0^\infty E\, n_{ph}(E) dE. \tag{B.4}$$

The total power injected in relativistic protons and electrons is a fraction of the luminosity of the corona, $L_{rel} = L_p + L_e = q_{rel} L_c$, with $q_{rel} = 10^{-2}$. For these species, we adopt an injection function that is a power-law in energy

$$Q(E) = Q_0\, E^{-\alpha} \exp\left(-\frac{E}{E_{max}}\right) \tag{B.5}$$

with a canonical spectral index $\alpha = 2.2$. As explained for the jet model, the normalization constant Q_0 can be obtained from the total power injected in relativistic protons or electrons. We consider proton-dominated models with $L_p/L_e = a = 100$, and equipartition models with $a = 1$.

The maximum energy E_{max} is calculated from the balance of the total cooling rate and the acceleration rate (we took $\eta = 10^{-2}$ for the acceleration efficiency parameter). For electrons (and also muons and secondary electron-positron pairs) the radiative cooling is due to synchrotron radiation, relativistic Bremsstrahlung, and inverse Compton scattering. For protons (and pions) is due to synchrotron radiation, and proton-proton (pion-proton) and proton-photon (pion-photon) inelastic collisions. We get maximum energies of $E_{max}^{(e)} \approx 7.9 \times 10^9$ eV and $E_{max}^{(p)} \approx 8.0 \times 10^{14}$ eV for primary electrons and protons, respectively. These values are compatible with the Hillas criterion, given the size of the corona.

We consider two target photon fields for IC and proton-photon interactions: the power-law photon field of the corona and the radiation field from the disc. The latter can be represented by a black body of temperature $kT_d = 0.1$ keV (Poutanen et al. 1997). The radiation field in the corona is diluted to account for the solid angle subtended by the disc as seen from the corona. This is performed by means of a parameter D, that represents the fraction of the radiation emitted in the disc that irradiates the corona, and the parameter S, that is the ratio of intrinsic seed photon production in the corona to the seed photon luminosity injected from outside. We take the estimates of D and S given in

Poutanen et al. (1997) for the low-hard state of Cygnus X-1. For additional details the reader is referred to Poutanen et al. (1997), and to Done et al. (2007) for a general picture of the Comptonization process.

Since the corona is considered homogeneous, we use the transport equation in the one-zone version to calculate the energy distributions of all non-thermal particle species,

$$\frac{d}{dE}\left(bN\right) + \frac{N}{T} = Q, \tag{B.6}$$

where $b(E) = dE/dt$ is the total energy loss rate. The rate of catastrophic losses is the sum of the decay rate (when it corresponds) and the rate of particle escape from the corona,

$$\frac{1}{T(E)} = \frac{1}{T_{\rm esc}} + \frac{1}{T_{\rm dec}(E)}. \tag{B.7}$$

We consider two types of corona, each with one relevant mechanism of particle escape. One is an ADAF-like corona, where matter is advected onto the black hole. This model was discussed in detail for Cygnus X-1 by Dove et al. (1997) and Esin et al. (1998). In this case, particles fall onto the compact object with a mean radial velocity of the order of the free-fall velocity $v \approx 0.1c$ (Begelman et al. 1990). The characteristic advection timescale is then

$$T_{\rm adv} = \frac{R_{\rm c}}{v}. \tag{B.8}$$

The other model considered here is a static corona (e.g., supported by magnetic fields, see Beloborodov 1999) where the relativistic particles can be removed by diffusion. The diffusion coefficient in the Bohm regime is $D(E) = r_{\rm gy}c/3$, where $r_{\rm gy} = E/(eB)$ is the gyroradius of the particle. The diffusion timescale is

$$T_{\rm diff} = \frac{R_{\rm c}^2}{2D(E)}. \tag{B.9}$$

Figure B.2 shows all the contributions of non-thermal particles to the total luminosity for $a = 100$ and different escape regimes - advection or diffusion.

The luminosities produced by hadrons and muons are higher in models with a static corona and diffusion of the relativistic particles. This is because, in models with diffusion, the time it takes for protons and pions to leave the corona is longer, and they can cool significantly. In models with $a = 100$, the non-thermal emission at $E_\gamma > 1$ MeV is dominated by synchrotron and IC radiation of secondary pairs. At very high energies, the main contributions to the spectrum are due to photomeson production in all models. We note that below $\sim$ 150 keV the source will be totally dominated by thermal Comptonization (not shown in these plots for clarity, see the right panels of the same figure).

There are two parameters that determine the relevant radiative processes: the hadronic content in the plasma and the advection velocity. If the hadronic content is high ($a = 100$ as shown here), then a large number of secondary particles are expected to increase the emission at high energies. Advection, however, also has an important role, because a significant part of the proton content will be engulfed by the black hole reducing the emission. The overall SED is then the result of the balance between the effect of these two parameters.

The total luminosities corrected by photon-photon absorption in the power-law radiation field of the corona (orange curves in Figure B.2, see Eq. (B.3)) are also shown. For 10 MeV $< E_\gamma <$ 1 TeV, almost all the non-thermal emission is absorbed.

Finally, we applied the non-thermal corona model to Cygnus X-1. Cygnus X-1 is a very bright X-ray binary, formed by a black hole of $(14.8 \pm 1.0)\ M_\odot$[2] and a companion O9.7 Iab star of $(19.2 \pm 1.9)\ M_\odot$ (Orosz et al. 2011), at an estimated distance of $\sim$ 1.86 kpc (Reid et al. 2011). The X-ray emission alternates between soft and hard states. The spectrum in both states can be approximately represented as the sum of a black body and a power-law with an exponential cutoff (e.g. Poutanen et al. 1997). During the soft state, the black body component is dominant and the power-law is steep, with a photon spectral index ~ 2.8 (e.g. Frontera et al. 2001). During the low-hard state more energy is in the power-law component, that is hard with a spectral index ~ 1.6 (e.g. Gierlinski et al. 1997).

[2]The results of Orosz et al. (2011) are very recent; here we used a previous estimate of $\sim 10.1\ M_\odot$ (Herrero et al. 1995) for the mass of the black hole. In Vieyro & Romero (2012) the new values are adopted.

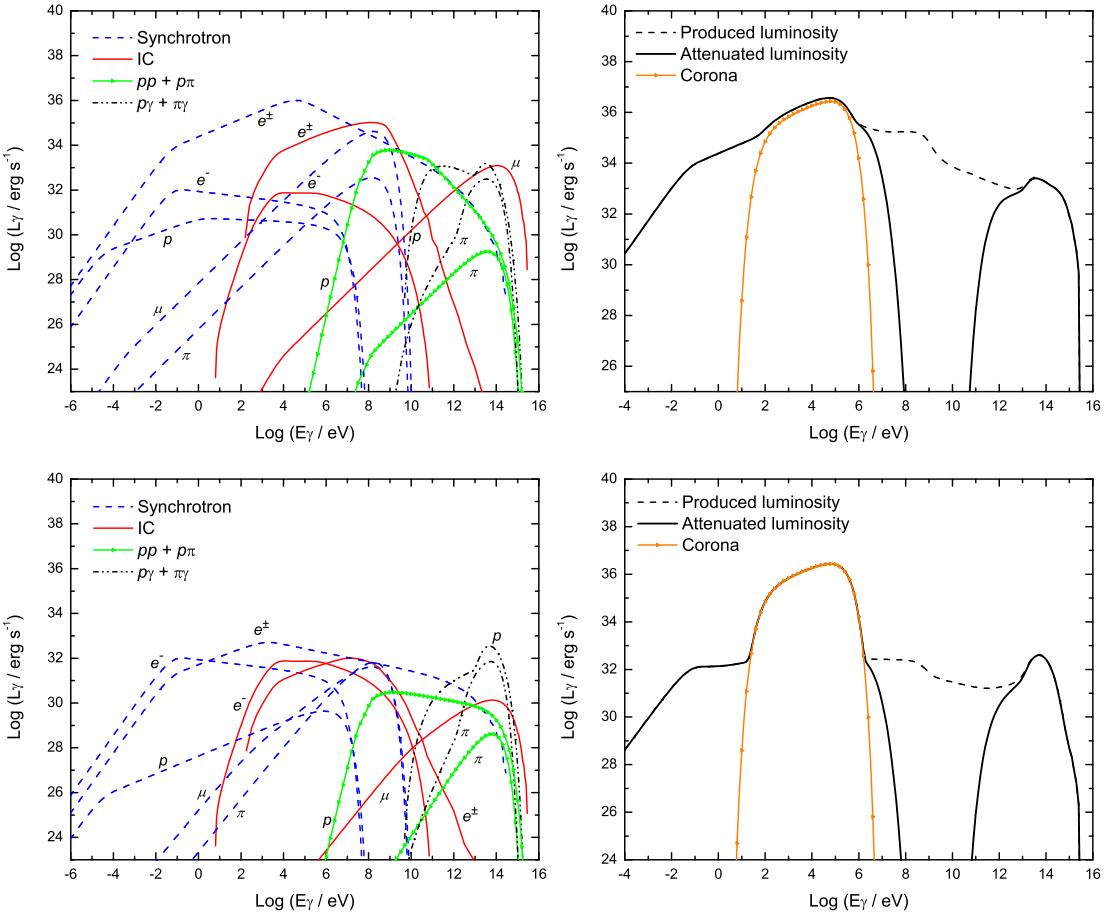

Figure B.2: Primary and absorbed spectral energy distributions obtained for $a = 100$, in a model with diffusion (top) or advection (bottom).

McConnell et al. (2000) reported a high-energy tail in the low X-ray state of Cygnus X-1, extending from 50 keV to $\sim$ 5 MeV. The data at MeV energies, collected with the COMPTEL instrument of the *Compton Gamma-Ray Observatory*, can be described as a power-law with a photon spectral index of 3.2. Observations with the satellite *INTEGRAL* have confirmed the existence of a supra-thermal tail in the spectrum (Cadolle Bel et al. 2006). So-called hybrid thermal/non-thermal models have been applied by Poutanen & Svensson (1996) and Coppi (1999) to fit the observed spectrum. These models consider a hybrid pair plasma with a thermal and a non-thermal component. In particular, using the EQPAIR code, McConnell et al. (2000) concluded that either the magnetic field in Cygnus X-1 is substantially below equipartition (at least

to within an order of magnitude), or the observed photon tail has a different origin than that related to locally accelerated electrons.

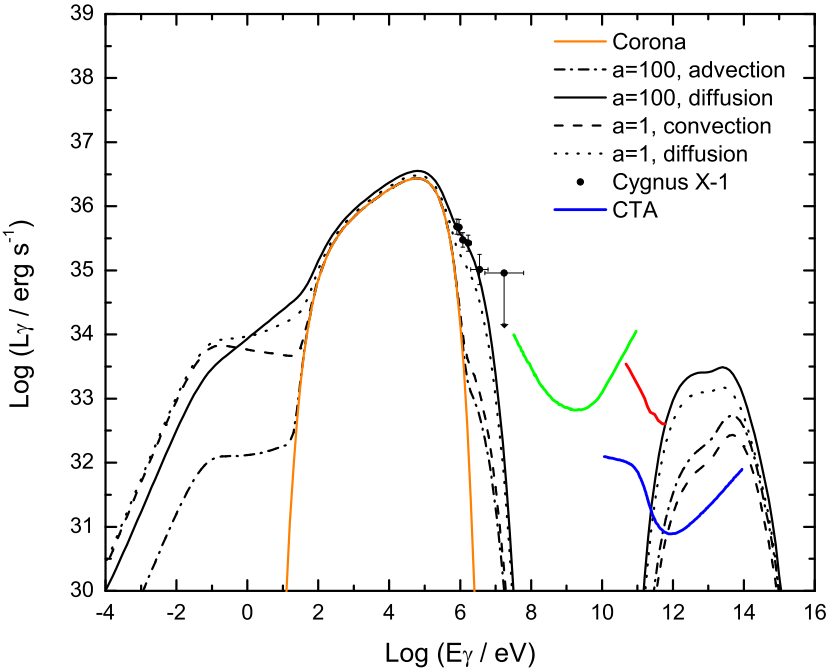

Figure B.3: Spectral energy distribution of Cygnus X-1 predicted by the non-thermal corona model, for different values of the parameters. Observational data from McConnell et al. (2000). The sensitivity curves of *Fermi* (green), MAGIC (red), and CTA (blue) are also plotted.

Figure B.3 shows the predictions of our corona model for Cygnus X-1. All the models assume equipartition magnetic fields. As expected, the emission in the MeV range is dominated by products of hadronic interactions and secondary pairs. The best fits are for a model with $a = 100$ and little or null advection, with absorption playing a major role in shaping the spectrum. At high-energies $E_\gamma > 1$ TeV, a bump produced mainly by photomeson interactions appears. It might be easily detectable in the near future with CTA, if Cygnus X-1 is within its declination range.

The flares at gamma-ray energies detected with MAGIC (Albert et al. 2007) and *AGILE* (Sabatini et al. 2010) were likely produced in the jet of Cygnus X-1 (e.g. Bosch-Ramon et al. 2008). In our corona model, even if large magnetic reconnection events were to modify the non-thermal population on short

timescales, the GeV emission would be totally suppressed by photon annihilation in the thermal bath of the corona. Gamma-ray flaring events at GeV energies, then, cannot arise from a strongly magnetized corona, at least in systems with luminous donor stars.

C

LIST OF PUBLICATIONS

This results presented in this thesis were published in the following articles:

An inhomogeneous lepto-hadronic model for the radiation of relativistic jets. Application to XTE J1118+480
G. S. Vila, G. E. Romero, & N. A. Casco
Astron. Astroph., 538, A97 (2012)

Leptonic/hadronic models for electromagnetic emission in microquasars: the case of GX 339-4
G. S. Vila & G. E. Romero
Mon. Not. R. Astron. Soc., 403, 1457-1468 (2010)

Non-thermal processes around accreting galactic black holes
G. E. Romero, F. L. Vieyro, & G. S. Vila
Astron. Astroph., 519, A109 (2010)

Non-thermal radiation from Cygnus X-1 corona
F. L. Vieyro, G. E. Romero, & G. S. Vila
Int. J. Mod. Phys. D, 19, 783-789 (2010)

On the nature of the AGILE galactic transient sources
G. E. Romero & G. S. Vila
Astron. Astroph. (Letters), 494, L33-L36 (2009)

The proton low-mass microquasar: high-energy emission
G. E. Romero & G. S. Vila
Astron. Astroph., 485, 623-631 (2008)

Models for gamma-ray production in low-mass microquasars
G. S. Vila & G. E. Romero
Int. J. Mod. Phys. D, 17, 1903-1908 (2008)

UNIVERSIDAD DE RU
ARCTMVRTVSROBVRT